UNIVERSITÀ
DEGLI STUDI
FIRENZE

PhD in
Physics and Astrophysics

CYCLE XXXIV

COORDINATOR Prof. Raffaello D'Alessandro

Numerical study of the properties of compact objects in general relativity and scalar-tensor theories

Academic Discipline (SSD) FIS/05

Doctoral Candidate
Dr. Soldateschi Jacopo

Supervisor
Prof. Bucciantini Niccolò
Prof. Del Zanna Luca

Coordinator
Prof. D'Alessandro Raffaello

Years 2018/2021

UNIVERSITÀ
DEGLI STUDI
FIRENZE

UNIVERSITÀ DEGLI STUDI DI FIRENZE

DIPARTIMENTO DI FISICA E ASTRONOMIA
CORSO DI DOTTORATO IN FISICA E ASTRONOMIA

NUMERICAL STUDY OF THE PROPERTIES OF COMPACT OBJECTS IN GENERAL RELATIVITY AND SCALAR-TENSOR THEORIES

Candidate
Jacopo Soldateschi

Supervisors
Prof. Niccolò Bucciantini

Prof. Luca Del Zanna

PhD Coordinator
Prof. Raffaello D'Alessandro

CICLO XXXIV, 2018-2021

Università degli Studi di Firenze, Dipartimento di Fisica e Astronomia.

To those who stood by me in the darkest times
and cheered with me in the most joyful moments

Abstract

Among the possible extensions of general relativity that have been put forward to address some long-standing issues in our understanding of the Universe, scalar-tensor theories have received a lot of attention for their simplicity. Interestingly, some of these predict a potentially observable non-linear phenomenon, known as spontaneous scalarisation, in the presence of highly compact matter distributions, as in the case of neutron stars. Spontaneous scalarisation allows some neutron stars to display strong and potentially observable deviations from their general-relativistic counterparts, while allowing scalar-tensor theories containing such effect to satisfy severe observational constraints. For this reason, neutron stars are fundamental to test some of the most studied theories of gravity alternative to general relativity. Moreover, neutron stars are ideal laboratories for investigating the properties of matter under extreme conditions and, in particular, they are known to harbour the strongest magnetic fields in the Universe. One of the consequences of harbouring such powerful fields is the deformation of the neutron star structure, leading, together with rotation, to the emission of continuous gravitational waves. On the one hand, the details of their internal magnetic fields are mostly unknown. Likewise, their internal structure, encoded by the equation of state, is highly uncertain. Unfortunately, the effects of the equation of state and of the scalar field are in some ways degenerate, further complicating the scenario.

In this work we present a detailed study of magnetised neutron stars in general relativity and scalar-tensor theories. First, we carry out a study of the parameter space considering the two extreme geometries of purely toroidal and purely poloidal magnetic fields, varying both the strength of the magnetic field and the intensity of scalarisation. We compare our results with magnetised general-relativistic solutions and unmagnetised scalarised solutions, showing how the mutual interplay between magnetic and scalar fields affect the magnetic and the scalarisation properties of neutron stars. Then, we focus our attention to their magnetic deformation, exploring how the scalar field affects the emission of continuous gravitational waves. In this regard, we present a study of magnetised neutron stars for various realistic equations of state considered viable by observations and nuclear physics constraints, showing that it is possible to

find simple relations between the magnetic deformation of a neutron star, its mass, and its radius. Such relations are quasi-universal, meaning that they are mostly independent from the equation of state of the neutron star. Thanks to their formulation in terms of potentially observable quantities, as we discuss, our results could help to constrain the magnetic properties of the neutron stars interior and to better assess the detectability of continuous gravitational waves by isolated neutron stars, without knowing their equation of state. These results are derived both in general relativity and in scalar-tensor theories, in this case by also considering the scalar charge. We show that even in this case, general relations that account for deviations from general relativity still hold, which could potentially be used to set constraints on the gravitational theory. Moreover, we show how the quasi-universal relations we find can be used to assess the detectability of continuous gravitational waves from pulsars in the Galaxy by gravitational waves detectors. Finally, we propose a novel way to test deviations from general relativity in the vicinity of accreting neutron stars, through the use of the Fe K_α fluorescent line at 6.4 keV. In fact, we show how the presence of a scalar field changes the expected line shape with respect to general relativity, revealing that even if those changes are in general of the order of a few percent, they are potentially observable with the next generation of X-ray satellites.

List of publications

International peer-reviewed journals

- Bucciantini, N. & Soldateschi, J. 2020, Monthly Notices of the Royal Astronomical Society: Letters, *Iron line from neutron star accretion discs in scalar tensor theories*, Volume 495, Issue 1, pp.L56-L60
- Soldateschi, J., Bucciantini, N., & Del Zanna, L. 2020, Astronomy & Astrophysics, *Axisymmetric equilibrium models for magnetised neutron stars in scalar-tensor theories*, Volume 640, id.A44, 24 pp.
- Soldateschi, J., Bucciantini, N., & Del Zanna, L. 2021, Astronomy & Astrophysics, *Magnetic deformation of neutron stars in scalar-tensor theories*, Volume 645, id.A39, 8 pp.
- Soldateschi, J., Bucciantini, N., & Del Zanna, L. 2021, Astronomy & Astrophysics, *Quasi-universality of the magnetic deformation of neutron stars in general relativity and beyond*, Volume 654, id.A162, 18 pp.
- Soldateschi, J. & Bucciantini, N. 2021, Galaxies, *Detectability of continuous gravitational waves from magnetically deformed neutron stars*, Volume 9, Issue 4, 20 pp.

International non peer-reviewed journals

- Soldateschi, J. & Bucciantini, N. 2021, Il Colle di Galileo, *Teorie alternative della gravità e stelle di neutroni*, Volume 10, Number 2

Proceedings of international conferences

- Soldateschi, J., Bucciantini, N., & Del Zanna, L. 2021, Contribution to the 2021 Gravitation session of the 55th Rencontres de Moriond, *Axisymmetric equilibrium models for magnetised neutron stars in scalar-tensor theories*, arXiv:2105.04889v2 [astro-ph.HE]
- Soldateschi, J., Bucciantini, N., & Del Zanna, L. 2021, Contribution to the Sixteenth Marcel Grossmann Meeting , *Quasi-universality of the magnetic deformation*

of neutron stars in general relativity and beyond, arXiv:2110.09301 [astro-ph.HE]

- Bucciantini, N. & Soldateschi, J. 2021, Contribution to the IAU Symposium 363, *Modeling the deformability of magnetized NSs in the light of future Continuous Gravitational Waves detection.*

Contents

Chapter 1

Introduction

In this chapter we introduce the setting of this work, that is neutron stars (NSs) in alternative theories of gravity (ATG). In particular, in Sect. 1.1 we present the main reasons that hint at the need to extend general relativity (GR), while in Sect. 1.2 we describe the relevance of NSs astrophysics, both per se and in the quest to unveil possible breakdowns of GR.

1.1 The need to extend general relativity

The theory of GR has collected an incredible number of successes in the more than 100 years since its creation. For this reason, it has been - and is currently - considered as the standard theory that describes the gravitational interaction. However, parallel to its successes, a number of issues and shortcomings have emerged in the last decades which hint at the possibility that it may not be the final theory of the gravitational interaction. These issues arise both from the theoretical framework on top of which GR is built and from observations of gravitational phenomena at the galactic and cosmological scale.

1.1.1 The theoretical point of view

The search for a 'theory of everything' - a hypothetical theoretical framework which encompasses all fundamental interactions of nature and is able to link together all physical aspects of the Universe - is one of the main challenges of theoretical physics. This goal has led, in the past decades, to several attempts to unify the laws of gravitation to the other interactions (Capozziello & de Laurentis 2011) through the conceptual apparatus of quantum mechanics to describe the fundamental physical fields permeating the Universe. While there is no final proof that the gravitational interaction should

have some quantum representation at high energies and small scales, or even that it should keep its nature as an interaction, there are many compelling reasons why it seems reasonable to unify GR with the quantum theory of fields.

This problem has been tackled from two different perspectives. The 'canonical' approach (Witten 1962) is based on the canonical quantisation procedure and consists in a Hamiltonian formulation of GR, such that the Hamiltonian, in the limit of flat spacetime, assumes the role of the generator of time translations. The 'covariant' approach (Wallace 2000) makes use of the toolbox of quantum field theory, and consists in splitting the spacetime metric into a kinematical, usually flat, part and a dynamical component which is small in magnitude with respect to the flat background. The geometry of the background spacetime is the Minkowski one, which allows one to define the notions of causality and time. Then, the quantisation procedure is applied to the dynamical part of the metric and the quanta arising from this procedure are spin two particles called gravitons. As suggested by these two approaches, the main problem in unifying the gravitational and the quantum domains is the fact the spacetime onto which the quantum fields are defined is a dynamical variable itself, and this generally prevents the introduction of basic notions such as causality, time and evolution. The covariant approach is the one closer to the known physics of particles and fields, in that it is possible to extend the perturbative methods of quantum electrodynamics to gravitation. However, covariant quantum gravity is not renormalisable at different orders of perturbation (Deser 2000), thus this approach is valid only in the low energy and large scales domain. While sufficiently far from the Planck scale GR and first order corrections describe the gravitational interaction, near the Planck era a full, but unknown, theory of gravity has to be invoked. Thus, in this approach it makes sense to add higher order terms to the Hilbert-Einstein action, that is the action that leads to Einstein's equations. Indeed, one of the main classes of extentions of GR is that of '$f(R)$ theories' (Buchdahl 1970; De Felice & Tanaka 2010), where the scalar curvature R in the Hilbert-Einstein action is replaced with a different functional dependence. An alternative approach is that of 'supergravity' (Van Nieuwenhuizen 1981), where gravity is treated neglecting the other fundamental interactions. This approach comes from the study of the electroweak interaction, where unification of the electromagnetic (EM) and the weak interaction suggests that a consistent theory of gravitation might be possible when it is coupled to matter. Its problem is that it is non-renormalizable at orders higher than two (Deser 2000). Finally, 'string theories' (Green et al. 1988) replace the very concept of particle by that of a string, an extended object. The usual particles, including the graviton, are considered excitations of the string. In these theories, a natural cut-off for the divergences at small scales is given by the string length, which is of Planck size. At scales larger that the Planck scale, the action can be written in terms of scalar and tensor fields, and this leads to an effective theory of gravitation which

includes scalar fields non-minimally coupled to gravity, as in 'scalar-tensor theories' (STTs) (Brans & Dicke 1961; Wagoner 1970; Fujii & Maeda 2003). We describe in detail the full theoretical framework of STTs in Chap. 2.

While a consistent - unitary and renormalisable - theory of quantum gravity does not yet exist, many possible ATG have been developed that account for some of its shortcomings. In the low energy and large scales regime - with respect to Planck scales - they show that GR can be extended by introducing in the Hilbert-Einstein action either terms of higher order in the curvature invariants [leading to $f(R)$ theories] or scalar fields non-minimally coupled to gravity (leading to STTs) and, at the first order, these generalisations lead to a consistent theory of gravitation. While these two theories are, arguably, the most natural and simple extension of GR - and are, to some extent, equivalent (Sotiriou 2006) - many other ATG have been studied. Just to name a few, 'Gauss-Bonnet gravity' (Lovelock 1971), which increases the dimensionality of the spacetime; 'scalar-tensor-vector gravity' (Moffat 2006), in which the gravitational interaction is mediated by a scalar and a vector field, in addition to the spacetime metric; 'bigravity' (Rosen 1940), in which the spacetime is described by two metric tensors.

1.1.2 The observational point of view

Astronomical observations in the last few decades have shown how the theoretical framework composed by GR and the standard model of particle physics is no longer able to perfectly explain how gravity works at galactic, extra-galactic and cosmological scales. Two main lines of reasoning can be followed to tackle this problem. On the one hand, we could try to retain GR as the true theory of gravity, but then, given the observations, we would need to suppose the existence of some kind of exotic matter-energy ('dark matter' and 'dark energy') which fills up $\sim$ 95% of the content of the Universe (Trimble 1987; Peebles & Ratra 2003). On the other hand, we could suppose that GR may not be the final theory of gravity, and this is the approach followed by ATG.

Our current cosmological model, the 'Λ cold dark matter model', assumes that the cosmological constant Λ describes dark energy and is responsible for driving the accelerated expansion of the Universe (Sahni & Starobinsky 2000). However, it fails in explaining why the observed value of Λ is roughly 120 orders of magnitude lower than the value predicted by particle physics (Burgess 2015). It also doesn't explain the so-called 'coincidence problem', that amounts to explain why the vacuum energy density Λ is comparable to the matter density at the present age (Burgess 2015). A popular tentative solution is that of 'quintessence' (Padmanabhan 2003; Copeland et al. 2006), where the cosmological constant is replaced with a scalar field rolling slowly down a potential. While successful in explaining data, the quintessence model still suffers from

the coincidence problem: while the quintessence dark energy evolves in the same way as matter for a long time, at late times it changes behaviour and begins to dominate akin to a dynamical cosmological constant, causing the dark energy and dark matter densities to be comparable just at the present era. Moreover, the supposed origin of the quintessence scalar field is not clear, and there is an uncertainty in choosing the right scalar field potential necessary to obtain the acceleration of the Universe. It is worth stressing that the present-day acceleration of the Universe requires a negative pressure component in its composition, but it tells nothing about the supposed origin or nature of the cosmic fluid causing it. For this reason, another solution which is advocated is that of 'unified dark energy' and 'unified dark matter' models (Kamenshchik et al. 2001; Padmanabhan 2002; Bassett et al. 2003; Nojiri & Odintsov 2006b,a), where a single cosmic fluid takes the role of the dark sector, behaving like dark matter at high densities and like dark energy at low densities. In this case, the coincidence problem is naturally solved.

As anticipated, a different way to approach the problem of cosmic acceleration is that of ATG, which suppose that the observed acceleration of the Universe does not imply the existence of unknown cosmic fluid, but rather the signal of a breakdown of the laws of gravitation as predicted by GR. For example, a quintessence-like behaviour can be obtained with higher-order gravity actions, which incorporate effective fundamental physics models (Capozziello & Fang 2002; Nojiri & Odintsov 2006; De Felice & Tanaka 2010; Capozziello & De Laurentis 2010; Faraoni & Capozziello 2011). These models are able to explain observational data by providing a geometrical explanation for the expansion of the Universe, thus eluding the problematic issue of the nature of a quintessence scalar field.

1.1.3 Why scalar-tensor theories?

As we have seen, the approach of modifying GR to try and solve its shortcomings can lead to a variety of different ATG. Here we explain why STTs are among the most promising alternatives to GR. We saw that they are predicted to be the low-energy limit of some possible theories of quantum gravity (Damour et al. 2002). In addition, most of them respect the 'weak equivalence principle' (WEP) - that is they are metric theories of gravity (Will 2014) - which has been extremely well tested (Touboul et al. 2017); however STTs violate the strong equivalence principle (SEP), which means that tests using self-gravitating bodies are ideal to constrain them (Barausse 2017). They also seem to be free of some of the pathologies affecting other extensions of GR (DeFelice et al. 2006; De Felice & Tanaka 2010; Bertolami & Páramos 2016). Finally, there is a compelling argument which goes under the name of 'Lovelock's theorem' (Lovelock 1971) that states that the only second-order, local gravitational field equations derivable from an action

depending solely on the four-dimensional metric tensor are the Einstein field equations with a cosmological constant. Then, the only possible ways to modify GR while retaining the action principle are to (Papantonopoulos 2015, Sec. 1.2): (i) consider more than four spacetime dimensions; (ii) add new fields other than the spacetime metric; (iii) consider derivatives of order higher than two in the field equations; (iv) give up on diffeomorphism invariance. Then, to modify GR, one could consider more than four spacetime dimensions. However, all experiments so far point to the spacetime having only four dimensions. Furthermore, considering low energy scenarios, we expect that any possible higher-dimensional theory has a four-dimensional effective theory; if this theory is not GR, it has to violate one of the other three assumptions. Considering these arguments, it makes sense to restrict to spacetimes having only four dimensions, at least in the low energy phenomenology. One could then relax the assumption of the dependence of the gravitational action only on the metric, allowing, for example, a dependence on a new field φ. Note that, if φ enters the matter action and couples directly to the matter fields, we would have violations on the extremely well-tested WEP. Then it is reasonable to assume that the matter action is independent of this additional field φ. The other possibility is to allow equations of motion of order higher than two. However, theories with this feature are plagued by instabilities due to the presence of 'ghosts', which are fields whose Hamiltonian is not bound from below. This aspect is called 'Ostrogradsky's instability' (Ostrogradsky 1850) and is such that a non-degenerate Lagrangian dependent on derivatives of order higher than two leads to a Hamiltonian linear in at least one of the momenta, and as such is not bound from below (Woodard 2015). The last way to modify GR is to give up on diffeomorphism invariance. However, there exists a procedure, called 'Stückelberg mechanism' (Stückelberg 1938), which allows one to restore symmetries by introducing extra fields. Hence, one can think of theories that are not invariant under diffeomorphisms as diffeomorphism-invariant theories with extra fields. By the previous considerations, these fields should not appear in the matter action. In the end we see that, by violating Lovelock's theorem to extend GR, the main outcome is always to add new fields to the gravitational action, the simplest of which is the scalar field. Since GR is so well tested on Solar System scales, ATG containing additional fields should also provide a 'hiding mechanism', that is some mechanism that hides the extra degrees of freedom on scales where no extra degree of freedom has been seen, while still allowing them to be present in other regimes. The 'spontaneous scalarisation' phenomenon, explained in Sect. 2.3, is one such mechanism which has boosted the viability of STTs since its discovery.

1.2 The importance of neutron stars

The most compact material objects in the known Universe are NSs, which are known to also harbour extremely powerful magnetic fields. Given their extreme environment, NSs are ideal laboratories to probe the properties of matter in conditions which are not reproducible in laboratories. While the hypothesis of their existence dates back to the 1930s (Landau 1932; Baade & Zwicky 1934), their actual discovery happened more than thirty years later. In 1967 it was pointed out that if NSs were spinning and harboured strong magnetic fields, they would emit electromagnetic waves (Pacini 1967); during the same year, regular radio pulses coming from a region of the sky were discovered (Hewish et al. 1968), and this 'pulsar' was later interpreted to be a NS (Gold 1968). Since then, thousands of NSs were discovered (Manchester et al. 2005), most of them as pulsars. A special kind of pulsar are millisecond pulsars (MSPs), pulsars with rotation periods under $\sim$ 20ms. Among the variety of observed NSs, a sub-class of them hosts the most powerful magnetic fields known to us: magnetars (Duncan & Thompson 1992; Thompson & Duncan 1993, 1995, 1996), whose name refers to NSs that were shown to exhibit energetic bursting (soft gamma repeaters) and persistent (anomalous X-ray pulsars) activity (Kouveliotou et al. 1998; Gavriil et al. 2002; Mereghetti et al. 2015). In fact, while the surface magnetic field of NSs has been inferred to be in the range of 10^{8-12}G for radio and γ-ray pulsars (Asseo & Khechinashvili 2002; Spruit 2009; Ferrario et al. 2015), estimates for magnetars have reached 10^{15}G (Olausen & Kaspi 2014; Popov 2016). However, magnetars represent a small subset of NSs: to this day, the known population of magnetars consists of just over 30 sources (Olausen & Kaspi 2014)[1], compared to a few thousand regular pulsars (Manchester et al. 2005)[2]; nonetheless, it is believed that they might represent a significant fraction of the young NS population (Kaspi & Beloborodov 2017).

1.2.1 The magnetic field of neutron stars

As opposed to the surface and magnetospheric magnetic field of NSs, which can be probed and constrained with some accuracy through a variety of different methods (Rea et al. 2010; Güver et al. 2011; Rea et al. 2012; Kontorovich 2015; Rodríguez Castillo et al. 2016; Jankowski et al. 2017; Staubert et al. 2019), the geometry and strength of their internal magnetic fields remain largely unknown. It has been predicted that it may reach values as high as 10^{16}G inside magnetars and up to 10^{17-18}G in newly born proto-NSs (Del Zanna & Bucciantini 2018; Ciolfi et al. 2019; Franceschetti & Del Zanna

[1] See the catalogue website for an up-to-date list of known magnetars: `http://www.physics.mcgill.ca/~pulsar/magnetar/main.html`.

[2] See the catalogue website for an up-to-date list of known pulsars: `https://www.atnf.csiro.au/research/pulsar/psrcat/`.

2020). Indeed, the possibility of highly magnetised and rapidly rotating proto-NSs is at the foundation of the so-called millisecond magnetar model for long and short gamma-ray bursts (Usov 1992; Metzger et al. 2011; Rowlinson et al. 2013); moreover, it has been suggested that these objects are a possible source of fast radio bursts (Lyubarsky 2014; Beloborodov 2017; Hessels 2018; Metzger et al. 2019; Platts et al. 2019; Dall'Osso & Stella 2021). What appears less clear is the geometry of their internal magnetic field. While it is widely known that neither purely poloidal nor purely toroidal configurations are stable (Prendergast 1956; Chandrasekhar & Prendergast 1956; Chandrasekhar & Kendall 1957; Tayler 1973; Markey & Tayler 1973, 1974; Tayler 1980; Bocquet et al. 1995; Oron 2002; Braithwaite & Nordlund 2006; Braithwaite & Spruit 2006; Braithwaite 2009; Frieben & Rezzolla 2012) - meaning that mixed configurations like the twisted-torus are more likely (Ciolfi & Rezzolla 2013; Uryū et al. 2014; Pili et al. 2014) - the stabilising role of a rigid crust and of the external magnetosphere is yet to be evaluated. Luckily these magnetic fields might have potentially observable consequences, which might offer us a way to constrain them: they have the ability to modify the torsional oscillations of NSs (Samuelsson & Andersson 2007; Sotani 2015), alter the cooling properties of their crust (Page et al. 2004; Aguilera et al. 2008), and act as a potential source of deformation (Haskell et al. 2008; Gomes et al. 2019). Among the many physical processes which can induce a deformation on the shape of a NS, we recall that mountains can form on their surface due to crustal deformations (Ushomirsky et al. 2000; Haskell et al. 2006) or due to magnetic burial in accretion processes (Melatos & Payne 2005); oscillation modes such as the r-mode can develop an instability (Andersson 1998), leading to the emission of gravitational waves (GWs) of continuous nature (CGWs) (Abbott et al. 2021a); finally, the magnetic field itself can be the source of a global quadrupole (Bocquet et al. 1995; Cutler 2002; Oron 2002; Dall'Osso et al. 2009; Frieben & Rezzolla 2012; Pili et al. 2014; Gomes et al. 2019). In the last case, all that is needed to produce CGWs is a NS whose magnetic axis is not aligned to the rotation axis. It was shown (Cutler 2002) that a strong toroidal magnetic field would force the NS to develop an instability, flipping it to an orthogonal rotator, thus maximising its emission in terms of CGWs. Indeed Lander & Jones (2018) showed that, for parameters close to those of the observed population of NSs, most configurations are expected to evolve to orthogonal rotators. Moreover, it was found (Biryukov & Abolmasov 2021) that accretion can lead to an increase in the misalignment between the rotation axis and the magnetic axis.

Since magnetic fields are supposed to be stronger in the deep interior, the magnetic deformation of NSs offers a way to probe conditions in their core, as opposed to other source of deformation (including rotation and tidal forces) which mostly act on their outer layers. Unfortunately, it seems that only magnetic fields of strength $B \gtrsim 10^{14}$G, much higher than the surface magnetic field observed in regular pulsars (Manchester

et al. 2005), can cause a significant deviation from spherical symmetry (Haskell et al. 2008). Barring the possibility of an interior superconducting phase, which could substantially enhance the effectiveness of the magnetic field in deforming the NS (Cutler 2002; Akgün & Wasserman 2008; Lander et al. 2012; Lander 2014), similar fields are likely to be found only inside magnetars and newly-born proto-NSs. Given the long spin period of observed classical magnetars, this leaves newly-born proto-NSs and millisecond magnetars (Dall'Osso & Stella 2021) as the most promising sources of significant CGWs emission. However, as we show in Chap. 8, also MSPs, especially if endowed with a superconducting core, could lie within the reach of future GWs detectors.

1.2.2 The equation of state of neutron stars

In addition to the uncertainties regarding the magnetic properties of NSs interiors, also their internal composition, encoded by the equation of state (EoS), remains mostly unconstrained. In this sense, the observation of NSs with a mass higher than $2M_\odot$ [e.g. the most massive NS observed to date, with a mass potentially reaching $\sim$2.28$M_\odot$ (Kandel & Romani 2020) or a $\sim$ 2.08$M_\odot$ NS (Fonseca et al. 2021)] rejected the validity of many proposed EoS, and the first observation of GWs emitted by a binary NS merger (Abbott et al. 2017b) set further limits on their stiffness (Abbott et al. 2018; Bauswein 2019). Moreover, if the low-mass component of the recent binary coalescence event GW190814 (Abbott et al. 2020) is interpreted as a NS, it would set extremely stringent limits on the maximum mass that a valid EoS must be able to reach (Kanakis-Pegios et al. 2021; Godzieba et al. 2021; Lim et al. 2021; Rather et al. 2021; Bombaci et al. 2021). This uncertainty is further enhanced by the fact that the strong magnetic fields inside NSs directly affect their particle composition, for example by determining the presence of exotic particles; thus their interplay may have a key role in answering particle physics questions like the hyperon puzzle (Zdunik & Haensel 2013; Chatterjee & Vidaña 2016), the Delta puzzle (Cai et al. 2015; Drago et al. 2016), the hadron-quark phase transition (Avancini et al. 2012; Ferreira et al. 2014; Costa et al. 2014; Roark & Dexheimer 2018; Lugones & Grunfeld 2019) and the possibility of the existence of a superconducting phase (Ruderman 1995; Lander 2013; Haskell & Sedrakian 2018).

Understanding and being able to constrain the interplay of the strong magnetic field with the EoS in determining the structure and properties of NSs is thus of great importance to advance our knowledge of these objects. Given that any time-varying deformation - like that caused by magnetic fields - leads to the emission of CGWs, gravitational astronomy can offer an independent constraint also on the interior magnetic field of NSs (Gomes et al. 2019; Sieniawska & Bejger 2019; Abbott et al. 2020; Dergachev & Papa 2020; Frederick et al. 2021; Cieślar et al. 2021).

1.2.3 Testing general relativity through neutron stars

The recent observation of GW and EM radiation coming from the merger of a binary neutron star system (Abbott et al. 2017b) has given us a new opportunity to test GR in the strong-field regime (Will 2014), beyond the vacuum case of binary black hole mergers (Abbott et al. 2016), and to probe the physics of compact objects in unprecedented detail (Abbott et al. 2017c,a), fostering a renewed interest in NSs as possible probes of new gravitational physics. Given the compactness of NSs (their typical radii are just about 3 times larger that the Schwarzschild radius of a black hole of the same mass), any meaningful estimate of their role as potential CGWs sources requires them to be modeled in the strong gravitational field regime. To this point, even if GR remains today the best theory to describe gravitation in the strong field regime, it has long been known that our understanding, within its framework, of the gravitational interaction on galactic and cosmological scales presents some issues, as we argued in Sect. 1.1.

In this scenario, the study of NSs to test GR is especially important, because since the first work on massless mono-scalar STTs (Damour & Esposito-Farèse 1993), a non-perturbative strong field effect called 'scalarisation' has been predicted, allowing the scalar field to exponentially grow in magnitude inside compact material objects. Even generalisations of STTs to massive scalar fields and other gravitational theories have been shown to be subject to a similar phenomenon (Salgado et al. 1998; Ramazanoğlu & Pretorius 2016; Ramazanoğlu 2017; Silva et al. 2018; Andreou et al. 2019). Unfortunately, black holes in STTs have been shown to fulfill the no-hair theorem (Hawking 1972; Berti et al. 2015), thus they are exactly identical as in GR and they show no usefulness in contraining such theories. Scalarisation can happen in various contexts: binary systems of merging NSs can undergo a 'dynamical scalarisation' process (Barausse et al. 2013), in which the initially non-scalarised NSs become scalarised once they get closer to each other; again, in a binary NS system, one scalarised star can prompt an 'induced scalarisation' on its non-scalarised companion (Barausse et al. 2013); or even in an isolated NS system, where 'spontaneous scalarisation' can develop (this was the first discovered non-perturbative strong field effect in STTs, Damour & Esposito-Farèse 1993). The importance of scalarisation is that STTs which include such effects predict strong deviations from GR only inside compact objects, while allowing the tight observational constraints in the weak-gravity regime to be fulfilled (Shao et al. 2017). As of today, the strongest limit on the strength of spontaneous scalarisation for massless STTs comes from observations of pulsars in binary and triple systems, in particular in systems characterised by a large mass difference between the two stars, where STTs predict the emission of dipole scalar waves, potentially observable in the dynamics of the inspiral (Freire et al. 2012; Will 2014; Shao et al. 2017; Anderson et al. 2019; Voisin et al. 2020). These, however, are systems with large separations and the constraints do not apply in the case of screening (Yazadjiev et al. 2016; Doneva & Yazadjiev 2016). In

fact, as we explain in greater detail in Sect. 2.4, if the scalar field in endowed with a mass its effects are suppressed at a distance from the compact object greater than its Compton wavelength. Being the stars in these systems far away from each other, their dynamic is not affected by non-GR effects in the case of screening.

Scalarisation modifies the relation between the mass and radius of the NS and its central density. In general, scalarised NSs have larger radii and higher maximum masses than the corresponding GR solutions computed with the same EoS. Moreover, scalarisation is more effective at higher compactness. The presence of a strong scalar charge could, in principle, have important consequences on the phenomenology of NSs, even if many of these effects might be degenerate with the EoS. A different dependence of the mass and radius from the central density could lead to appreciable changes in the thermal evolution of NSs (Dohi et al. 2021), given the dependence of many cooling processes on the density itself (Yakovlev et al. 2005). Changes in radii could potentially be observable in the distribution function of millisecond pulsars (Papitto et al. 2014). The same holds for the distribution of NS masses, and the expected maximum mass [the recent measure of a 13km radius for a $1.44\mathrm{M}_{\odot}$ NS by NICER (Miller et al. 2019) suggests larger NSs radii than previously thought (Özel & Freire 2016)]. Spontaneous scalarisation might impact the dynamics and evolution of the post-merger remnant of binary NSs coalescence (Abbott et al. 2017; Raithel et al. 2018). Indeed, there is some observational evidence suggesting the presence of long lived NSs powering the X-ray afterglow of short gamma-ray bursts (GRBs) (Rowlinson et al. 2013), suggesting values of the maximum NS mass $\gtrsim 2.2 M_{\odot}$ (Gao et al. 2016; Margalit & Metzger 2017). Scalar fields can affect the deformability of NSs (Doneva et al. 2013, 2018), leaving an imprint in the pre-merger inspiral, and in the spin-down history of millisecond proto-magnetar as possible engines of GRBs (Dall'Osso et al. 2009). Scalarised NSs differ in the frequency of their normal modes (Sotani & Kokkotas 2005). On top of this STTs predicts also a new scalar wave emission, potentially detectable with future GWs observatories (Gerosa et al. 2016; Hagihara et al. 2020). Unfortunately, part of the phenomenology of STTs is degenerate with the EoS of NSs, for example regarding their mass-radius relation or deformability. For this reason, it is important to find ways to disentangle them, such that a more unambiguous interpretation of observations will be possible.

In GR, the first magnetised model of NS dates back to Chandrasekhar & Fermi (1953). Throughout the years, many magnetised models were proposed (Ferraro 1954; Roberts 1955; Prendergast 1956; Woltjer 1960; Monaghan 1965, 1966; Roxburgh 1966; Ostriker & Hartwick 1968; Miketinac 1975), up to more recent works (Tomimura & Eriguchi 2005; Yoshida et al. 2006; Fujisawa & Eriguchi 2015). Due to the non-linearity of the general-relativistic magnetohydrodynamics (GRMHD) equations, an accurate study of the structure of NSs must be done in a numerical way, and only recently numerical results in the full GR regime have appeared. Many of these models focus on either

purely toroidal (Kiuchi & Yoshida 2008; Kiuchi et al. 2009; Frieben & Rezzolla 2012) or purely poloidal (Bocquet et al. 1995; Konno 2001; Yazadjiev 2012) magnetic field configurations [see also Pili et al. (2014, 2017)]. However, such models are shown to develop an instability which causes the magnetic field to rearrange in a mixed configuration, called twisted torus, which is roughly axisymmetric (Prendergast 1956; Tayler 1973; Wright 1973; Braithwaite & Nordlund 2006; Braithwaite & Spruit 2006; Braithwaite 2009; Lasky et al. 2011). Twisted torus configurations have been studied only very recently (Ciolfi & Rezzolla 2013; Pili et al. 2014; Uryū et al. 2014; Bucciantini et al. 2015; Uryū et al. 2019), because they require to solve a large set of coupled non-linear elliptic PDEs, which can be numerically unstable.

So far, only non-magnetised models of NSs have been studied in STTs in the full non-linear regime (see e.g. Suvorov 2018 for a perturbative approach to the magnetised scenario). Most of them focus on static (Damour & Esposito-Farèse 1993; Harada 1998; Novak 1998a; Taniguchi et al. 2015; Anderson & Yunes 2019; Doneva & Yazadjiev 2020) or slowly rotating (Damour & Esposito-Farèse 1996; Sotani 2012; Pani & Berti 2014; Silva et al. 2015) stars, while recently some work has been done for rapidly (Doneva et al. 2013; Doneva & Yazadjiev 2016; Pappas et al. 2019) and differentially (Doneva et al. 2018) rotating models. Models of NSs have also been studied beyond the massless limit, and in the presence of a screening potential (Doneva & Yazadjiev 2016; Yazadjiev et al. 2016; Brax et al. 2017; Staykov et al. 2018; Doneva & Yazadjiev 2020; Staykov et al. 2019). Given that the powerful magnetic fields contained in NSs can heavily affect their phenomenology, it is important to extend previous studies to the case of magnetised models of NSs.

In this work, we present the first numerical computations of equilibrium, magnetised NSs models in a massless STT of gravity in the full non-linear regime. We wish to investigate how the mutual interplay of a strong magnetic field and a scalar field modifies both the magnetic properties of NSs, with respect to GR, and their scalarisation properties with respect to the un-magnetised case. For this reason we are going to provide a characterisation as complete as possible of our equilibrium configurations, including a parametrisation of their deformation, and to carry a comparison with GR, not just in terms of global quantities but also in the specific internal distribution of density and magnetic field. The purpose is to quantify, for example, how much the presence of a scalar field affects the magnetic deformability of NSs, which is a key parameter to evaluate the relative importance of GW vs EM dipole emission in the early spin-down of proto-NSs (Dall'Osso et al. 2009), and to assess the validity of the millisecond-magnetar model for long GRBs (Metzger et al. 2011). Moreover, we study how the presence of an additional channel for the emission of quadrupolar waves - that of scalar waves - affects the overall emission of quadrupolar GWs, establishing the extent to which the emission of scalar waves competes with the tensor one. On the other

hand, we also want to evaluate if the presence of a magnetic field favours or disfavours the scalarisation of NSs, and how it changes the scalarisation range, or the maximum NS mass. For this reason we limit our analysis only to the two extreme cases of purely poloidal or purely toroidal magnetic fields, neglecting rotation. Building upon results we find in the case of a simple, but widely used in the literature, polytropic EoS, we perform a detailed analysis of the effect of a variety of different EoS allowed by the latest observational and nuclear physics constraints in the structure of NSs, both in GR and in a massless STT. Our aim is twofold. First, to better understand the interplay between different EoS and the magnetic field of a NS, in order to understand whether there exist some kind of EoS-independent relation between the NS deformation and its observable quantities, like mass and radius; this would help to shed some light into the properties of the internal magnetic field of NSs, or set limits on their possible CGWs emission. Second, to look for similar relations in the case of a scalarised NS, in which case EoS-independent scalings could be useful to disentangle the effect of the scalar field to that of the EoS. In this sense our work is both an extension of the existing literature on magnetised models of NSs in GR, and of un-magnetised models in STTs.

We also take the opportunity to introduce a computational strategy, which, for the sake of simplicity, we discuss in detail just in the case of non-rotating NSs, but that can easily be generalised to rotating (see App. A) and even dynamical regimes and that allows a straightforward extension of well established algorithms for GRMHD to handle magnetohydrodynamics (MHD) in STTs. Our algorithm is an extension of the well-tested `XNS` solver (Pili et al. 2014, 2017) to the case of a generic STT. It is based on the eXtended Conformally Flat Condition (XCFC) for the metric (Wilson et al. 1996; Wilson & Mathews 2003; Cordero-Carrión et al. 2009; Bucciantini & Del Zanna 2011), which, even if not formally exact, has proved to be highly accurate for rotating NSs (Camelio et al. 2019). We wish to point here that the accuracy of the solution with respect to full GR depends on which parameter, that is the central rotation rate or the surface ellipticity, is held fixed in the comparison (larger deviations have been found for differentially rotating models having the same surface ellipticity Iosif & Stergioulas 2014). The XCFC system has several advantages from a numerical point of view. These, as we are going to show, are retained also in STTs, and that can easily be adapted to the more complex case of time dependent dynamical evolution.

1.3 Outline

This work is structured as follows. In Chap. 2 we recap the main properties of STTs, describing how the first STT was conceived, its evolution towards a general STT, the discovery of the important phenomenon of spontaneous scalarisation and the latest observational constraints. In Chap. 3 we describe the mathematical setting of this work:

the choice of the action describing an an ideal magnetised fluid at thermodynamic equilibrium; the '3+1 formalism', which is commonly used in GR to cast the tensorial equations in a form which is more suitable for numerical computations, and its extension to STTs; the equations describing the spacetime metric, the scalar field and the magnetic field. In Chap. 4 we describe the `XNS` code: the numerical scheme, the numerical solvers and strategy and the numerical setup we used. In Chap. 5 we describe our results regarding magnetised, equilibrium models of axisymmetric NSs in STTs, first focusing on the uniqueness of scalarised models, then detailing the results in the case of purely toroidal and purely poloidal magnetic field configurations in the case of a strong scalarisation; then, we consider the case of lower scalarisation scenarios; afterwards, we describe our results regarding the stability of magnetised and scalarised models. In Chap. 6 we expand on these results, focusing on the role of the scalar field on the magnetic deformations of NSs and on the emission GWs. In Chap. 7 we build upon these findings to extend our study to EoS allowed by observational and nuclear physics constraints, in which case we find simple parametrisations of the magnetic deformation of NSs in an EoS-independent way. In Chap. 8 we apply these results to the NSs population in the Galaxy, both observed and obtained through a population synthesis approach, to assess the detectabilty of CGWs by future GWs detectors. In Chap. 9 we present a novel test of GR in the setting of low-mass X-ray binary systems, first descrbing the use of ray-tracing in vacuum STTs and then showing how modifications to the iron line emitted by these systems by a scalar field could be detected. Finally, in Chap. 10 we present our conclusions.

Chapter 2

Scalar-tensor theories of gravity in a nutshell

In this chapter we introduce the full mathematical framework of STTs, focusing on massless theories containing the spontaneous scalarisation phenomenon. In Sect. 2.1 we explain the reasoning that led to the development of the first STT, while in Sect. 2.2 we explain how it can be expanded to a more general theory. In particular, in Sect. 2.3 we focus on the important phenomenon of spontaneous scalarisation, predicted by some STTs. Finally, in Sect. 2.4 the latest observational constraints regarding the parameters of massless STTs are shown.

In the following we assume a signature $\{-,+,+,+\}$ for the spacetime metric and use Greek letters μ, ν, λ, ...(running from 0 to 3) for 4D spacetime tensor components, while Latin letters i, j, k, ...(running from 1 to 3) are employed for 3D spatial tensor components. Moreover, we use the dimensionless units where $c = G = \mathrm{M}_\odot = 1$, and we absorb the $\sqrt{4\pi}$ factors in the definition of the EM quantities. Variables denoted with a tilde, $\tilde{\cdot}$, are calculated in the Jordan frame, while quantities denoted with a bar, $\bar{\cdot}$, are expressed in the Einstein frame.

2.1 Where it all started: the Brans-Dicke theory

The foundations of STTs were laid by Brans & Dicke (1961) in a seminal paper, in which the authors modified the Einstein-Hilbert action of GR attempting to bring it in conformity with Mach's principle by replacing the gravitational constant G by a scalar field non-minimally coupled to the spacetime metric, giving birth to the Jordan-Fierz-Brans-Dicke theory (BD). In particular, in BD G^{-1} is replaced by a scalar field φ, which is a function of the spacetime position. The action that gives rise to the BD equations

of motion is[1]

$$\tilde{S} = \frac{1}{16\pi} \int d^4x \sqrt{-\tilde{g}} \left[\varphi \tilde{R} - \frac{\omega_{\rm BD}}{\varphi} \tilde{g}^{\mu\nu} \tilde{\nabla}_\mu \varphi \tilde{\nabla}_\nu \varphi \right] , \tag{2.1}$$

where $\tilde{g}$ is the determinant of the spacetime metric $\tilde{g}_{\mu\nu}$, $\tilde{\nabla}_\mu$ its associated covariant derivative, $\tilde{R}$ its Ricci scalar and $\omega_{\rm BD}$ is a constant, the only free parameter of the theory. The field equations are found by performing the variation $\delta\tilde{S}/\delta\tilde{g}^{\mu\nu}$, leading to

$$\tilde{G}_{\mu\nu} = \frac{\omega_{\rm BD}}{\varphi^2} \left[\tilde{\nabla}_\mu \varphi \tilde{\nabla}_\nu \varphi - \frac{1}{2} \tilde{g}_{\mu\nu} \tilde{\nabla}_\lambda \varphi \tilde{\nabla}^\lambda \varphi \right] + \frac{1}{\varphi} \left[\tilde{\nabla}_\mu \varphi \tilde{\nabla}_\nu \varphi - \tilde{g}_{\mu\nu} \tilde{\nabla}_\mu \tilde{\nabla}^\mu \varphi \right] , \tag{2.2}$$

where $\tilde{G}_{\mu\nu} = \tilde{R}_{\mu\nu} - \frac{1}{2}\tilde{g}_{\mu\nu}\tilde{R}$ is the Einstein tensor and $\tilde{R}_{\mu\nu}$ is the Ricci tensor associated to $\tilde{g}_{\mu\nu}$. By performing the variation $\delta\tilde{S}/\delta\varphi$, we find the equation of motion of the scalar field:

$$\tilde{\nabla}_\mu \tilde{\nabla}^\mu \varphi = 0 . \tag{2.3}$$

We note that the scalar field φ is present in Eqs. 2.2,2.3 only though its derivatives, which implies that $\varphi =$ const. is a solution of BD and it corresponds to a GR solution, but with a re-scaled gravitational constant $G = \varphi^{-1}$. In this sense, if φ is not constant, it can be interpreted as a spacetime-varying gravitational 'constant', which is exactly what guarantees the accordance between BD and Mach's principle. Moreover, it can be shown that if $\omega_{\rm BD} \to \infty$ the scalar field converges to a constant value φ_0, meaning that the solution approaches a GR one with a re-scaled gravitational constant. As we show in Sect. 2.4, BD is no longer considered viable due to the extremely high value of $\omega_{\rm BD}$ needed to explain observations, which means that the theory must be heavily fine tuned and its effects in modifying GR are negligible.

2.2 Massless scalar tensor theories

The most general action $S_{\rm J}$ that describes the mutual interplay of an ideal magnetised fluid at thermodynamic equilibrium with a gravitational spacetime containing one scalar field φ non-minimally coupled to the metric $\tilde{g}_{\mu\nu}$, is invariant under spacetime diffeomorphisms, is at most quadratic in the derivatives of the fields, and which satisfies the WEP, can be written as the sum of two terms. The first term $\tilde{S}_{\rm g}[\tilde{g}_{\mu\nu}, \varphi]$,

[1] In this and subsequent expressions of the gravitational actions we neglect the Gibbons-York-Hawking boundary term, which is needed to pose a well-defined variational principle in case of a spacetime with boundary $\partial\mathcal{M}$. In this regard, in STTs we need to impose both $\delta g_{\mu\nu} = 0$ and $\delta R = 0$ on $\partial\mathcal{M}$, due to the additional scalar degree of freedom (Dyer & Hinterbichler 2009).

encoding the information about the gravitational fields, according to the 'Bergmann-Wagoner formulation' (Bergmann 1968; Wagoner 1970; Berti et al. 2015) is

$$\tilde{S}_{\rm g} = \frac{1}{16\pi}\int d^4x\sqrt{-\tilde{g}}\left[\varphi\tilde{R} - \frac{\omega(\varphi)}{\varphi}\tilde{\nabla}_\mu\varphi\tilde{\nabla}^\mu\varphi - U(\varphi)\right] , \tag{2.4}$$

where $\omega(\varphi)$ and $U(\varphi)$ are, respectively, the coupling function and the potential of the scalar field φ. We note that Eq. 2.4 is simply the BD action Eq. 2.1 where $\omega_{\rm BD}$ is replaced with a generic function $\omega(\varphi)$ and a potential $U(\varphi)$ has been added. The second term $\tilde{S}_{\rm p}[\tilde{g}_{\mu\nu}, \tilde{\Psi}]$ contains information on the other physical (EM and fluid) fields $\tilde{\Psi}$. For now we leave the functional form of $\tilde{S}_{\rm p}$ unspecified; in Sect. 3.1 we adopt a particular choice used for ideal fluids.

The frame where the action reads $S_{\rm J} = \tilde{S}_{\rm g} + \tilde{S}_{\rm p}$ is called the 'Jordan frame' (J-frame), and quantities denoted with a tilde, $\tilde{}$, are defined in this frame. Variation of the action with respect to the various fields leads to the Euler-Lagrange field equations (and to the constraints). We note that, since $\tilde{S}_{\rm p}$ does not depend explicitly on φ, the WEP is guaranteed to hold in this frame; in other words, test particles follow the geodesics of the spacetime metric $\tilde{g}_{\mu\nu}$ in the J-frame. This means that the scalar field does not interact directly with the physical fields in this frame, but only through its effects on the spacetime metric. The consequence of this is that the equations describing the behaviour of the physical quantities, i.e. MHD equations, are unaffected by the presence of the scalar field. By performing the variation $\delta\tilde{S}_{\rm J}/\delta\tilde{g}^{\mu\nu}$ we obtain the field equations in the J-frame (Berti et al. 2015):

$$\tilde{G}_{\mu\nu} = \frac{8\pi}{\varphi}\tilde{T}_{{\rm p}\,\mu\nu} + \frac{\omega(\varphi)}{\varphi^2}\left[\tilde{\nabla}_\mu\varphi\tilde{\nabla}_\nu\varphi - \frac{1}{2}\tilde{g}_{\mu\nu}\tilde{\nabla}_\lambda\varphi\tilde{\nabla}^\lambda\varphi\right] + \tag{2.5}$$

$$+ \frac{1}{\varphi}\left[\tilde{\nabla}_\mu\tilde{\nabla}_\nu\varphi - \tilde{g}_{\mu\nu}\tilde{\nabla}_\mu\tilde{\nabla}^\mu\varphi\right] - \frac{U(\varphi)}{2\varphi}\tilde{g}_{\mu\nu} , \tag{2.6}$$

where

$$\tilde{T}^{\mu\nu}_{\rm p} = -\frac{2}{\sqrt{-\tilde{g}}}\frac{\delta\tilde{S}_{\rm p}\left(\tilde{g}_{\mu\nu}, \tilde{\Psi}\right)}{\delta\tilde{g}_{\mu\nu}} \tag{2.7}$$

is the energy-momentum tensor of the physical fields in the J-frame and $\tilde{T}_{\rm p} = \tilde{g}^{\mu\nu}\tilde{T}_{{\rm p}\,\mu\nu}$ is its trace. On the other hand, by performing the variation $\delta\tilde{S}_{\rm J}/\delta\varphi$ we obtain the scalar field equation in the J-frame:

$$\tilde{\nabla}_\mu\tilde{\nabla}^\mu\varphi = \frac{1}{3+2\omega(\varphi)}\left[8\pi\tilde{T}_{\rm p} - 16\pi\varphi\frac{\partial\tilde{T}_{\rm p}}{\partial\varphi} - \frac{d\omega}{d\varphi}\tilde{\nabla}_\lambda\varphi\tilde{\nabla}^\lambda\varphi + \varphi\frac{dU}{d\varphi} - 2U(\varphi)\right] . \tag{2.8}$$

The right-hand side of Eq. 2.5 contains higher-order derivatives of the scalar field, and its associated energy density is not positively defined (Santiago & Silbergleit 2000). As

a consequence, in the J-frame the generalisation of Einstein's field equations has a different mathematical structure than in GR, implying that standard solution techniques and algorithms developed for GR cannot be naively applied. However, it is possible to show (Santiago & Silbergleit 2000) that, by performing a conformal transformation of the metric,

$$\bar{g}_{\mu\nu} = \varphi \tilde{g}_{\mu\nu} \,, \tag{2.9}$$

and introducing a new scalar field χ related to φ according to

$$\frac{\mathrm{d}\chi}{\mathrm{d}\ln\varphi} = \sqrt{\frac{\omega(\varphi)+3}{4}} \,, \tag{2.10}$$

the gravitational part of the action becomes

$$\bar{S}_{\mathrm{g}} = \frac{1}{16\pi}\int d^4x\sqrt{-\bar{g}}\left[\bar{R} - 2\bar{\nabla}_\mu\chi\bar{\nabla}^\mu\chi - V(\chi)\right] \,, \tag{2.11}$$

where $\bar{g}$ is the determinant of the spacetime metric $\bar{g}_{\mu\nu}$, $\bar{\nabla}_\mu$ its associated covariant derivative, $\bar{R}$ its scalar curvature, and $V(\chi) = U(\varphi)/\varphi^2$ the potential of the scalar field χ. The action of the physical fields is changed by the conformal transformation Eq. 2.9 to $\bar{S}_{\mathrm{p}}[\varphi^{-1}(\chi)\bar{g}_{\mu\nu}, \tilde{\Psi}]$. The frame where the action reads $S_{\mathrm{E}} = \bar{S}_{\mathrm{g}} + \bar{S}_{\mathrm{p}}$ is known as the 'Einstein frame' (E-frame) and quantities denoted with a bar, $\bar{\cdot}$, are defined in this frame. We see that now $\bar{S}_{\mathrm{p}}$ does not depend on the spacetime metric $\bar{g}_{\mu\nu}$ alone, but through the combination $\varphi^{-1}(\chi)\bar{g}_{\mu\nu}$; thus, test particles do not follow the geodesics of the spacetime metric. In other words, the WEP does not hold in the E-frame, and as a consequence MHD equations in the E-frame have a more complicated form that in GR. Interestingly, Maxwell's equations retain their form, as expected from their pre-metric nature (van Dantzig & Dirac 1934; Cartan 1986; Delphenich 2005). As a consequence, in the E-frame standard methods, techniques, and algorithms developed in MHD, based on the conserved nature of the various physical quantities, and the locality of the EoS, cannot be naively applied. In the E-frame the equations of motion of the spacetime metric and of the scalar field are found by performing the variations $\delta\bar{S}_{\mathrm{E}}/\delta\bar{g}^{\mu\nu}$ and $\delta\bar{S}_{\mathrm{E}}/\delta\chi$ respectively, leading to (Berti et al. 2015):

$$\bar{G}_{\mu\nu} = 2\left(\bar{\nabla}_\mu\chi\bar{\nabla}_\nu\chi - \frac{1}{2}\bar{g}_{\mu\nu}\bar{\nabla}_\lambda\chi\bar{\nabla}^\lambda\chi\right) - \frac{1}{2}\bar{g}_{\mu\nu}V(\chi) + 8\pi\bar{T}_{\mathrm{p}\,\mu\nu} \tag{2.12}$$

and

$$\bar{\nabla}_\mu\bar{\nabla}^\mu\chi = -4\pi\alpha_{\mathrm{s}}(\chi)\bar{T}_{\mathrm{p}} + \frac{1}{4}\frac{dV}{d\chi} \,, \tag{2.13}$$

where $\bar{G}_{\mu\nu} = \bar{R}_{\mu\nu} - \frac{1}{2}\bar{g}_{\mu\nu}\bar{R}$ is the Einstein tensor, $\bar{R}_{\mu\nu}$ is the Ricci tensor associated to $\bar{g}_{\mu\nu}$,

$$\bar{T}^{\mu\nu}_{\mathrm{p}} = -\frac{2}{\sqrt{-\bar{g}}}\frac{\delta\bar{S}_{\mathrm{p}}\left[\varphi^{-1}(\chi)\bar{g}_{\mu\nu}, \tilde{\Psi}\right]}{\delta\bar{G}_{\mu\nu}} \tag{2.14}$$

is the E-frame physical energy-momentum tensor and $\bar{T}_{\rm p} = \bar{g}^{\mu\nu}\bar{T}_{{\rm p}\,\mu\nu}$ its trace, and

$$\alpha_{\rm s}(\chi) = -\frac{{\rm d}\ln\varphi(\chi)}{2{\rm d}\chi} \,. \tag{2.15}$$

We note that the right-hand side of Eq. 2.12 can be written as

$$\bar{G}^{\mu\nu} = 8\pi\left(\bar{T}_{\rm s}^{\mu\nu} + \bar{T}_{\rm p}^{\mu\nu}\right) \,, \tag{2.16}$$

where

$$\bar{T}_{\rm s}^{\mu\nu} = \frac{1}{4\pi}\left[\bar{\nabla}^{\mu}\chi\bar{\nabla}^{\nu}\chi - \frac{1}{2}\bar{g}^{\mu\nu}\bar{\nabla}_{\lambda}\chi\bar{\nabla}^{\lambda}\chi\right] \,, \tag{2.17}$$

is the scalar field energy-momentum tensor. Thus, we see that in the E-frame the metric field equations are equivalent to those of GR, and the scalar field acts only as an extra energy-momentum source term.

We note from Eq. 2.13 that the only direct sources of a massless scalar field (i.e. such that $U = V = 0$) in the E-frame are those physical fields with a non-vanishing trace of the energy-momentum tensor; as such, the EM field is not a direct source of the scalar field, and for the same reason purely metric black holes in massless STTs are undistinguishable from those in GR (Hawking 1972; Berti et al. 2015). Analogously, in the ultra-relativistic asymptotically free regime of an ideal fluid the same considerations apply. In the following we consider only massless STTs, thus without a scalar potential.

The fact that MHD equations retain their usual GR form in the J-frame and the tensor-scalar field equations are written as in GR with an additional source in the E-frame, suggests that a simultaneous use of the E-frame (to compute the metric and scalar fields) and of the J-frame (to compute the physical fields) by performing the conformal transformations between the two whenever necessary, enables us to easily extend the standard numerical techniques of GRMHD to the case of STTs, as we show in Chap. 4.

One consideration is due: we have so far introduced two different frames, the J-frame and the E-frame, each with its own properties and set of equations, and both are possible settings to study STTs. Are the two frames physically equivalent? If not, which one is to be considere the real, physical frame? In other words, among the infinitely-many frames connected by conformal transformations, whose predictions are to be compared with experiments? This issue is long-standing, with different possible interpretations, and a definitive answer does not exist at this point. We report here only a few points of view on the subject, while a more thorough overview on the problem can be found in Capozziello & de Laurentis (2011). One argument (Dicke 1962) states that a conformal transformation is merely a local rescaling of units and, as such, it leaves the physics invariant; in other words, the two frames are physically equivalent provided

that the units in the E-frame are rescaled with appropriate powers of the conformal factor. However, this argument is purely classical and, even though there doesn't exist a full and consistent quantum gravity theory, in some approaches that try to quantize the metric tensor inequivalent theories are found (Capozziello & de Laurentis 2011). On the other hand, the fact that the WEP holds in the J-frame but not in the E-frame can be thought of as an argument against the physical equivalence of the frames. However, one could also argue that the WEP is formulated in such a way as to be dependent on the specific conformal frame. Moreover, the scalar field in BD can violate all of the energy conditions in the J-frame, while satisfying them in the E-frame, meaning that even if the conformal frames turn out to be physically equivalent in this theory, their interpretation is not. Furthermore, in some cosmological models the Universe accelerates in one frame but not in the other and as such, from the point of view of observations, they definitely do not seem to be physically equivalent (Capozziello et al. 2006). In any case, since the WEP is observed to hold with great accuracy, we expect the J-frame to be the physical frame, i.e. the one where observations are made. That is, any physical variable that observations measure is the J-frame version of that quantity.

2.3 Spontaneous scalarisation

As black holes in massless STTs are equivalet to those in GR, they do not provide us an effective way to test these STTs. Unlike black holes, NSs allow a coupling of the scalar field to their composing matter, thus their structure changes in the presence of a massless scalar field. For this reason NSs constitute a valuable probe of STTs, even more so because of the existence of non-perturbative strong field effects like 'spontaneous scalarisation'. The importance of theories contanining this non-linear phenomenon is that they allow the scalar field to develop appreciable deviations from GR inside compact material objects - namely NSs - while still satisfying the tight observational constraints valid in the weak-field regime.

It is possible to get an insight in the principle behind spontaneous scalarization by considering the limit in which the E-frame massless scalar field χ is just a small perturbation around a GR solution (Berti et al. 2015), that is $\hat{\chi} = \chi - \chi_0 \to 0$, where χ_0 is the constant asymptotic value of the scalar field at distance $r \to \infty$ from the NS. In this limit $\alpha_s(\chi) \approx \alpha_0 + \beta_0\hat{\chi}$. Observational constraints, as we detail in Sect. 2.4, require that α_0 be extremely small when the scalar field tends to its asymptotic value: thus, a configuration with $\chi \approx \chi_0$ and $\alpha_0 \approx 0$ should be an approximate solution of the STT set of equations. Then, in this case any GR solution is a solution to the STT field equations Eq. 2.12 at first order, while the scalar field equation Eq. 2.13 reads

$$\left[\bar{\nabla}_\mu \bar{\nabla}^\mu - \mu_s^2(x^\nu)\right] \hat{\chi} = 0 \,, \tag{2.18}$$

where $\mu_s^2(x^\nu) = -4\pi\beta_0\bar{T}$. We see that this is a Klein-Gordon equation for the E-frame scalar field with an effective mass $\mu_s(x^\nu)$ which depends on the spacetime position. Depending on the sign of $\beta_0\bar{T}$, the squared effective mass can be positive or negative. In most situations $\bar{T} < 0$; thus, if also $\beta_0 < 0$, perturbations of the scalar field around the GR solutions can devlop an instability which is associated with an exponentially growing mode. The requirement that the modes have a wavelength which is contained inside the NS radius leads to a condition on the compactness of the star, which must be sufficiently high, thus revealing that compact material objects like NSs are fundamental to test the viability of STTs. As an example, in the case of a spherically-symmetric NS spontaneous scalarisation happens for $\beta_0 \lesssim -4.35$ (Harada 1998). We note that, in the case of strongly-interacting systems, it can happen that $\bar{T} > 0$ (Haensel et al. 2007): in this case, spontaneous scalarisation develops for $\beta_0 > 0$ (Mendes & Ortiz 2016).

Spontaneous scalarisation is associated to the growth of a scalar 'hair' in NSs, in a process akin to ferromagnetism (Damour & Esposito-Farèse 1996). To see this let's expand the scalar field arount its asymptotic value χ_0:

$$\chi(r) = \chi_0 + \frac{\omega_A}{r} + \mathcal{O}\left(\frac{1}{r^2}\right) , \tag{2.19}$$

where the monopole coefficient of the expansion ω_A is akin to a 'scalar charge' of the NS hosting the scalar field. It can be shown that (Damour & Esposito-Farese 1992)

$$\omega_A = -\frac{\partial m_A}{\partial \chi_0} , \tag{2.20}$$

where m_A is the ADM mass (Gourgoulhon 2012) of the NS. This allows one to give an interpretation of spontaneous scalarisation based on the well-known theory of ferromagnetism. Ferromagnets immersed in an external magnetic field $\mathbf{B_0}$, when below the Curie temperature T_C, develop a spontaneous symmetry breaking: given their free energy E, their magnetisation

$$\mathbf{M} = -\frac{\partial E}{\partial \mathbf{B_0}} \tag{2.21}$$

is non-zero even if $|\mathbf{B_0}| \to 0$. This is in contrast with nonferromagnetic materials, where $\mathbf{M}$ and $\mathbf{B_0}$ are proportional, the proportionality constant being the magnetic suceptibility. This effect is a second-order phase transition, where $\mathbf{M}$ is the order parameter in the case of ferromagnets; by analogy, ω_A takes the role of order parameter in the case of spontaneous scalarisation. A weakly self-gravitating object develops a scalar charge $\omega_A \propto \chi_0$, where the proportionality factor is a 'scalar susceptibility' analogue to the magnetic one, which implies that their scalar charge vanishes in the limit of zero external scalar field χ_0. In the case of strongly self-gravitating objects, the scalar analogues of the thermodynamic quantities are found by minimizing the total energy

$m_{\rm A}$ as a function of both the external field and the order parameter, assuming that the Legendre transform of the energy function $\mu(\omega_{\rm A})$ (the Landau free energy) develops a minimum for $\omega_{\rm A}$ when some control parameter varies:

$$m_A\left(\omega_A, \varphi_0\right) = \mu(\omega_A) - \omega_A \varphi_0 \, . \tag{2.22}$$

By fixing the shape of the scalar coupling function $\alpha_{\rm s}$ we can set the control parameter as the baryon mass of the star $\bar{m}_{\rm A}$, which can be thought of as the scalar analogue of the temperature in thermodynamics. For example, let's consider the Landau ansatz as a simple model exhibiting spontaneous scalarisation: $\mu(\omega_{\rm A}) = a(\bar{m}_{\rm cr} - \bar{m}_{\rm A})\omega_{\rm A}^2/2 + b\omega_{\rm A}^4/4$, where a and b are constants and $\bar{m}_{\rm cr}$ is the critical transition point. If $\chi_0 = 0$, $m_{\rm A}$ develops a minimum in $\omega_{\rm A} = 0$ (the trivial solution) if $\bar{m}_{\rm A} < \bar{m}_{\rm cr}$, while $\omega_{\rm A} = \pm\sqrt{a(\bar{m}_{\rm A} - \bar{m}_{\rm cr})/b}$ (the non-trivial solution) if $\bar{m}_{\rm A} > \bar{m}_{\rm cr}$. Thus, if the baryonic mass of the star is sufficiently large, there appear two energetically favoured non-trivial solutions for the scalar charge. At the critical transition point $\bar{m}_{\rm A} = \bar{m}_{\rm cr}$, $d\omega_{\rm A}/d\bar{m}_{\rm A}$ diverges as in a second-order phase transition. As in the ferromagnetic case, the scalar susceptibility $\chi_A = \partial\omega_{\rm A}/\partial\chi_0$ diverges as $|\bar{m}_{\rm A} - \bar{m}_{\rm cr}|^{-1}$ near the critical point, while a non-zero external field χ_0 smoothes the transition.

2.4 The current status of observational constraints

Most STTs are designed to be metric theories of gravity, i.e. they respect the Einstein equivalence principle (Will 2014). For this reason, the precision tests of the WEP, of the local Lorentz invariance and of the local position invariance in a flat spacetime are not useful in constraining these theories (Will 2014; Berti et al. 2015; Will 2018). On the other hand, since these theories generally violate the SEP[2], tests of this principle using self-gravitating bodies are ideal to constrain the theory of gravity.

One class of tests of the SEP consists in measuring the effective gravitational constant G_{ab} entering the gravitational interaction between two bodies a and b (Voisin et al. 2020). At the Newtonian level, the acceleration of body a in the gravitational field of body b is given by

$$\ddot{\mathbf{x}}_{\mathbf{a}} = -G_{ab} m_b \frac{\mathbf{r_{ab}}}{|\mathbf{r_{ab}}|^3} + \mathcal{O}\left(c^{-2}\right) \, , \tag{2.23}$$

where m_b is the inertial mass of body b, $\mathbf{r_{ab}} = \mathbf{x_a} - \mathbf{x_b}$ is the coordinate separation between the two bodies and c is the speed of light. Since G_{ab} depends on the properties of the two bodies, in the weak-field limit it can be interpreted as a mismatch between

[2]There are arguments suggesting that GR is the only gravity theory in four spectime dimensions that fully satisfies the SEP (Di Casola et al. 2015; Will 2018). Actually, also Nördstrom's conformally-flat STT fulfills the SEP, but its viability is ruled out by Solar System experiments (Deruelle 2011).

the inertial and the gravitational masses (m and $m_{\rm G}$ respectively) of the bodies:

$$G_{ab} = \left(\frac{m_{\rm G}}{m}\right)_a \left(\frac{m_{\rm G}}{m}\right)_b G \,. \tag{2.24}$$

If one considers an isolated two-body system with unknown masses, any violation of the SEP is degenerate with a rescaling of the masses, due to the symmetries of the equations of motion. On the other hand, if a third body enters the setting, the symmetry is broken and one can compare the rate of free-fall of two self-gravitating objects in the gravitational field of a third one. An example of this class of tests is the Lunar Laser Ranging experiment (LLR) (Müller et al. 2019), where one considers the Earth-Moon system in the gravitational field of the Sun: since the Earth and the Moon possess different fractional binding energies, if the SEP is violated they should fall in the Sun's gravitational field with a slightly different acceleration, causing a polarisation of the Earth-Moon orbit called 'Nordtvedt effect' (Nordtvedt 1968). The latest results on the Nordtvedt effect found no deviation from GR (Hofmann & Müller 2018):

$$\left(\frac{m_{\rm G}}{m}\right)_{\rm Earth} - \left(\frac{m_{\rm G}}{m}\right)_{\rm Moon} = (-3.0 \pm 5.0) \times 10^{-14} \,. \tag{2.25}$$

Another class of SEP tests consists in the measurement of the 'Shapiro delay' (Shapiro 1964): an EM signal passing in the vicinity of a massive body will take a slightly longer time to travel back and forth to the observer than if the body were not present, due to the presence of a spacetime curvature. Belonging to this class of tests are the measurements on the travel time of signals sent to the Cassini spacecraft (Bertotti et al. 2003). In this case, the time delay measurements can be recast in terms of the γ Post-Newtonian parameter, which is unity in GR. Meaningful deviations from GR have not been found:

$$\gamma - 1 = (2.1 \pm 2.3) \times 10^{-5} \,. \tag{2.26}$$

By choosing a specific theory of gravity one can recast these results in terms of constraints on the parameters of the theory. In the quadratic, massless mono-scalar tensor theory by Damour & Esposito-Farèse (1993), to which we focus in the present work, the scalar coupling function is chosen to be

$$\alpha_{\rm s}(\chi) = \alpha_0 + \beta_0 \chi \,, \tag{2.27}$$

where α_0 and β_0 are the only two parameters of the theory. As explained in Sect. 2.3, β_0 control the non-linear effects of the scalar field - i.e. spontaneous scalarisation - while α_0 is associated to the weak-field effects. This is the most simple extension of BD, which corresponds to $\alpha_0^{-2} = 2\omega_{\rm BD} + 3$ and $\beta_0 = 0$. The measurements of the deviations from GR described before can be recast in terms of constraints on α_0 and β_0 (Freire et al. 2012), keeping in mind that GR corresponds to $\alpha_0 = \beta_0 = 0$. The results of the LLR and Cassini measurements, along with tests of the SEP using timing of a set

of NS-white dwarf low-eccentrity binaries (Gonzalez et al. 2011), are shown in Fig. 2.1, where constraints coming from three binary NS systems [B1913+16 (Weisberg et al. 2010), J0737–3039 (Kramer et al. 2006), and B1534+12 (Stairs et al. 2002)] and two NS-white dwarf systems [J1141–6545 (Bhat et al. 2008) and J1738+0333 (Freire et al. 2012)] are also shown. While the results shown in Fig. 2.1 already show that very severe

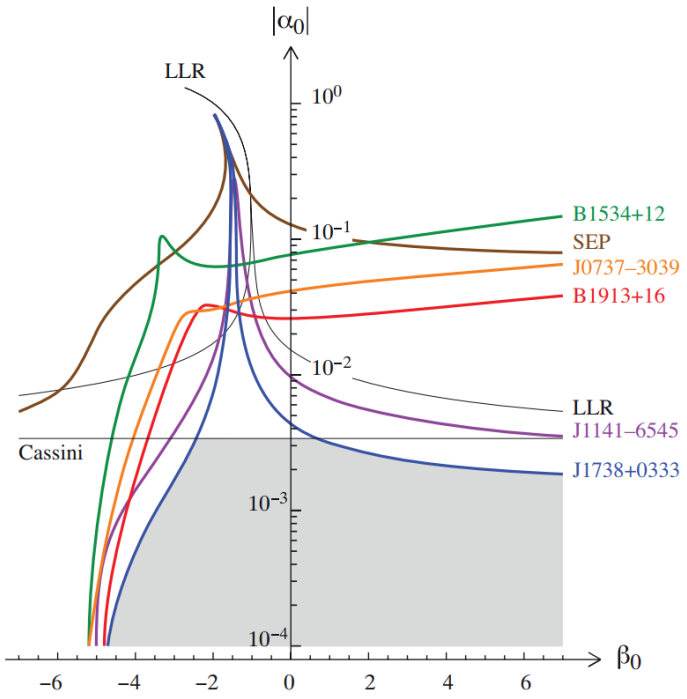

Figure 2.1: Bounds on the α_0 and β_0 parameters from Solar System and binary pulsar measurements. LLR stands for results of the LLR experiment, Cassini for the Shapiro delay measurements using the Cassini spacecraft, and SEP for tests of the SEP using timing of a set of NS-white dwarf low-eccentrity binaries. B1913+16, J0737–3039, and B1534+12 stand for measurements obtained using three binary NS systems, while J1141–6545 and J1738+0333 are found by observations of two NS-white dwarf systems. See text for more details. The shaded region marks the allowed parameter space. GR is found at $\alpha_0 = \beta_0 = 0$. Image reproduced from Freire et al. (2012), copyright by the authors.

restrictions apply to spontaneous scalarisation, some of the most stringent bounds on the α_0 and β_0 parameters to date were found by combining limits from binary pulsar experiments with data from the pulsar PSR J0337+1715 (Boyles et al. 2013; Lynch et al. 2013), the only pulsar confirmed to be in a tripe stellar system (Ransom et al. 2014). An improvement of several orders of magnitude on the SEP test over previous pulsar tests was achieved using this triple stellar system (Archibald et al. 2018; Voisin et al. 2020). In particular, it was found that $|\alpha_0| \lesssim 1.3 \times 10^{-3}$ and $\beta_0 \gtrsim -4.3$. The constraint on α_0 translates into a lower bound on the BD parameter: $\omega_{\rm BD} > 140\,000$, which renders

BD not viable in the sense that its predictions are practically equivalent to those of GR. Moreover, we mention the recent results (Kramer et al. 2021) that build upon previous findings (Kramer et al. 2006) regarding the double pulsar PSR J0737-3039: depending on the EoS, the limit on β_0 may be as strong as $\beta_0 \gtrsim -4$.

All the results described so far are valid in the case of a massless STT. For massive scalar fields, lower values of β_0 are still allowed (Yazadjiev et al. 2016), as long as the screening radius is smaller than the binary separation. In fact, in case the scalar field χ is endowed with a mass m_χ, its effects are suppressed as we move away from the scalarised object as $\chi \sim r^{-1}\exp\{-r/\lambda_\chi\}$, where $\lambda_\chi = 2\pi/m_\chi$ is the Compton wavelength of the scalar field, i.e. the screening radius. This means that the dynamics and interaction of the systems described above, if the mass is sufficiently large, are not affected by the presence of the scalar field, which remains hidden behind the screening radius.

Chapter 3

The mathematical setting

This chapter deals with the full mathematical setting used in our work. In particular, in Sect. 3.1 we focus on the action of the physical fields describing an ideal magnetised fluid at thermodynamic equilibrium. In Sect. 3.2 we introduce the '3+1 formalism' used to cast the equations in a form which is suitable for numerical solvers and explain how it generalises to STTs. In Sect. 3.3 we present the metric equations, focusing on the case of static, axisymmetric, circular spacetimes which is suitable for our study. In Sect. 3.4 we describe the wave equation for the scalar field. Finally, in Sect. 3.5 we detail the equations describing the magnetic configuration of our models, focusing on the case of purely poloidal and purely toroidal magnetic fields.

3.1 The action of the physical fields

In Sect. 2.2 we introduced the action of monoscalar STTs as the sum of a gravitational action and of a physical action. We now specify the form of the physical action in the case of an ideal magnetised fluid at thermodynamic equilibrium: $\tilde{S}_{\rm p}[\tilde{g}_{\mu\nu}, \tilde{N}^\mu, \tilde{A}^\mu, \tilde{\varepsilon}, \tilde{s}]$ contains information on the physical (matter and electromagnetic) fields and it is a function of the mass current density $\tilde{N}^\mu = \tilde{\rho}\tilde{u}^\mu$, expressed as a function of the rest mass density $\tilde{\rho}$ and four-velocity $\tilde{u}^\mu$, the specific entropy $\tilde{s}$, the internal energy density $\tilde{\varepsilon}(\tilde{\rho}, \tilde{s})$, and the electromagnetic four-potential $\tilde{A}^\mu$. For an ideal fluid neglecting polarisation, magnetisation (Chatterjee et al. 2015; Franzon et al. 2016), dynamo or resistivity (Bucciantini & Del Zanna 2013; Del Zanna et al. 2016; Del Zanna & Bucciantini 2018; Tomei et al. 2020), it is

$$\tilde{S}_{\rm p} = \int d^4x \sqrt{-\tilde{g}} \left[\tilde{\varepsilon}(\tilde{N}^\mu \tilde{N}_\mu, \tilde{s}) + \zeta \tilde{\nabla}_\mu \tilde{N}^\mu + \eta \tilde{N}^\mu \tilde{\nabla}_\mu \tilde{s} \tilde{F}_{\mu\nu} \tilde{F}^{\mu\nu} + \tau_\nu \tilde{N}_\mu \tilde{F}^{\mu\nu} \right] , \qquad (3.1)$$

where $\tilde{F}_{\mu\nu} = \tilde{\nabla}_\mu \tilde{A}_\nu - \tilde{\nabla}_\nu \tilde{A}_\mu$ is the Faraday tensor, $\tilde{A}_\nu$ is the vector potential, and ζ, η, τ_ν are Lagrangian multipliers that enforce mass conservation, entropy conservation, and the ideal MHD condition $\tilde{u}_\mu \tilde{F}^{\mu\nu} = 0$ respectively (Hawking & Ellis 1973; Brown 1993; Bekenstein & Oron 2001). Variations with respect to the four potential $\tilde{A}_\mu$ lead to the inhomogeneous Maxwell's equations:

$$\delta S_{\mathrm{J}} / \delta \tilde{A}_\mu = 0 \;\Rightarrow\; \tilde{\nabla}_\mu \tilde{F}^{\mu\nu} = -\tilde{J}^\nu \,, \tag{3.2}$$

where $\tilde{J}^\nu$ is the electromagnetic four-current. Variations with respect to the matter four-current $\tilde{N}^\mu$ lead, ultimately, to the fluid Euler's equation and to the energy-momentum conservation law:

$$\delta S_{\mathrm{J}} / \delta \tilde{N}^\mu = 0 \;\Rightarrow\; \tilde{\nabla}_\mu \tilde{T}^{\mu\nu}_{\mathrm{p}} = 0 \,, \tag{3.3}$$

where the energy momentum tensor is

$$\tilde{T}^{\mu\nu}_{\mathrm{p}} = [\tilde{\rho} + \tilde{\varepsilon} + \tilde{p}] \tilde{u}^\mu \tilde{u}^\nu + \tilde{p} \tilde{g}^{\mu\nu} + \tilde{F}^\mu{}_\lambda \tilde{F}^{\nu\lambda} - \frac{1}{4} \tilde{F}^{\lambda\kappa} \tilde{F}_{\lambda\kappa} \tilde{g}^{\mu\nu} \tag{3.4}$$

and $\tilde{p}$ is the pressure. Given that the scalar field does not enter $\tilde{S}_{\mathrm{p}}$, the equations describing the behaviour of the physical quantities are unaffected by the presence of the scalar field. Introducing the Hodge dual of the Faraday tensor $\tilde{F}^{\star\mu\nu} = \frac{1}{2} \tilde{\epsilon}^{\mu\nu\lambda\kappa} \tilde{F}_{\lambda\kappa}$, where $\tilde{\epsilon}_{\mu\nu\lambda\kappa} = -(-\tilde{g})^{1/2} [\mu\nu\lambda\kappa]$ is the Levi-Civita pseudo-tensor and $[\mu\nu\lambda\kappa]$ is the alternating Levi-Civita symbol, one can write the energy momentum tensor of ideal MHD in terms of the comoving magnetic field $\tilde{b}^\mu = \tilde{u}_\nu \tilde{F}^{\star\mu\nu}$ as

$$\tilde{T}^{\mu\nu}_{\mathrm{p}} = \left(\tilde{\rho} \tilde{h} + \tilde{b}^2 \right) \tilde{u}^\mu \tilde{u}^\nu - \tilde{b}^\mu \tilde{b}^\nu + \left(\tilde{p} + \frac{1}{2} \tilde{b}^2 \right) \tilde{g}^{\mu\nu} \,, \tag{3.5}$$

where $\tilde{b}^2 = \tilde{b}_\mu \tilde{b}^\mu$ and $\tilde{h} = 1 + (\tilde{\varepsilon} + \tilde{p}) / \tilde{\rho}$ is the specific enthalpy.

3.2 The 3+1 formalism

The idea behind the 3+1 formalism is to choose a family of spacelike hypersurfaces and break down the covariant form of the general-relativistic equations in a process called 'foliation' or 'slicing'. According to the 3+1 formalism (Alcubierre 2008; Gourgoulhon 2012), any globally hyperbolic spacetime (it makes sense to restrict ourselves to this kind of spacetime because it covers most astrophysical and cosmological scenarios) admits a foliation with a family of spacelike hypersurfaces Σ_t with normal timelike vector n^μ (which is, by definition, the velocity of the so-called 'Eulerian observer', such that $n_\mu n^\mu = -1$). Calling $x^\mu = [t, x^i]$ the coordinates adapted to the foliation, the geometry in the spacetime region between two adjacent spatial hypersurfaces Σ_t and Σ_{t+dt} is defined by

- a three-dimensional 'induced metric' γ_{ij}, with Riemannian signature $(+,+,+)$, which measures proper distances $dl^2 = \gamma_{ij}dx^i dx^j$ on each hypersurface;
- a 'lapse function' $\alpha(t, x^i)$, which keeps track of the difference in proper time $d\tau = \alpha dt$ measured by observers moving along the worldline orthogonal to the hypersurfaces (i.e. Eulerian observers);
- a 'shift vector' $\beta^i(t, x^i)$, which measures the difference in velocity between Eulerian observers and the lines of constant spatial coordinates: $x^i(t + dt) = x^i(t) - \beta^i dt$.

Since the chosen foliation is arbitrary, α and β^i are not unique, and contain information about the choice of coordinates. The three-metric induced on Σ_t is $\gamma_{\mu\nu} = g_{\mu\nu} + n_\mu n_\nu$ (and the induced rank-3 Levi-Civita pseudo tensor is $\epsilon^{ijk} = \epsilon^{ijk\mu}n_\mu$). The generic line element takes the form

$$ds^2 = -\alpha^2 dt^2 + \gamma_{ij}\left(dx^i + \beta^i dt\right)\left(dx^j + \beta^j dt\right) . \tag{3.6}$$

If $\beta^i = 0$, the spacetimes is said to be static. Tensors n_μ and $\gamma_{\mu\nu}$ allow one to project any tensor according to the foliation. The 4-dimensional metric is then

$$g_{\mu\nu} = \left(\begin{array}{c|c} -\alpha^2 + \beta_i\beta^i & \beta_i \\ \hline \beta_j & \gamma_{ij} \end{array}\right) , g^{\mu\nu} = \left(\begin{array}{c|c} -1/\alpha^2 & \beta^i/\alpha^2 \\ \hline \beta^j/\alpha^2 & \gamma^{ij} - \beta^i\beta^j/\alpha^2 \end{array}\right) .$$

The 4-dimensional volume element is given by $\sqrt{-g} = \alpha\sqrt{\gamma}$, where $g = \det(g_{\mu\nu})$ and $\gamma = \det(\gamma_{ij})$. The 4-vector n^μ is

$$n^\mu = \left(1/\alpha, -\beta^i/\alpha\right) , n_\mu = (-\alpha, 0) .$$

Note that γ_{ij} can be thought of as an orthogonal projector on Σ_t.

In STTs, the relation between the E-frame Eulerian observer and J-frame one is: $\tilde{n}_\mu = \mathcal{A}\bar{n}_\mu$, $\tilde{\gamma}_{\mu\nu} = \mathcal{A}^2\bar{\gamma}_{\mu\nu}$, where we have introduced the conformal function $\mathcal{A} = 1/\sqrt{\varphi(\chi)}$ coupling the two frames. The standard 3+1 decomposition of any vector is

$$U^\mu = U_\parallel n^\mu + U^\mu_\perp , \tag{3.7}$$

where $U_\parallel = -n_\mu U^\mu$ and $n_\mu U^\mu_\perp = 0$, while any rank-2 symmetric $X^{\mu\nu}$ and antisymmetric $A^{\mu\nu}$ tensor can be written as

$$X^{\mu\nu} = Y n^\mu n^\nu + Z^\mu n^\nu + Z^\nu n^\mu + W^{\mu\nu} , \tag{3.8}$$

$$A^{\mu\nu} = C^\mu n^\nu - C^\nu n^\mu + \epsilon^{\mu\nu\lambda\kappa}D_\lambda n_\kappa , \tag{3.9}$$

where $n_\mu Z^\mu = 0 = n_\mu W^{\mu\nu}$ and $n_\mu C^\mu = n_\mu D^\mu = 0$. In particular, the 3+1 decomposition of the energy-momentum and Faraday tensors are:

$$\tilde{T}^{\mu\nu}_{\rm p} = \tilde{E}_{\rm p}\tilde{n}^\mu\tilde{n}^\nu + \tilde{S}^\mu_{\rm p}\tilde{n}^\nu + \tilde{n}^\mu\tilde{S}^\nu_{\rm p} + \tilde{W}^{\mu\nu}_{\rm p} \ , \tag{3.10}$$

$$\bar{T}^{\mu\nu}_{\rm s} = \bar{E}_{\rm s}\bar{n}^\mu\bar{n}^\nu + \bar{S}^\mu_{\rm s}\bar{n}^\nu + \bar{n}^\mu\bar{S}^\nu_{\rm s} + \bar{W}^{\mu\nu}_{\rm s} \ , \tag{3.11}$$

$$\tilde{F}^{\mu\nu} = \tilde{n}^\mu\tilde{E}^\nu - \tilde{E}^\mu\tilde{n}^\nu + \tilde{\epsilon}^{\mu\nu\lambda\kappa}\tilde{B}_\lambda\tilde{n}_\kappa \ , \tag{3.12}$$

$$\tilde{F}^{\star\mu\nu} = \tilde{n}^\mu\tilde{B}^\nu - \tilde{B}^\mu\tilde{n}^\nu - \tilde{\epsilon}^{\mu\nu\lambda\kappa}\tilde{E}_\lambda\tilde{n}_\kappa \ . \tag{3.13}$$

The relations between the J-frame and E-frame physical energy-momentum and Faraday tensors are $\mathcal{A}^6\tilde{T}^{\mu\nu} = \bar{T}^{\mu\nu}$ and $\mathcal{A}^4\tilde{F}^{\mu\nu} = \bar{F}^{\mu\nu}$, and one can easily recover the following relations among the various projections:

$$\tilde{\Gamma} = -\tilde{n}_\mu\tilde{u}^\mu = -\bar{n}_\mu\bar{u}^\mu = \bar{\Gamma} \ , \tag{3.14}$$

$$\mathcal{A}\tilde{v}^j = \tilde{\gamma}^j{}_\mu\mathcal{A}\tilde{u}^\mu = \bar{\gamma}^j{}_\mu\bar{u}^\mu = \bar{v}^j \ , \tag{3.15}$$

$$\mathcal{A}^4\tilde{E}_{\rm p} = \mathcal{A}^{-2}\tilde{n}_\mu\tilde{n}_\nu\mathcal{A}^6\tilde{T}^{\mu\nu}_{\rm p} = \bar{n}_\mu\bar{n}_\nu\bar{T}^{\mu\nu}_{\rm p} = \bar{E}_{\rm p} \ , \tag{3.16}$$

$$\mathcal{A}^5\tilde{S}^j_{\rm p} = -\mathcal{A}^{-1}\tilde{n}_\mu\tilde{\gamma}^j{}_\nu\mathcal{A}^6\tilde{T}^{\mu\nu}_{\rm p} = -\bar{n}_\mu\bar{\gamma}^j{}_\nu\bar{T}^{\mu\nu}_{\rm p} = \bar{S}^j_{\rm p} \ , \tag{3.17}$$

$$\mathcal{A}^6\tilde{W}^{ij}_{\rm p} = \tilde{\gamma}^i{}_\mu\tilde{\gamma}^j{}_\nu\mathcal{A}^6\tilde{T}^{\mu\nu}_{\rm p} = \bar{\gamma}^i{}_\mu\bar{\gamma}^j{}_\nu\bar{T}^{\mu\nu}_{\rm p} = \bar{W}^{ij}_{\rm p} \ , \tag{3.18}$$

$$\mathcal{A}^3\tilde{B}^\mu = \mathcal{A}^4\tilde{F}^{\star\mu\nu}\tilde{n}_\nu\mathcal{A}^{-1} = \bar{F}^{\star\mu\nu}\bar{n}_\nu = \bar{B}^\mu \ , \tag{3.19}$$

$$\mathcal{A}^3\tilde{E}^\mu = \mathcal{A}^4\tilde{F}^{\mu\nu}\tilde{n}_\nu\mathcal{A}^{-1} = \bar{F}^{\mu\nu}\bar{n}_\nu = \bar{E}^\mu \ , \tag{3.20}$$

These relation show, for example, that the Lorentz factor Γ is the same in the two frames. The energy conservation law in the J-frame, $\tilde{\nabla}_\mu\tilde{T}^{\mu\nu} = 0$, together with the mass conservation $\tilde{\nabla}(\tilde{\rho}\tilde{u}^\mu) = 0$ and Maxwell's equations, can be cast into a system for the evolution of the projected quantities $\tilde{E}_{\rm p}, \tilde{S}^j_{\rm p}, \tilde{B}^\mu, \tilde{E}^\mu$, once an EoS and a closure for the electromagnetic currents (e.g. the Ideal MHD conditions) are provided, according for example to Del Zanna et al. (2007) and Bucciantini & Del Zanna (2011). Then, the above equations allow one to rescale those quantities to the E-frame, where they are used to solve the 3+1 evolutionary equations for the metric and the scalar field. For this purpose one needs also the 3+1 projection of the latter. This is only done in the E-frame, given that it is not needed in the J-frame, according to:

$$\bar{\nabla}^\mu\chi = P\bar{n}^\mu + Q^\mu \ , \tag{3.21}$$

$$\bar{E}_{\rm s} = \bar{n}_\mu\bar{n}_\nu\bar{T}^{\mu\nu}_{\rm s} = Q^2 + P^2 \ , \tag{3.22}$$

$$\bar{S}^j_{\rm s} = -\bar{n}_\mu\bar{\gamma}^j{}_\nu\bar{T}^{\mu\nu}_{\rm s} = PQ^j \ , \tag{3.23}$$

$$\bar{W}^{ij}_{\rm s} = \bar{\gamma}^i{}_\mu\bar{\gamma}^j{}_\nu\bar{T}^{\mu\nu}_{\rm s} = Q^iQ^j + (Q^2 + P^2)\bar{\gamma}^{ij} \ , \tag{3.24}$$

where Q^μ is purely spatial and Eq. 2.13 can also be cast into a set of evolutionary equations for P and Q^i (Salgado 2006; Salgado et al. 2008).

From now on, for the sake of clarity, and for ease of reading, we will drop the $\bar{\cdot}$ and $\tilde{\cdot}$ notation. All quantities referring either to the metric or the scalar field are assumed to be taken in the E-frame, while the MHD and fluid ones are to be considered in the J-frame. Whenever necessary, in case of possible ambiguity, the bar and tilde notation will be restored to specify the frame of reference for the given quantity.

3.3 The metric equations

For the problem we are interested in, we chose spherical-like coordinates $x^\mu = [t, r, \theta, \phi]$ and considered only configurations that are stationary and axisymmetric. This means that there exist two commuting Killing vectors, the timelike $t^\mu = (\partial_t)^\mu$ and the spacelike $\phi^\mu = (\partial_\phi)^\mu$ (Carter 1970, 2009, 2010). These two vectors span a timelike two-plane $\Pi = \mathrm{Vect}(t^\mu, \phi^\mu)$. Any vector $V^\mu \in \Pi$ is said to be toroidal, and takes the form $V^\mu = c_t t^\mu + c_\phi \phi^\mu$; instead, it is said to be poloidal if it lies in the spacelike two-plane orthogonal to Π. Given the generalised Einstein's equations for the metric, Eq. 2.12, if both the scalar and physical energy-momentum tensors obey the relations

$$\begin{aligned} t_\mu \bar{T}^{\mu[\nu} t^\kappa \phi^{\lambda]} &= 0 \,, \\ \phi_\mu \bar{T}^{\mu[\nu} t^\kappa \phi^{\lambda]} &= 0 \,, \end{aligned} \tag{3.25}$$

where the square brackets mean anti-symmetrisation with respect to the enclosed indices, then the spacetime has the additional property of being 'circular' (Kundt & Trümper 1966; Carter 1969). In this case, $\beta^r = \beta^\theta = 0$, $\gamma_{r\phi} = \gamma_{\theta\phi} = \gamma_{r\theta} = 0$ and all the remaining metric components depend solely on r and θ.

In case of circular spacetimes and spherical-like coordinates, the line element simplifies to

$$ds^2 = -\alpha^2 dt^2 + \psi^4 \left(dr^2 + r^2 d\theta^2 \right) + R_{\mathrm{qi}}^2 \left(d\phi + \beta^\phi dt \right)^2 , \tag{3.26}$$

where $R_{\mathrm{qi}} = \sqrt{\gamma_{\phi\phi}}$ is the quasi-isotropic radius and ψ is the conformal factor. A metric in the form of Eq. 3.26 is said to be 'quasi-isotropic'. Stationarity and axisymmetry are enough to ensure that $\bar{T}_{\mathrm{s}}^{\mu\nu}$ satisfies Eq. 3.25. However they are not enough to ensure the same for the physical part $\bar{T}_{\mathrm{p}}^{\mu\nu}$. Given that the energy-momentum tensor of the E and J-frame are related by a simple conformal transformation, and the same holds for the Killing vectors and the metric, the conditions that ensure circularity in one of them will also ensure it in the other. For an ideal plasma, having an energy-momentum tensor as in Eq. 3.5, on top of stationarity and axisymmetry, circularity requires the four-velocity to be toroidal, $u^r = u^\theta = 0$, and the magnetic field b^μ to be either purely toroidal or purely poloidal (in this latter case, rotation must also be uniform). On the contrary, even if the configuration is static and axisymmetric, for a magnetic field with a mixed configuration, Eq. 3.25 does not hold, and in principle the metric of Eq. 3.26 is no longer

correct. However, even in this case it has been shown in GR (Oron 2002; Shibata & Sekiguchi 2005; Dimmelmeier et al. 2006; Ott et al. 2007; Bucciantini & Del Zanna 2011; Pili et al. 2014, 2017) that Eq. 3.26 provides a good approximation of the correct metric, and leads to small errors in the structure of rotating stars, mostly in the outer layers close to the surface, even in the extreme cases of a rotation at the mass-shedding limit, and magnetic fields as strong as 10^{19}G. Moreover it can be also shown that in GR the difference $R_{\rm qi} - \psi^2 r \sin\theta$ is at most of order of 10^{-3} (Pili et al. 2017). Thus, to a good level of accuracy, the metric can be further simplified to the conformally flat (CFC) approximation (Wilson & Mathews 2003; Isenberg 2008), for which

$$ds^2 = -\alpha^2 dt^2 + \psi^4 \left[dr^2 + r^2 d\theta^2 + r^2 \sin^2\theta \left(d\phi + \beta^\phi dt \right)^2 \right] , \tag{3.27}$$

where we have a common factor multiplying all flat-space metric terms in spherical coordinates.

From now on we shall restrict our analysis to static configurations alone, that is to the case of non-rotating stars, for which $v^i = 0$ and $\beta^i = 0$ (see App. A for a discussion on rotators). As a consequence, the ideal-MHD electric field $E_i = -\tilde{\epsilon}_{ijk} v^j B^k = -\mathcal{A}^{-3} \bar{\epsilon}_{ijk} v^j B^k = 0$ and $S^i = 0$. Then, it can be shown that the extrinsic curvature $K_{ij} = 0$, which means that maximal slicing, $K = 0$, holds [see Gourgoulhon (2012) for a discussion of the properties of this kind of slicing]. Under these assumptions, Einstein's equations reduce to a system of two Poisson-like elliptic equations for ψ and α:

$$\Delta\psi = \left[-2\pi \hat{E} \right] \psi^{-1} , \tag{3.28}$$

$$\Delta\left(\alpha\psi\right) = \left[2\pi \left(\hat{E} + 2\hat{S} \right) \psi^{-2} \right] \left(\alpha\psi\right) , \tag{3.29}$$

where $\Delta = f^{ij} \hat{\nabla}_i \hat{\nabla}_j$ and $\hat{\nabla}_i$ are, respectively, the 3D Laplacian and nabla operator of the flat space metric f_{ij}. We note that the two equations are decoupled, such that Eq. 3.28 can be solved before Eq. 3.29. The source terms take the form

$$\begin{aligned} \hat{E} &= \psi^6 \left\{ \mathcal{A}^4 \left[e + \frac{1}{2} B^2 \right] + \frac{1}{8\pi} Q^2 \right\} , \\ \hat{S} &= \psi^6 \left\{ \mathcal{A}^4 \left[3p + \frac{1}{2} B^2 \right] - \frac{1}{8\pi} Q^2 \right\} . \end{aligned} \tag{3.30}$$

3.4 The scalar field equation

Under the same conditions, it can be shown that Eq. 2.13 reduces to

$$\Delta\chi = -4\pi\psi^4 \alpha_{\rm s}(\chi) \mathcal{A}^4 T_{\rm p} - \partial \ln\left(\alpha\psi^2\right) \partial\chi , \tag{3.31}$$

where $\partial f \partial g = \partial_r f \partial_r g + (\partial_\theta f \partial_\theta g)/r^2$ and $T_{\rm p} = 3p - \varepsilon - \rho$ is the trace of the J-frame energy momentum tensor. We note that the Poisson-like Eqs. 3.28,3.29 for ψ and $\alpha\psi$ have the form $\Delta u = s u^q$. In GR ($\mathcal{A} = 1$, $Q^i = 0$) they satisfy the criterion for local uniqueness, $sq \geq 0$. In STTs ($Q^i \neq 0$), this is no longer true; in fact, the source term in Eq. 3.29, $s = 2\pi\psi^{-2}\{\mathcal{A}^4[\varepsilon + 6p + 3B^2/2] - Q^2/8\pi\}$ includes an additional factor $-Q^2/8\pi$ such that it cannot be excluded that in particular conditions, when the scalar field is extremely strong one has $s < 0$. However we verified that this does not happen in any of the many configurations we computed, not even the most compact ones. Still, it remains to be verified that this holds also in the case of the collapse to a black hole. Concerning instead Eq. 3.31 at first order in χ, neglecting the higher order second term on the right, it has the form $\Delta u = s f(u)$. It can be shown that the condition for local uniqueness is $s(\mathrm{d}f/\mathrm{d}u) \geq 0$. Now $s = -4\pi\psi^4 T_{\rm p} > 0$. This implies that if $\alpha_{\rm s}(\chi)\mathcal{A}^4$ is a decreasing function of χ, as it happens to be for STTs with spontaneous scalarisation, Eq. 3.31 will not satisfy local uniqueness, and multiple solutions are expected. This will be further investigated and discussed in Sect. 5.1

3.5 The magnetic field equations

We begin by showing how the Grad-Shafranov formalism used in GR (Del Zanna & Chiuderi 1996; Pili et al. 2017), for the case of equilibrium configurations with a purely poloidal magnetic field, can be extended to the case of STTs. The solenoidal condition of the magnetic field allows us to write it as a function of the ϕ-component of the vector potential, A_ϕ. In conformally-flat metric

$$B^r = \frac{\partial_\theta A_\phi}{\mathcal{A}^3\psi^6 r^2 \sin\theta}\ ,\ B^\theta = -\frac{\partial_r A_\phi}{\mathcal{A}^3\psi^6 r^2 \sin\theta}\ , \tag{3.32}$$

and we recall that all metric terms are in the E-frame. Function A_ϕ is also called the magnetic flux function, and its iso-surfaces $A_\phi = $ const., called magnetic surfaces, contain the magnetic poloidal field lines.

The Euler equation describing the static MHD equilibrium is

$$\partial_i p + (\varepsilon + p)\,\partial_i \ln(\mathcal{A}\alpha) = \epsilon_{ijk} J^i B^k / \mathcal{A}^3 = L_i\ , \tag{3.33}$$

where $J^i = \mathcal{A}^2\alpha^{-1}\epsilon^{ijk}\partial_j(\mathcal{A}\alpha B_k)$ and L_i is the Lorentz force.

Often, NSs are assumed to be well described by a barotropic EoS, that is $\varepsilon = \varepsilon(\rho)$ and $p = p(\rho)$. Then, also $h = h(\rho)$ and Eq. 3.33 becomes (Pili et al. 2014) the 'generalised Bernoulli integral' [1]

$$\ln\left(\frac{h}{h_{\rm c}}\right) + \ln\left(\frac{\mathcal{A}\alpha}{\mathcal{A}_{\rm c}\alpha_{\rm c}}\right) - \mathcal{M} = 0\ , \tag{3.34}$$

[1] In analogy with the non-relativistic case, the relativistic Bernoulli integral can be defined, in hydro-

where the magnetisation function $\mathcal{M}(A_\phi)$ defines the Lorentz force through

$$L_i = \rho h \frac{d\mathcal{M}}{dA_\phi} \partial_i A_\phi \ , \tag{3.35}$$

and h_c, α_c, and $\mathcal{A}_c$ are the values of h, α and $\mathcal{A}$ at the center of the star, respectively (we have assumed $\mathcal{M}_c = 0$). By working out the derivatives of the poloidal components of the magnetic field, one can find an equation for J^ϕ:

$$J^\phi = -\frac{1}{\mathcal{A}^4 \psi^8 r^2 \sin^2\theta} \left[\Delta_* A_\phi + \partial A_\phi \partial \ln\left(\alpha \psi^{-2}\right) \right] \ , \tag{3.36}$$

where $\Delta_* = \partial_r^2 + r^{-2}\partial_\theta^2 - r^{-2}(\tan\theta)^{-1}\partial_\theta$. Given that, from Eq. 3.35, $J^\phi = \rho h(\mathrm{d}\mathcal{M}/\mathrm{d}A_\phi)$, we can obtain the Grad-Shafranov equation

$$\check{\Delta}_3 \check{A}_\phi + \frac{\partial A_\phi \partial \ln\left(\alpha\psi^{-2}\right)}{r\sin\theta} + \mathcal{A}^4 \psi^8 r \sin\theta \left(\rho h \frac{d\mathcal{M}}{dA_\phi} \right) = 0, \tag{3.37}$$

where $\check{A}_\phi = A_\phi/(r\sin\theta)$ and $\check{\Delta}_3 \check{A}_\phi = \Delta_* A_\phi/(r\sin\theta)$. Eq. 3.37 allows one to find the magnetic field and current components once the metric (α and ψ) is known and the free function $\mathcal{M}$ has been chosen. The simplest choice, found for example in Pili et al. (2014), is

$$\mathcal{M} = k_{\rm pol} A_\phi \ , \tag{3.38}$$

where $k_{\rm pol}$ is the poloidal magnetisation constant. This leads to dipolar magnetic field configurations and guarantees that the currents are confined within the star.

For a purely toroidal magnetic field, $\mathcal{M}$ in Eq. 3.34 is no longer a function of A_ϕ and $L_i = \rho h \partial_i \mathcal{M}$. Deriving the generalised Bernoulli integral and writing the Lorentz force in terms of the magnetic field components, we obtain

$$\partial_i \ln h + \partial_i \ln(\mathcal{A}\alpha) + \frac{\mathcal{A}\alpha B_\phi \partial_i \left(\mathcal{A}\alpha B_\phi\right)}{\rho h \mathcal{A}^4 \mathcal{R}^2} = 0 \ , \tag{3.39}$$

where $\mathcal{R}^2 = \alpha^2 \psi^4 r^2 \sin^2\theta$. This equation becomes integrable if we assume that the last term can be written as the gradient of a scalar function. Defining

$$\mathcal{G} = \rho h \mathcal{A}^4 \mathcal{R}^2 \ , \tag{3.40}$$

this becomes possible if

$$B_\phi = \frac{\mathcal{I}(\mathcal{G})}{\mathcal{A}\alpha}, \text{ and } \mathcal{M}(\mathcal{G}) = -\int \frac{\mathcal{I}}{\mathcal{G}} \frac{d\mathcal{I}}{d\mathcal{G}} d\mathcal{G} \ . \tag{3.41}$$

dynamics, from the conservation law of hu_t along the trajectories of a stationary flow (see Friedman & Stergioulas 2013). This is a special case of the global first integral of Euler's equation for iso-entropic flows which, for stationary cases, reduces to Eq. 3.34. This is the reason why we refer to Eq. 3.34 as the generalised Bernoulli integral.

It is customary to assume a barotropic expression for $\mathcal{I}$ (Kiuchi & Yoshida 2008; Frieben & Rezzolla 2012):

$$\mathcal{I} = k_{\rm tor}\mathcal{G}^{\rm m} \text{ and } \mathcal{M} = -\frac{mk_{\rm tor}^2}{2m-1}\mathcal{G}^{2m-1} \,, \tag{3.42}$$

where $k_{\rm tor}$ is the toroidal magnetisation constant and $m \geq 1$ is the toroidal magnetisation index. This form of $\mathcal{I}$ ensures that the magnetic field is confined within the star and that its configuration is symmetric with respect to the equatorial plane. The generalised Bernoulli integral then becomes

$$\ln\left(\frac{h}{h_{\rm c}}\right) + \ln\left(\frac{\mathcal{A}\alpha}{\mathcal{A}_{\rm c}\alpha_{\rm c}}\right) + \frac{mk_{\rm tor}^2}{2m-1}\left(\rho h\mathcal{A}^4\mathcal{R}^2\right)^{2m-1} = 0 \,. \tag{3.43}$$

Chapter 4

The XNS code

The XNS code[1] is a numerical solver for the coupled equations of the metric, scalar field and MHD structure of a NS under the assumptions of stationarity and axisymmetry, adopting conformal flatness and maximal slicing. It is based on an iterative scheme, which computes the various quantities separately. It has been applied also to the case of white dwarves (Das & Mukhopadhyay 2015) and to non-barotropic NSs (Camelio et al. 2019). The code is built upon the routines developed for the X-ECHO code for GRMHD in dynamical spacetimes (Bucciantini & Del Zanna 2011), which, in turn, is based on the ECHO code (Del Zanna et al. 2007). During this Ph.D. project, we updated the XNS code - which previously worked only in GR and for simple polytropoic EoS (Pili et al. 2014, 2015, 2017) - in order to account for the presence of a scalar field non-minimally coupled to the metric, i.e. to solve for the structure of a magnetised NS in a general, massless STT. While, as previously anticipated, we focus only on one particular scalar coupling function, the code is built in such a way that it is straightforward to consider a different massless STT. Moreover, we updated XNS to allow the use of any tabulated, realistic EoS. In this chapter we describe the workflow of XNS (Sect. 4.1), the numerical techniques used to solve the equations (Sect. 4.2) and the numerical setup of our configurations (Sect. 4.3).

4.1 The numerical scheme

Given the non-linear nature of the elliptic equations described in Chap. 3, these are solved iteratively. If the source terms do not satisfy local-uniqueness, iterative schemes might fail to converge. This issue is particularly relevant for Eq. 3.31 for the scalar

[1]The downloadable versione of XNS, along with a guide on its usage, can be found at https://www.arcetri.inaf.it/science/ahead/XNS/html/intro.html. See App. C for a brief description of the package contents.

field. As we discussed, the very nature of spontaneous scalarisation is tied to the non-uniqueness of the solutions. In the iterative scheme used to solve Eq. 3.31 we opted to keep fixed the trace of the energy-momentum tensor in the J-frame, and not in the E-frame. Fixing the trace in the E-frame leads to a source term of the form $-4\pi\psi^4\alpha_s\bar{T}_p$, which can be shown to violate local uniqueness for all values of χ. Fixing it in the J-frame instead leads to a source term of the form $-4\pi\psi^4\alpha_s\mathcal{A}^4T_p$, and it can be shown that local uniqueness is violated only in a finite range of values for χ. This ensures at least the boundedness of the solution.

The code computes at the beginning the solution for a spherically symmetric non-rotating and un-magnetised NS in isotropic coordinates, at the desired central density ρ_c, solving the generalisation of the Tolman-Oppenheimer-Volkoff (TOV) equations (Tolman 1939; Oppenheimer & Volkoff 1939) to STTs - the 'S-TOV' system. This is achieved with a nested shooting technique requiring that in the final solution the ratio $Q_r/\partial_r \ln\alpha$ is constant outside the NS, and that the conformal factor ψ corresponds to the Just metric (Just 1959) in isotropic coordinates. In particular, the S-TOV system of equations can be derived setting $B^i = 0$ in Eqs. 3.28,3.29,3.31,3.33:

$$\frac{4}{\psi}\frac{d\psi}{dr} = \xi\,, \tag{4.1}$$

$$\frac{d\chi}{dr} = Q_r\,, \tag{4.2}$$

$$\frac{d\xi}{dr} = -\frac{\xi^2}{4} - \frac{2}{r}\xi - 8\pi\psi^4\mathcal{A}^4\left(\rho h - p\right) - Q_r^2\,, \tag{4.3}$$

$$\frac{d\alpha}{dr} = \frac{\alpha}{4+2r\xi}\left(-\frac{r}{2}\xi^2 - 2\xi + 16\pi r\mathcal{A}^4 p\psi^4 - 2rQ_r^2\right), \tag{4.4}$$

$$\frac{d}{dr}\left(\mathcal{A}^4 p\right) = -\frac{\mathcal{A}^4\rho h}{\alpha}\frac{d\alpha}{dr} + \alpha_s(\chi)\mathcal{A}^4\left(4p - \rho h\right)Q_r\,, \tag{4.5}$$

$$\frac{dQ_r}{dr} = -Q_r\left[\frac{1}{\alpha}\frac{d\alpha}{dr} + \frac{\xi}{2} + \frac{2}{r}\right] - 4\pi\psi^4\alpha_s(\chi)\mathcal{A}^4\left(4p - \rho h\right). \tag{4.6}$$

These must be supplemented by a barotropic EoS $p = p(\rho), \varepsilon = \varepsilon(\rho)$. This system can be solved given the value at $r = 0$ of the density ρ_c, the conformal factor ψ_c and the scalar field χ_c (recalling that all radial derivatives of scalar quantities vanish in $r = 0$). The value of the lapse function at the center, α_c, is irrelevant to the solution per se, since only its derivative appears in Eqs. 4.1-4.6. This means that the lapse function is derived minus an arbitrary constant, which is then chosen in order to satisfy the correct asymptotic behaviour at $r \to \infty$.

The correct STT solution satisfies the following requirements:

- The ratio $C = \alpha Q_r/2\partial_r\alpha$ must be constant outside the NS, because it can be shown that it is equal to the ratio $Q_s/2M$ between the net scalar charge Q_s and twice the

Komar mass $\bar{M}_{\rm k}$ in the E-frame (see their definitions in App. B).

- In vacuum α and ψ must behave like the Just metric (Just 1959) in isotropic coordinates.

Given that the Just metric in isotropic coordinates has no analytical form, we provide here an approximation that proves to be accurate with a precision $\sim 10^{-4}$, already at a couple of NS radii. If one writes the metric terms ψ and α, outside of the NS surface, as

$$\psi^4(r) = \left[1 + \frac{1}{2r}\sum_{i=0}^{\infty}\frac{m_i}{r^i}\right]^4 , \tag{4.7}$$

$$\alpha^2(r) = \left[1 - \frac{1}{2r}\sum_{i=0}^{\infty}\frac{n_i}{r^i}\right]^2 \left[1 + \frac{1}{2r}\sum_{i=0}^{\infty}\frac{m_i}{r^i}\right]^{-2} , \tag{4.8}$$

one finds that the first values of m_i for $i > 0$ are:

$$m_1 = -C^2 m_0^2 , \tag{4.9}$$

$$m_2 = -C^2 m_0^3/6 , \tag{4.10}$$

$$m_3 = -C^2(1+3C^2) m_0^4/12 , \tag{4.11}$$

$$m_4 = -C^2(3+11C^2) m_0^5/120 , \tag{4.12}$$

$$m_5 = -C^2(9+58C^2+90C^4) m_0^4/720 , \tag{4.13}$$

$$m_6 = -C^2(45+334C^2+618C^4) m_0^5/10080 , \tag{4.14}$$

and $n_i = (-1)^i m_i$. When $Q_{\rm s} = 0$ one finds $m_0 = n_0$ and $m_i = n_i = 0$ for $i > 0$, recovering the GR solution.

Once the S-TOV solution has been found, starting with an initial guess, the `XNS` code performs iteratively the following steps until a converged solution is found:

1. Given a distribution of the physical and scalar fields, Eqs. 3.28,3.29 for a new spacetime metric in the E-frame are solved in sequence.
2. Using the new metric in the E-frame and the old physical fields, scalar field Eq. 3.31 is solved, allowing one to define a new metric in the J-frame.
3. If the magnetic field is purely toroidal, Eq. 3.43 is solved, and new values of the physical fields, including the magnetic field components through Eq. 3.41, are found in the J-frame. If the magnetic field is purely poloidal, first the equation for the vector potential Eq. 3.37 and then Eq. 3.34 are solved, determining the new physical fields in the J-frame.
4. Convergence is checked and, if not reached, the new physical metric and scalar fields are used to define a new starting model.

4.2 The numerical solvers

As we discussed in Sects. 3.3-3.5, the equations for the scalar quantities $\psi, \alpha\psi, \chi$ involve the Δ operator and the Grad-Shafranov equation can be reduced to a non-linear vector Poisson equation for $\check{A}_\phi$. Due to their non-linearity, the equations for ψ and $\alpha\psi$ are better solved iteratively for the quantities $\psi_n - 1$ and $\alpha_n\psi_n - 1$, where n is the numerical step, effectively solving for the deviation from asymptotic flatness $\psi = \alpha = 1$.

There are three main categories of numerical methods available to solve elliptic PDEs (Grandclément et al. 2001; Dimmelmeier et al. 2005; Grandclément & Novak 2009; Bucciantini & Del Zanna 2011): direct inversion, full relaxation, spectral decomposition. Their features can be summarised as follows.

- Direct inversion methods solve the full CFC system of equations at once using a Newton-Raphson solver on the entire computational grid. They rapidly converge to the solution, but the initial guess must be close enough to the solution to achieve convergence on the global minimum and their memory requirements are large.
- Full relaxation schemes are fast and do not require large memory allocations, but suffer from some poor convergence properties, for example they might fail on the axis or center of the star because of singularities in the quantities to be solved for.
- Spectral codes are characterised by the decomposition of the CFC system of equations into a combination of spherical harmonics - in the angular direction - and Chebyshev polynomial - in the radial direction. While this ensures a correct behaviour of the solution on the axis and at the center, these methods require specific grids and appropriate boundary conditions.

The metric solver of `XNS` is mixed, and works by decomposing the solutions into spherical harmonics in the angular direction and solving the ODEs obtained for each harmonic using direct inversion over the same grid. At second-order accuracy for the discretisation into finite differences, the solution of the scalar Poisson equations is reduced to the inversion of tridiagonal matrices. In particular, the solutions for $u(r,\theta) = \{\psi - 1, \alpha\psi - 1, \chi\}$ are found as a sum of spherical harmonics $Y_l(\theta)$ with coefficients $A_l(r)$ according to

$$u(r,\theta) = \sum_{l=0}^{\infty} \left[A_l(r) Y_l(\theta) \right] \ , \tag{4.15}$$

and similarly for the vector potential,

$$\check{A}_\phi(r,\theta) = \sum_{l=0}^{\infty} \left[C_l(r) \partial_\theta Y_l(\theta) \right] \ , \tag{4.16}$$

where

$$Y_l(\theta) = Y_l^0(\theta) = \sqrt{\frac{2l+1}{4\pi}} P_l(\cos\theta) \,, \tag{4.17}$$

with P_l the Legendre polynomial of degree l and $m = 0$ is set to impose the axisymmetry condition. This choice leads to a series of radial, second order boundary values ODEs for the coefficients $A_l(r)$ and $C_l(r)$. In particular:

$$\frac{d^2A_l}{dr^2} + \frac{2}{r}\frac{dA_l}{dr} - \frac{l(l+1)}{r^2}A_l = H_l \,, \tag{4.18}$$

where the source term is

$$H_l(r) = \oint H(r,\theta) Y_l(\theta) d\Omega \tag{4.19}$$

with $H(r,\theta)$ the source terms in Eqs. 3.28,3.29,3.31, $d\Omega = 2\pi \sin\theta d\theta$ and the integral runs from $\theta = 0$ to $\theta = \pi$ due to axisymmetry. Similarly, we obtain

$$\frac{d^2C_l}{dr^2} + \frac{2}{r}\frac{dC_l}{dr} - \frac{l(l+1)}{r^2}C_l = H_l^\phi \,, \tag{4.20}$$

where the source term is

$$H_l^\phi(r) = \frac{1}{l(l+1)} \oint H^\phi(r,\theta) \partial_\theta Y_l(\theta) d\Omega \,, \tag{4.21}$$

$H^\phi(r,\theta)$ being the source terms in Eq. 3.37.

These ODEs are solved using a tridiagonal matrix inversion. The decomposition in terms of spherical harmonics ensures the correct behaviour of the solutions on the symmetry axis, and allows us to enforce the proper boundary conditions at $r = 0$, where $A_l(r)$ and $C_l(r)$ go to zero with parity $(-1)^l$, and at the outer radial boundary, where we assume that $A_l(r)$ and $C_l(r)$ go to zero as $r^{-(l+1)}$.

4.3 The numerical setup

We used a 2D numerical grid and spherical coordinates: the radial coordinate r extends over the range $r \in [0, 100]$ in dimensionless units, corresponding to a maximum range of $\sim$ 150km; the angular coordinate θ extends over $\theta \in [0, \pi]$. For the results shown in Chap. 5,6 (Chap. 7) the grid has 400 (900) points in the r-direction, the first 200 (600) of which are equally spaced over the range $r \in [0, 20]$ ($r \in [0, 10]$) in dimensionless units, while the remaining 200 (300) points are logarithmically spaced, meaning that $\Delta r_i / \Delta r_{i-1} = \text{const}$. The angular grid is composed of 200 (100) equally spaced points. For the reference models shown in Sects. 5.2,5.3, the radial resolution was doubled. We have verified that at these resolutions our results have an accuracy of the order

of 10^{-3}, that the radius of the outer edge is far enough not to affect the solution, and the same holds for the choice of a stretched grid. In all cases the elliptic solvers use up to 20 spherical harmonics. We found that in order to avoid strongly oscillatory behaviours in the relaxation scheme of `XNS`, iterations over the various quantities Q had to be under-relaxed according to: $Q_{\rm new} = [Q_{\rm new} + Q_{\rm old}]/2$. The results shown in Chap. 5,6 are found using a simple polytropic EoS $p = K_{\rm a}\rho^{\gamma_{\rm a}}$, with an adiabatic index $\gamma_{\rm a} = 2$ and a polytropic constant $K_{\rm a} = 110$ (in dimensionless units). This is done for the ease of comparison, and in line with previous literature in GR (Bocquet et al. 1995; Kiuchi & Yoshida 2008; Frieben & Rezzolla 2012; Pili et al. 2014), where it was also used as an approximation of more complex and physically motivated EoS (Lattimer & Prakash 2007; Baym et al. 2018) above nuclear densities. In Chap. 7 we instead use a variety of realistic, tabulated EoS, as detailed in Sect. 7.1. Concerning the magnetic field structure, for purely toroidal magnetic fields we chose a magnetic barotropic law, Eq. 3.42, with toroidal magnetisation index $m = 1$, while for purely poloidal magnetic fields we opted for the simplest choice Eq. 3.38 (for more complex choices see Pili et al. 2014).

The coupling function $\mathcal{A}(\chi)$ is the only free function of a STT with zero potential. As introduced in Damour & Esposito-Farèse (1993), and used in many subsequent works (Novak 1998b; Mendes & Ortiz 2016), we adopt the choice of an exponential coupling function:

$$\mathcal{A}(\chi) = \exp\left[\alpha_0\chi + \frac{\beta_0}{2}\chi^2\right] , \tag{4.22}$$

where the parameters α_0 and β_0 are chosen to be $\alpha_0 = -2 \times 10^{-4}$ and $\beta_0 \in \{-6, -5.75, -5.5, -5.25, -5, -4.75, -4.5\}$. The GR configurations correspond to $\alpha_0 = \beta_0 = 0$. Such low values are chosen to both highlight the effects of scalarisation and to show its effects at the edge of the permitted parameter space, keeping in mind that our results hold also for scalar fields with a mass such that their screening radius is larger than the NS radius. In fact, as we explained in Sect. 2.4, in this case the effect of the scalar field is suppressed outside the screening radius, i.e. outside the NS surface, but it remains mostly untouched inside the compact object. For this reason, a massive scalar field is expected to deform the NS interior in a similar fashion to what we find. Moreover, the emission of dipolar waves is hindered. Since these are not observed to date and imply extremely severe constraints on the parameters of STTs (Zhang et al. 2017, 2019), the presence of a scalar field mass allows them to be satisfied.

Chapter 5

Axisymmetric equilibrium models of magnetised neutron stars in scalar-tensor theories

The results shown in this chapter were published in the paper Soldateschi et al. 2020 (hereafter SBD20).

We present here a detailed study of magnetised NSs in STTs. First, we show that, unlike in GR, in STTs NSs with the same mass but different central density can exist (Sect. 5.1). Then, we carry out a study of the parameter space considering the two extreme geometries of purely toroidal (Sect. 5.2) and purely poloidal (Sect. 5.3) magnetic fields, varying the strength of the magnetic field, for a scalarisation parameter of $\beta_0 = -6$. Then, we consider a weaker scalarisation: $\beta_0 = -5$ (Sect. 5.4) and $\beta_0 = -4.5$ (Sect. 5.5). We compare our results with magnetised GR solutions and un-magnetised scalarised solutions, showing how the mutual interplay between magnetic and scalar fields affect the magnetic and the scalarisation properties of NSs. In particular, we focus our discussion on magnetic deformability, maximum mass, and range of scalarisation. Then, we show how the interplay between the scalar and the magnetic fields can lead to a new kind of instability (Sect. 5.6). Finally, we discuss our results (Sect. 5.7).

The global quantities used in the following are defined in App. B. It can be shown that in the E-frame the Komar and ADM masses have the same value, while in the J-frame they differ by an amount proportional to the scalar charge. For this reason, in the following, when referring generically to the mass of the NS, we always mean the Komar mass in the E-frame ($M = \bar{M}_{\rm k}$), and we will use the two symbols interchangeably. On the other hand, given that the circumferential radius is a potentially measurable quantity, when referring to it we always mean its value in the J-frame. Moreover, since

the metric field equations in the E-frame have the same mathematical structure as in GR, it is most natural to provide the quadrupole deformations in the E-frame, as this is where GWs should be studied. In any case, we recall (see the discussion about frames in Sect. 2.2) that this is only a matter of convenience: observations measure quantities in the J-frame, which can then be converted to the E-frame through the conformal factor $\mathcal{A}$.

5.1 Uniqueness of scalarised neutron stars

It can be shown that, given a central density ρ_c, NSs in STTs admit multiple solutions. If $\mathcal{A}$ is an even function of χ then α_s is an odd-function (e.g. if $\alpha_0 = 0$ in Eq. 4.22) and Eq. 3.31 is invariant under the transformation $\chi \to -\chi$ (the same holds for Eqs. 3.28,3.29 and Eqs. 3.34,3.43). This implies that there are three possible NS solutions: one corresponding to $\chi = 0$, identical to GR, and two with $\chi \neq 0$, that only differ by the sign of χ. If α_s is an arbitrary function of χ, this symmetry breaks. If $\alpha_0 \neq 0$ in Eq. 4.22, then these three solutions split into three branches: the GR solution becomes a 'weakly scalarised' solution $\mathcal{S}_w$, where the total scalar charge Q_s is such that $\alpha_0 Q_s > 0$, while the other two scalarised branches split into two 'strongly scalarised' solutions: one, $\mathcal{S}_s^+$, with $\alpha_0 Q_s > 0$; the other, $\mathcal{S}_s^-$, with $\alpha_0 Q_s < 0$.

In Fig. 5.1, we illustrate qualitatively how these three branches behave in terms of their mass M as a function of the central density ρ_c. The range of spontaneous scalarisation, $\rho_b < \rho_c < \rho_t$, can be divided into 4 subregions depending on the relative values of the masses of the branches:

- for $\rho_b < \rho_c < \rho_1$ we have $M[\mathcal{S}_s^-] < M[\mathcal{S}_s^+] < M[\mathcal{S}_w]$;
- for $\rho_1 < \rho_c < \rho_2$ we have $M[\mathcal{S}_s^+] < M[\mathcal{S}_s^-] < M[\mathcal{S}_w]$;
- for $\rho_2 < \rho_c, < \rho_3$ we have $M[\mathcal{S}_s^+] < M[\mathcal{S}_w] < M[\mathcal{S}_s^-]$;
- for $\rho_3 < \rho_c, < \rho_t$ we have $M[\mathcal{S}_w] < M[\mathcal{S}_s^+] < M[\mathcal{S}_s^-]$.

The densities $\rho_{1,2,3}$ correspond to the points where two branches have the same mass. Almost always, the $\mathcal{S}_s^-$ branch is the one where the mass shows the largest deviation from the GR (or from $\mathcal{S}_w$) and is also the one with the maximum mass. In Tab. 5.1, we report the values of global quantities characterising solutions of the three branches, for few selected values of the central density, assuming $\alpha_0 = -0.05$ and $\beta_0 = -6$ in Eq. 4.22, for spherically symmetric un-magnetised and non-rotating NSs. Such a non-physical high value of α_0 was chosen in order to enhance the differences between the $\mathcal{S}_s^-$ and $\mathcal{S}_s^+$ branches. We found that, in terms of the net scalar charge, $Q_s[\mathcal{S}_w] < Q_s[\mathcal{S}_s^+] < Q_s[\mathcal{S}_s^-]$, and similarly in terms of the NS circumferential radius

Table 5.1: Values of various physical quantities describing the solutions $\mathcal{S}_{\rm w}, \mathcal{S}_{\rm s}^{+}$ and $\mathcal{S}_{\rm s}^{-}$, for $\alpha_0 = -0.05$ and $\beta_0 = -6$, and for selected values of the central density $\rho_{\rm c}$ (in the J-frame), corresponding from top to bottom to: $\rho_{\rm b} < \rho_{\rm c} < \rho_1$, $\rho_3 < \rho_{\rm c} < \rho_{\rm t}$, $\rho_{\rm c} = \rho_1, \rho_2, \rho_3$. M is the Komar mass in the E-frame, $Q_{\rm s}$ the scalar charge in the E-frame, $R_{\rm c}$ the circumferential radius in the J-frame, W the gravitational binding energy in the E-frame. See App. B for their definition: Eqs. B.2,B.7,B.8,B.11.

$\rho_{\rm c}[10^{15}{\rm g\ cm^{-3}}]$	$M[M_\odot]$	$Q_{\rm s}[M_\odot]$	$R_{\rm c}[{\rm km}]$	$\lvert W\rvert[M_\odot]$
	$\mathcal{S}_{\rm w}; \mathcal{S}_{\rm s}^{+}; \mathcal{S}_{\rm s}^{-}$	$\mathcal{S}_{\rm w}; \mathcal{S}_{\rm s}^{+}; \mathcal{S}_{\rm s}^{-}$	$\mathcal{S}_{\rm w}; \mathcal{S}_{\rm s}^{+}; \mathcal{S}_{\rm s}^{-}$	$\mathcal{S}_{\rm w}; \mathcal{S}_{\rm s}^{+}; \mathcal{S}_{\rm s}^{-}$
1.000	1.601; 1.402; 1.307	-0.154; -0.679; 0.815	13.46; 13.68; 13.83	0.2709; 0.1304; 0.0779
2.500	1.696; 1.986; 2.166	-0.149; -0.894; 1.190	10.60; 12.40; 13.68	0.4870; 0.3607; 0.3022
1.648	1.714; 1.683; 1.683	-0.113; -0.996; 1.150	11.90; 13.33; 13.89	0.4021; 0.1562; 0.1044
1.695	1.715; 1.708; 1.715	-0.112; -1.010; 1.170	11.81; 13.33; 13.93	0.4088; 0.1618; 0.1093
1.710	1.716; 1.716; 1.726	-0.112; -1.010; 1.180	11.78; 13.33; 13.93	0.4109; 0.1637; 0.1110

$R_{\rm c}[\mathcal{S}_{\rm w}] < R_{\rm c}[\mathcal{S}_{\rm s}^{+}] < R_{\rm c}[\mathcal{S}_{\rm s}^{-}]$. In this sense the $\mathcal{S}_{\rm s}^{-}$ solution is the one with the largest deviation from GR. One can compare the three branches also in terms of their compactness $\mathcal{C} = M/R_{\rm c}$, or in terms of their gravitational binding energy, defined as the difference between the Komar and proper masses in the E-frame, $W = M - M_{\rm p}$. We find that $\mathcal{S}_{\rm s}^{-}$ is the one with the smallest compactness and highest gravitational binding energy. If we interpret spontaneous scalarisation as an effective phase-transition (Damour & Esposito-Farèse 1996), then the difference in binding energy between the $\mathcal{S}_{\rm s}^{\pm}$ and $\mathcal{S}_{\rm w}$ branches can be though of as an effective latent heat that the appearance of a scalar field releases into the system, inflating the star and reducing $|W|$. Within this interpretation, it is reasonable to expect that NSs undergoing spontaneous scalarisation should settle in the $\mathcal{S}_{\rm s}^{-}$ branch, which is the one with the lowest $|W|$. Indeed we find that our code always selects the $\mathcal{S}_{\rm s}^{-}$ solution [we note that for $\alpha_0 = 0$, `XNS` always selects the GR solution, and that $\alpha_0 \neq 0$ is required to get a scalarised one; see Bucciantini et al. (2015) for a discussion of this issue with relaxation schemes for elliptic equations]. It remains to be understood, in a dynamical evolving system, which branch is selected and under what physical conditions.

In the following, we will refer to strongly scalarised solutions, in the regime where spontaneous scalarisation leads to sizeable scalar charges, simply as 'scalarised', while weakly scalarised solutions or in general solutions showing a negligible scalar charge, will be referred to as 'de-scalarised' or 'GR-like'.

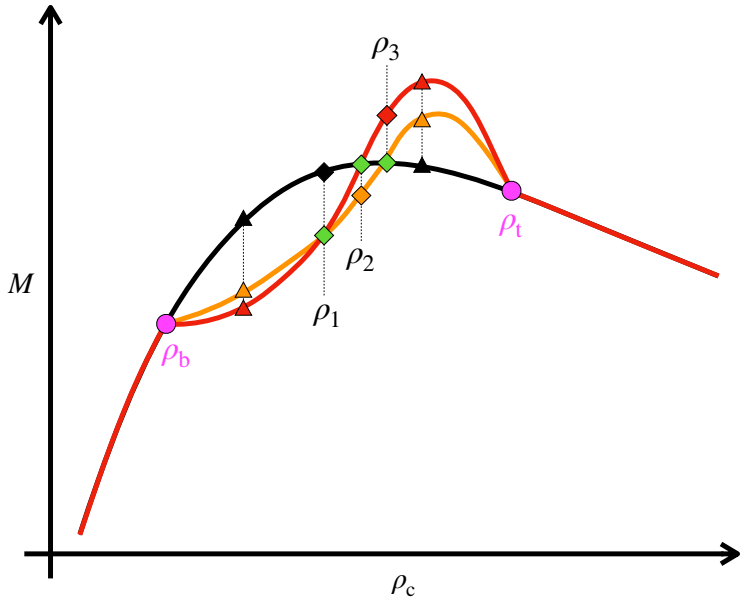

Figure 5.1: Qualitative behaviour of multiple solutions for NSs in STTs, in terms of the relation of their mass to the central density ρ_c . The black, orange and red sequences represent, respectively, the weakly scalarised solutions $\mathcal{S}_w$ and the strongly scalarised solutions $\mathcal{S}_s^+$ and $\mathcal{S}_s^-$. Green diamonds mark the position with central densities $\rho_c = \rho_1, \rho_2, \rho_3$ where two branches have the same mass; triangles select intermediate densities (see e.g. the values in Tab. 5.1); ρ_b and ρ_t (magenta circles) represent the lower and upper limits of the central density for which spontaneous scalarisation happens.

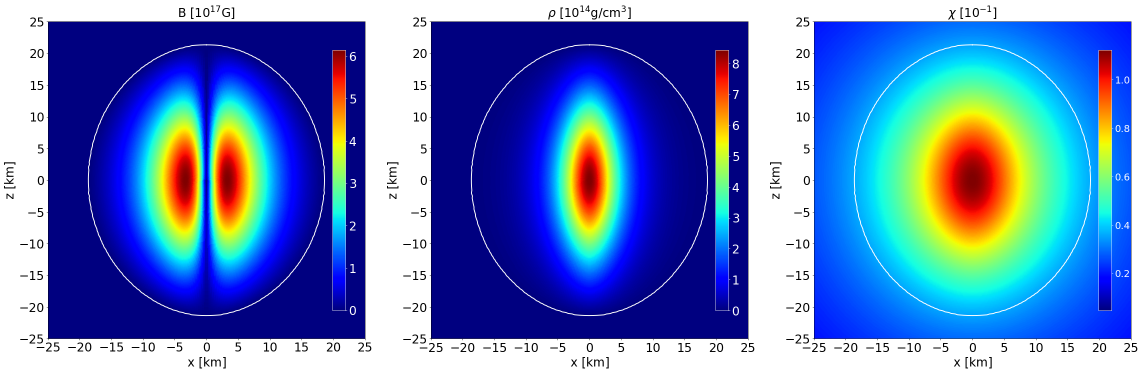

Figure 5.2: From left to right: meridional distribution of the magnetic field strength $B = \sqrt{B^\phi B_\phi}$, of the density ρ and of the scalar field χ for a model with a toroidal magnetic field of maximum strength $B_{max} = 6.134 \times 10^{17}$G and central density $\rho_c = 8.440 \times 10^{14}$g cm^{-3}. The white curve represents the surface of the star. More quantitative details on this configuration can be found in Tab. 5.2, where it is named 'model T'.

Table 5.2: Global quantities (see App. B) of the reference equilibrium models with a toroidal (T) and poloidal (P) magnetic field, displayed in Figs. 5.2,5.8 respectively, together with their un-magnetised counterparts, T_0 and P_0.

Model	ρ_c $[10^{14}\text{g cm}^{-3}]$	M_k $[M_\odot]$	M_0 $[M_\odot]$	Q_s $[M_\odot]$	R_c [km]	r_p/r_e	e $[10^{-1}]$	e_s $[10^{-1}]$	Φ $[10^{30}\text{g cm}^{-2}]$	μ $[10^{35}\text{erg G}^{-1}]$
T_0	8.44	1.30	1.38	0.64	14.08	1.00	0.00	0.00	0.00	0.00
T	8.44	1.46	1.52	0.47	20.59	1.15	-8.71	1.91	1.48	0.00
P_0	5.15	1.25	1.33	0.17	15.73	1.00	0.00	0.00	0.00	0.00
P	5.15	1.36	1.42	0.56	16.71	0.67	2.90	-1.52	0.00	2.20

5.2 Toroidal field models with $\beta_0 = -6$

In order to illustrate how a purely toroidal magnetic field affects the properties of scalarised NSs, and to allow a comparison with GR, in Fig. 5.2 we show the distribution of the magnetic field strength $B = \sqrt{B^\phi B_\phi}$, of the density ρ, and of the scalar field χ, for a reference model chosen in order to have the same central density, $\rho_c = 8.440 \times 10^{14}\text{g cm}^{-3}$, and the same maximum value of the magnetic field, $B_{\max} = 6.134 \times 10^{17}\text{G}$, as in Pili et al. (2014), for $\alpha_0 = -2 \times 10^{-4}$ and $\beta_0 = -6$. Comparing Fig. 5.2 to the GR solution (Pili et al. 2014, Fig. 1), we see that the overall distribution of the magnetic field and of the density are very similar, both in their shape and in their values: as expected for a toroidal field, the magnetic field vanishes on the symmetry axis and reaches a maximum deep inside the star, close to its center. Again, as expected, the star displays a prolate shape in density, caused by the magnetic field stress, and the outer layers are inflated to large radii by the magnetic pressure. We note that this deformation is much more pronounced in the inner parts of the star compared to its outer layers, where the density isosurfaces show only a mild deviation from a spherical shape. On the other hand, we see that the effect of the magnetic stress on the shape of the scalar field is far less evident than on the density, and the scalar field isosurfaces show the same level of prolateness throughout the star.

In Tab. 5.2, we give the values of various global quantities characterising this model (T). Its mass $M = 1.460\text{M}_\odot$ is lower than that of its GR counterpart, $1.596\text{M}_\odot$, by roughly 10%. The same holds for the baryonic mass which now is $M_0 = 1.520\text{M}_\odot$, lower than in the GR case where its value is $1.680\text{M}_\odot$. With reference to the regimes shown in Fig. 5.1, our reference model sits between ρ_b and ρ_2, on the $\mathcal{S}_s^-$ sequence. Interestingly, the circumferential radius $R_c = 20.59\text{km}$ is just 2% higher than in GR. The 'radius ratio' between the surface radial coordinate at the pole, r_p, and at the equator, r_e, is $r_p/r_e = 1.15$, not much higher than 1, and only marginally higher than the corresponding GR value. The same holds for the quadrupole deformation e (see App. B for its definition).

This might seem counterintuitive, because the scalar field is known to make NSs more spherical (Doneva et al. 2013), in part because the contribution of the scalar field to the quadrupole deformation has the opposite sign with respect to the matter, in part because the scalar field pressure tends to counteract matter deformations. We also provide an estimate of the quadrupolar deformation of the scalar field through the quantity e_s, that corresponds to the quadrupolar deformation of the trace of $\bar{T}^{\mu\nu}_{\rm p}$ (see App. B). It is meaningful to compare our reference model also to an un-magnetised model in STT with the same central density, which is characterised in Tab. 5.2 as T_0. The main differences to note are the lower values of both the Komar and baryonic mass, and of the circumferential radius with respect to the magnetised case. This gives a quantitative estimate of how strong the effects of the magnetic field are and, as in GR, it shows that the magnetic field can provide extra pressure support to sustain a larger total mass. On the other hand, the compactness is higher: $\mathcal{C} = 0.09$ without a magnetic field versus $\mathcal{C} = 0.07$ in the magnetised model. This reflects in the fact the the scalar charge Q_s is higher in the un-magnetised model, by about one third.

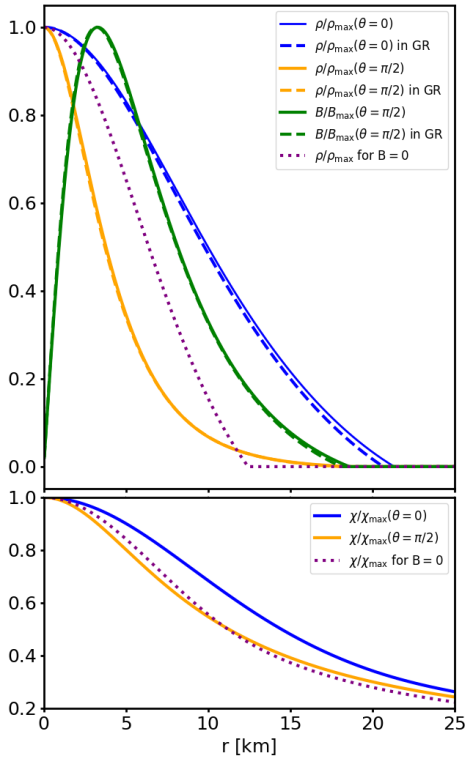

Figure 5.3: Upper panel: profile of the polar (solid blue lines) and equatorial (solid orange lines) density, and of the magnetic field strength at the equator (solid green lines), normalised to their maximum values, for the equilibrium model T (with purely toroidal magnetic field) of Tab. 5.2. These are to be compared to the corresponding GR model at the same ρ_c and B_{max} (dashed lines), and with the density of the scalarised and un-magnetised model at the same ρ_c, T_0 (dotted purple line). Lower panel: profile of the equatorial (orange line) and polar (blue line) scalar field, normalised to the maximum value, for the equilibrium model T (solid), compared to the un-magnetised model T_0 (dotted purple).

To provide a more accurate comparison of model T with the corresponding GR one, in Fig. 5.3 we plot for both of them the profiles of B and ρ, normalised to their maximum value. In particular, we clearly see that the STT profiles are virtually coincident with the GR ones: only the polar radius gets slightly larger. This agrees with the fact that apart from integrated quantities, that differ at most $\sim$ 10%, all other quantities characterising those models are very close, suggesting that it is not the dy-

namical action of the scalar field that gives rise to the differences in mass, but more likely changes in the volume element, associated to small changes in the metric. In the same figure we also compare model T to the un-magnetised model T_0, clearly showing the magnetic induced deformation on the density profile, that affects mostly the low-density outer part of the NS, nearly doubling the star's polar radius. We also compare the profiles of χ, normalised to its maximum value $\chi_{\rm max}$. While in the central part of the star, $r \lesssim 7$km, the equatorial and polar profiles are respectively steeper and shallower than in the un-magnetised case, in the outer part of the star and outside it they are both shallower than in the un-magnetised case, as expected for a lower total scalar charge.

In line with Pili et al. (2014), in order to characterize the interplay of the scalar and magnetic field, in Fig. 5.4, for equilibrium models having all the same baryonic mass $M_0 = 1.68 M_\odot$, we plot the deviations Δ of $\rho_{\rm c}$, M, $R_{\rm c}$ and e with respect to the un-magnetised case, as functions of the maximum value of the magnetic field strength inside the star $B_{\rm max}$. The deviation of a quantity f is defined as

$$\Delta f = \frac{f\left(B_{\rm max}, M_0\right) - f\left(0, M_0\right)}{f\left(0, M_0\right)} \,, \tag{5.1}$$

except for e, in which case we just plot its value, since $e(0, M_0) = 0$. The results are compared with the GR sequence having the same baryonic mass. It is immediately evident that the qualitative trends are unchanged. The sequence shows that at a fixed baryonic mass there is a limit to the strength of the magnetic field that a NS can host. We find that in out STT models this value is 1.05×10^{18}G, almost twice with respect to the one of the equivalant GR sequence, 6.13×10^{17}G. As the magnetisation parameter $k_{\rm m}$ increases, so does at the beginning also $B_{\rm max}$, until it reaches its limiting value. A further increase of $k_{\rm m}$ leads to a reduction of the magnetic field. The central density first rises with $k_{\rm m}$, reaching a value about 10% larger at $B_{\rm max} \simeq 9 \times 10^{17}$G and then beginning to decrease. For weak magnetisations, we find that, for the same $B_{\rm max}$, the deviation is about one fourth than in GR. However, once the magnetisation parameter $k_{\rm m}$ increases beyond the point where the limiting magnetic field is reached, the deviation of our STT models becomes about a factor two higher than GR. We also find that, as the magnetisation increases even farther, solutions de-scalarise (cyan dotted line), becoming equivalent to GR. When looking at ΔM or $\Delta R_{\rm c}$, one recovers similar trends, with deviations that are smaller than in GR for weak magnetic fields. Interestingly, along the scalarised part of our sequence, there seems to be a maximum value of $\Delta M = 0.05$ at $B_{\rm max} = 8 \times 10^{17}$G, a behaviour not present in GR. Similarly, the quadrupolar deformation e is about one fourth than that of GR for weak magnetisations and, again, GR is recovered at high magnetisations, when the NS de-scalarises. Just focusing on the weakly magnetised part of the sequence, before the limiting magnetic field is reached, we found that the

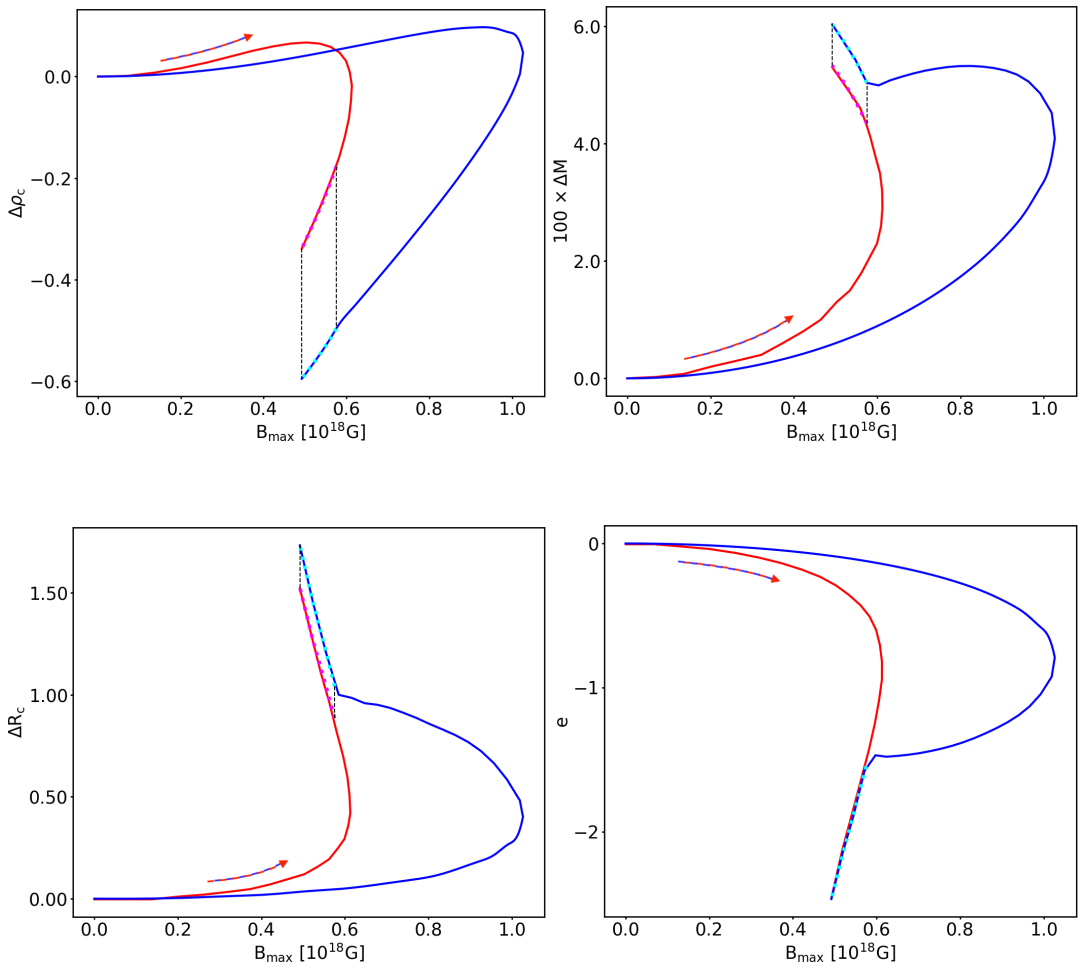

Figure 5.4: Variation, with respect to the un-magnetised model, of various quantities along the equilibrium sequence with constant $M_0 = 1.68\mathrm{M}_\odot$ for purely toroidal magnetic field. From left to right, top to bottom: central density ρ_c, Komar mass M, circumferential radius R_c and quadrupole deformation e. The blue lines represent our STT results, to be compared to the red lines, describing the GR models in Pili et al. (2014, Fig. 2). The cyan dotted lines highlight the de-scalarised configurations; it is connected by the black dashed segments to the magenta dotted lines, which represent the same STT deviations when calculated with respect to the un-magnetised model in GR. The arrows show the direction of increasing magnetisation.

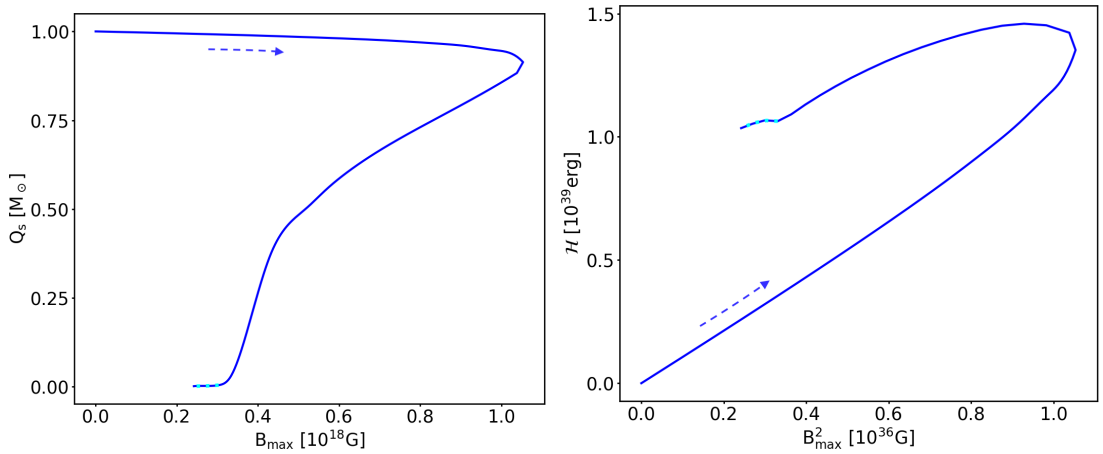

Figure 5.5: Scalar charge Q_s, normalised to its value for the un-magnetised model (left panel), and magnetic field energy $\mathcal{H}$ (right panel) as functions of B_{max} along the equilibrium sequence with constant $M_0 = 1.68 M_\odot$ and purely toroidal magnetic field. The cyan dotted line highlights the de-scalarised configurations. The arrows show the direction of increasing magnetisation.

same deviations are usually achieved at twice the value of B_{max} with respect to GR. This indicates that NSs in STTs are far less deformable than their GR counterparts of the same baryonic mass. The origin of this behaviour is to be looked for in the effective pressure support provided by the scalar field. A purely toroidal magnetic field exerts a stress on the star that leads to a prolate matter distribution. This, as a consequence, acting as a source for the scalar field, leads to a prolate distribution of the scalar field itself. Given that the effective pressure of χ depends on its gradient, a prolate distributions leads, with respect to a spherically symmetric one, to an increased outward-pointing force along the equator and a decreased one along the polar axis (see e.g. the scalar field profiles on a prolate system shown in Fig. 5.3). This might seem to contradict what was found before, where we showed only marginal differences between STT and GR. But while previously the comparison was done at the same central density, here is instead done at the same baryonic mass.

In Fig. 5.5, we show how the magnetic energy $\mathcal{H}$ and the scalar charge Q_s change with B_{max}. As the magnetisation parameter k_m rises, the magnetic energy scales with good approximation as $\mathcal{H} = 1.1 \times 10^{39} (B_{max}/10^{18}\text{G})^2 \text{erg}$ up to $B_{max} \simeq 10^{18}$G. As the magnetisation rises beyond the point where $B_{max} = 1.05 \times 10^{18}$G, the magnetic field energy, in the scalarised part, reaches a maximum of $\mathcal{H} = 1.46 \times 10^{39}$erg at $B_{max} = 9 \times 10^{17}$G, finally relaxing to the GR profile when the sequence de-scalarises around $B_{max} = 3 \times 10^{17}$G. The scalar charge, instead, drops with increasing magnetisation, being about 10% smaller at $B_{max} = 1.05 \times 10^{18}$G. Beyond this point, the scalar charge drops substantially until the NS completely de-scalarises.

In Fig. 5.6, we show how the Komar mass changes with central density holding fixed the magnetic flux Φ (top panel) or the baryonic mass M_0 (middle panel). The lower bound for scalarised models, ρ_b, moves to higher densities from $\rho_b = 5 \times 10^{14}$g cm^{-3} for $\Phi = 0$ to $\rho_b = 7.5 \times 10^{14}$g cm^{-3} for $\Phi = 2.55 \times 10^{30}$G cm^2, while the corresponding Komar (baryonic) mass changes from 1.25M$_\odot$ (1.33M$_\odot$) to 1.75M$_\odot$ (1.81M$_\odot$). We find no evidence suggesting the existence of an upper bound to the mass of the possible de-scalarised models. Analogously, the upper bound ρ_t for scalarised models increases from $\rho_t = 3.5 \times 10^{15}$g cm^{-3} for $\Phi = 0$ to $\rho_t = 4 \times 10^{15}$g cm^{-3} for $\Phi = 1.46 \times 10^{30}$G cm^2, while the corresponding Komar (baryonic) mass changes from 1.60M$_\odot$ (1.73M$_\odot$) to 1.62M$_\odot$ (1.71M$_\odot$).

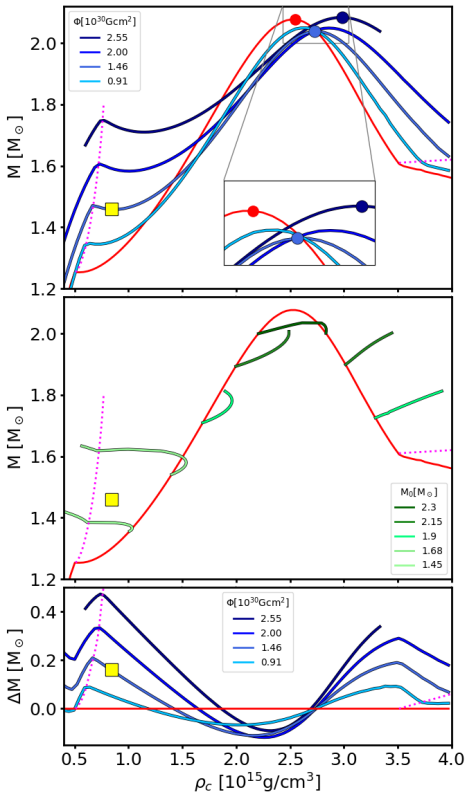

Figure 5.6: Mass-density sequences for models with purely toroidal magnetic field and $\beta_0 = -6$. Upper panel: sequences computed at fixed values of the magnetic flux Φ (blue lines), compared with the un-magnetised case (red line). The dotted magenta lines represent the limit for spontaneous scalarisation. Dots mark the position of the maximum mass models UM$_0$ (red), TM$_1$ (light blue) and TM$_2$ (dark blue) of Tab. 5.3. The yellow square represents model T of Fig. 5.2. Middle panel: sequences computed at fixed baryonic mass (green lines). Lower panel: mass difference of sequences at fixed Φ with respect to the un-magnetised one.

Contrary to GR, where it is found that the maximum mass of sequences at fixed Φ increases with the magnetic flux while the central density of the related models first rises and then drops (Pili et al. 2014, Fig. 4), in our STT sequences we found that the behaviour is more complex. At densities just above ρ_b, the mass of magnetised models is found to be always larger than the un-magnetised one. However, as the density increases, the trend is reversed and we find magnetised models having a lower mass than the un-magnetised configuration at the same central density. This is reversed again once the density exceeds 2.72×10^{15}g cm^{-3} as a consequence of the shift of the position of the maximum mass. This trend is also evident by looking at configurations at fixed baryonic mass and when sequences are parametrised at fixed values of B_{max} or at fixed e, in Fig. 5.7. It is interesting to notice that close to $\rho_c \simeq$

Table 5.3: Global quantities (see App. B) of the maximum mass models with a purely toroidal (TM_1,TM_2) and purely poloidal (PM_1,PM_2) magnetic field, displayed in Figs. 5.6,5.11 respectively, together with their un-magnetised counterpart (UM_0).

Model	ρ_c $[10^{15}\text{g cm}^{-3}]$	M_k $[M_\odot]$	M_0 $[M_\odot]$	Q_s $[M_\odot]$	R_c [km]	B_{max} $[10^{18}]$G	Φ $[10^{30}\text{g cm}^{-2}]$	μ $[10^{35}\text{erg G}^{-1}]$	e $[10^{-1}]$	e_s $[10^{-1}]$
UM_0	2.55	2.08	2.41	1.01	12.1	0.0	0.0	0.0	0.0	0.0
TM_1	2.72	2.04	2.29	1.01	13.2	1.37	1.46	0.0	-0.236	0.107
TM_2	2.95	2.08	2.26	1.04	15.8	1.99	2.55	0.0	-0.656	0.200
PM_1	2.46	2.12	2.45	1.04	12.3	1.33	1.06	1.16	0.074	-0.048
PM_2	2.42	2.15	2.49	1.04	12.5	1.76	1.40	1.57	0.118	-0.078

2.72×10^{15}g cm^{-3} the Komar mass is independent of the magnetisation. Quantitatively, the density at which the maximum is reached always increases from $\rho_c = 2.55 \times 10^{15}$g cm^{-3} for $\Phi = 0$ to $\rho_c = 2.95 \times 10^{15}$g cm^{-3} for $\Phi = 2.55 \times 10^{30}$G cm^2, while the value of the maximum mass drops initially from $2.08M_\odot$ to $2.04M_\odot$ for $\Phi = 1.46 \times 10^{30}$G cm^2 and then rises again to $2.08M_\odot$ for $\Phi = 2.55 \times 10^{30}$G cm^2. The full characterisation of the models at maximum mass is given in Tab. 5.3.

In a similar way, in Fig. 5.7, we have also analysed how the scalar charge Q_s changes with magnetisation. The maximum of the scalar charge goes from $Q_s = 1.16M_\odot$ at $\Phi = 0$,to $Q_s = 1.14M_\odot$ when $\Phi = 2.55 \times 10^{30}$G cm^2, while the density at which this maximum is reached increases from 2.09×10^{15}g cm^{-3} to 2.46×10^{15}g cm^{-3}. Globally, this appears as a shift to higher density of the sequences. The maximum of the scalar charge is always reached before the maximum of the mass. Analogously to the mass, we find that close to $\rho_c \simeq 2.33 \times 10^{15}$g cm^{-3} the scalar charge is independent of the magnetisation.

5.3 Poloidal field models with $\beta_0 = -6$

As it was done in the toroidal case, also for purely poloidal magnetic fields, our reference model was chosen in order to have the same central density $\rho_c = 5.15 \times 10^{14}$g cm^{-3} and the same maximum value of the magnetic field $B_{max} = 6.256 \times 10^{17}$G, as in Pili et al. (2014). Analogously to the previous toroidal case, this model sits in the part of Fig. 5.1 between ρ_b and ρ_2, on the sequence $\mathcal{S}_s^-$. In Fig. 5.8, we show the distribution of the magnetic field strength $B = \sqrt{B^r B_r + B^\theta B_\theta}$, of the density ρ and of the scalar field χ for this model. Comparing them to the GR ones in Pili et al. (2014, Fig. 5), we see that, even for a purely poloidal magnetic field, the overall distributions of the various quantities are very similar to GR, both in their shape and in their values. As expected

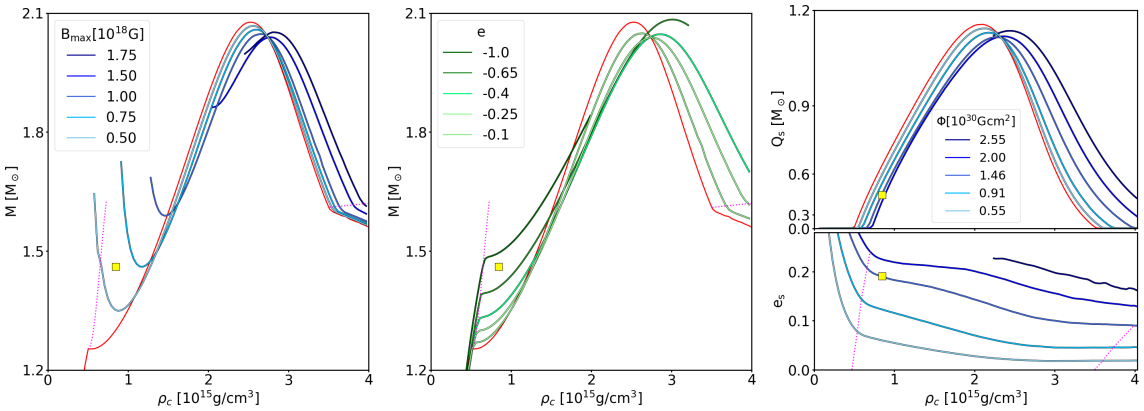

Figure 5.7: Sequences for the models with purely toroidal magnetic field and $\beta_0 = -6$. Left panel: mass-density relation computed at fixed $B_{\max}$ (blue lines) compared with the un-magnetised sequence (red line). Middle panel: mass-density relation computed at fixed e (green lines) compared with the un-magnetised sequence (red line). Right panel: on top, scalar charge computed at fixed Φ (blue lines) compared with the un-magnetised sequence (red line); on bottom, trace quadrupole deformation e_s. In all panels, the dotted magenta lines represent the limit for spontaneous scalarisation and the yellow square represents model T of Fig. 5.2.

for a poloidal field, the magnetic field reaches a maximum at the center of the star, and vanishes in an equatorial ring located at $r \simeq 12$km. The star displays an oblate shape in density, caused by the magnetic field stress, with an equatorial density profile which is almost flat close to the center. As in GR, increasing farther the magnetic field strength produces configurations where the density maximum is no longer at the center (analogously to Pili et al. 2014, Fig. 6). Again, we see that the effect of the magnetic stress on the shape of the scalar field is far less pronouced than on the density.

In Tab. 5.2, we give the values of various global quantities characterizing this model (P). The Komar mass $M = 1.360\mathrm{M}_\odot$, is lower than the GR mass, $1.597\mathrm{M}_\odot$ by roughly 15%, and the same holds for the baryonic mass which is $M_0 = 1.42\mathrm{M}_\odot$, compared to the value of the GR counterpart, $1.680\mathrm{M}_\odot$. The radius ratio $r_p/r_e = 0.67$ is instead marginally smaller than the GR value of 0.69. On the other hand, its circumferential radius $R_c = 16.71$km is less than 1% smaller than the GR one. The quadrupole deformation e is the same as in GR. As before, it seems that the presence of a scalar field, at the same central density and for the same maximum magnetic field, does not affect the distribution of fluid quantities. Moreover, we provide an estimate of the quadrupolar deformation of the scalar field through the quantity e_s, which is comparable in strength to the quadrupole deformation e.

We can also make a comparison to the un-magnetised model with the same central density, characterised in Tab. 5.2 under the name P_0. The main differences are the

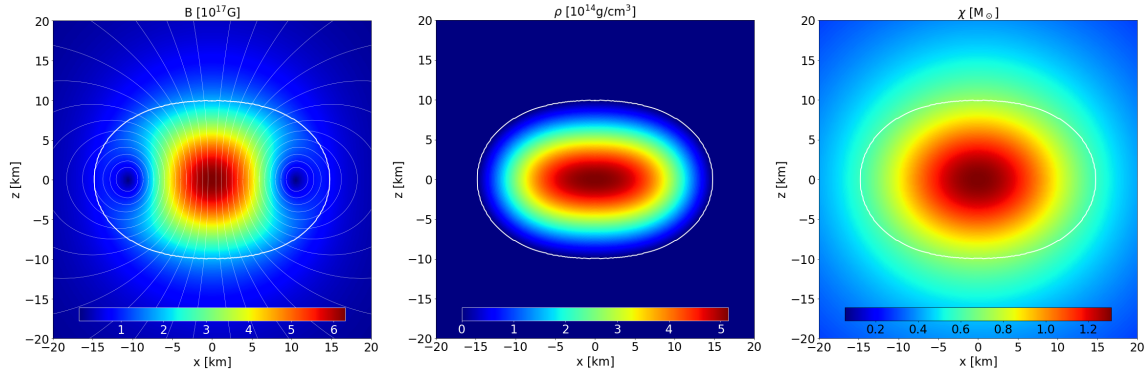

Figure 5.8: From left to right: meridional distribution of the magnetic field strength $B = \sqrt{B^r B_r + B^\theta B_\theta}$, of the density ρ and of the scalar field χ for a model with a poloidal magnetic field of maximum strength $B_{\rm max} = 6.256 \times 10^{17}$G and central density $\rho_{\rm c} = 5.15 \times 10^{14}$g cm^{-3}. The white curve represents the surface of the star. The light white lines on the left panel represent magnetic surfaces. More quantitative details on this configuration can be found in Tab. 5.2, where it is named 'model P'.

values of the masses and of the circumferential radius, that are smaller for $B = 0$. Also the compactness is slightly lower: $\mathcal{C} = 0.0795$ without a magnetic field versus $\mathcal{C} = 0.0814$ in the magnetised model. Differently than in the toroidal case, the scalar charge $Q_{\rm s}$ is much higher in the magnetised model. In Fig. 5.9, we show the profiles of the magnetic field B and and densityρ, normalised to their maximum value, for the model P (solid lines) and for the corresponding GR model (dashed lines) with the same $B_{\rm max}$ and $\rho_{\rm c}$ together with the un-magnetised model $\rm P_0$. We also plot the profiles of χ, normalised to its maximum value $\chi_{\rm max}$, for the models P and $\rm P_0$. Again, the STT profiles are almost coincident with the GR ones: only the equatorial radius gets marginally increased. This is slightly different than the effect of the magnetic field, which changes the density profile and decreases the star's polar radius and increases the equatorial one. The profile of the scalar field reflects the oblateness of the matter distribution, showing deviations that are somewhat smaller than the toroidal case. The same conclusions drawn in the toroidal case apply here too.

In Fig. 5.10, we show the deviations Δ as it was done in Fig. 5.4. The qualitative trends are the same as in GR, and do not show the complexity of the toroidal case. In GR there was some evidence indicating that the maximum magnetic field for a NS of $1.68 M_\odot$ could not exceed $\approx 6.2 \times 10^{17}$G. In STT we found instead that up to values or order of 1×10^{18}G there is no evidence of a saturation or limit of the maximum value of the magnetic field, which does not rule out the possibility that it might exist above 10^{18}G. The behaviour of all quantities appears to be monotonic in $B_{\rm max}$: the central density decreases, while the mass, the circumferential radius and the quadrupole deformation rise. As in the toroidal case, for a given value of $B_{\rm max}$ the deviation appears to be about

one fourth than in GR, while the same deviation is reached for values of $B_{\rm max}$ about twice higher than in GR. There is no evidence that the sequence would de-scalarise. As in the poloidal case, this trend can again be understood based on the effective pressure support provided by the scalar field. A purely poloidal magnetic field exerts a stress on the star that leads to an oblate matter distribution. This leads to an oblate distribution of the scalar field itself which, in turn, increases the outward-pointing force along the pole and decreases the one along the equator with respect to a spherically symmetric model.

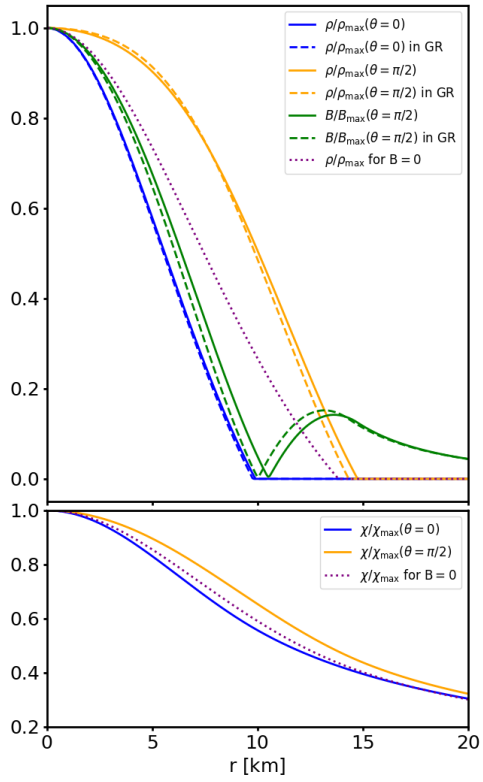

Figure 5.9: Top panel: profile of the polar (solid blue lines) and equatorial (solid orange lines) density, and of the magnetic field strength (solid green lines) at the equator, normalised to their maximum values, for the equilibrium model P (with purely poloidal magnetic field) of Tab. 5.2. These are to be compared to the corresponding GR model at the same $\rho_{\rm c}$ and $B_{\rm max}$ (dashed), and with the density of the scalarised and un-magnetised model at the same $\rho_{\rm c}$, P0 (dotted purple line). Bottom panel: profile of the equatorial (orange line) and polar (blue line) scalar field, normalised to their maximum value, for the equilibrium model P (solid), compared to the un-magnetised model P0 (dotted purple).

We found that, up to $B_{\rm max} \approx 10^{18}$G, the total magnetic field energy $\mathcal{H}$ scales with a good approximation as $\mathcal{H} = 0.55 \times 10^{39}(B_{\rm max}/10^{18}{\rm G})^2$erg, and the scalar charge increases by about 2% with respect to the un-magnetised case. We also found that the magnetic dipole scales as $\mu = 1.5 \times 10^{35}(B_{\rm max}/10^{18}{\rm G})$erg G^{-1}, about 30% less than in GR. Given that the dipole moment is ultimately a measure of the net toroidal current, this can be considered a kind of global measure of a quantity integrated throughout the NS; as such, even in this case strongly affected by variations in the value of the volume element, related to the metric itself. In Fig. 5.11, we show how the Komar mass changes with central density holding fixed the magnetic dipole moment μ or the baryonic mass M_0 (top panel). The lower bound $\rho_{\rm b}$ for scalarised models now moves to lower densities - from $\rho_{\rm b} = 5 \times 10^{14}$g cm^{-3} for $\mu = 0$ to $\rho_{\rm b} = 4.3 \times 10^{14}$g cm^{-3} for $\mu = 1.57 \times 10^{35}$erg/G - while the corresponding Komar (baryonic) mass rises, going to $1.31{\rm M}_\odot$ ($1.38{\rm M}_\odot$). Contrary to the toroidal case, we see from Fig. 5.12 (left panel) that, for purely

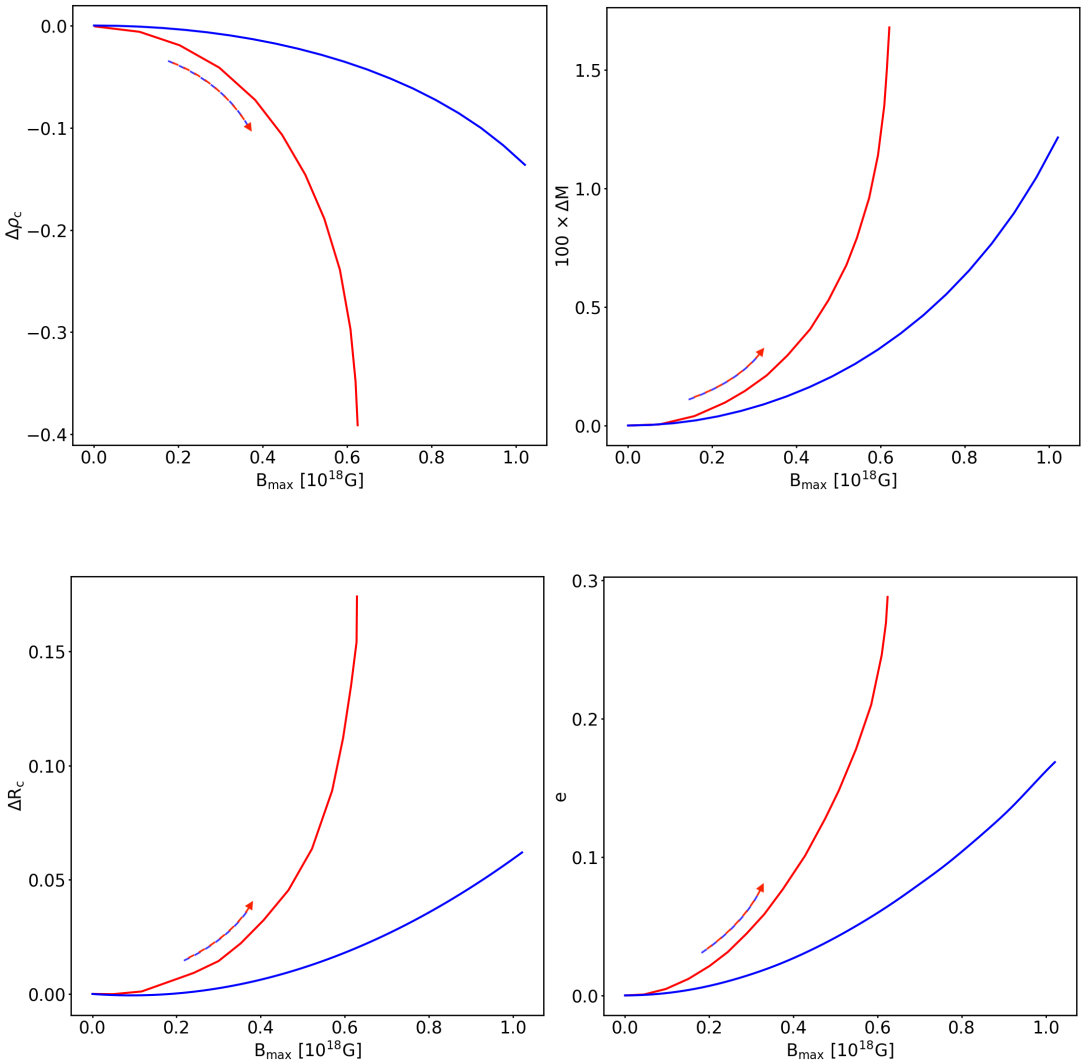

Figure 5.10: Variation, with respect to the un-magnetised model, of various quantities along the equilibrium sequence with constant $M_0 = 1.68\mathrm{M}_\odot$ for purely poloidal magnetic field. From left to right, top to bottom: central density ρ_c, Komar mass M, circumferential radius R_c and quadrupole deformation e. The blue line represents our STT results, to be compared to the red line, describing the GR models of Pili et al. (2014, Fig. 7). The arrows show the direction of increasing magnetisation.

poloidal magnetic fields, above a Komar mass of $1.34\mathrm{M}_\odot$ there are no de-scalarised models. Analogously, the upper bound ρ_t for scalarised models decreases - from $\rho_\mathrm{t} = 3.5 \times 10^{15}\mathrm{g\ cm}^{-3}$ for $\mu = 0$ to $\rho_\mathrm{t} = 3.42 \times 10^{15}\mathrm{g\ cm}^{-3}$ for $\mu = 0.45 \times 10^{35}\mathrm{erg/G}$ - while the Komar mass remains almost unchanged. As in GR, it is found that the maximum mass of sequences at fixed μ increases with the magnetic dipole moment, and the central density at which the maximum is reached drops. The characterisation of the models at maximum mass is given in Tab. 5.3. Similarly to GR we found that, at a given central density, the mass of equilibrium configurations is always above the un-magnetised case (in the stable part of the sequence). This same trend is also evident when sequences are parametrised at fixed values of B_max or at fixed e, in Fig. 5.12. Again, close to $\rho_\mathrm{c} \simeq 2.72 \times 10^{15}\mathrm{g\ cm}^{-3}$ the Komar mass is independent on the magnetisation. We have also analysed in Fig. 5.12 how the scalar charge changes with magnetisation. The maximum of the scalar charge changes from $Q_s = 1.16\mathrm{M}_\odot$ to $Q_s = 1.21\mathrm{M}_\odot$ when $\mu = 0.54 \times 10^{35}\mathrm{erg/G}$, while the density at which the maximum is reached drops to $1.96 \times 10^{15}\mathrm{g\ cm}^{-3}$. Globally, this appears as a shift to lower density of the sequences. Analogously to the mass, we find that close to $\rho_\mathrm{c} \simeq 2.33 \times 10^{15}\mathrm{g\ cm}^{-3}$ the scalar charge is independent on the magnetisation.

5.4 Magnetised models with $\beta_0 = -5$

In order to understand how our results depend on the specific choice of the STT parameter β_0, we have computed equilibrium configurations also for $\beta_0 = -5$ and $\beta_0 = -4.5$, closer to the limit for spontaneous scalarisation, both in the case of pure toroidal and purely poloidal magnetic fields. For $\beta_0 = -5$, the un-magnetised model with baryonic mass $M_o = 1.680\mathrm{M}_\odot$ is scalarised. It is then possible to compute deviations of various quantities with respect to their un-magnetised values, at fixed baryonic mass $M_o = 1.680\mathrm{M}_\odot$, as was done for $\beta_0 = -6$.

In Fig. 5.13, we show how the quadrupole deformation e changes with the maximum strength of the magnetic field B_max. Again, we find that the scalarised part of the sequence shows a lower quadrupole deformation than in GR, but now this difference is not as strong as for $\beta_0 = -6$. In general e is about $2/3$ of the value of the corresponding GR counterpart at the same B_max, both in the toroidal and poloidal magnetic field case. For purely toroidal magnetic fields, there is some indication that the scalarised part reaches a maximum value $B_\mathrm{max} \simeq 5.8 \times 10^{17}\mathrm{G}$, before it de-scalarises, and then reaches a new maximum corresponding to the GR value of $6.13 \times 10^{17}\mathrm{G}$. We can conclude that in STTs with $\beta_0 > -5$ the upper limit to B_max is reached after the solution de-scalarises, while for $\beta_0 < -5$ it is reached for scalarised configurations. On the other hand in models with a purely poloidal magnetic field, we observe no evidence for de-scalarisation with increasing k_pol. However, there seems to be an asymptote to a

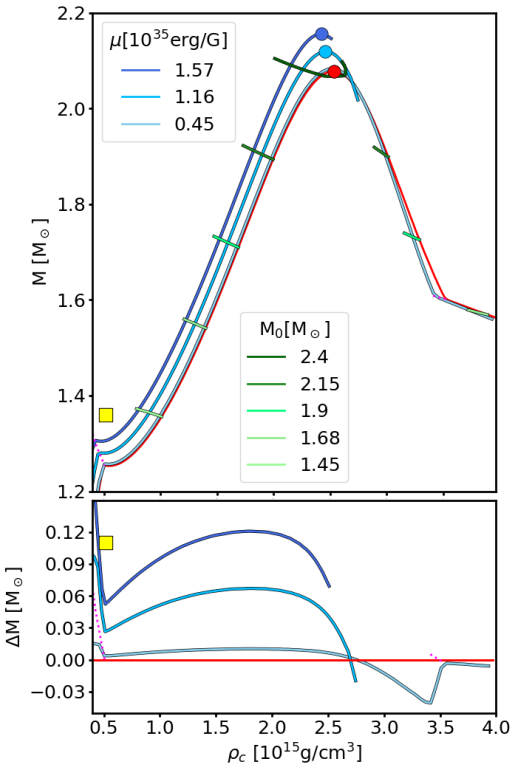

Figure 5.11: Mass-density sequences for models with purely poloidal magnetic field and $\beta_0 = -6$. Upper panel: sequences computed at fixed values of the magnetic dipole moment μ (blue lines) and at fixed baryonic mass (green lines), compared with the un-magnetised case (red line). The dotted magenta lines represent the limit for spontaneous scalarisation. Dots mark the position of the maximum mass models UM_0 (red), PM_1 (light blue) and PM_2 (dark blue) of Tab. 5.3. The yellow square represents the model of Fig. 5.8. Lower panel: mass difference of sequences at fixed μ with respect to the un-magnetised one.

maximum value of $B_{\rm max}$ of $\simeq 7.5 \times 10^{17}$G, slightly higher than in GR for $\beta_0 = -5$. The same conclusions can be found looking at the deviations of other variables. What we see is that changes with respect to GR depend in a strongly non-linear way on the values of β_0.

In Fig. 5.14, we repeat the same analysis of Fig. 5.6, for purely toroidal fields. We show how the Komar mass and scalar charge change with central density holding fixed the magnetic flux Φ, and the Komar mass for fixed values of the baryonic mass M_0. The region of de-scalarisation $\rho_{\rm c} = [\rho_{\rm b}, \rho_{\rm t}]$ is smaller, but the behaviour of the lower and upper bounds with magnetisation is the same. The lower bound $\rho_{\rm b}$ moves to higher densities, from $\rho_{\rm b} = 7.07 \times 10^{14}$g cm^{-3} for $\Phi = 0$ to $\rho_{\rm c} = 1.06 \times 10^{15}$g cm^{-3} for $\Phi = 2 \times 10^{30}$G cm^2, and the corresponding Komar (baryonic) mass from $1.461 M_\odot$ ($1.57 M_\odot$) to $1.75 M_\odot$ ($1.84 M_\odot$). Again we find no evidence suggesting the existence

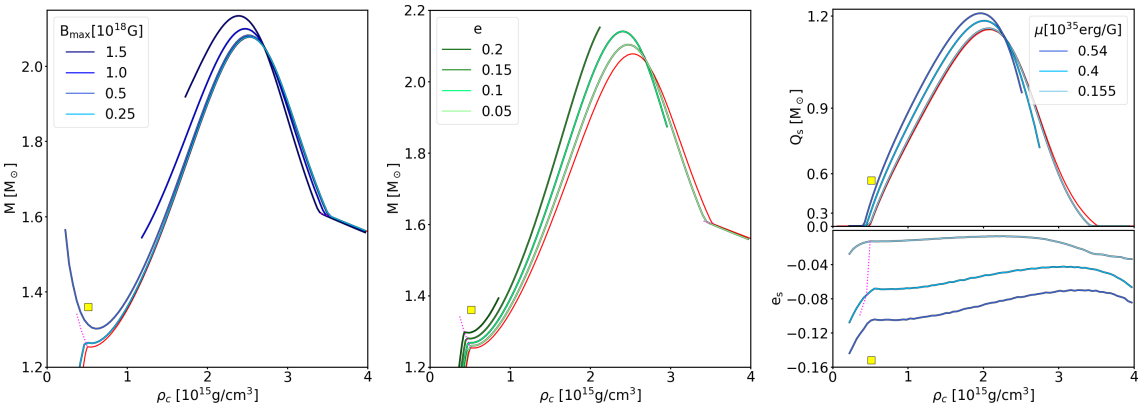

Figure 5.12: Sequences for models with purely poloidal magnetic field and $\beta_0 = -6$. Left panel: mmass-density relation computed at fixed $B_{\max}$ (blue lines) compared with the un-magnetised sequence (red line). Middle panel: mass-density relation computed at fixed e (green lines) compared with the un-magnetised sequence (red line). Right panel: on top, scalar charge-density relation computed at fixed μ (blue lines) compared with the un-magnetised sequence (red line); on bottom, trace quadrupole deformation e_s. In all panels, the dotted magenta lines represent the limit for spontaneous scalarisation and the yellow square represents model P of Fig. 5.8.

of an upper bound to the mass of the possible de-scalarised models. Analogously, the upper bound ρ_t for scalarised models increases, from $\rho_b = 2.65 \times 10^{15}$g cm^{-3} for $\Phi = 0$ to $\rho_c = 3.05 \times 10^{15}$g cm^{-3} for $\Phi = 2 \times 10^{30}$G cm^2, and the corresponding Komar (baryonic) mass from 1.67M$_\odot$ (1.83M$_\odot$) to 1.77M$_\odot$ (1.85M$_\odot$). Again, we find that for toroidal magnetic fields the density at which the maximum is reached increases, and the value of the maximum mass first remains almost constant at 1.81M$_\odot$, and then rises to 1.86M$_\odot$ for $\Phi = 2 \times 10^{30}$G cm^2. In this case we also see that on sequences with $\Phi \geq 1.64 \times 10^{30}$G cm^2 the mass of equilibrium models is always larger than the relative un-magnetised counterpart at the same central density.

For poloidal magnetic fields, we observe in Fig. 5.15 a more regular trend, similar to the case with $\beta_0 = -6$, where the maximum mass initially seems to remain unchanged to then rises at higher magnetisation. We find that, for poloidal fields, above a Komar mass of 1.7M$_\odot$ there are no de-scalarised models.

It is evident that now the magnetic field plays a more dominant role that the scalar field, and the general trends of the various sequences tend to approach what was found in GR. However, in the region where the scalar charge reaches its maximum, the trends are still in line with more scalarised configurations.

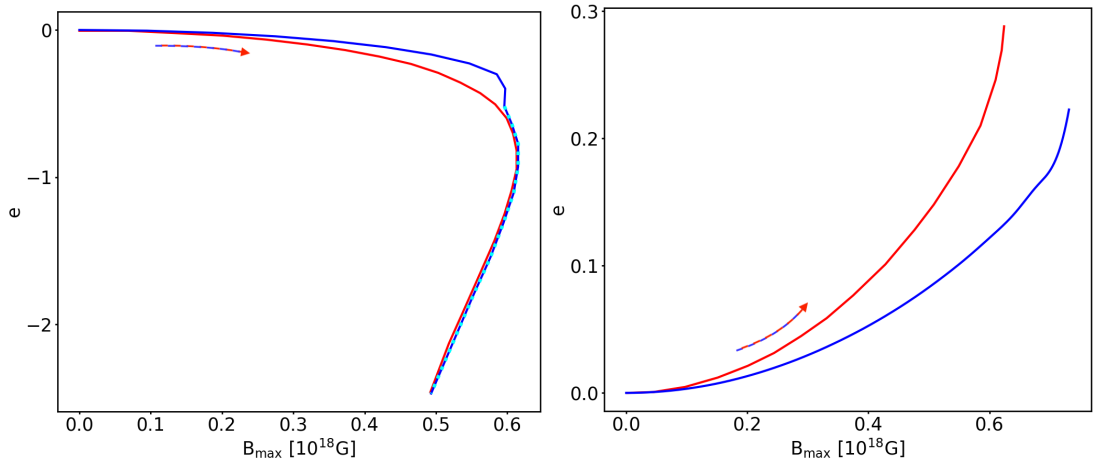

Figure 5.13: Value of the quadrupole deformation e along the equilibrium sequence with constant $M_0 = 1.68\mathrm{M}_\odot$, as a function of $B_{\max}$, for $\beta_0 = -5$ (blue lines) vs GR (red lines). The cyan dotted line highlights the un-scalarised configurations. Left panel: purely toroidal magnetic field; right panel: purely poloidal magnetic field. The arrows show the direction of increasing magnetisation.

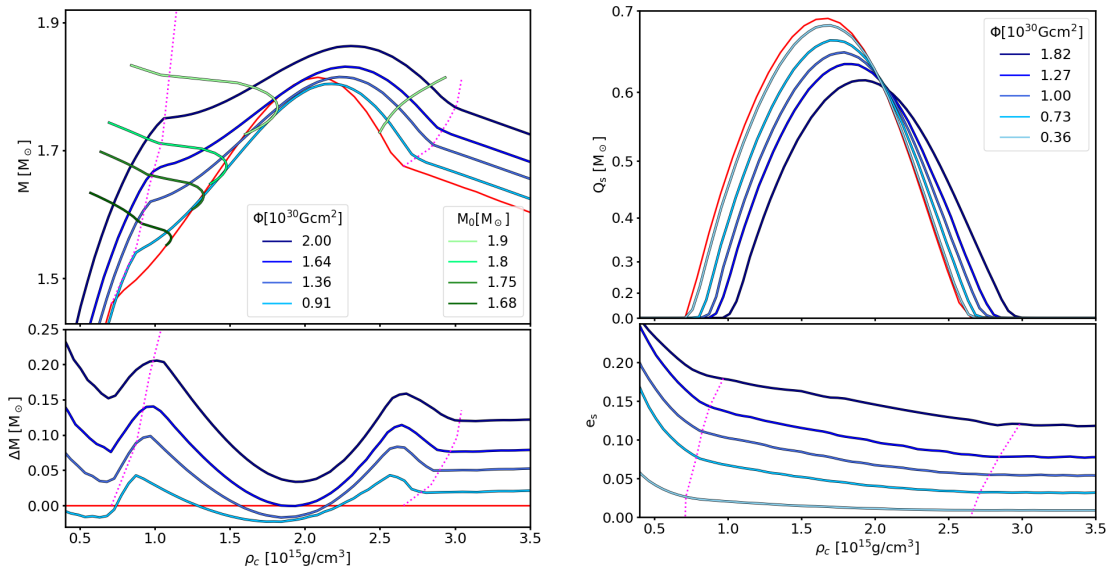

Figure 5.14: Models with purely toroidal magnetic field and $\beta_0 = -5$. Left panel: on top, sequences computed at fixed values of the magnetic flux Φ (blue lines) and at fixed baryonic mass (green lines), compared with the un-magnetised case (red line); on bottom, mass difference with respect to the un-magnetised case. Right panel: on top, scalar charge on sequences at fixed Φ; on bottom, trace quadrupole e_s on the same sequences. The dotted magenta lines represent the limit for spontaneous scalarisation.

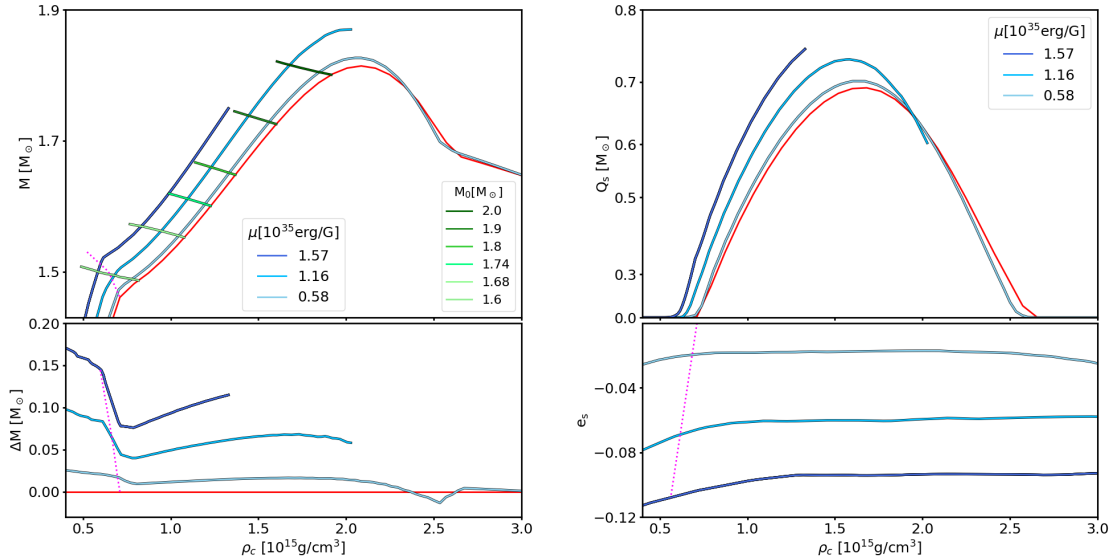

Figure 5.15: Models with purely poloidal magnetic field and $\beta_0 = -5$. Left panel: on top, sequences computed at fixed values of the magnetic dipole moment μ (blue lines) and at fixed baryonic mass (green lines), compared with the un-magnetised case (red line); on bottom, mass difference with respect to the un-magnetised case. Right panel: on top, scalar charge on sequences at fixed μ; on bottom, trace quadrupole e_s on the same sequences. The dotted magenta lines represent the limit for spontaneous scalarisation.

5.5 Magnetised models with $\beta_0 = -4.5$

We consider here the case $\beta_0 = -4.5$, which is close to the upper limit on massless STTs set by binary pulsar constraints (Freire et al. 2012; Shao et al. 2017; Anderson et al. 2019). In Fig. 5.16, we show how the Komar mass changes holding fixed the magnetic flux Φ for configurations with a purely toroidal magnetic field. The scalarised range is now strongly reduced. For the un-magnetised models, $\rho_b = 9.3 \times 10^{14}$g cm^{-3} and $\rho_t = 2.0 \times 10^{15}$g cm^{-3}, with a Komar mass that changes from 1.58M$_\odot$ to 1.71M$_\odot$. As the magnetic flux increases, the typical scalarised trend in the mass-density relation becomes progressively less evident: already at $\Phi = 0.9 \times 10^{30}$G cm^2 the sequence is almost indistinguishable from GR. This is made even more evident looking at the scalar charges in Fig. 5.16, where we observe simultaneously both a reduction of Q_s and of the scalarisation range.

In case of a purely poloidal magnetic field, the trend is instead quite different, as can be seen in Fig. 5.16. Increasing the magnetic flux Φ, both the scalar charge and the scalarisation range increase, with ρ_b moving to lower values. The maximum mass rises, and there is no evidence for the de-scalarisation.

This difference, in part already present at lower β_0, can be understood if one recalls

that spontaneous scalarisation can be seen, from a dynamical point of view, as an instability (Damour & Esposito-Farèse 1996) (see Chap. 2), which can be excited only if the minimum wavelength of unstable modes (a function of β_0) is smaller or of the order of the typical highscale of the matter distribution (roughly the size of the compact star). Detailed calculations set this limit for NSs around $\beta_0 \approx -4.2, -4.0$. It is obvious, that close to this threshold limit, any process that modifies the distribution of matter in compact stars can have deep consequances on their spontaneous scalarisability. A strong toroidal magnetic field leads to a prolate distribution of density, that on average corresponds to a reduction of the typical highscale of the matter distribution, potentially pushing the NS below the threshold for spontaneous scalarisation. On the other way a strong poloidal magnetic field leads to an oblate distribution of density, corresponding to an increase of the typical highscale of the matter distribution, potentially pushing the NS above the threshold for spontaneous scalarisation.

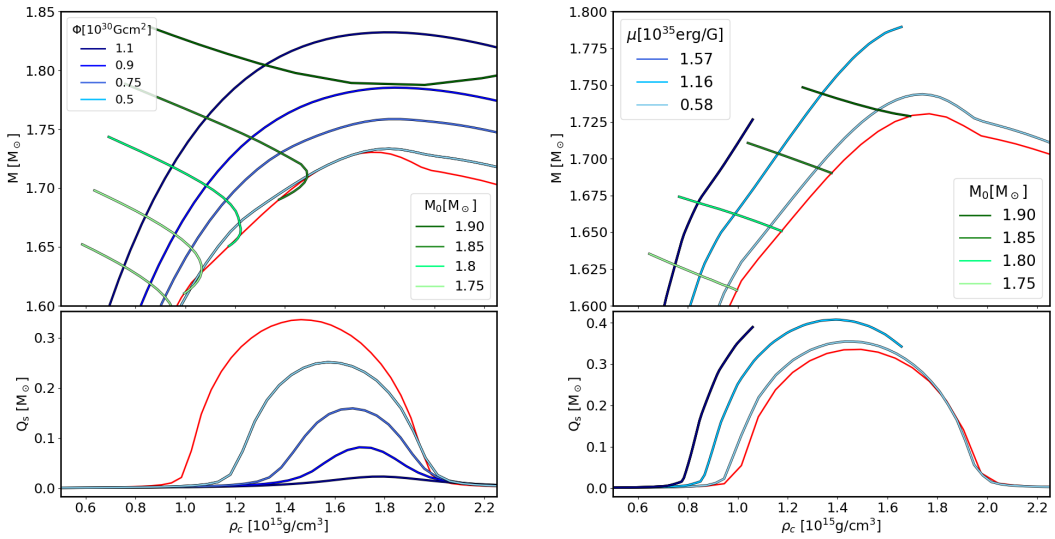

Figure 5.16: Left figure: models with purely toroidal magnetic field and $\beta_0 = -4.5$. Upper panel: sequences computed at fixed values of the magnetic flux Φ (blue lines) and at fixed baryonic mass (green lines), compared with the un-magnetised case (red line). Bottom panel: value of the scalar charge on the same sequences at fixed Φ. Right figure: models with purely poloidal magnetic field and $\beta_0 = -4.5$. Upper panel: sequences computed at fixed values of the magnetic dipole moment μ (blue lines) and at fixed baryonic mass (green lines), compared with the un-magnetised case (red line). Bottom panel: value of the scalar charge on the same sequences at fixed μ.

5.6 The stability of magnetised equilibrium models

It is well known that NSs endowed with either a purely toroidal or a purely poloidal magnetic field are unstable against non-axisymmetric perturbations (Braithwaite & Nordlund 2006; Braithwaite & Spruit 2006; Braithwaite 2009). This is due to a magnetofluid instability that, on a typical Alfvénic timescale, leads to a reconfiguration of the magnetic field geometry toward a more tangled structure. Magnetic stability requires mixed configurations, with comparable amount of energy in the poloidal and toroidal components of the magnetic field.

With respect to axisymmetric perturbations, on the other hand, it is found that, purely poloidal magnetic fields are stable, while the stability of purely toroidal magnetic fields, against interchange modes, depends on their stratification. Toroidal configurations with $m = 1$ are found to be stably stratified (Schubert 1968; Fricke 1969).

Independently of their magnetofluid stability, we are going to show that in STTs, NSs with purely toroidal magnetic fields, are also gravitationally unstable against spontaneous scalarisation. The criterion for gravitational instability for non-rotating and un-magnetised NS is

$$\frac{\partial M_0}{\partial \rho_c} \leq 0 \,, \tag{5.2}$$

where the equality defines the maximum mass. We note that in GR and STTs it is the baryonic mass that formally enters the criterion, and not the Komar mass, given that the former is the dynamically conserved quantity. However in GR and STTs the Komar mass is always a monotonically increasing function of the baryonic mass and one can safely use it to evaluate stability. This criterion can be generalised to magnetic configurations. Recalling that the flux-freezing condition of ideal MHD, ensures that the magnetic flux Φ is conserved in axisymmetry, one has that NSs with a purely toroidal magnetic field are unstable when

$$\left.\frac{\partial M_0}{\partial \rho_c}\right|_{\Phi} \leq 0 \,. \tag{5.3}$$

In Fig. 5.17, we plot how the baryonic mass of various equilibrium configurations change with density at fixed values of the magnetic flux Φ. It is immediately evident that each sequence shows four parts:

- a gravitationally stable de-scalarised GR part;
- a gravitationally unstable scalarised part;
- a gravitationally stable scalarised part (up to the density of the model of maximum mass for the entire sequence);

- a gravitationally unstable scalarised part (beyond the density of the model of maximum mass for the entire sequence).

This is in sharp contrast to GR, where only two parts are found (stable and unstable), separated by the model with maximum mass. In principle now we can have two maxima for the mass of NSs with purely toroidal magnetic fields: one corresponding to the de-scalarised part and one to the scalarised one. In the mass-density diagram there is a region where models are gravitationally unstable. Moreover, for any given value of Φ, there is a range of masses where both de-scalarised and scalarised solutions are possible. On the other hand, there is a lower limit to the values of the magnetic flux that can support de-scalarised configurations of a given baryonic mass. Lowering the magnetic flux beyond this limit could lead to a gravitational instability where the star jumps from the de-scalarised branch to the scalarised one. This is a gravitational instability, unrelated to rearrangements of the magnetic field geometry, that will take place on a typical scalarisation timescale, of the order of the light crossing time of the NS. For example, with reference to Fig. 5.17, a de-scalarised configuration with $\mathrm{M}_0 = 1.68\mathrm{M}_\odot$ can only exist for $\Phi > 2.06 \times 10^{30}\mathrm{G\ cm}^2$ and $\rho_\mathrm{c} < 7.12 \times 10^{14}\mathrm{g\ cm}^{-3}$; below this limiting value of the magnetic flux, the NS will jump at the same baryonic mass but with a central density $\rho_\mathrm{c} > 1.32 \times 10^{15}\mathrm{g\ cm}^{-3}$, and a scalar charge $Q_s = 0.8\mathrm{M}_\odot$. Interestingly, these two limiting configurations have not just the same baryonic mass, and magnetic flux, but also the same Komar mass $M = 1.62\mathrm{M}_\odot$. We have repeated this analysis also for higher values of β_0 and found that this effect already disappears at $\beta_0 = -5$. However, for $\beta_0 = -4.5$ we found that two configurations, one scalarised and the other un-scalarised, with the same baryonic mass still exist, but in this case they have the same central density.

Independently of the specific choice of magnetic field distribution, that in our case is dictated by the request of an integrable form for the generalised Bernoulli equation, our results have shown that a strong toroidal magnetic field can support de-scalarised configurations, and that, in principle, if such magnetic field drops below a limiting value (for example because of non ideal processes or magnetic instabilities) such configuration can undergo a rapid 'magnetically-induced spontaneous scalarisation'. In the case of purely poloidal configurations, the quantity that is dynamically conserved for axisymmetric perturbations is the net flux of the toroidal current J^ϕ. This can be equivalently parametrised by the magnetic dipole moment. If we repeat the same analysis done in the toroidal case, considering sequences at fixed magnetic dipole moment, we see no evidence for the presence of an unstable part.

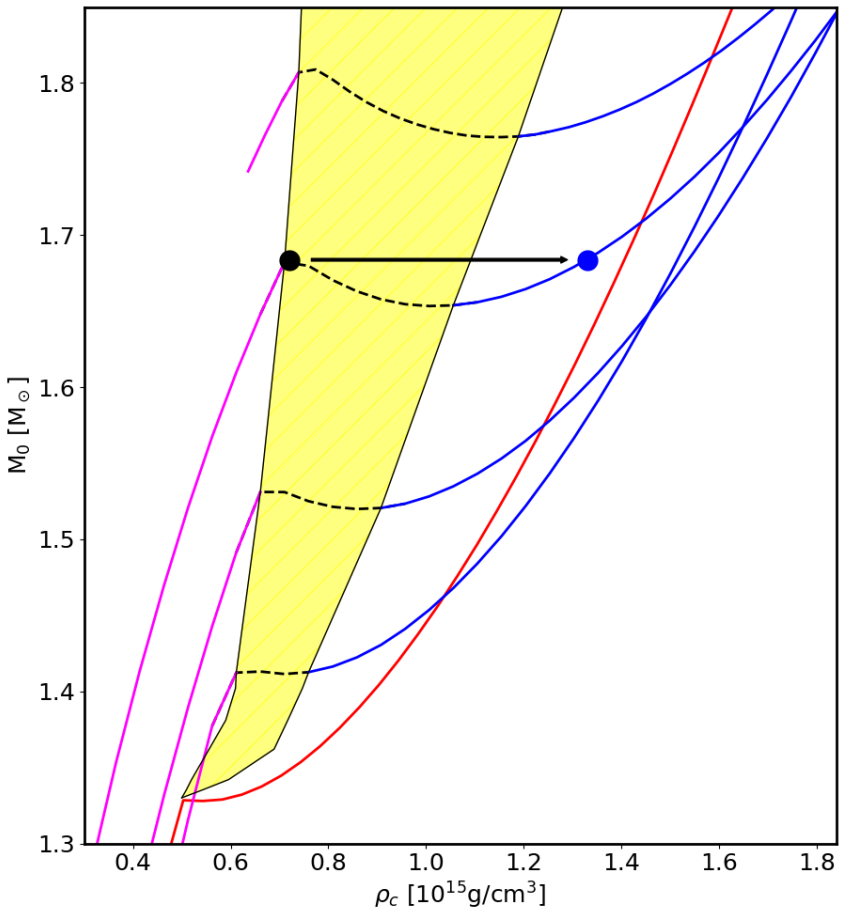

Figure 5.17: Sequences at fixed magnetic flux Φ, computed in the case $\beta_0 = -6$. The red curve is the un-magnetised solution. From bottom to top the other curves are computed at $\Phi = [2.55, 2.06, 1.46, 0.91] \times 10^{30}$G cm^2. The various parts are: gravitationally stable de-scalarised branch (solid magenta); gravitationally unstable scalarised branch (black dashed); gravitationally stable scalarised branch (solid blue). The yellow region corresponds to gravitationally unstable models. The black dot represents the de-scalarised configuration with $M_0 = 1.68 M_\odot$ and $\Phi = 2.06 \times 10^{30}$G cm^2, while the arrow points to the blue dot where the configuration is expected to jump because of magnetically-induced spontaneous scalarisation.

5.7 Discussion

In the work presented in this chapter we carried out a detailed study of the properties of magnetised NSs in STT with spontaneous scalarisation, trying to characterise them as completely as possible, not just in term of their masses or radii, but also considering how the interplay of the magnetic and scalar fields affect their internal structure and deformation. We also tried to characterise the deformation of the scalar field, and introduced the parameter e_s related to the emission of quadrupolar scalar waves. In general, we found that the action of different configurations of the magnetic field on the overall structure of a NS leads to qualitatively similar results: a toroidal magnetic field produced prolate configurations, while a poloidal field leads to oblate one. However, significative changes are found when we proceed to a quantitative comparison. When comparing STT to GR models, computed at the same central density ρ_c and maximum value of the magnetic field B_{max}, we found that the distribution of density and magnetic field vary less than few percent. This suggests that GR models can be used as good proxy for the internal structure of magnetised NSs in STT. On the other hand, when for the same models we compare global integrated quantities like the mass, or the quadrupole deformation, we found deviations from GR up to 10-20%. This difference can be easily understood recalling that while the distributions of density and magnetic field depend on the ratio α/α_c (i.e. on relative changes of the metric terms), the value of integrated quantities depends on the conformal factor ψ^6 through the volume element (i.e. on the absolute values of the metric terms). On top of this, the quadrupole deformation e, used to estimate the possible emission of GWs from deformed system, is properly computed in the E-frame, where the metric equations have the same mathematical structure of GR.

We have also investigated sequences at fixed baryonic mass, which is the conserved quantity from a dynamical and evolutionary perspective, and compared typical trends with those of GR for the same baryonic mass. We found that, in general, the presence of a scalar field reduces the deformability of NSs and tends to reduce the typical deviations from the spherically symmetric un-magnetised configuration. This also implies that with respect to GR, NSs at the same baryonic mass can host stronger magnetic fields. For configurations with purely toroidal magnetic fields we also showed that as the magnetisation rises the models de-scalarise. This effect was evaluated for various values of β_0 showing that there is a strong dependency. We have then shown, using various parametrisations, how the mass-density relation changes with the magnetisation of the system, revealing both how this affects the region of spontaneous scalarisation and the location of the configuration with maximum mass, together with its value. In particular, we have shown that while for toroidal magnetic fields there is a de-scalarised region, for purely poloidal magnetic fields there is a limiting mass

above which only scalarised solutions are possible. We have also shown that contrary to GR, where the maximum mass is always an increasing function of magnetisation, in STTs, for purely toroidal magnetic fields, the maximum mass decreases with increasing magnetisation for systems with $B_{\rm max}$ lower than a threshold magnetic field, and then rises. We verified that the quadrupolar term arising from magnetic deformations in the source of the scalar field equation is of the same order of the one in Einstein's equations, suggesting comparable levels of gravitational losses in tensor and scalar waves.

In general, we found that for weakly magnetised models the presence of a scalar field dominates the properties of NSs, and its effect is to counter-balance the magnetic stresses, either by reducing the deformation, or leading to saturation of the values of the maximum mass. We verified, by changing the value of β_0, that when scalarisation effects become smaller the typical trends of GR tend to be recovered, with the significative difference that while for purely toroidal fields a rise in magnetisation leads to de-scalarisation, for purely poloidal magnetic fields, on the contrary, it increases the total scalar charge. Depending on its geometry, the magnetic field can either favour or suppress spontaneous scalarisation when β_0 is close to the threshold limit on the range of this effect.

Finally, we have also shown that the mutual interplay of a scalar and toroidal magnetic field, in the presence of strong scalarisation effects, leads to unstable configurations and potentially to events of spontaneous scalarisation due to the loss of magnetic support - a 'magnetically-induced spontaneous scalarisation'. The work presented in this chapter is mostly devoted to a global study of the properties of magnetised NSs in STT, with a particular focus on the comparison with their respective GR counterparts. For this reason, we adopted a simple polytropic EoS and considered only the two extreme cases of purely toroidal and purely poloidal magnetic fields, focusing the discussion on the case $\beta_0 = -6$ to enhance and highlight the main differences. In Chaps. 6,7 we investigate in more detail how the deformability of NSs in STT depends on the choice of β_0 and on the EoS (Pili et al. 2016), and how it scales with the mass, radius, and compactness of NSs, revealing that it is possible to derive scaling laws that can parametrise the magnetic deformability in a similar way to what has been previously done in GR (Pili et al. 2017).

Chapter 6

Magnetic deformation of neutron stars in scalar-tensor theories

The results shown in this chapter were published in the paper Soldateschi et al. (2021) (hereafter SBD21).

Given the extremely powerful magnetic fields hosted by NSs, it is important to study the interplay between the magnetic and the scalar field in shaping their quadrupolar deformation, even more so because of its connection to the emission of GWs. Moreover, this is relevant to the study of how the presence of an additional channel for the emission of quadrupolar waves - that of scalar waves - affects the overall emission of quadrupolar GWs, establishing the extent to which the emission of scalar waves competes with the tensor one.

In the work presented in this chapter we build upon SBD20 (see Chap. 5), where we studied the general problem of axisymmetric models of NSs in STTs in the presence of spontaneous scalarisation to investigate the magnetic deformation of NSs in a class of STTs containing spontaneous scalarisation in light of GW emissions. In SBD20, we showed that the scalar field is expected to modify the magnetic deformation of NSs, but we investigated just a few selected configurations for a single STT. Here we investigate the full parameter space.

In Sect. 6.1 we show our results regarding the magnetic deformation of NSs in STTs; then, we describe the consequences regarding the emission of gravitational and scalar radiation in Sect. 6.2. Finally, we discuss our results in Sect. 6.3.

6.1 The distortion coefficients

In the following, we focus on the case of static NSs in the weak magnetic field regime, meaning that the effects induced by the magnetic field on the deformation of the star are well-approximated by a perturbative approach; this was shown to be the case for $B_{\rm max} \lesssim 10^{17}$G (Pili et al. 2015; Bucciantini et al. 2015). This is much less than the critical field strength, of the order of 10^{19}G, set by the energy associated to the characteristic NS density (Lattimer & Prakash 2007). Moreover, we focus only on the mass range of stable configurations.

The Newtonian quadrupole deformation e of a NS in STTs is formally defined as in Eq. B.14:

$$e = \frac{I_{zz} - I_{xx}}{I_{zz}} \,, \tag{6.1}$$

where I_{zz} and I_{xx} are the Newtonian moments of inertia in the E-frame, accounting for both the physical and scalar fields energy density (see App. B). This definition has the advantage that it is given as an integral over the star. As is already known in Newtonian gravity (Wentzel 1960; Ostriker & Gunn 1969) and in GR (Frieben & Rezzolla 2012; Pili et al. 2017), in the limit of weak magnetic fields and slow rotation rates, the quadrupole deformation can be expressed as a bilinear combination of $B^2_{\rm max}$, where $B_{\rm max} = \max[\sqrt{B_i B^i}]$, with B as the NS magnetic field, and its rotation rate (Pili et al. 2017). Equivalently, instead of using $B^2_{\rm max}$ one can parametrise the quadrupole deformation also in terms of $\mathcal{H}/W$, where $\mathcal{H}$ is the magnetic energy of the NS, defined in the J-frame, and with W as its binding energy, which in STTs is properly defined in the E-frame (see App. B). The true gravitational quadrupole moment is properly defined from the asymptotic structure of the metric terms (Bonazzola & Gourgoulhon 1996; Gourgoulhon 2010; Doneva et al. 2014), while the moment of inertia is only properly defined for rotators; however, it has been found that the Netwonian approximation is quite reliable (Pili et al. 2015). We note here that Eq. A2 in Pili et al. (2015) is not formally correct, because it neglects frame dragging, while it can be shown that, for compact systems like NSs, this contributes about 10-15% to the moment of inertia.

In our STT scenario, we found that e still follows a linear trend with $B^2_{\rm max}$ (or $\mathcal{H}/W$), although with coefficients that bear a potentially much stronger dependence on the baryonic mass M_0 (defined as in App. B) than in GR, depending on the value of the parameter regulating spontaneous scalarisation, β_0 (see below for its definition). In particular, in the limit $B_{\rm max} \to 0$, keeping fixed M_0 and β_0:

$$|e| = c_{\rm B} B^2_{\rm max} + \mathcal{O}\left(B^4_{\rm max}\right) , \; |e| = c_{\rm H} \frac{\mathcal{H}}{W} + \mathcal{O}\left(\frac{\mathcal{H}^2}{W^2}\right) , \tag{6.2}$$

where $c_{\rm B} = c_{\rm B}(M_0, \beta_0)$ and $c_{\rm H} = c_{\rm H}(M_0, \beta_0)$ are the 'distortion coefficients', and $B_{\rm max}$ is normalised to 10^{18}G. We note that the distortion coefficients are defined in terms of

the absolute value of the quadrupolar deformation: thus, while purely poloidal and purely toroidal fields cause a quadrupolar deformation on the NS that is opposite in sign, the distortion coefficients are always positive-definite. As a result, the distortion coefficients of a NS endowed with a mixed field are expected to be always smaller than those of a NS endowed with a 'pure' configuration.

In order to compute the distortion coefficients of NSs in the low magnetic field regime, we computed several numerical models of magnetised NSs with stronger magnetic fields, and then we interpolated the results according to the functional form of Eq. 6.2. We studied only configurations belonging to the stable branch of the mass-density diagram, that is with masses and central densities lower than that of the configuration with maximum mass. We recall that we used an exponential coupling function, $\mathcal{A}(\chi) = \exp\left[\alpha_0\chi + \beta_0\chi^2/2\right]$, in which the α_0 parameter controls the weak field effects of the scalar field and β_0 regulates spontaneous scalarisation. The most stringent observational constraints, as described in Sect. 2.4, require that for massless scalar fields, $|\alpha_0| \lesssim 1.3 \times 10^{-3}$ and $\beta_0 \gtrsim -4.3$ (Voisin et al. 2020; see also Will 2014 for a comprehensive review on tests of GR). For massive ones or for scalar fields endowed with a screening potential, lower values are still allowed (Doneva & Yazadjiev 2016) as long as the screening radius is smaller than the binary separation (see the discussion in Sect. 2.4). However, as we explained in Sect. 4.3, results found in a massless STT for the structure of NSs are also valid for screened STTs as long as the screening radius is larger than the NS radius. This leaves open a large parameter space in terms of screening properties. We chose $\alpha_0 = -2 \times 10^{-4}$ and $\beta_0 \in [-6, -4.5]$. By choosing this range of values, we want to highlight the effects of scalarisation while also showing its effects for values at the edge of the permitted parameter space for massless fields. We briefly recall here that the only known formalism to compute equilibria (even magnetised ones) in the full non-linear regime, beyond the first order linear perturbation theory and beyond the Cowling approximation, is through the use of the generalised Bernoulli integral, including the case of differentially rotating stars, where the rotation rate is taken to be a function of the specific angular momentum (Bocquet et al. 1995; Kiuchi & Yoshida 2008; Frieben & Rezzolla 2012; Iosif & Stergioulas 2014; Pili et al. 2017), or through mathematically equivalent approaches. This sets severe constraints on the possible distribution of currents and, thereby, on the possible geometry of the magnetic field (the full functional dependence of the current density distribution can be found in Chap. 3). For example, in the case of poloidal fields, the configuration is always dominated by the dipole term, but also contains higher order multipoles. Our models have no surface currents. Typically, models with surface currents are not in true equilibria because they neglect the associated surface Lorentz force.

We decided to parametrise the solution as a function of the baryonic mass M_0, which is the same in the E and J-frames. The relation with the E-frame Komar mass M is

$M \approx M_0 - cM_0^2$, with $c = 0.04$ (0.05) for purely toroidal (poloidal) magnetic fields, and is the same in STT and GR. The behaviour of $c_{\rm B}$ and $c_{\rm H}$ as functions of M_0, for various β_0, are shown in Fig. 6.1, for NSs endowed with a purely toroidal or a purely poloidal magnetic field. The red line represents GR. The other lines represent the cases with a decreasing β_0, starting with $\beta_0 = -4.5$ and going down to $\beta_0 = -6$. We note that more scalarised sequences reach higher masses than less scalarised ones, because one of the effects of scalarisation is to increase the maximum possible mass of a stable NS, so that only heavily scalarised sequences are able to reach a baryonic mass as high as $\approx 2.4\,{\rm M}_\odot$ with our EoS. The effect of scalarisation is clearly visible due to the distinctive rapid variation in the slope as the scalarised sequences depart from the GR one. Decreasing the value of β_0 has the effect of enhancing the modifications with respect to GR and enlarging the scalarisation range. At a fixed M_0, scalarised NSs have a lower distortion coefficient - and a lower quadrupole deformation - than the corresponding GR models for most of the scalarisation range. In moving towards masses close to the maximum, the difference becomes increasingly small until it changes sign at the very end of the GR sequence.

From a more quantitative point of view, the maximum relative difference between $c_{\rm B}$ in GR and in STT in the purely toroidal case is roughly 63% for $\beta_0 = -6$ and $M_0 \approx 1.5{\rm M}_\odot$. This difference decreases approaching 0 as β_0 increases. Moreover, as the baryonic mass increases, we can see that all sequences tend to coincide and reconnect to the GR one as the scalarisation range ends. As for $c_{\rm H}$, its maximum difference in STT relative to GR is roughly 72% at $M_0 \approx 1.8{\rm M}_\odot$, for $\beta_0 = -6$. Again, this difference decreases as β_0 increases. We note, however, that the various sequences of $c_{\rm H}$ do not seem to be reconnecting as the scalarisation range ends. This behaviour is to be attributed to the fact that the ratio $\mathcal{H}/W$ depends on M_0, and, as such, it too exhibits the effect of scalarisation. In other words W, at a fixed M_0, depends on β_0, which implies that in STTs $c_{\rm H}$ as defined in Eq. 6.2 is not directly comparable to GR at the same $\mathcal{H}$: first, it is needed to factor out the dependence of $\mathcal{H}/W$ on M_0 and add it to $c_{\rm H}$. The same holds for purely poloidal magnetic fields. The maximum relative difference of $c_{\rm B}$ with respect to GR is 70% for $\beta_0 = -6$ at $M_0 \approx 1.5{\rm M}_\odot$, while for $c_{\rm H}$ it is 72% at $M_0 \approx 1.8{\rm M}_\odot$ for $\beta_0 = -6$.

As we have seen, the distortion coefficients in STTs depart from the GR ones in a non-trivial way. Interestingly it looks like, apart from a scaling factor, both $c_{\rm H}$ and $c_{\rm B}$ have the same trend for toroidal and poloidal magnetic fields. In the case of $c_{\rm B}$, as can be seen from Fig. 6.1, for $M_0 < 1.6{\rm M}_\odot$, the values for toroidal magnetic fields are about a factor 1.5 higher than the cases with poloidal magnetic field. However, at higher masses, the trends are no longer similar between the two cases. Nonetheless, we have found that in the full range $1.2 \leq M_0/{\rm M}_\odot \lesssim 2.4$ and $-6 \leq \beta_0 \leq -4.5$, they are well approximated (to a few percents precision everywhere, except for the small range

of masses in which scalarisation is triggered, where the error can reach a few tens of percents) by a combination of power laws of three global quantities defined for the corresponding unmagnetised model: the baryonic mass M_0, the J-frame circumferential radius R_c and the E-frame scalar charge Q_s (see App. B). We note that these are not independent (for GR there is a one to one relation between mass and radius), but treating them as independent allows us to use simple power-law scalings in terms of global quantities. In particular:

$$c_B \approx c_1 M_{1.6}^{\alpha} R_{10}^{\beta} \left[1 - c_2 Q_1^{\gamma} M_{1.6}^{\delta} R_{10}^{\rho}\right] , \tag{6.3}$$

where the parameters are listed in Tab. 6.1, $M_{1.6}$ is M_0 in units of $1.6M_\odot$, R_{10} is R_c in units of 10km, and Q_1 is Q_s in units of $1M_\odot$. The first term of Eq. 6.3 describes the distortion coefficient in GR, while the second term describes the deviation due to the presence of a scalar charge. First, for the GR term, we note that the coefficient c_1 of the models with toroidal field is about twice that of those with a poloidal one. The mass dependence is similar, while the exponent of the radius is higher by one for the poloidal field (this is likely due to the different geometry, prolate and oblate, of the configurations). From the coefficients in Tab. 6.1, we see that the second term of Eq. 6.3 has a more complex behaviour: the dependence on the scalar charge is similar, there is a weaker dependence on the mass for the poloidal field, while again the dependence on the radius is stronger by one power of R_{10} in the poloidal case. The similarity between NSs with poloidal and toroidal magnetic fields is much stronger for c_H, to the point that it is possible to derive a universal functional form over the entire mass range with an accuracy of few percents:

$$c_H \approx 0.5 + \mathcal{F}(M_0)\mathcal{T}(M_0, Q_s, R_c) \times \begin{cases} 0.65 \text{ for toroidal} \\ 1.02 \text{ for poloidal} \end{cases} , \tag{6.4}$$

where $\mathcal{F}(M_0)$ represents the GR part and encodes the role of the EoS, $\mathcal{T}(M_0, Q_s, R_c)$ represents the correction due to scalarisation, and the oblate versus prolate geometry induced by the different magnetic field is encoded in the last factor. We find that:

$$\mathcal{F}(M_0) = 4.98 - 1.95 M_{1.6}, \tag{6.5}$$

$$\mathcal{T}(M_0, Q_s, R_c) = 1 - \frac{1.90}{R_{10}^{2.45}} \left(\frac{Q_1}{M_{1.6}}\right)^{1.3} . \tag{6.6}$$

It is well known that in GR, the coefficient c_H is only weakly dependent on the the mass, to the point that it can almost be taken as a constant. This is because the specific properties of the NS cancel out if the deformation is given as a function of $\mathcal{H}/W$. What we found here is that the same holds in STTs. The deformation is smaller than in GR, but the functional form of the correction is independent of the specific STT. Moreover, the geometry of the magnetic field is completely encoded in a constant coefficient that likely traces the oblate or prolate geometry of the star.

Table 6.1: Values of the parameters for the approximations of c_B in Eq. 6.3 for purely toroidal and purely poloidal magnetic fields.

Parameter	Toroidal	Poloidal
c_1	0.16	0.077
α	-2.22	-1.99
β	4.86	5.80
c_2	0.87	1.38
γ	1.32	1.22
δ	-1.27	-0.86
ρ	-2.21	-3.49

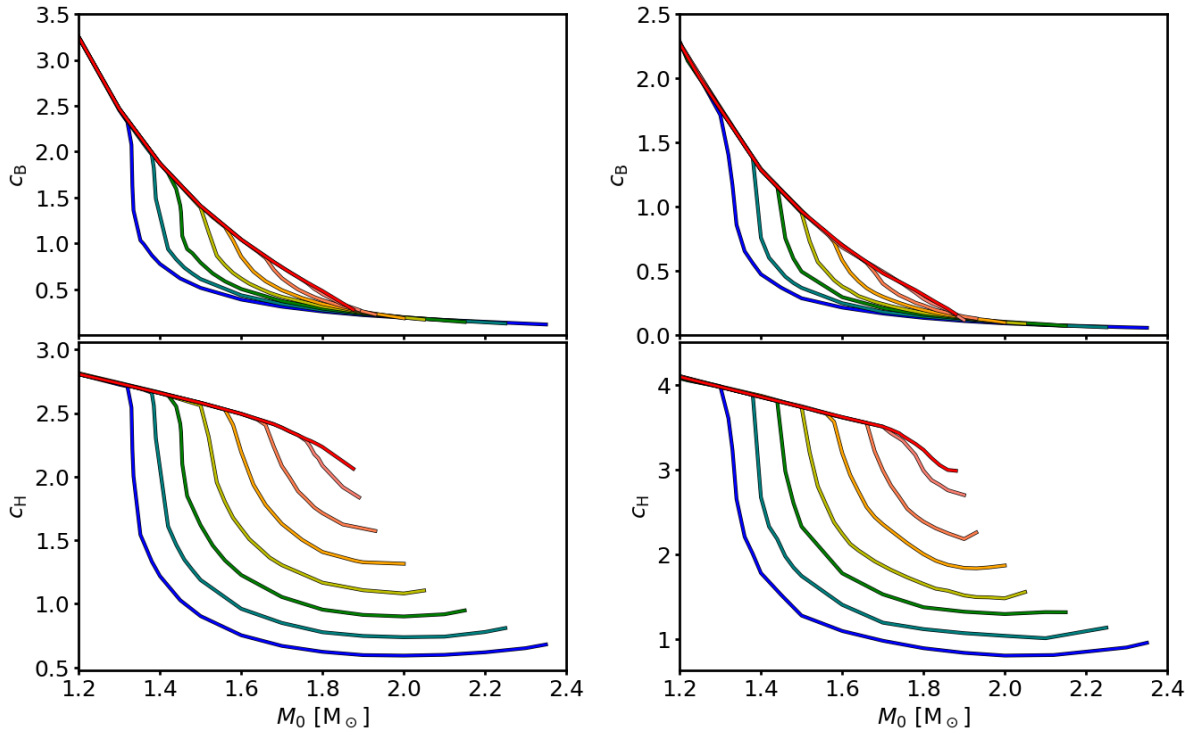

Figure 6.1: Distortion coefficients c_B (top panels) and c_H (bottom panels) as functions of the baryonic mass M_0 of models with a purely toroidal magnetic field (left panels) and with a purely poloidal magnetic field (right panels), for various value of β_0: from $\beta_0 = -6$ (blue curve) to $\beta_0 = -4.5$ (light red curve) increasing by 0.25 with every line. The red curve corresponds to GR.

6.2 Gravitational waves: scalar mode vs. tensor mode

Since a quadrupolar deformation of the NS results in the emission of quadrupolar waves, both tensor and scalar, it is interesting to analyse what fraction of the energy contained in them is due to the quadrupole moment of the scalar field. For this purpose, we define the following ratios:

$$\mathcal{S} = \left| \frac{q_{\rm s}}{q_{\rm g}} \right| , \; \mathcal{G} = \left| \frac{q_{\rm g}}{q_{\rm g}^0} \right| , \tag{6.7}$$

where

$$q_{\rm s} = 2\pi \int \alpha_{\rm s} \mathcal{A}^4 T_{\rm p} \left(3\sin^2\theta - 2 \right) r^4 \sin\theta {\rm d}r{\rm d}\theta \, , \tag{6.8}$$

$$q_{\rm g} = \int \left[\pi \mathcal{A}^4 (\varepsilon + \rho) - \frac{1}{8} (\partial\chi)^2 \right] r^4 \sin\theta \left(3\sin^2\theta - 2 \right) {\rm d}r{\rm d}\theta. \tag{6.9}$$

These are, respectively, the Newtonian approximations of the 'trace quadrupole' and of the 'mass quadrupole' of the NS. The mass quadrupole $q_{\rm g}$ is just $I_{zz} - I_{xx} = eI_{zz}$ (see Eq. B.14). We found that, in the mass range we investigated, I_{zz} ranges from 6×10^{44}g cm^2 to 4×10^{44}g cm^2. This is consistent with GR, where the moment of inertia weakly depends on the mass (Lattimer & Prakash 2001), showing that the quadrupole is primarily encoded in the parameter e. The quantities ε and ρ are respectively the J-frame internal energy density and rest-mass density, while $(\partial\chi)^2 = (\partial_r\chi) + r^{-2}(\partial_\theta\chi)^2$, and $q_{\rm g}^0$ is $q_{\rm g}$ calculated in GR. The quadrupole $q_{\rm s}$ is closely related to the 'quadrupolar deformation of the trace' (see App. B), which acts as the source of scalar waves. We note that these scalar waves are of a quadrupolar nature and differ from standard scalar monopolar GWs, which we do not consider here. In fact, a monopolar scalar wave, being monopoles rotationally invariant, can only arise following time-dependent monopolar variations of the structure of the NS (e.g. when the star collapses, Gerosa et al. 2016) and is not triggered by the rotation of deformed NSs, to which our present results apply. This does not mean that rotation plays no role in monopolar waves emission since the vibrating eigenmodes depend on the NS structure, which also reflects the underlying rotational profile. We note that the distinction between monopolar and quadrupolar waves depends only on the energy distribution of the waves (the multipolar pattern of the radiation), while the distinction between scalar and tensor modes depends on the nature of the waves (the spin of the wave carriers). The quantity of $\mathcal{S}$ gives a measure of which fraction of the energy lost in quadrupolar waves is contained in scalar modes, compared against tensor modes, while $\mathcal{G}$ quantifies the ratio of the energy of tensor modes in STTs versus GR. We note that the tensor GW luminosity scales approximately with e^2, while it is the strain amplitude that scales with e, so $\mathcal{S}$ and $\mathcal{G}$ are actually a measure of the variation in the

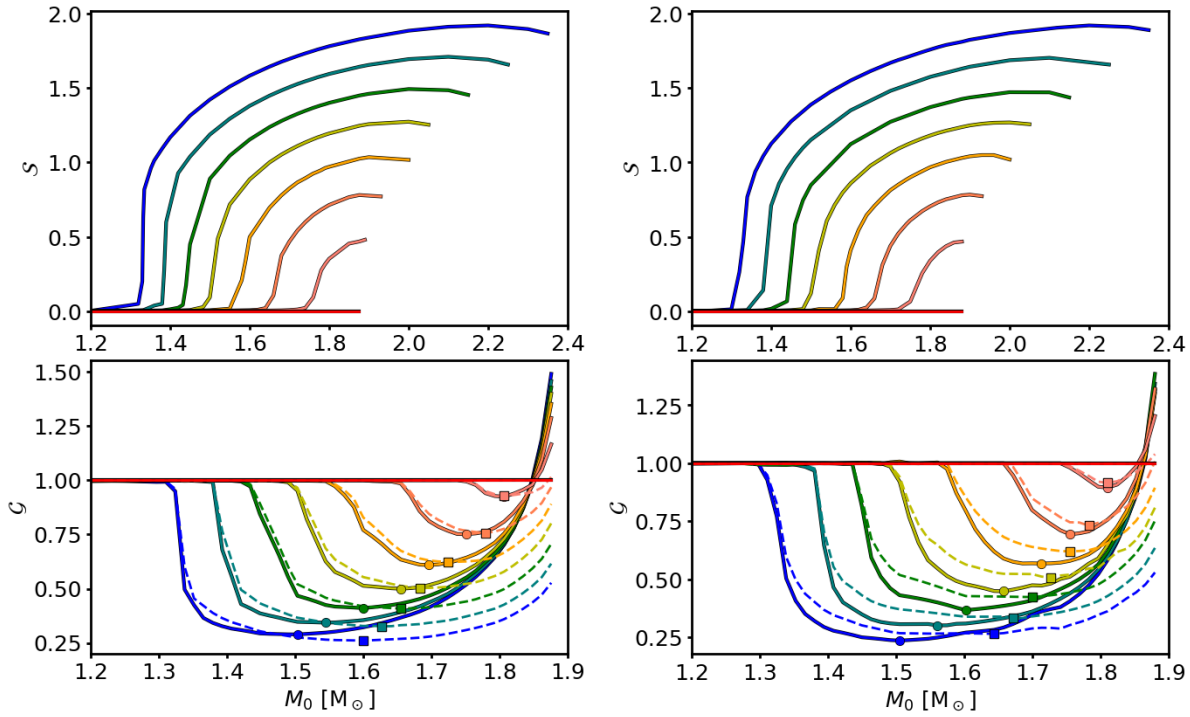

Figure 6.2: Ratios $\mathcal{S}$ (top panels) and $\mathcal{G}$ (bottom panels) as functions of the baryonic mass M_0 of models with a purely toroidal magnetic field (left panels) and with a purely poloidal magnetic field (right panels), for different value of β_0: from $\beta_0 = -6$ (blue curve) up to $\beta_0 = -4.5$ (light red curve) increasing by 0.25 with every line. The red line corresponds to GR, where $\mathcal{S} = 0$ and $\mathcal{G} = 1$. Solid lines are the ratios computed by keeping $B_{\max}$ fixed, while dashed lines are obtained by keeping $\mathcal{H}/W$ fixed. Markers show the models with minimum $\mathcal{G}$: circles for solid lines and squares for dashed lines.

strain, and it is their square to be related to the variation in the energy loss. It is worth pointing out that these ratios can be calculated by keeping fixed either $B_{\max}$ or $\mathcal{H}/W$ and that unlike $B_{\max}$, $\mathcal{H}/W$ depends on M_0 through W in different ways for different theories of gravity. Let's call this dependence $f(M_0, \beta_0)$ in our case, where the difference between STT and GR is encoded only by a varying β_0. This means that, in general, computing the ratios keeping fixed these two quantities does not yield the same result. In particular, ratios of quantities calculated with respect to models with the same β_0, like $\mathcal{S}$, are exactly the same in the two cases; instead, the ratio of a quantity in STTs over a quantity in GR, like $\mathcal{G}$, differ by a factor $f(M_0, \beta_0)/f(M_0, 0)$.

In Fig. 6.2, we show the ratios in Eq. 6.7 for NSs endowed with a purely toroidal and a purely poloidal magnetic field, respectively. The top panels show that, when scalarisation occurs and $\mathcal{S}$ departs from zero, very rapidly $q_s > q_g$ for $\beta_0 \lesssim -5$, while sequences with $\beta_0 \gtrsim -5$ do not reach $\mathcal{S} = 1$. This means that heavily scalarised NSs, once scalarisation kicks in, are dominated by losses due to scalar radiation, while less scalarised

ones are always dominated by tensor radiation. Differences in $\mathcal{S}$ between the purely toroidal and the purely poloidal cases are minimal, both in the scalarisation range and in the entity of its effect. The bottom panels of Fig. 6.2 show that once scalarisation is triggered, $\mathcal{G}$ quickly falls down towards very low values; then, for NSs with a higher baryonic mass, $\mathcal{G}$ rises again very steeply. At a fixed M_0 below a threshold mass, the more scalarised the NS, the less energy is lost in tensor waves with respect to GR. On the other hand, the more scalarised the NS, the more energy is injected in the scalar mode channel, as shown before with the $\mathcal{S}$ ratio, which increases almost monotonically with M_0. However, more massive NSs have a quadrupole deformation that is closer to GR than less massive stars, which reflects in the rise of $\mathcal{G}$ at high M_0. For masses close to the maximum, tensor waves losses can be even higher than in GR. It is interesting to note that all sequences intersect the line $\mathcal{G} = 1$ at the same threshold mass $M_0 \approx 1.85\mathrm{M}_\odot$. The reduction of the tensor GW strain is as high as 70% (75%) for $M_0 = 1.50\mathrm{M}_\odot$ ($1.50\mathrm{M}_\odot$) for purely toroidal (poloidal) magnetic fields, for $\beta_0 = -6$, while it is roughly 10% for $M_0 = 1.80\mathrm{M}_\odot$ and $\beta_0 = -4.5$, for either purely toroidal or purely poloidal magnetic fields (see the blue and light red circles in Fig. 6.2). The same panels also show the ratio $\mathcal{G}$ computed by keeping fixed $\mathcal{H}/W$. We can see that, in this case, the drop and especially the subsequent rise are less steep; in the case of a purely poloidal magnetic field, $\mathcal{G}$ is almost saturated to a constant value before slightly rising.

As was done before with the distortion coefficient, we found that $\mathcal{S}$ is well approximated (to a few percents precision everywhere but in the small range of masses where scalarisation occurs and the steepening is too strong to be well described by a simple power law) by

$$\mathcal{S} \approx 1.7 \left(\frac{R_{10}}{M_{1.6}^2} \right)^{0.2} Q_1^{1.2} \tag{6.10}$$

for both the toroidal and the poloidal cases. This shows again that it is possible to find a unifying functional dependence, even for scalar modes. Also, the value of $\mathcal{G}$ looks very similar for the poloidal and toroidal cases, except at the largest masses above $1.6\mathrm{M}_\odot$ (we note that being a ratio with respect to GR it can only be computed up to maximum GR mass). On the other hand, due to its more complex behaviour, we did not find a satisfying approximation for $\mathcal{G}$ based on power laws of the quantities $M_0, Q_\mathrm{s}, R_\mathrm{c}$.

It is evident that the power emitted in tensor modes by scalarised NSs is smaller, for masses below $\approx 1.85\mathrm{M}_\odot$, than for the model in GR of the same mass and same EoS, even if the minimum does not correspond to the configuration with the strongest scalar charge. The trend changes for higher masses, where the losses in tensor modes in STTs are higher than for the corresponding GR models. Given that the scalar modes also contribute to the total energy losses, we see that as the mass rises, we first find a regime at the beginning of scalarisation, where the total GW emission is suppressed

with respect to GR, which is then followed by a regime that is closer to the maximum mass where, due to the scalar channel, losses might even be enhanced by a factor of between 2 and 3.

The minimum value of $\mathcal{G}$ (marked by the circles and squares in Fig. 6.2) scales quadratically, with β_0 at fixed $B_{\max}$ and $\mathcal{H}/W$:

$$\min\left(\mathcal{G}\right)\big|_{B_{\max}} \approx \begin{cases} 7.79 + 2.36\beta_0 + 0.185\beta_0^2 \text{ for toro.} \\ 7.98 + 2.44\beta_0 + 0.190\beta_0^2 \text{ for polo.} \end{cases}, \tag{6.11}$$

and

$$\min\left(\mathcal{G}\right)\big|_{\mathcal{H}/W} \approx \begin{cases} 6.91 + 2.0\beta_0 + 0.150\beta_0^2 \text{ for toro.} \\ 6.34 + 1.8\beta_0 + 0.130\beta_0^2 \text{ for polo.} \end{cases}. \tag{6.12}$$

Analogously, the mass at which the minimum of $\mathcal{G}$ occurs scales linearly with β_0:

$$M_{0,\min}\big|_{B_{\max}} \approx 2.74 + 0.21\beta_0 \text{ for toro. and polo.}, \tag{6.13}$$

and

$$M_{0,\min}\big|_{\mathcal{H}/W} \approx \begin{cases} 2.45 + 0.143\beta_0 \text{ for toro.} \\ 2.32 + 0.113\beta_0 \text{ for polo.} \end{cases}. \tag{6.14}$$

6.3 Discussion

In the work presented in this chapter we explore how the addition of a scalar field that is non-minimally coupled to the metric affects the magnetic quadrupolar deformation of a NS in the weak field regime ($B_{\max} \lesssim 10^{17}$G). We find, as in Newtonian gravity and in GR, in this limit the quadrupolar deformation e can be well-approximated by a linear function of either $B_{\max}^2$ or $\mathcal{H}/W$, for fixed baryonic mass, M_0, and scalarisation parameter, β_0. We find that the coefficients of the linear expansion strongly depart from those of GR for sufficiently negative values of β_0: for the range of parameters investigated here, spontaneous scalarisation can decrease the magnetic deformation of a NS by up to $\approx$ 70% of the GR value, for $\beta_0 = -6$. For values of $\beta_0 \gtrsim -4.3$, we find that the results in massless STTs without screening are indistinguishable from GR. This behaviour can be attributed to the interplay between various effects. First, given a certain EoS, we find that NSs in STTs have a different central density than those in GR with the same mass. In particular, below a threshold mass in the stable branch of the mass-central density diagram, scalarised models have a higher central density than the GR models with the same mass, which causes the inner region of the star to be less prone to deformation; the opposite happens for masses above the threshold, which are more susceptible to deformation than the corresponding GR models with the same mass. This tendency explains why $\mathcal{G}$ is higher than unity for $M_0 \gtrsim 1.85\mathrm{M}_\odot$,

which is very close to the threshold mass, which we found to be $M_0 \approx 1.88\mathrm{M}_\odot$ for low magnetisations. Moreover, NSs endowed with a purely toroidal magnetic field have a prolate shape, with a more pronounced density gradient at the equator than at the pole, which, in turn, generates a steeper gradient of the scalar field at the equator than at the pole. Given that the effective pressure of the scalar field depends on its spatial derivatives and has the same sign as the fluid pressure, we see that its effect is to reduce the deformation of the star, making it more spherical. The same qualitative behaviour is exhibited by a star endowed with a purely poloidal magnetic field and which possesses an oblate shape with a steeper density gradient at the pole, thus causing the scalar field to apply more pressure in the polar direction than in the equatorial one. As expected, a more pronounced scalarisation (i.e. a more negative β_0) reflects in a stronger pressure of the scalar field, rendering the star even more spherical, thus reducing the distortion coefficients further. It is known that the scalar field can act as a 'stabiliser' for NSs, rendering their shape more spherical. Finally, the scalar field acts as an effective coupling term (it replaces the inverse of the gravitational constant of GR) between matter and the metric. In more scalarised systems, or in the NS central region where the scalar field is larger, this coupling is weaker, and this also holds for perturbations of the energy momentum tensor. Thus, the same structural deformation of the NS produces a weaker metric deformation. All these effects depend on where the deformation is located (centre versus the outer layers).

It is interesting to note that unlike the quadrupolar deformation of NSs caused by their rotation (see e.g. Doneva et al. 2014), the magnetic quadrupolar deformation, as we have seen, decreases in STTs with respect to GR, except for masses close to the maximum. This difference can be explained by the fact that rotation, unlike a magnetic field, affects mostly the outer layers of the NS, which in scalarised systems are less gravitationally bound than in GR (scalarized NS have larger radii than in GR), increasing their deformability with respect to GR. Magnetic deformation seems to be instead mostly regulated by the density in the central region where the magnetic field strength peaks.

Regarding GWs, STTs predict the existence of scalar waves, which, as we show here, can have an amplitude comparable to standard tensor waves and might even dominate the GW losses for strongly scalarised NSs. This can lead to a point when the total emission is even larger than in GR.

We find that a good approximation of the distortion coefficients is given by a simple power-law dependence on M_0, R_c , and Q_s. More interestingly, we found that in terms of the ratio of magnetic to binding energy the effect of a scalar field on the NS deformation and the ratio of scalar to tensor waves emission can be parametrised by a unique function independently of the magnetic field structure or of the STT parameters. It

seems that the presence of a scalar charge can easily be factorised. This is a generalisation of what was already known for GR, that is, with $c_{\rm H}$ being almost a constant. As we described above, the magnetic deformability of NSs heavily depends on their internal structure, determined by the EoS. We leave to a future work to verify how much the functional form and the coefficients entering such function depend on the EoS.

Since the quadrupolar deformation of NSs, at a fixed M_0 and for most of the scalarisation range, is reduced in STTs with respect to GR, it is expected that the energy lost in tensor GWs by deformed NSs is also reduced in STTs; on the other hand, it is enhanced for masses close to the maximum mass for a stable NS in GR. In fact, we found that strongly scalarised stars with a baryonic mass around $1.5{\rm M}_\odot$ have a tensor GW strain, h_0, that is up to 75% lower than for the corresponding stars in GR, while it is roughly 10% lower, for $\beta_0 = -4.5$, for masses of $1.8{\rm M}_\odot$. This means that, for values of β_0 currently allowed by observations, a less than 10% variation in h_0 is to be expected for massless scalar fields. This is much smaller than the typical uncertainties over the distances and the strength of magnetic fields, even for well-constrained galactic objects. Higher values might hold for massive scalar fields and this could lead to serious underestimations (or overestimations, depending on the mass) of the energetics of the system and all that follows from that, such as its distance or the strength of its magnetic field. If similar results on the role of the scalar field in the modification of tensor modes hold as well for other kinds of deformation (e.g. tidal deformations of scalarised NSs in mergers), this could have a deep impact on our understanding of binary NS merger events (Abbott et al. 2017b). More interestingly, we found that the scalar mode can be emitted carrying an energy comparable to the tensor one. However, its strain is suppressed by a factor $\alpha_0 \sim 10^{-5} - 10^{-4}$, which weakens the coupling of the scalar mode to the detector and renders the possibility of it being detected even fainter.

Our results are computed in the full non-linear regime. We also computed the quadrupole deformation, holding both the metric and the scalar field fixed, which can be thought of as a Cowling approximation in STTs. In this case we found that for the mass range we investigated, the coefficients $c_{\rm B}$ and $c_{\rm H}$ are smaller by a factor $\approx 0.5 - 0.65$.

The current sensitivities of the LIGO-Virgo observatories (Abbott et al. 2018) could be enough to detect tensor CGWs emitted by galactic neutrons stars remnants form merger events, with millisecond period (lasting few seconds), if the quadrupole deformation is $e \gtrsim 10^{-5}$ (Lasky 2015; Abbott et al. 2020). Future GW detector of the class of Einstein Telescope (Punturo et al. 2010) and Cosmic Explorer (Reitze et al. 2019) could detect deformations as low as $e \gtrsim 10^{-6}$. This means that, for what concerns continuous scalar waves, detectors with same sensitivity could reveal them from millisecond NSs, spinning for few seconds, only if the scalar quadrupole is α_0^{-1} time bigger, which means magnetic field strength of the order of few 10^{17}G, at the limit of the values that

can be reached (Ciolfi et al. 2019). For the same magnetic fields, tensor waves could be much more easily detected. Instead, the detection of scalar CGWs from slowly spinning magnetars with internal fields of few 10^{17}G (Olausen & Kaspi 2014; Frederick et al. 2021) requires instruments with a sensitivity at least one order of magnitude better than DECIGO (Kawamura et al. 2008) and BBO (Harry et al. 2006).

We caution the reader that there is evidence that the magnetic field at the surface or in the magnetosphere of NSs can have strong multipoles (Bignami et al. 2003; Bilous et al. 2019; Parthasarathy et al. 2020; Raynaud et al. 2020). However, the interpretation of the data is not unambiguous (e.g. the magnetic field inferred from cyclotron lines changes if either electron or proton cyclotron are assumed). It is even less clear how these apply to the magnetic field in the interior, whose geometry is totally unknown. From a theoretical point of view, it is reasonable to expect a difference between the interior and surface magnetic fields. The evolution of the latter is mostly dictated by the Hall term associated to crustal impurities, which leads to the formation of small-scale structures and higher order multipoles (Pons & Viganò 2019; De Grandis et al. 2020), while the dissipation of the former is mostly Ohmic, preferentially suppressing small-scale structure and higher multipoles (Haensel et al. 1990). Given that here we are mostly interested in the deviation with respect to GR, we can consider the purely toroidal and purely poloidal cases as two extrema of the much larger space of possible magnetic configurations. Our results showing that the deviations with respect to GR due to a scalar field are very similar in these two extrema lend us confidence to the consideration that similar deviations with respect to GR will also apply in more complex magnetic field geometries (Mastrano et al. 2013, 2015).

Chapter 7

Quasi-universality of the magnetic deformation of neutron stars in general relativity and beyond

The results shown in this chapter were published in the paper Soldateschi, J. et al. (2021) (hereafter SBD21EOS).

In this study we build upon the works of SBD20 (see Chap. 5) and SBD21 (see Chap. 6), presenting a comprehensive study of the magnetic deformability of NSs in the case of poloidal and toroidal magnetic field configurations, for a large sample of different EoS, in GR and STTs, and for all masses in the stable range above $1M_{\odot}$. In this regard, the work presented in this chapter aims to build upon and complement several previous studies: Frieben & Rezzolla (2012), who investigated the magnetic deformation of toroidal configurations in GR for various EoS at a single NS mass of $1.4M_{\odot}$; Pili et al. (2014), who investigated toroidal, poloidal, and mixed configurations in GR for various masses but only for a simple polytropic EoS; SBD21, where we studied, for the first time, the problem of the magnetic deformation of NSs endowed by spontaneous scalarisation with a massless scalar field for a simple polytropic EoS, for toroidal and poloidal magnetic fields and for various masses in the stable range (see Chap. 6).

Our aim is twofold: firstly, it is to better understand the interplay between different EoS and the magnetic field of a NS and explore whether some kind of EoS-independent relation between the NS deformation and its observable quantities exists, such as mass and radius. This would help to shed some light onto the properties of the internal magnetic field of NSs or set limits on their possible CGW emission. Secondly, we look for similar relations in the case of a scalarised NS, in the case of which EoS-independent scalings could be useful for disentangling the effect of the scalar field to that of the

EoS. Let us recall here that despite their over-simplicity (see the discussion in Chap. 6, also concerning limitations related to the equilibrium formalism), purely toroidal and purely poloidal cases represent the two extrema of the much larger space of possible magnetic configurations (Akgün et al. 2013; Mastrano et al. 2013, 2015) and that for any given magnetic field energy, they maximize the NS quadrupolar deformation, be it prolate or oblate [as in mixed configurations, where the two components are expected to balance each other out; see Tayler (1980)]. Thus, estimates in these two limits form reliable bounds on possible CGWs emission scenarios.

This chapter is structured as follows. In Sect. 7.1 we introduce the EoS that we considered in this study, along with the rationale behind our choice. In Sect. 7.2 we explain the setup of our numerical code and of the physical parameters we adopted. In Sect. 7.3 we show our results for the magnetic deformation of NSs in GR and STTs; first for 'traditional' NSs and then for strange quark stars. In Sect. 7.4 we elaborate on the possible applications of our findings for constraining the NS EoS and magnetic structure and their detectability by way of CGWs. Finally, we discuss our results in Sect. 7.5.

7.1 Selection of equations of state

We chose a selection of 13 different EoS that span a diverse range of calculation methods and particle contents: from zero-temperature and β-equilibrium purely nucleonic EoS to more particle-rich and finite temperature ones, considering also EoS for strange quark stars and a polytropic one. Moreover, all the EoS we used, except the polytropic one (which was used as a comparison to previous works in the literature), were chosen based on the fact that they were still in line with the observational constraints: 1) reaching a maximum mass of at least $\sim$2.05$M_\odot$; 2) satisfying various nuclear physics constraints (Fortin et al. 2016); 3) not too stiff (Guerra Chaves & Hinderer 2019); and 4) providing a radius between $\sim$10km and $\sim$14km for 1.4$M_\odot$ mass models (Bauswein et al. 2017; Bombaci & Logoteta 2018; Kim et al. 2021; Miller et al. 2021; Raaijmakers et al. 2021; Riley et al. 2021). The scope of the work presented in this chapter is not focussed on analysing a very large sample of EoS, but a sample as diverse as possible in terms of physics, particle content, and computational methods, within a range that is in reasonable agreement with present constraints. In this sense, we note that the existence of strange quark stars is considered a possible way out of the hyperon and Delta puzzles, according to which the high densities reached at the centre of hadronic stars would soften the EoS, causing a less-than-2$M_\odot$ maximum mass to be reached (Drago et al. 2016); such stars could be observed, for example, through the emission of multimessenger signals caused by the conversion of a NS to a strange quark star (Kuzur et al. 2021).

In the following, we summarise the main feature of each EoS, grouped according to the particle content: 'nucleonic' for EoS that contain only $npe\mu$ particles; 'hyperonic' for EoS that contain also hyperons; 'quarkionic' for EoS that contain an uds quark matter domain treated with the Nambu-Jona-Lasinio model; 'strange quark matter' for EoS containing uds quarks treated with the MIT bag model or perturbative QCD. We note that this last class of EoS predicts that for certain values of their parameters, the quark matter phase has an energy-per-baryon at zero pressure lower than that of ^{56}Fe (Bodmer 1971; Witten 1984), leading to the possible existence of strange quark stars (Madsen 1991; Glendenning 2000). For convenience, we provide a detailed description of the selected EoS here, characterising their main physical properties and assumptions.

7.1.1 Nucleonic

APR: Zero temperature and β-equilibrium $npe\mu$ matter by Akmal et al. (1998), computed using variational techniques with the two-nucleon interaction A18, the boost correction due to nearby nucleons δv and the three-body interaction term UIX* in the baryon number density range of $7.6 \times 10^{-2} < n_\mathrm{b}/\mathrm{fm}^{-3} < 1.34$ (the liquid core). We note that this EoS is usually called APR4 in the literature. The inner crust, in the range of $2.1 \times 10^{-4} < n_\mathrm{b}/\mathrm{fm}^{-3} < 7.6 \times 10^{-2}$, is calculated with the SLy4 EoS (Douchin & Haensel 2001) and attached to the liquid core; the outer crust, in the range of $8 \times 10^{-15} < n_\mathrm{b}/\mathrm{fm}^{-3} < 2.1 \times 10^{-4}$, is from Baym et al. (1971) and attached to the inner crust. Data is taken from the CompOSE database (Typel et al. 2013)[1][2].

SLY9: Zero temperature and beta-equilibrium $npe\mu$ matter unified EoS by Gulminelli & Raduta (2015), taken from the CompOSE database where it is named 'RG(SLY9)'. Cluster energy functionals are those of Danielewicz & Lee (2009). The high density part $10^{-7} < n_\mathrm{b}/\mathrm{fm}^{-3} < 1.51$ is calculated using the effective interaction SLy9 (Chabanat 1995). This is the only Skyrme-type EoS that seems to satisfy various nuclear physics constraints (Fortin et al. 2016). The low density part $8.6 \times 10^{-11} < n_\mathrm{b}/\mathrm{fm}^{-3} < 10^{-7}$ has been added to the original CompOSE table using the EoS by Togashi et al. (2017). Beware that the EoS from Fortin et al. (2016) (thus, also from CompOSE) has been joined at $n_\mathrm{b} = 0.04\mathrm{fm}^{-3}$ in a thermodinamically unstable way (Raduta private communication), because the pressure drops with increasing density. We adjusted this point, but it still results in a minor density jump in the models.

BL2: Zero temperature and beta–equilibrium $npe\mu$ matter obtained using realistic two-body and three-body nuclear interactions derived in the framework of chiral pertur-

[1]See the CompOSE databse website for details: `https://compose.obspm.fr/home`.

[2]We note that the pseudo-enthalpy h is not available in the CompOSE database, and was thus computed when needed.

bation theory, including the $\Delta(1232)$ isobar intermediate state. The high density part $8 \times 10^{-2} < n_b/\mathrm{fm}^{-3} < 1.29$ is from Bombaci & Logoteta (2018), where it is named N3LOΔ+N2LOΔ, and is derived using Brueckner-Bethe-Goldstone quantum many-body theory in the Brueckner-Hartree-Fock approximation. The crust EoS is taken from Douchin & Haensel (2001), in the density range of $7.9 \times 10^{-15} < n_b/\mathrm{fm}^{-3} < 8.0 \times 10^{-2}$. Data is taken from the CompOSE database, where it is named 'BL_EOS with crust'.

DDME2: Zero temperature and beta-equilibrium EoS by Fortin et al. (2016), computed in the high density range of $2.5 \times 10^{-4} < n_b/\mathrm{fm}^{-3} < 1.2$ with a relativistic-mean-field theory model where nucleons interact via the exchange of σ, ω, ρ mesons with density dependent meson-nucleon couplings by Lalazissis et al. (2005), where it is named 'DD-ME2'. The outer crust follows the SLy9 EoS by Chabanat (1995) in the high density regime $10^{-7} < n_b/\mathrm{fm}^{-3} < 2.5 \times 10^{-4}$, while it is taken from Douchin & Haensel (2001) for the low desity regime $n_b < 10^{-7}\mathrm{fm}^{-3}$. Data tables are found in the supplemental materials of Fortin et al. (2016).

NL3$\omega\rho$: Zero temperature and beta-equilibrium EoS by Fortin et al. (2016), computed in the high density range of $3 \times 10^{-4} < n_b/\mathrm{fm}^{-3} < 1.2$ with a relativistic-mean-field theory Walecka model where nucleons interact via the exchange of σ, ω, ρ mesons with non-linear meson-meson coupling terms by Horowitz & Piekarewicz (2001). The outer crust follows the SLy9 EoS by Chabanat (1995) in the high-density regime $10^{-7} < n_b/\mathrm{fm}^{-3} < 3 \times 10^{-4}$, while it is taken from Douchin & Haensel (2001) for the low desity regime $n_b < 10^{-7}$. Data tables are found in the supplemental materials of Fortin et al. (2016).

SFH: finite 0.1MeV temperature and beta–equilibrium npe matter EoS from Steiner et al. (2013) in the range of $10^{-12} < n_b/\mathrm{fm}^{-3} < 1.9$. It is calculated with the statistical model with excluded volume and interactions of Hempel & Schaffner-Bielich (2010), with relativistic mean-field-theory interactions SFHo. A power-law extrapolation at low densities is used to avoid the effects of finite temperature, which emerge as a pressure saturation around $n_b \approx 10^{-10}$. Data is taken from the CompOSE database[3], where it is named 'SFHO (with electrons)'.

7.1.2 Hyperonic

DDME2-Y: Equivalent to the DDME2 EoS, but with the inclusion of the six lightest hyperons Λ^0 (for $n_b > 0.34\mathrm{fm}^{-3}$), $\Sigma^{0,\pm}$ (for $n_b > 0.41\mathrm{fm}^{-3}$) and $\Xi^{\pm}$ (for $n_b > 0.37\mathrm{fm}^{-3}$) with the hidden strangeness vector-isoscalar ϕ meson. Hyperon-meson coupling co-

[3]See also the website `https://astro.physik.unibas.ch/en/people/matthias-hempel/equations-of-state/` for more details.

efficients are calculated according to Fortin et al. (2016) using relativistic-mean-field theory calculations. Data tables are found in the supplemental materials of Fortin et al. (2016).

NL3$\omega\rho$-Y: equivalent to the NL3$\omega\rho$ EoS, but with the inclusion of the six lightest hyperons Λ^0 (for $n_\mathrm{b} > 0.31\mathrm{fm}^{-3}$), $\Sigma^{0,\pm}$ (for $n_\mathrm{b} > 0.49\mathrm{fm}^{-3}$) and $\Xi^\pm$ (for $n_\mathrm{b} > 0.34\mathrm{fm}^{-3}$) with the hidden strangeness vector-isoscalar ϕ meson. Hyperon-meson coupling coefficients are calculated according to Fortin et al. (2016) using relativistic-mean-field theory calculations. Data tables are found in the supplemental materials of Fortin et al. (2016).

7.1.3 Quarkionic

BH8: Zero-temperature and β-equilibrium unified EoS by Baym et al. (2018)[4]. The EoS is divided into four distinct domains: the crust ($1.6 \times 10^{-10} < n_\mathrm{b}/\mathrm{fm}^{-3} < 4.16 \times 10^{-2}$) is taken from Togashi et al. (2017); the nuclear liquid ($4.16 \times 10^{-2} < n_\mathrm{b}/\mathrm{fm}^{-3} < 0.32$) is taken from Akmal et al. (1998); the hadron-quark crossover and quark matter domains ($0.32 < n_\mathrm{b}/\mathrm{fm}^{-3} < 1.6$) are taken from Baym et al. (2018). It is necessary to note that the nuclear liquid contains a pion condensate, where n_b jumps from $0.21\mathrm{fm}^{-3}$ to $0.245\mathrm{fm}^{-3}$. The quark matter EoS (including up, down, and strange quarks) is calculated using the Nambu-Jona-Lasinio model within the mean field approximation. Its parameters (g_V, H), which quantify the strength of the repulsive density-density interaction and the attractive pairing interaction between quarks respectively, have been chosen to be $(0.80, 1.50)G_\mathrm{s}$, where G_s is the scalar coupling of the Nambu-Jona-Lasinio model for quark matter, which are compatible with hadron physics. Data is taken from the CompOSE database, where it is named 'QHC18'.

BF9: zero-temperature and β-equilibrium unified EoS by Baym et al. (2019). The EoS is divided into three distinct domains: the crust and nuclear liquid ($7.58 \times 10^{-11} < n_\mathrm{b}/\mathrm{fm}^{-3} < 0.32$) are taken from Togashi et al. (2017), while the hadron-quark crossover and quark matter domains ($0.32 < n_\mathrm{b}/\mathrm{fm}^{-3} < 1.58$) are taken from Baym et al. (2019), model-B (corresponding to $g_\mathrm{V} = 0.80G_\mathrm{s}$ and $H = 1.49G_\mathrm{s}$). There are no phase transitions. The quark matter EoS (including up, down, and strange quarks) is calculated using the Nambu-Jona-Lasinio model within the mean field approximation. Data is taken from the CompOSE database, where it is named 'QHC19-B'.

[4]See also the website `https://user.numazu-ct.ac.jp/~sumi/eos/index.html#QHC18` for more details.

7.1.4 Strange quark matter

SQM1: obtained by Alcock et al. (1986) [see also Farhi & Jaffe (1984)] using the MIT bag model, setting the strong interaction coupling constant $\alpha_c = 0$ and assuming the strange quark mass $m_s = 0$, leading to a vanishing electron density. No pairing is present. The MIT bag constant was chosen to be $B = (141.4\text{MeV})^4$, corresponding to a zero pressure density of $n_b = 0.259\text{fm}^{-3}$ and a maximum mass of $\sim 2.1\text{M}_\odot$.

SQM2: based on the parametrisation of the perturbative QCD calculations at finite chemical potential according to Fraga et al. (2014) [see also Drago et al. (2016); Pili et al. (2016) for other works using this EoS], setting the strong interaction coupling constant at the Z mass scale $\alpha_c = 0.118$ and assuming the strange quark mass $m_s = 94\text{MeV}$ (at the 2GeV scale). The scale parameter X, which is the ratio between the renormalisation scale and the baryon chemical potential, have been chosen to be $X = 3.5$, for which the maximum mass of quark stars is $2.54\text{M}_\odot$. Quark matter is unpaired. The zero-pressure density is $n_b = 0.140\text{fm}^{-3}$.

Finally, we also used the POL2 polytropic EoS, widely used in previous literature (Bocquet et al. 1995; Kiuchi & Yoshida 2008; Frieben & Rezzolla 2012; Pili et al. 2014): $p = K_a \rho^{\gamma_a}$, with $K_a = 110$ (in dimensionless units) and $\gamma_a = 2$. In the following nucleonic, hyperonic and quarkionic EoS are generally referred as 'standard EoS', and NSs that are computed via these EoS are noted as 'standard NS'.

7.1.5 Characterisation of the equations of state

In Fig. 7.1, we plot the Komar mass M_k against the circumferential radius R_c for models of un-magnetised, static NSs computed with the described EoS. The left panel refers to GR, while the right panel refers to a STT with $\beta_0 = -6$. The maximum mass models, as well as the radius for the models having a Komar mass of $1.4\text{M}_\odot$, are characterised for each EoS in Tab. 7.1, in GR and in STT with $\beta_0 = -6$. From Fig. 7.1 (left panel) we see that the NS radii have values ranging from $\sim$10km to $\sim$14km for most EoS, while the less compact SQM2, and especially the POL2, can reach radii higher than $15 - 16$km. The maximum masses are concentrated in the range of $\sim$2-2.2$\text{M}_\odot$ for most EoS, while they can reach the exceptionally high value of $\sim 2.77\text{M}_\odot$ for the NL3$\omega\rho$ EoS, as well as the very low value of $\sim 1.72\text{M}_\odot$ for the POL2 EoS. We note that the versions of the DDME2 and NL3$\omega\rho$ EoS containing hyperons, DDME2-Y and NL3$\omega\rho$-Y, respectively, detach from their non-hyperonic counterparts for models having central densities such that the six lightest hyperons may appear, corresponding to typical masses in the range of 1.70-1.75$\text{M}_\odot$. As is known (Drago et al. 2016), the appearance of hyperons causes a reduction of the maximum mass achievable by the NS.

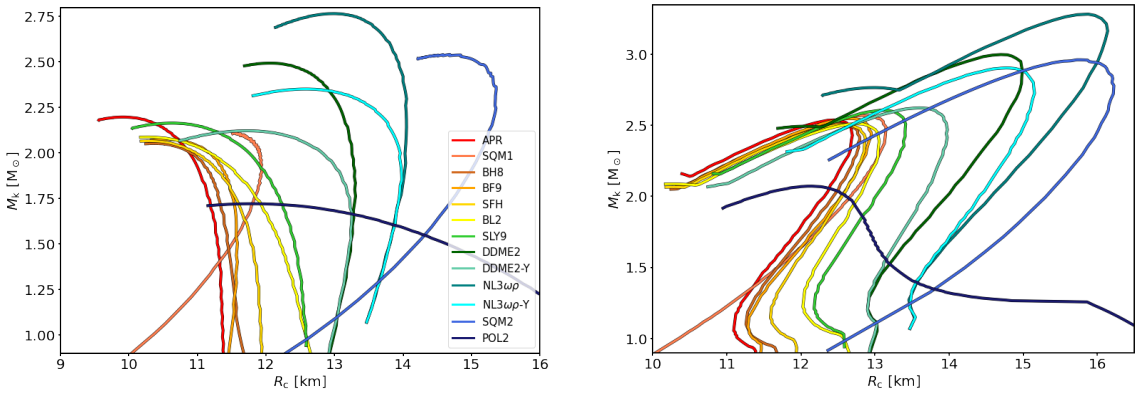

Figure 7.1: Komar mass M_k against circumferential radius R_c for un-magnetised, static models of NSs computed with the EoS described in Sect. 7.1 in GR (left plot) and in STTs with $\beta_0 = -6$ (right plot). The EoS are colour-coded, and ordered in the legend, according to the compactness $C = M_k/R_c$ calculated at $M_k = 1.4\mathrm{M}_\odot$ in GR: red for the highest compactness and blue for the lowest compactness.

Table 7.1: Characterisation of the maximum mass models in GR (STT with $\beta_0 = -6$), for each EoS described in Sect. 7.1 and plotted in Fig. 7.1: M_k^{max} is the Komar mass, R_c^{max} is the circumferential radius, ρ_c^{max} is the central density and Q_s^{max} is the scalar charge. Moreover, for each EoS the circumferential radius for the model with $M_k = 1.4\mathrm{M}_\odot$, $R_{1.4}$, is listed.

EoS	$M_k^{max}[\mathrm{M}_\odot]$	R_c^{max}[km]	$\rho_c^{max}[10^{15}\mathrm{g\ cm}^{-3}]$	$Q_s^{max}[\mathrm{M}_\odot]$	$R_{1.4}$[km]
APR	2.20(2.54)	9.91(12.44)	1.92(1.35)	(1.12)	11.33(11.41)
SQM1	2.11(2.57)	11.57(12.82)	1.55(2.21)	(1.27)	11.33(11.46)
BH8	2.05(2.51)	10.36(12.52)	1.88(1.50)	(1.15)	11.48(11.54)
BF9	2.07(2.55)	10.54(12.69)	1.81(1.48)	(1.18)	11.58(11.61)
SFH	2.07(2.50)	10.27(12.57)	1.91(1.48)	(1.13)	11.83(11.78)
BL2	2.09(2.51)	10.26(12.76)	1.93(1.45)	(1.14)	12.29(12.10)
SLY9	2.16(2.61)	10.63(13.15)	1.78(1.35)	(1.19)	12.47(12.28)
DDME2	2.49(3.00)	12.06(14.70)	1.36(1.02)	(1.34)	13.20(13.04)
DDME2-Y	2.12(2.62)	11.73(13.59)	1.54(1.50)	(1.23)	13.20(12.99)
NL3$\omega\rho$	2.77(3.28)	12.99(15.88)	1.14(0.83)	(1.47)	13.74(13.58)
NL3$\omega\rho$-Y	2.35(2.90)	12.58(14.77)	1.31(1.21)	(1.35)	13.74(13.56)
SQM2	2.54(2.96)	14.68(15.77)	1.00(1.79)	(1.59)	13.96(13.96)
POL2	1.72(2.07)	11.79(12.15)	1.80(2.52)	(1.02)	15.18(13.50)

7.2 Model setups

In the following, we focus on magnetised, stable models of static NSs with maximum magnetic fields $B_{\rm max} \lesssim 10^{17}$G. This value is much lower than the critical field strength, on the order of $\sim 10^{19}$G, set by the energy associated with the characteristic NS density (Lattimer & Prakash 2007).

As we discussed in Sect. 4.3, if modifications to the internal NS structure are needed, it is worth also investigating the STT with $\beta_0 \gtrsim -4.3$, as representative of the effects of screened scalar fields. We chose $\alpha_0 = -2 \times 10^{-4}$ and $\beta_0 \in \{-6, -5.75, -5.5, -5\}$. Such low values are chosen to both highlight the effects of scalarisation and to show its effects at the edge of the permitted parameter space, keeping in mind that our results hold also for scalar fields with a mass such that their screening radius is larger than the NS radius.

Our models are computed for purely poloidal and purely toroidal magnetic field configurations, the details of which are explained in Sect. 3.5. The choice of these simple, 'pure' magnetic configurations, while simplifying the computations, also provides us with the results for extremal magnetic configurations: a poloidal magnetic field affects the NS deformation in an opposite way with respect to a toroidal field; as such, we expect configurations with mixed fields to show a deformation which is, in absolute value, smaller than those obtained with purely poloidal and toroidal configurations.

To compute the results shown in this chapter, we first used the full `XNS` code to compute roughly 65000 numerical models with stronger magnetic fields and then we interpolated the results according to the approximations in Eq. 6.2. The large number of models used allows us to limit the errors introduced in the interpolation process. We studied only those configurations belonging to the stable branch of the mass-density diagram, that is, with a central density, $\rho_{\rm c}$, lower than that of the maximum mass model. Many results shown in Sect. 7.3 and, in particular, the quasi-universal relations, were obtained through a 'principal component analysis' (PCA). Briefly, PCA is a dimensionality reduction technique used to find correlations among a given set of data. In particular, the PCA algorithm computes the D 'principal components' of some input D-dimensional data, namely, the hyperplanes that best fit the input data and are orthogonal to each other. While the first principal component is the single hyperplane that maximises the variance of data projected onto it, the last (D-th) principal component is the hyperplane around which data is spread out the least. For this reason, the quasi-universal relations that we show in the following are precisely the equations of the last PCA component, that is, the hyperplane that best fits the input data. In providing the input data to the PCA algorithm, we selected only those configurations with a mass, $M_{\rm k} > 1{\rm M}_\odot$, both in GR and in STT, in order to analyse only models with a real-

istic mass value. Moreover, in the STT case, we selected scalar charges of $Q_s > 0.4M_\odot$; this is done because, as we go on to show, in STTs, we are mostly interested in deviation from GR. In this respect models with small scalar charges, especially in the small region where spontaneous scalarisation abruptly develops, tend to be less accurate. Let us remark, however, that in terms of the total quadrupolar deformation (excluding such low values of the scalar charge from the PCA) does not change our results in an appreciable way: when the value of the scalar charge approaches zero, the deviation from GR becomes increasingly negligible, and the GR quasi-universal relations hold. In practice, large relative errors translate into small absolute ones.

7.3 Quasi-universal relations

In this section, we first describe how different EoS affect the magnetic structure of our NS models. Then we detail the results obtained on the distortion coefficients using all EoS described in Sect. 7.1 and show the quasi-universal relations we found, considering only viable EoS that describe standard NSs, that is, excluding SQM1, SQM2, and POL2. Afterwards, we comment on how these results apply to polytropes. We perform this analysis first for GR and then for STTs. Finally, we comment on how our results apply to models of strange quark stars.

Our poloidal models are characterised by a magnetic field whose magnitude is always maximum at the star centre, vanishing in an equatorial current ring located typically at $\sim 60-70\%$ of the NS radius, followed by smaller secondary maximum just underneath the surface. At the surface, the maximum is always reached at the pole and typically is $\sim 20-25\%$ of the central value. On the other hand, the models endowed with a purely toroidal magnetic field possess a simpler magnetic structure: the magnitude of the magnetic field is zero on the axis, reaches a maximum inside the NS, typically at $\sim 40-60\%$ of the NS radius, and then decreases to zero at the surface. The exact profile of the magnetic field components depends on the EoS. In fact, while the general behaviour of the magnetic field is in line with that just described above, the particular composition of the NS causes a shift in the location of the maxima and in the smoothness of the magnetic field profile. As described in Sect. 7.1, the BH8 EoS contains a pion condensate, leading to the appearance of a jump in density. As a consequence, the magnetic field of purely toroidal models display a jump in the magnetic field magnitude at the same location where the condensate appears. On the other hand, purely poloidal models show no sudden change in the magnetic profile (the jump is present in the current distribution). In the case of models described by the SQM1 and SQM2 EoS, for purely poloidal magnetic fields, the equatorial ring where the magnetic field vanishes is located at a radius, which is $\sim 10\%$ higher than for the standard EoS. In the case of purely toroidal models, this shift is such that the magnetic profile is abruptly

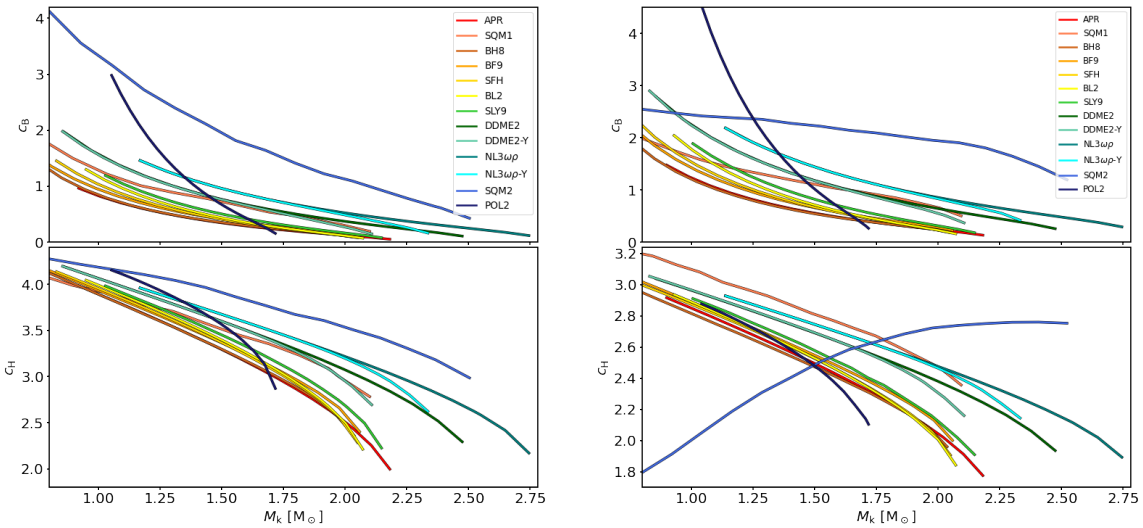

Figure 7.2: Distortion coefficients c_B and c_H, calculated according to Eq. 6.2, as functions of the Komar mass M_k for purely poloidal (left panel) and purely toroidal (right panel) magnetic fields, in GR. The EoS are colour-coded, and ordered in the legend, according to the compactness $C = M_k/R_c$ calculated at $M_k = 1.4M_\odot$ in GR: red for the highest compactness and blue for the lowest compactness.

truncated at the star surface; in some cases, the magnetic field strength monotonically rises all the way to the surface, where it reaches its maximum and then jumps to zero. As we comment in Sect. 7.3.3, this behaviour leads us to consider these models as not true equilibria, since a non-vanishing Lorentz force at the NS surface remains unbalanced. As for the hyperonic EoS, the appearance of hyperons causes an increase in the maximum magnitude of the magnetic field with respect to models of the same central density computed with the corresponding non-hyperonic EoS. Finally, we note that although the profiles of the density and of the magnetic field are affected by the EoS (condensates, appearance of new particles, etc..) as we just described, all the integrated, global quantities, such as the mass, radius, magnetic energy, scalar charges, or quadrupolar deformation of the NS, show no sign of discontinuities or jumps.

7.3.1 General relativity

The distortion coefficients, c_B and c_H (see Eq. 6.2), for our NSs models, calculated in GR, are shown in Fig. 7.2 as functions of the NS Komar mass, M_k[5]. The left panel

[5]The distortion coefficients, c_B and c_H, are shown separately for each EoS described in Sect. 7.1, both in GR and in STTs, in the supplementary materials: `https://doi.org/10.5281/zenodo.5336222`.

refers to models endowed with a purely poloidal magnetic field, while the right panel refers to purely toroidal magnetic fields. The EoS are colour-coded according to the compactness $C = M_k/R_c$, calculated at $M_k = 1.4M_\odot$ in GR: red for the highest compactness and blue for the lowest compactness. We can see that sequences for both coefficients are only roughly ordered according to the compactness of the EoS: models with the same mass have lower distortion coefficients for more compact EoS only on average, the main exceptions to this rule being the SQM1, SQM2 and POL2 EoS. This is especially true for c_H in the toroidal case, where the POL2 EoS (the least compact one) reaches a lower distortion coefficient than the APR EoS (the most compact one) close to its maximum-mass model and the SQM2 EoS displays a completely different behaviour. We note that while it is to be expected that more compact EoS have a lower deformation, the particular definition of compactness we use (calculated for $1.4M_\odot$ models) clearly impacts the ordering of the EoS, as can be seen from the mass-radius relations in Fig. 7.1. If we exclude the SQM1, SQM2, and POL2 EoS, we see that all sequences are more closely packed: the relative difference, in the poloidal (toroidal) cases, $2(c_B^+ - c_B^-)/(c_B^+ + c_B^-)$ between the uppermost sequence (+ superscript, for the NL3$\omega\rho$ EoS) and the lowermost sequence (- superscript, for the APR EoS) in the poloidal (toroidal) case is $\sim 1.26(\sim 1.14)$ at $M_k \sim 2.0M_\odot$ and $\sim 0.83(\sim 0.79)$ at $M_k \sim 1.2M_\odot$, indicating that above $1.7M_\odot$, various EoS can differ by order unity. For c_H, in the poloidal (toroidal) case, the difference $2(c_H^+ - c_H^-)/(c_H^+ + c_H^-)$ ranges from ~ 0.25 (~ 0.19) at $M_k \sim 2.0M_\odot$, to ~ 0.07 (~ 0.07) at $M_k \sim 1.2M_\odot$. These numbers show that while c_B vastly differs between the sequences for the APR and the NL3$\omega\rho$ EoS, the value of c_H remains almost constant across the whole mass range, changing at most by a factor of ~ 1.5. Since the SQM1, SQM2, and POL2 EoS display such a different behaviour, for the moment, we focus only on those EoS describing standard NS (thus excluding SQM1 and SQM2) allowed by observations (thus excluding POL2), which we refer to as 'standard EoS'.

Given the similarity between the distortion coefficients for all standard EoS when plotted against the Komar mass, it is reasonable to wonder whether adding the dependence on other variables could further reduce the spread. We thus chose to consider the dependence also on another potentially observable quantity, namely the circumferential radius R_c, and adopted a PCA algorithm to find the best-fit relation between $c_{B,H}$, M_k, and R_c. We found that these formulas approximate $c_{B,H}$ to a satisfying level of accuracy for all standard EoS:

$$c_B^{PCA} = \begin{cases} 0.13^{+0.03}_{-0.02} R_{10}^{5.45} M_{1.6}^{-2.41} \text{ for poloidal,} \\ \\ 0.25^{+0.03}_{-0.03} R_{10}^{5.03} M_{1.6}^{-2.07} \text{ for toroidal,} \end{cases} \tag{7.1}$$

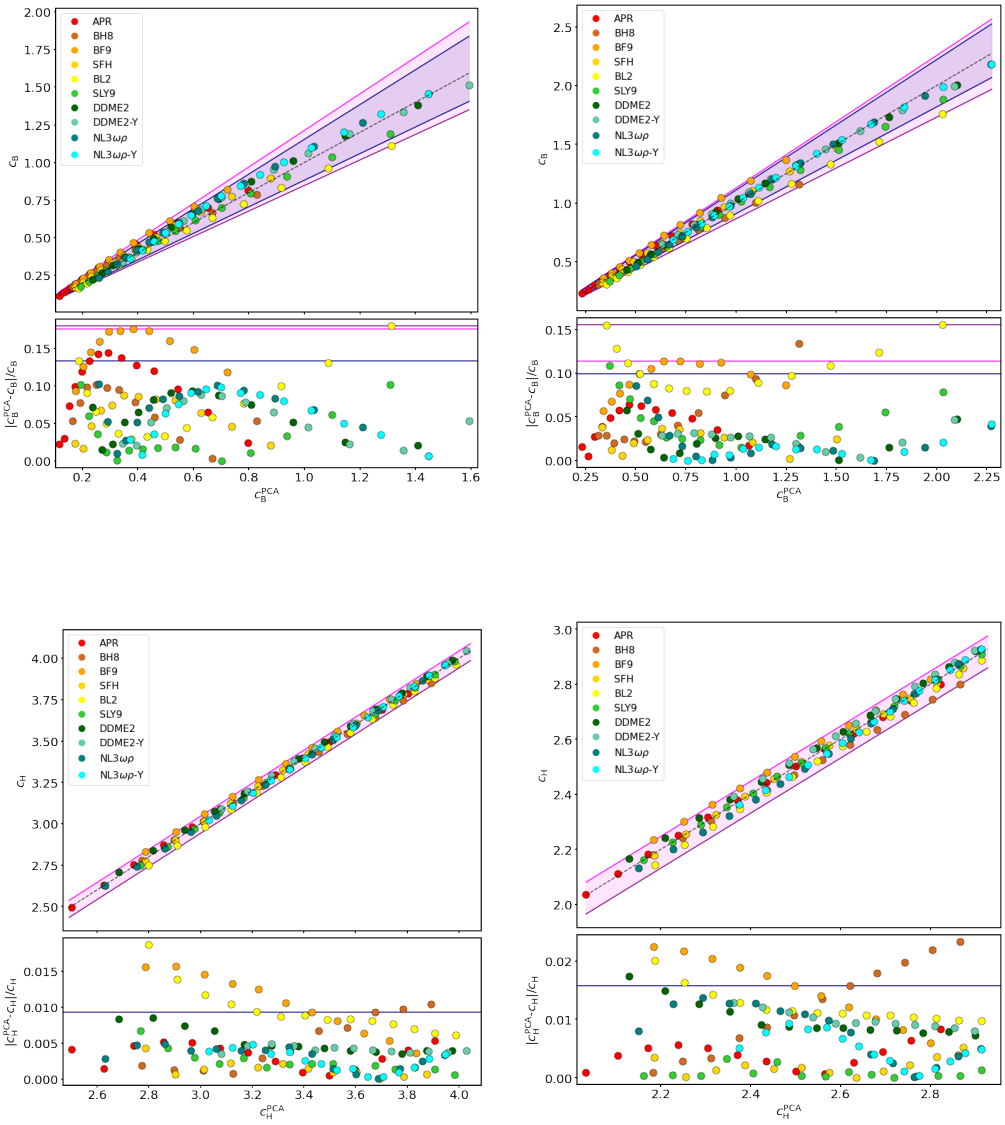

Figure 7.3: Distortion coefficients $c_{\rm B}$ (top panels) and $c_{\rm H}$ (bottom panels), calculated according to Eq. 6.2 in GR, versus their approximations $c_{\rm B}^{\rm PCA}$ and $c_{\rm H}^{\rm PCA}$, calculated with the relations in Eqs. 7.1,7.2 (top plot in each panel). The corresponding relative deviations from the PCA are given in the bottom plot in each panel. The top left and bottom left panels refer to purely poloidal magnetic fields; the top right and bottom right panels refer to purely toroidal magnetic fields. The dashed black line is $c_{\rm B,H} = c_{\rm B,H}^{\rm PCA}$. The magenta shaded area comprises all data points and the purple and magenta lines represent the upper and lower bounds of Eqs. 7.1,7.2. The dark blue lines bounding the shaded blue area mark the 90th percentile error region. The EoS are colour-coded, and ordered in the legend, according to the compactness $C = M_{\rm k}/R_{\rm c}$ calculated at $M_{\rm k} = 1.4{\rm M}_\odot$ in GR: red for the highest compactness and blue for the lowest compactness.

$$c_{\rm H}^{\rm PCA} = \begin{cases} 5.77^{+0.04}_{-0.06} - 0.77R_{10} - 4.14M_{1.6} - 0.27M_{1.6}^2 + \\ \quad +0.07R_{10}^2 + 2.28M_{1.6}R_{10} \text{ for poloidal,} \\ \\ 7.02^{+0.05}_{-0.07} - 5.22R_{10} - 2.76M_{1.6} - 0.12M_{1.6}^2 + \\ \quad +1.92R_{10}^2 + 1.51M_{1.6}R_{10} \text{ for toroidal,} \end{cases} \tag{7.2}$$

where $R_{10} = R_{\rm c}/10$km and $M_{1.6} = M_{\rm k}/1.6{\rm M}_\odot$. We refer to these formulas, as well as the analogue ones described in the following, as 'quasi-universal relations', since they hold for all standard EoS we considered. The distortion coefficients computed using formulas from Eqs. 7.1,7.2 are plotted against their 'real' value, computed with formulas Eq. 6.2, as shown in in Fig. 7.3 (top plot in each panel) for purely poloidal (left panels) and purely toroidal (right panels) magnetic field configurations. In each panel, the bottom plot displays the relative error $|c_{\rm B,H}^{\rm PCA} - c_{\rm B,H}|/c_{\rm B,H}$ committed when using the quasi-universal relations to approximate the distortion coefficients. The dashed black line is a reference $c_{\rm B,H} = c_{\rm B,H}^{\rm PCA}$ bisecting line, which stands for a perfect approximation. The superscripts and subscripts in the first coefficient of Eqs. 7.1,7.2 are the values that define the purple and magenta lines bounding the magenta shaded area in Fig. 7.3, top plots in each panel. The dark blue lines, which bound the shaded blue area in the plots of $c_{\rm B}$, mark the 90th percentile of the relative errors (the bounds containing 90% of the results). The corresponding values of these errors are showed with lines of the same colour in the bottom plots of each panel for $c_{\rm B}$. In the case of $c_{\rm H}$, given the form of the quasi-universal relation Eq. 7.2, the bounds in the top plots do not correspond to a unique constant value of the relative error, thus we omit them in the bottom plots; likewise, we omit the 90th percentile line in the top plots. We note that the magenta regions contain all the points, and, in this sense, the bounds in Eqs. 7.1,7.2 represent the maximum spread of the results; however, in general, typical deviations with respect to the PCA approximations are about 3/4 to 1/2 of those values. We see that the relations for $c_{\rm B}$, in the poloidal case (top left panel), hold with a maximum relative error of $\sim$ 17%, and the 90th percentile stands at $\sim$ 14%; in the toroidal case (top right panel), they are $\sim$ 16% and $\sim$ 10%, respectively. The approximation for $c_{\rm H}$ is much more accurate, with a maximum relative error of $\sim$ 2% in both magnetic configurations, and mostly under $\sim$ 1% in the poloidal case (bottom left panel) and under $\sim$ 1.5% in the toroidal case (bottom right panel). We see no dependence of the deviation from the PCA results on the compactness of the EoS. We note that the coefficients for $c_{\rm H}^{\rm PCA}$ in Eq. 7.2 in the toroidal case can be used also in the poloidal case, but in this case, the 90th percentile relative error increases to $\sim$ 27%. However, similarly to what we found in SBD21 for $c_{\rm H}$ (see Chap. 6), performing $c_{\rm H}^{\rm PCA} \to 5/3 c_{\rm H}^{\rm PCA} - 0.9$ allows one to use the toroidal coefficients in the poloidal case with a $\sim$ 2% error.

The distortion coefficients as defined in Eq. 6.2 contain quantities that are not directly

accessible by observations, since they require knowledge of the details of the internal structure and magnetic field geometry of NS. In this respect, the quasi-universal relations Eqs. 7.1,7.2 may be used to get information on the internal structure of the magnetic field, as we discuss in Sect. 7.4. However, from an observational prospective, it is useful to introduce another distortion coefficient, defined using a quantity that may be observed:

$$|e| = c_{\rm s} B_{\rm s}^2 + \mathcal{O}\left(B_{\rm s}^4\right) , \tag{7.3}$$

where $B_{\rm s}$ is the magnetic field calculated at the pole of the NS, at the surface, normalised to 10^{18}G. Obviously this coefficient is defined only for configurations endowed with a poloidal magnetic field (the toroidal one being hidden under the surface). As it was done for $c_{\rm B}$ and $c_{\rm H}$, we performed a PCA and found the corresponding quasi-universal relation:

$$c_{\rm s}^{\rm PCA} = 2.97^{+0.12}_{-0.23} R_{10}^{4.61} M_{1.6}^{-2.80} . \tag{7.4}$$

The distortion coefficient $c_{\rm s}$ computed using formula Eq. 7.4 is plotted against its 'real' value, computed with formula Eq. 7.3, in Fig. 7.4 (top plot), along with the relative error of the approximation (bottom panel). We note that the values of $c_{\rm s}$ are roughly one order of magnitude higher than those of $c_{\rm B}$ because the magnetic field at the surface is lower than the internal one, while the normalisation used is the same for both coefficients. We see that the approximation $c_{\rm s}^{\rm PCA}$ holds to a satisfying accuracy, with a maximum relative error of 8%, but mostly concentrated under 4%.

As can be seen from Fig. 7.2, applying the PCA derived from standard EoS, Eqs. 7.1,7.2,7.4, to the model computed with the POL2 EoS leads to a large errors: the PCA approximation is larger by a factor of ~ 1.9 for $c_{\rm B}$ both in the poloidal (at $1.05{\rm M}_\odot$) and toroidal (at $1.55{\rm M}_\odot$) case, and a factor of ~ 1.8 larger at $1.4{\rm M}_\odot$; instead, the relative deviation reaches $\sim$ 7% at $1.56{\rm M}_\odot$ ($\sim$ 20% at $1.04{\rm M}_\odot$) for $c_{\rm H}$ in the poloidal (toroidal) case, while it is $\sim$ 6%($\sim$ 17%) for $1.4{\rm M}_\odot$ models in the poloidal (toroidal) case; similarly, the maximum error for $c_{\rm s}$ is $\sim$ 20% at $1.05{\rm M}_\odot$, while it is $\sim$ 2% at $1.4{\rm M}_\odot$.

7.3.2 Scalar-tensor theories

In the case of STTs, we find quasi-universal relations for $\Delta c_{\rm B} = |c_{\rm B} - c_{\rm B}^{\rm GR}|$, $\Delta c_{\rm H} = |c_{\rm H} - c_{\rm H}^{\rm GR}|$ and $\Delta c_{\rm s} = |c_{\rm s} - c_{\rm s}^{\rm GR}|$, where $c_{\rm B}^{\rm GR}$, $c_{\rm H}^{\rm GR}$ and $c_{\rm s}^{\rm GR}$ are the relations found in the GR case: Eqs. 7.1,7.2,7.4, respectively. We chose this approach instead of approximating the bare distortion coefficients for two reasons: on the one hand, since we already found satisfying approximations in GR, it makes sense to focus only on the difference given by scalarisation; on the other hand, this allows us to exclude the few models with a low scalar charge, which are located in the mass-radius diagram in Fig. 7.1 (right

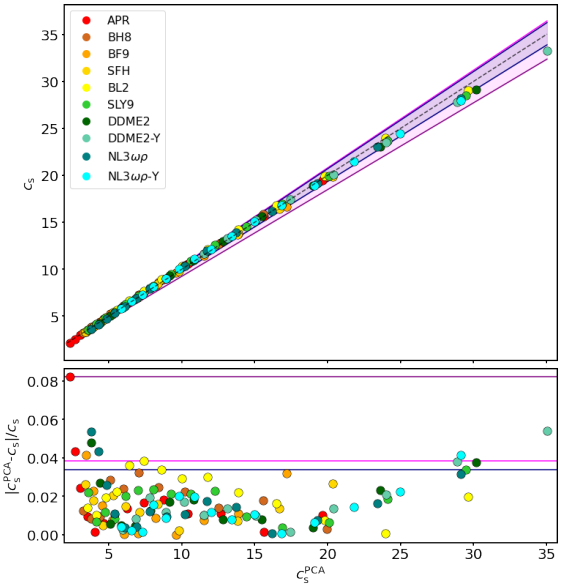

Figure 7.4: Distortion coefficient c_s, calculated according to Eq. 7.3 in GR, versus its approximation c_s^{PCA} calculated with the quasi-universal relation in Eq. 7.4 (top plot). The corresponding relative deviation from the PCA is given in the bottom plot. The dashed line is $c_{B,H} = c_{B,H}^{PCA}$. The magenta shaded area comprises all data points and the purple and magenta lines represent the upper and lower bounds of Eq. 7.4. The dark blue lines bounding the shaded blue area mark the 90th percentile error region. The EoS are colour-coded, and ordered in the legend, according to the compactness $C = M_k/R_c$ calculated at $M_k = 1.4M_\odot$ in GR: red for the highest compactness and blue for the lowest compactness.

panel), close to the sharp onset of scalarisation, and which may not be as accurately computed as the rest of the sequence. In computing the PCA in the STT case, we considered also the dependence of the distortion coefficients on the scalar charge, Q_s. We found the following relations:

$$\Delta c_B^{PCA} = \begin{cases} 0.03^{+0.05}_{-0.03} R_{10}^{8.23} M_{1.6}^{-5.08} Q_1^{2.60} \text{ for poloidal,} \\ \\ 0.06^{+0.09}_{-0.05} R_{10}^{5.96} M_{1.6}^{-3.52} Q_1^{1.95} \text{ for toroidal,} \end{cases} \tag{7.5}$$

$$\Delta c_H^{PCA} = \begin{cases} 1.96^{+0.17}_{-0.18} R_{10}^{0.72} M_{1.6}^{-1.96} Q_1^{1.54} \text{ for poloidal,} \\ \\ 1.49^{+0.26}_{-0.17} R_{10}^{0.75} M_{1.6}^{-1.81} Q_1^{1.55} \text{ for toroidal,} \end{cases} \tag{7.6}$$

$$\Delta c_s^{PCA} = 0.92^{+0.20}_{-0.27} R_{10}^{4.77} M_{1.6}^{-4.50} Q_1^{1.71}, \tag{7.7}$$

where Q_1 is Q_s normalised to $1M_\odot$. The relations Eqs. 7.5,7.6 are plotted against the corresponding value Δc_B and Δc_H, computed using formulas Eq. 6.2, in Fig. 7.5 (top

plot in each panel) for purely poloidal (left panels) and purely toroidal (right panels) magnetic field configurations. Instead, Eq. 7.7 is plotted against the corresponding value $\Delta c_{\rm s}$, computed using formula Eq. 7.3, in Fig. 7.6 (top plot). In each figure and panel, the bottom plot displays the relative error of the quasi-universal relations. The dashed lines are a reference $\Delta c_{\rm B,H} = \Delta c^{\rm PCA}_{\rm B,H}$ and $\Delta c_{\rm s} = \Delta c^{\rm PCA}_{\rm s}$ bisecting lines, which stand for a perfect approximation. We see from the bottom plots in each panel of Figs. 7.5,7.6 that the overall relative errors are larger than in the GR case. This is to be expected for two reasons: on the one hand, we are approximating the $\Delta c_{\rm B,H,s}$, which, by definition, are computed on the difference with an already approximated quantity, $c^{\rm PCA}_{\rm B,H,s}$; on the other hand, especially at low values of the scalar charge (bottom-left of each top plot), the onset of scalarisation causes an abrupt change in the mass-radius relation compared to GR, inevitably decreasing the accuracy of NS models. We see that the relations for $\Delta c_{\rm B}$, both in the poloidal (top left panel) and in the toroidal case (top right panel), hold with a 90th percentile relative error of $\sim 50\%$. The approximation for $\Delta c_{\rm H}$ is more accurate, with a relative error of $\sim 5\%$ in the poloidal case (bottom left panel) and $\sim 7\%$ in the toroidal case (bottom right panel). In any case, we see no dependence of the error on the compactness of the EoS. As for $\Delta c_{\rm s}$, its approximation in Fig. 7.6 holds with a relative error mostly under $\sim 10\%$. We note that the coefficients for $\Delta c^{\rm PCA}_{\rm H}$ in Eq. 7.6 in the toroidal case can be used also in the poloidal case, but in this case the 90th percentile relative error increases to $\sim 30\%$. However, similarly to what we found in the GR case, performing $c^{\rm PCA}_{\rm H} \to 3/2 c^{\rm PCA}_{\rm H} - 0.2$ allows one to use the toroidal coefficients in the poloidal case with a $\sim 10\%$ error.

If we apply Eq. 7.5 to approximate $\Delta c_{\rm B}$ in models computed using the POL2 EoS, errors remain roughly the same in the poloidal case, while they increase by $\sim 20\%$ in the toroidal case. Instead, $\Delta c_{\rm H}$ approximated using Eq. 7.6 holds also for the POL2 EoS, at the expense of an error reaching $\sim 15\% (\sim 30\%)$ in the poloidal (toroidal) case. If we approximate $\Delta c_{\rm s}$ using Eq. 7.7 for models computed with the POL2 EoS, the PCA approximation presents a deviation mostly under $\sim 40\%$.

We note here that the deformation coefficient, $c_{\rm B}$, computed for STT models at the same central density is approximately the same for any value of $\beta_0 \in \{-6, -5.75, -5.5, -5\}$; this happens both for purely poloidal and purely toroidal magnetic configurations. This suggests that it is ultimately the central density that determines the deformation coefficient $c_{\rm B}$ of a NS: the role of the scalar field is that of merely shifting the central density of a model with the same mass to different values with respect to GR. For the same reason, models for STTs computed at a fixed Komar mass have different $c_{\rm B}$: their central density varies with β_0.

A time-varying quadrupolar deformation leads to the emission of GWs. While in GR these are only of tensor nature (i.e. the wave carrier is a spin-2 particle), in the case

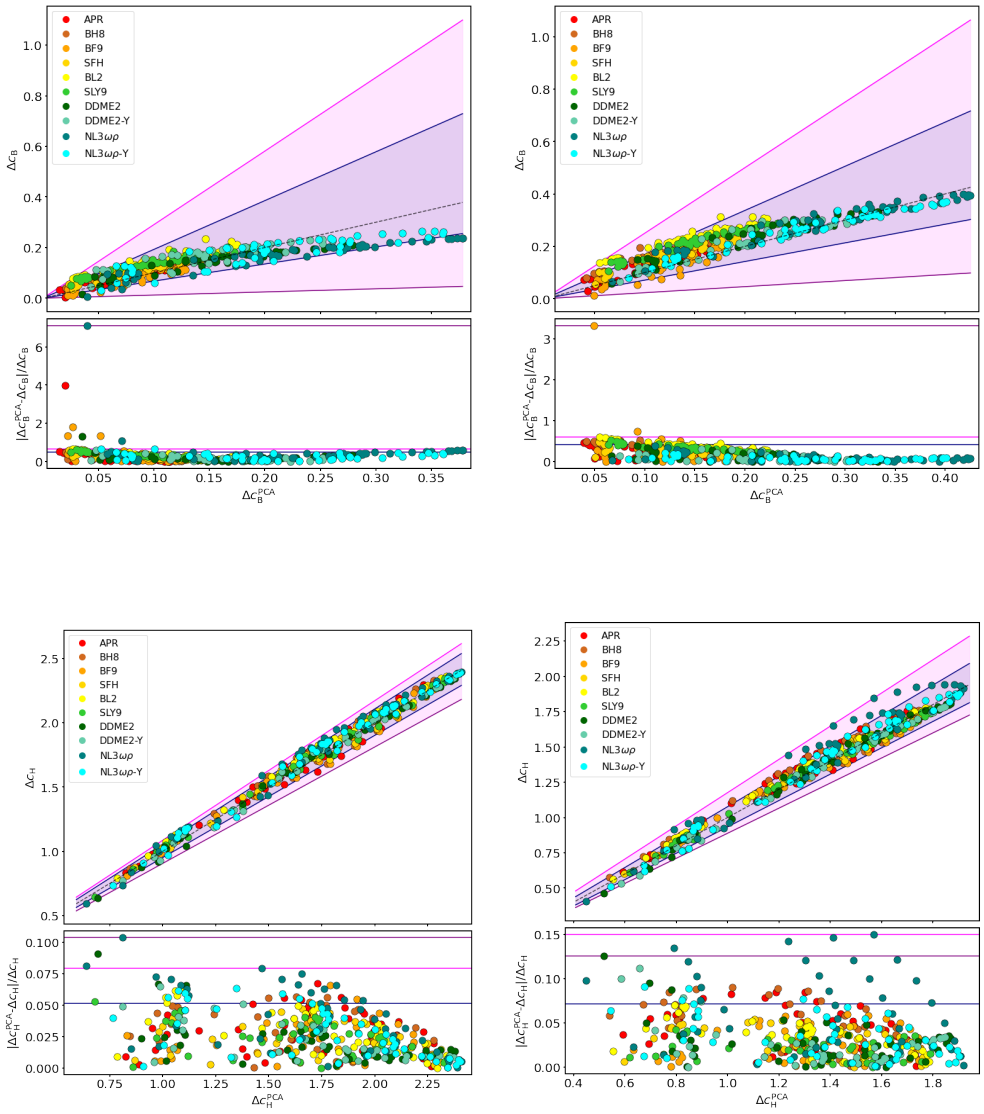

Figure 7.5: Differences $\Delta c_{\rm B}$ (top panels) and $\Delta c_{\rm H}$ (bottom panels) between the distortion coefficients $c_{\rm B}$ and $c_{\rm H}$, calculated according to Eq. 6.2 for STTs, with $\beta_0 \in \{-6, -5.75, -5.5, -5\}$, and the GR relations in Eq. 7.1,7.2, respectively. These are plotted versus $\Delta c_{\rm B}^{\rm PCA}$ and $\Delta c_{\rm H}^{\rm PCA}$and calculated as in Eqs. 7.5,7.6 (top plot in each panel). The corresponding relative deviations from the PCA are given in the bottom plot in each panel. The top left and bottom left panels refer to purely poloidal magnetic fields; the top right and bottom right panels refer to purely toroidal magnetic fields. The dashed line is $\Delta c_{\rm B,H} = \Delta c_{\rm B,H}^{\rm PCA}$. The magenta shaded area comprises all data points and the purple and magenta lines represent the upper and lower bounds of Eqs. 7.5,7.6; the dark blue lines bounding the shaded blue area mark the 90th percentile error region. The EoS are colour-coded, and ordered in the legend, according to the compactness $C = M_{\rm k}/R_{\rm c}$ at $M_{\rm k} = 1.4{\rm M}_\odot$ in GR: red for the highest compactness and blue for the lowest.

of a STT, a scalar channel is also present (whose energy is carried by a spin-0 particle). While the multipolar pattern of the energy carried by tensor GWs cannot contain lower-than-quadrupole modes, scalar GWs can contain any multipolar component. A time-dependent monopolar variation in the structure of a scalarised NS leads to the emission of monopolar waves; being that monopoles rotationally invariant, this cannot happen simply due to the rotation of the NS, but there must also be some kind of radial time-dependent variation [for instance, when the star collapses (Gerosa et al. 2016)]. For this reason, we only focus on quadrupolar modes of GWs, both tensor and scalar in nature. Given that NSs for GR and for STTs can posses rather different quadrupolar deformations (see e.g. Figs. 7.5,7.6), it is interesting to compare the amount of GWs emitted by NS in these two modes. To this end, we recall that the ratio $\mathcal{S}$ (see Eq. 6.7) computed for a NS model measures in which channel that model will emit most quadrupolar GWs, either the tensor ($\mathcal{S} < 1$) or the scalar channel ($\mathcal{S} > 1$). We found that the following quasi-universal relations hold for $\mathcal{S}$:

$$\mathcal{S}^{\rm PCA} = \begin{cases} 1.98^{+0.18}_{-0.05} R_{10}^{-0.71} M_{1.6}^{-0.54} Q_1^{1.22} \text{ for poloidal,} \\ \\ 1.99^{+0.18}_{-0.07} R_{10}^{-0.74} M_{1.6}^{-0.60} Q_1^{1.23} \text{ for toroidal.} \end{cases} \tag{7.8}$$

The values of $\mathcal{S}$, computed through Eq. 6.10 for $\beta_0 \in \{-6, -5.75, -5.5, -5\}$, are plotted in Fig. 7.7, against their PCA approximation, computed via Eq. 7.8. We see that the approximation is quite accurate in both the poloidal and the toroidal case, with a maximum relative error of $\sim 8\%$ in both cases, but mostly concentrated under $\sim 4\%$. We see that the coefficients in Eq. 7.8 are practically identical in the poloidal and the toroidal case; in fact, using the coefficients of the PCA approximation of the toroidal case in the poloidal case leads to an only slightly larger error (around $\sim 1\%$ higher). As we discuss in Sect. 7.4, we believe that this similarity points to the existence of a relation between the mass and trace quadrupoles that does not depend on either the magnetic field geometry or the EoS.

7.3.3 Equations of state containing strange quark matter

As we see in Fig. 7.2, the EoS describing strange quark stars exhibit quite different behaviours in the distortion coefficients than the other EoS, especially with regard to the SQM2 EoS, and even more so in the case of $c_{\rm H}$ in the toroidal case (right panel, bottom plot). Overall, we see that stars described by the SQM2 EoS are more deformable than all of the other EoS, when compared at the same mass. The reason for this is easily seen from the mass-radius relation in Fig. 7.1: at the same mass, strange quark stars described by the SQM2 EoS possess a larger radius, and are thus less compact and more prone to deformation. Instead, the SQM1 EoS, for masses lower than $\sim 1.3 M_\odot$,

is the most compact one; however, we note that while the compactness of an EoS is indeed related to its deformability as defined in Eq. B.14, it is not the only ingredient: the interplay of the internal magnetic field of the star and its density distribution is another effect that plays an important role on how the magnetic field deforms the star structure. Indeed, strange quark stars possess a much 'flatter' density distribution than standard NSs, in which the density gradient is larger. As we anticipated in Sect. 7.3, toroidal models described by the SQM1 and SQM2 EoS show a discontinuity in the magnetic field profile at the surface; since this behaviour leads to a non-vanishing Lorentz force, we caution the reader that these models might not be true equilibria, and thus our results in this case might not be completely accurate. Moreover, we note that the definition of the gravitational binding energy W in Eq. 6.2, being the same for all EoS, does not include the contribution of the QCD vacuum energy: the distortion coefficient, $c_{\rm H}$, we find is the one computed ignoring this additional energy, and is roughly a fraction $W/W^{\rm QCD}$ different from the 'real' coefficient, where $W^{\rm QCD}$ is the binding energy which includes the QCD vacuum. The QCD vacuum energy is expected to have a more important contribution to the binding energy in models which possess a low mass, thus possibly explaining the different behaviour of the SQM2 curve in the bottom plot of the right panel in Fig. 7.2. Due to the extent of these differences, applying the quasi-universal relations we found for standard NSs to the case of SQM1 and SQM2 leads to greater errors: in GR, $c_{\rm B}^{\rm PCA}$ is a factor of $\sim 0.4-0.8$ lower than $c_{\rm B}$ for both purely poloidal and toroidal magnetic fields. For $c_{\rm H}$, using Eq. 7.2 the maximum error increases to $\sim 8\%(\sim 12\%)$ for purely poloidal (toroidal) magnetic fields in the case of SQM1, and $\sim 5\%(\sim 40\%)$ for purely poloidal (toroidal) magnetic fields in the case of SQM2. As for $c_{\rm s}^{\rm PCA}$, it is at most a factor of ~ 1.4 higher than $c_{\rm s}$. For STTs, $\Delta c_{\rm B}^{\rm PCA}$ in the poloidal case is around a factor of ~ 2 lower (higher) than $\Delta c_{\rm B}$ for the SQM1 (SQM2) EoS, excluding a few outlier points; in the toroidal case, it is a factor of ~ 2 lower for both SQM1 and SQM2. For $\Delta c_{\rm H}$, using Eq. 7.6 the maximum error increases to $\sim 30\%(\sim 50\%)$ for purely poloidal (toroidal) magnetic fields, again ignoring few outlier points. In the case of $\Delta c_{\rm s}^{\rm PCA}$, it is around a factor of ~ 1.7 lower than $\Delta c_{\rm s}$.

7.4 EoS and magnetic structure constraints

As argued in Sect. 1.2, among the major uncertainties in NS physics are the EoS and the magnetic field structure of their inner regions. The quasi-universal relations we found may be useful in this sense, given that they are independent of the EoS of standard NSs, thus leaving the NS internal magnetic structure as the only major unknown in GR. We stress that only some of the relations we find may be considered as truly quasi-universal: the approximations $c_{\rm H}^{\rm PCA}, c_{\rm s}^{\rm PCA}, \Delta c_{\rm H}^{\rm PCA}, \Delta c_{\rm s}^{\rm PCA}, \mathcal{S}^{\rm PCA}$ are the most accurate, their errors remaining under 10% for standard NSs. On the other hand, these relations

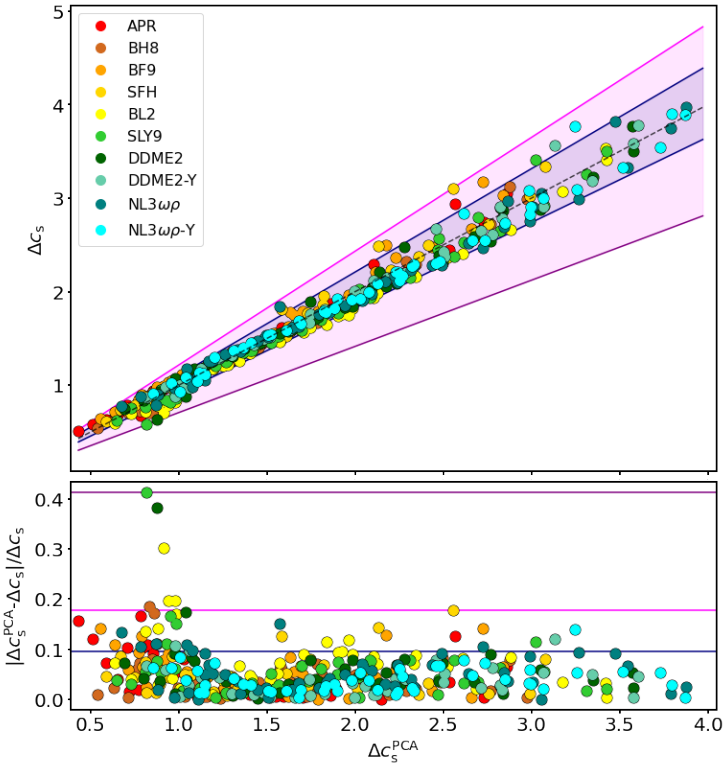

Figure 7.6: Difference, Δc_s, between the distortion coefficient c_s, calculated according to Eq. 7.3 for STTs with $\beta_0 \in \{-6, -5.75, -5.5, -5\}$, and the GR quasi-universal relation in Eq. 7.4. This is plotted versus its approximation $\Delta c_s^{\rm PCA}$, calculated with the relation in Eq. 7.7 (top plot). The corresponding relative deviation from the PCA is given in the bottom plot. The dashed line is $\Delta c_s = \Delta c_s^{\rm PCA}$. The magenta shaded area comprises all data points and the purple and magenta lines represent the upper and lower bounds of Eq. 7.7. The dark blue lines bounding the shaded blue area mark the 90th percentile error region. The EoS are colour-coded, and ordered in the legend, according to the compactness $C = M_{\rm k}/R_{\rm c}$ calculated at $M_{\rm k} = 1.4{\rm M}_\odot$ in GR: red for the highest compactness and blue for the lowest compactness.

in the case of the POL2, SQM1 and SQM2 EoS, or the approximations $c_{\rm B}^{\rm PCA}$ and $\Delta c_{\rm B}^{\rm PCA}$ in all cases, are less accurate and for this reason their range of applicability is smaller. In particular, the most promising relation is that of c_s. On the one hand, c_s can be computed from its definition Eq. 7.3 if one is able to measure both the magnetic field strength at the surface of the NS, B_s, and its quadrupolar deformation e. The latter is in turn inferable from the strain of CGWs emitted by the NS, $h_0 \propto eI$, where I is the moment of inertia of the NS along its rotation axis, which must be unaligned to its magnetic axis. The moment of inertia, I, is a function of the NS mass and radius,

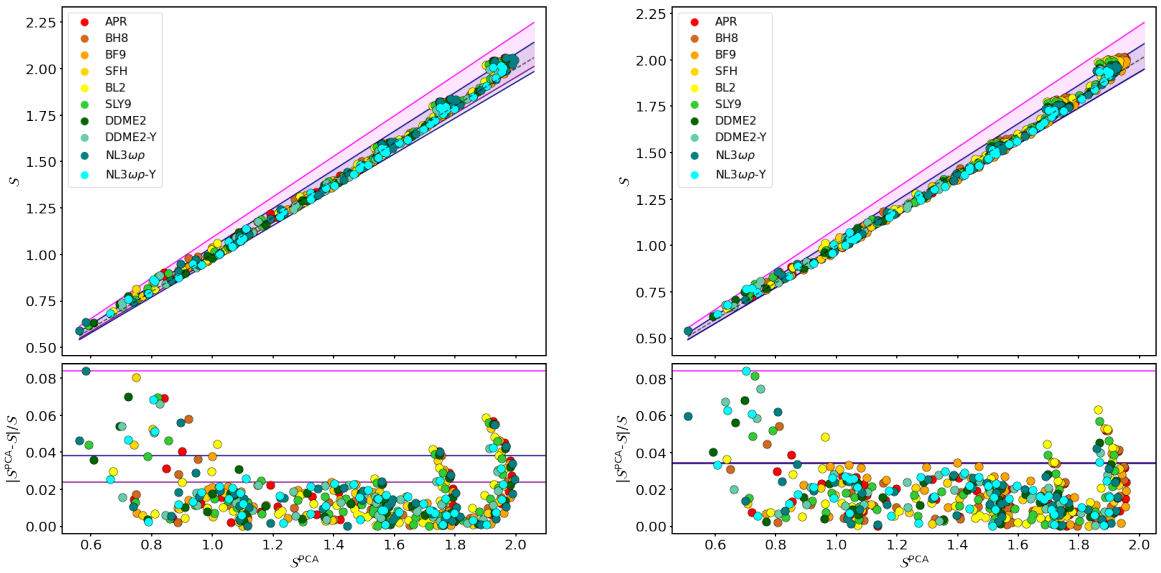

Figure 7.7: Ratio $\mathcal{S}$ between scalar and tensor quadrupolar GW losses, calculated according to Eq. 6.10 for STTs with $\beta_0 \in \{-6, -5.75, -5.5, -5\}$. This is plotted versus its approximation $\mathcal{S}^{\rm PCA}$, calculated with the quasi-universal relations in Eq. 7.8 (top plot in each panel). The corresponding relative devitations from the PCA are given in the bottom plot in each panel. The left panel refers to a purely poloidal magnetic field; the right panel refers to a purely toroidal magnetic field. The dashed line is $\mathcal{S} = \mathcal{S}^{\rm PCA}$. The magenta shaded area comprises all data points and the purple and magenta lines represent the upper and lower bounds of Eq. 7.8. The dark blue lines bounding the shaded blue area mark the 90th percentile error region. The EoS are colour-coded, and ordered in the legend according to the compactness $C = M_{\rm k}/R_{\rm c}$ calculated at $M_{\rm k} = 1.4{\rm M}_\odot$ in GR: red for the highest compactness and blue for the lowest compactness.

and, in principle, it depends on the EoS. However, Breu & Rezzolla (2016)[6] have found that an EoS-independent relation between I, the NS mass and its radius exists. On the other hand, Eq. 7.4 allows us to estimate $c_{\rm s}^{\rm PCA}$ by knowing just the NS mass and radius (see Fig. 7.8, where a few $c_{\rm s}^{\rm PCA} = $ const. isolines are plotted). Thus, three possible informative scenarios may arise:

1. $c_{\rm s} < c_{\rm s}^{\rm PCA}$ and I is computed with the EoS-independent relation by Breu & Rezzolla (2016): the only assumption made is that of a very specific purely poloidal

[6]We note that the moment of inertia I used in Breu & Rezzolla (2016) is defined as the ratio of the angular momentum to the angular velocity, and is different from the definition of $I_{zz,xx}$ we use in this work, which is Newtonian. While the two moments of inertia can differ, it was found that the quadrupolar deformation e defined as in Eq. B.14, being a ratio, is very similar in both regimes (Pili et al. 2015).

magnetic field permeating the NS. In this case, the deformation coefficient is reduced by the presence of a toroidal component, which counteracts the deformation of the poloidal one. The strength of the toroidal component increases with respect to the poloidal one the larger c_s deviates from c_s^{PCA}.

2. $c_s > c_s^{PCA}$ and I is computed with the EoS-independent relation by Breu & Rezzolla (2016): Since the star is more deformed than what the extremal case of a purely poloidal field can produce, there must be another source of deformation other than the magnetic field .

3. $c_s > c_s^{PCA}$ and I is computed by assuming an EoS: either there is another source of deformation, other than the magnetic field, or the assumed EoS in not consistent, because it predicts a moment of inertia, I, that is not compatible with the deformation coefficient of the star.

If $c_s < c_s^{PCA}$ and I is computed by assuming an EoS, not much can be said without further information because both the magnetic field geometry and the EoS are assumed. We stress that our analysis, and thus the three informative scenarios just described, are valid in the case of a purely poloidal magnetic configuration that satisfies the criterion for equilibrium in the Bernoulli formalism: different magnetic configurations should be explored to possibly strengthen our conclusions, even if it is not clear whether purely poloidal equilibria that significantly differ from the one we have adopted do exist. To recap, once the quantities M_k, R_c of a NS are measured, a point in the mass-radius diagram Fig. 7.8 can be placed. On the one hand, its deformation coefficient c_s can be computed if one is able to measure also the quantities h_0, B_s; on the other hand, c_s^{PCA} is computed from Eq. 7.4, corresponding to a certain isoline in Fig. 7.8. Depending on whether $c_s < c_s^{PCA}$ or $c_s > c_s^{PCA}$ and on whether one has computed the NS moment of inertia I through the EoS-independent relation of Breu & Rezzolla (2016) or by assuming an EoS, various conclusions on the NS internal magnetic structure or on the consistency of the EoS can be asserted. We recall here that, as we explained in Sect. 2.2, all quantities are measured in the J-frame, that is the physical frame. Once a quantity is measured, it then can be converted to the E-frame through the conformal factor $\mathcal{A}$.

Similar conclusions can be drawn if one considers the other two deformation coefficients, c_B and c_H, instead of c_s, with the caveat that these quantities are defined also for purely toroidal magnetic fields and require one to be able to measure the maximum strength of the magnetic field, B_{max}, or the ratio $\mathcal{H}/W$, respectively. However, such quantities are much less likely to be measured than the magnetic field at the surface. Moreover, the applicability of the relation for c_B^{PCA} remains more contained due to the larger error in the approximation of the real distortion coefficient. For this reason, relations Eqs. 7.1,7.2 may be more useful to constrain B_{max} or $\mathcal{H}/W$ themselves. More

specifically, $B_{\rm max} \approx (e/c_{\rm B})^{1/2}$ and $\mathcal{H}/W \approx e/c_{\rm H}$; given that $c_{\rm B,H} < c^{\rm PCA}_{\rm B,H}$, once the NS mass and radius are known, it is possible to estimate a lower bound for both $B_{\rm max}$ and $\mathcal{H}/W$ by using the quasi-universal relations found in the purely poloidal and purely toroidal case. We note that the relations for $c_{\rm B}$ and $c_{\rm H}$, as well as that of $c_{\rm s}$, are in any case useful for the purpose of numerical simulations and theoretical estimations, allowing us to quickly and easily determine the distortion coefficients from the mass and radius of a model – without going through a full numerical simulation.

In STTs, the scalar charge is also unkown. As discussed in Sect. 1.2, some of the effects of changing the NS EoS are degenerate with the presence of a non-negligible scalar charge. For this reason, the relations in Eqs. 7.5,7.6,7.7 may help us to understand whether a distortion coefficient inferred from observations, via the relations in Eqs. 6.2,7.3, is compatible with a non-zero scalar charge of the observed NS, independently from its EoS. To this end, the relation in Eq. 7.8 may prove to be more promising because it does not require any knowledge of the strength of the magnetic field. In particular, since Eq. 7.8 is essentially the same in both poloidal and toroidal magnetic configurations, it is possible that $\mathcal{S}$ is independent of the magnetic field altogether. In this case $\mathcal{S} \approx \mathcal{S}^{\rm PCA}$, and the observation of CGWs from a given source of known mass, radius, distance d and spin period P translates into an upper bound for a function of the scalar charge: $g(Q_{\rm s}, q_{\rm s}) < f(M_{\rm k}, R_{\rm c}, d, P, h_0^{\rm min})$, where $h_0^{\rm min}$ is the sensitivity of a given GW detector at the frequency $2/P$ and $g(Q_{\rm s}, q_{\rm s})$ is zero for a non-scalarised NS.

Next, we comment on how our results compare to the previous findings of Cutler (2002). There, the author found that in Newtonian theory, for an incompressible, constant-density NS, the distortion coefficient $c_{\rm H} = 15/4 \sim 3.75$ in the case of a purely toroidal magnetic field, while it is $c_{\rm H} \sim 15/2 \sim 7.50$ for a purely poloidal model. As we showed in Fig. 7.2, we found that $c_{\rm H}$ ranges from ~ 2 to ~ 3 (from ~ 2.5 to ~ 4) for toroidal (poloidal) models. Therefore, by using the constant coefficients of Cutler (2002), found under some simplifying assumptions, one would find a $c_{\rm H}$ that is a factor of $\sim 1.25 - 1.88 (\sim 1.88 - 3.00)$ higher than our estimates; this could in part be the result of having different magnetic field geometries, in turn stemming from different assumptions on the NS structure. Finally, as explained in Frieben & Rezzolla (2012), when considering a NS with a superconducting core, one expects to find an increase in $c_{\rm H}$, with respect to a non-superconducting star, which is roughly a factor of $\langle B B_{\rm c1} \rangle / \langle B^2 \rangle$, where B is the magnitude of the magnetic field, $B_{\rm c1} \approx 10^{15}$G is the first critical magnetic field strength and $\langle \dots \rangle$ indicates volume average. This is valid only as a first approximation for $\langle B \rangle < 10^{15}$G. Thus, in this limit, for superconducting models, we expect to find distortion coefficients that are roughly a factor of $B_{\rm c1}/\langle B \rangle$ higher than what we found.

7.5 Discussion

In the work presented in this chapter, we explore the relation among the magnetic deformability and the main observable quantities of NS models described by a variety of different EoS allowed by observational and nuclear physics constraints. We did so in the case of static, axisymmetric configurations endowed by specific choices of either purely poloidal or purely toroidal magnetic fields based upon two different theories of gravitation: GR and a massless STT containing the spontaneous scalarisation phenomenon. We used 12 different EoS which satisfy the latest astrophysical and nuclear physics constraints, plus a polytropic law that has been widely used in the literature. These EoS span a wide range of calculation methods and particle contents, ranging from zero-temperature to finite-temperature ones, from nucleonic EoS to those containing hyperons or quark degreees of freedom; moreover, we considered two EoS that are capable of describing strange quark stars.

We first obtained the distortion coefficients which describe the magnetic deformation of NSs in the limit of non-extreme magnetic fields, that is, when the quadrupolar magnetic deformation of the star follows a quadratic law with the magnetic field magnitude. In particular, we studied three different coefficients by parametrising the quadrupolar deformation of our models with their maximum magnetic field strength, their magnetic energy to gravitaitonal binding energy ratio, and their superficial magnetic field strength: $c_{\rm B}$, $c_{\rm H}$, and $c_{\rm s}$ respectively. While the first two may be most useful for the purpose of computing the deformation of NS models without going through a full numerical simulation, the latter may be of help in constraining the magnetic properties in NS interiors. We find that while $c_{\rm H}$ varies by a maximum factor of 1.5 among all the models we studied, $c_{\rm B}$ and $c_{\rm s}$ exhibit a much stronger dependence on the NS mass. Moreover, the behaviour of $c_{\rm B,H}$ is qualitatively similar for poloidal and toroidal configurations. Since the polytropic EoS POL2 and the strange quark matter EoS SQM1 and SQM2 exhibit a radically different behaviour with respect to all other EoS, we focus mainly on the ten EoS - allowed by the observations - describing standard NSs.

Subsequently, we looked for relations among the three coefficients, the NS Komar mass, and their circumferential radius; in the case of STTs, we also consider the dependence on their scalar charge. Specifically, we are most interested in EoS-independent relations, or quasi-universal relations. We find that there are equations at hand to describe the distortion coefficients in term of the NS mass, radius, and scalar charge (in STTs) that are valid for all the ten standard EoS to a satisfying level of accuracy. These relations have a simple form, consisting only of power laws or polynomials. We find that these relations can be applied also to the case of the POL2, SQM1, and SQM2 EoS, but with a (sometimes significantly) reduced accuracy. This is due to a number of reasons: the POL2 EoS is a simple polytrope, which we include only for reference, and it

lacks all the facets of various particle contents that are described by the other EoS; the SQM1 and SQM2, instead, describe a different type of star, which is predicted to exist - in which case it would help to solve a number of problems regarding NS astrophysics - but one that possesses a radically different structure than a standard NS. In particular, the density profile throughout quark stars is nearly flat, with a discontinuity at the surface: this leads, in some cases, to a discontinuity in the toroidal magnetic field at the star surface, thus rendering these models not accurate in terms of a true equilibria. Moreover, strange quark stars are able to sustain very large masses with large radii, leading to a magnetic deformation that is, in general, higher than that of standard NSs. Finally, we do not consider the contribution of the QCD vacuum energy to the binding energy of our models.

In the case of STTs, we find other quasi-universal relations linking the mass, radius, and scalar charge of the NS to the ratio of the scalar-to-tensor GWs strain, $\mathcal{S}$. We find that $\mathcal{S}$ is, within the numerical accuracy of our code, well approximated by a single expression, $\mathcal{S}^{\rm PCA}$, both in the purely poloidal and purely toroidal cases. This suggests that $\mathcal{S}$ may be a quantity which is independent of the magnetic field altogether, although this point should be better addressed by simulations involving NS models endowed with mixed fields.

The quasi-universal relations we find depend on potentially observable quantities. In particular, by knowing the NS mass and radius, it is possible to directly compute its distortion coefficients as predicted by the relations we found, which are valid in the case of purely poloidal or purely toroidal magnetic fields. By comparing such values with those we computed through the definitions Eqs. 6.2,7.3, we can infer information on the magnetic structure hidden in the NS interior. This is possible because the pure magnetic configurations we consider are extremal, in the sense that purely poloidal and purely toroidal magnetic fields act on the quadrupolar deformation of the NS in an opposite way; as such, a pure configuration exerts the maximum deformation on a NS, while deviations from this case may imply a different magnetic configuration than the one we assume. Since only the superficial magnetic field is accessible through direct observations, we expect the relation regarding $c_{\rm s}$, Eq. 7.4, to be the most useful in this sense. However, Eqs. 7.1,7.2 may also show their utility for computing the distortion coefficients of a NS model by knowing only its mass and radius, without going through a full numerical simulation. We stress that only specific choices of purely poloidal and toroidal magnetic configurations have been investigated, and different choices of the magnetisation functions should be explored to possibly strengthen our conclusions.

The relation involving $\mathcal{S}$, namely, Eq. 7.8, along with the considerations we described regarding pure magnetic configurations, translates into an upper bound on the scalar charge of a NS whose mass, radius, and quadrupolar deformation are known. For this

reason, it may be useful in constraining the theory of gravity.

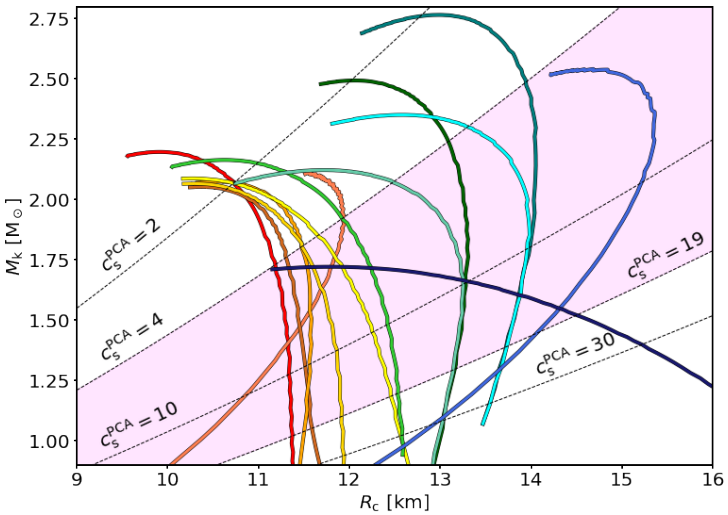

Figure 7.8: Komar mass M_k against circumferential radius R_c for un-magnetised, static models of NSs computed with the EoS described in Sect. 7.1 in GR. The EoS are colour-coded, and ordered in the legend, according to the compactness $C = M_k/R_c$ calculated at $M_k = 1.4M_\odot$ in GR: red for the highest compactness and blue for the lowest compactness. The black dashed lines denote $c_s^{PCA} = \text{const.}$ isolines. The two values $c_s^{PCA} = 4 - 19$ containing the magenta highlighted area are those found in the case of the example in Sect. 7.5.

We note that in order to obtain the quadrupolar deformation of an isolated NS, it is necessary to detect CGWs emitted by them. While this is within the scope of current GW observations [see e.g. Abbott et al. (2021b), where it is suggested that the particular spin-down and glitch behaviour of pulsar PSR J0537-6910 ought to be attributed to the emission of CGWs], no signature has been found yet. We can use the quasi-universal relations we found to assess the detectability of known NSs. For example, using Eq. 7.4 and the quasi-universal relation for I found by Breu & Rezzolla (2016), we can set limits on the minimum surface magnetic field strength B_s^{min} that produces a deformation leading to detectable CGWs. Using the distance $d = 0.16$kpc and rotation period $P = 5.758$ms of the closest known millisecond pulsar [J0437-4715, see Manchester et al. (2005)], which has a mass of $1.44M_\odot$, and taking a radius in the range of $10 - 14$km (corresponding to $c_s^{PCA} = 4 - 19$ respectively, see Fig. 7.8), we find $B_s^{min} = 1.4 \times 10^{13} - 4.1 \times 10^{13}$G for a 2 year long observation with the advanced LIGO detector (aLIGO), $B_s^{min} = 8.6 \times 10^{12} - 2.6 \times 10^{13}$G for a 1 month long observation with the advanced Einstein Telescope (ET) detector, $B_s^{min} = 4.3 \times 10^{12} - 1.3 \times 10^{13}$G for a two-year long observation with ET.

When considering NSs endowed with a superconducting core, as previously explained,

the effective magnetic field entering the distortion coefficients increases, which reflects in a lower B_s^{min}: $B_s^{min} = 1.8 \times 10^{11} - 1.6 \times 10^{12}$G for a two-year long observation with aLIGO, $B_s^{min} = 7.4 \times 10^{10} - 6.6 \times 10^{11}$G for a one-month long observation with ET, $B_s^{min} = 1.8 \times 10^{10} - 1.6 \times 10^{11}$G for a two-year long observation with ET. We note that these values are found in the best case scenario, namely, when the magnetic and the rotation axes are orthogonal and the latter points towards the observer. These values, while they are not unrealistically high, they are, in the best case, about one order of magnitude larger than the average surface dipole magnetic fields measured in millisecond pulsars (Cruces et al. 2019). However, such measured values may be low because of a variety of reasons, ranging from screening due to accreted matter (Romani 1990) to ambipolar diffusion (Cruces et al. 2019). Since the magnetic field producing the distortion in Eq. 7.3 is the one below any accreted material, namely, the un-screened one, the possibility of the magnetic deformation producing CGWs that would be detectable by future GW detectors may be more promising. In the case of millisecond magnetars, the surface magnetic field is expected to be on the order of $\sim 10^{14-15}$G (Dall'Osso & Stella 2021), which would significantly enhance the possibility of their detection by CGWs emissions.

In the work presented in this chapter, we focus only on the quadrupolar deformation of NSs due to either purely poloidal or purely toroidal magnetic fields. While we expect that mixed-fields configurations, such as the twisted-torus one, yield deformations contained between the limiting values we found in the pure cases we studied (and, thus, distortion coefficients which are smaller than those we found), this point should be better addressed by numerical simulations containing mixed-fields geometries. We stress that although only very special configurations have been investigated and, therefore, the results we find can probably only give order-of-magnitude estimates for other magnetic field structures, the dependence on stellar parameters might be universal, and this aspect could be investigated with other examples. We recall that the only known formalism to compute equilibria in the full non-linear regime is through the approach we use, that is, through the use of the generalised Bernoulli integral, which sets severe constraints on the possible magnetic field geometry. As an example, poloidal configurations are dominated by the dipole term, but also contain higher order multipoles. It has been found (Mastrano et al. 2013) that higher order multipoles can contribute to the magnetic energy even more than the dipole field, consequently increasing the deformation and, thus, the detectability of these systems. Moreover, it is expected that at least some NSs contain also higher-multipole magnetic fields, due to a mismatch between the surface magnetic field strength obtained by observed X-ray spectra and the inferred dipole field (Güver et al. 2011). It would also be interesting to understand whether a quasi-universal relation like those we find exists also for the quadrupole deformation e, without expanding it in terms of the distortion

coefficients.

Finally, while we opted for the PCA algorithm to search for simple relations between the physical quantities of interest, it would be interesting to use a different technique, for instance, autoencoders; with the main difference being that the former looks for linear relations in the data, while the latter is a generalisation to non-linear maps. This means that while we must adopt some analytical form of the relation we wish the PCA to find, more freedom is allowed via the application of autoencoders.

Chapter 8

Detectability of continuous gravitational waves from magnetically-deformed neutron stars

The results shown in this chapter have been submitted as the paper Soldateschi & Bucciantini (2021).

In this chapter we apply our recent results (SBD20; SBD21; SBD21EOS) (see Chaps. 5-7) regarding a quasi-universal relation linking the NS mass, radius, magnetic deformation and surface magnetic field both to the case of the Galactic pulsar population as contained in the ATNF catalogue (Manchester et al. 2005) and simulated through a population synthesis approach. In particular, we assess the detectability of CGWs through the use of GW detectors, showing that a significant fraction of the MSP population in the Galaxy may be observable even with existing detectors when they reach their design sensitivity, while canonical pulsars seem to be beyond the reach even of 3rd generation ones.

This chapter is structured as follows. In Sect. 8.1 we introduce the problem of computing the CGWs strain emitted by NSs in the Galaxy and the approach we used to simulate the Galactic NSs population. In Sect. 8.2 we present our results in relation to the possibility of detection by GW observatories. Finally, we discuss our results in Sect. 8.3.

8.1 Gravitational waves by the neutron stars population in the Galaxy

The CGWs strain h_0 emitted by a NS rotating with frequency $f_{\rm rot}$, at distance d from the detector is

$$h_0 = \frac{16\pi^2 G}{c^4}\frac{\mathcal{Q} f_{\rm rot}^2}{d} \,, \tag{8.1}$$

where G is Newton's gravitational constant, c the speed of light, and $\mathcal{Q}$ is the quadrupole moment. The quadrupole moment can be written as the product of the relativistic moment of inertial $\mathcal{I}$ times the quadrupolar deformation of the NS, e. We recall that in the Newtonian limit, when the deformation is caused by a purely poloidal magnetic field, the shape of the NS is axisymmetric, and e is given by Eq. B.14:

$$e = \left| \frac{I_{\rm zz} - I_{\rm xx}}{I_{\rm zz}} \right| \tag{8.2}$$

where $I_{\rm xx}$, $I_{\rm zz}$ are the moments of inertia of the NS, computed in the Newtonian limit, and the z axis is the symmetry axis of the system (see App. B). It was shown that the Newtonian value of e is a good approximation for the correct GR one (Pili et al. 2015). We have found (SBD21; SBD21EOS) that, for typical magnetic fields of NSs, the magnetic deformation e of a NS is well approximated by the formula Eq. 7.3

$$e \approx c_{\rm s} B_{\rm s}^2 \,, \tag{8.3}$$

where $B_{\rm s}$ is the surface magnetic field at the pole, in units of 10^{18}G, and $c_{\rm s}$ is called 'distortion coefficient'. Moreover, we have found, by computing $\sim$ 65000 full GR, multi-dimensional axisymmetric magnetised equilibrium models of NSs with the `XNS` code (Bucciantini & Del Zanna 2011; Pili et al. 2014; SBD20), that $c_{\rm s}$ can be approximated with great accuracy by the quasi-universal relation Eq. 7.4:

$$c_{\rm s} = 2.97 R_{10}^{4.61} M_{1.6}^{-2.80} \,, \tag{8.4}$$

where $R_{10} = R_{\rm c}/10{\rm km}$, $M_{1.6} = M/1.6{\rm M}_\odot$, and $R_{\rm c}$ and M are the circularisation radius and the Komar mass of the NS, respectively (see Gourgoulhon 2010 and Gourgoulhon 2012 for their definition). Incidentally, we remark that it is not the energy of the magnetic field per se that directly gives a gravitational quadrupole, but the oblate/prolate distortion that magnetic pressure and tension produce in the matter distribution inside the NS. This holds for several EoS that satisfy current observational and particle physics constraints, computed according to various techniques and with different particle contents. We have found that this approximation holds also for two EoS describing strange quark stars, although with a smaller accuracy, and for this reason we do not consider those EoS here. Moreover, it was previously found (Breu & Rezzolla

2016) that also the GR moment of inertia $\mathcal{I}$ is well approximated by a function of just the mass and radius of the NS, for a large sample of EoS. Then, if the rotation frequency, distance, surface magnetic field, mass and radius of a NS are known, one can estimate the strain of CGWs that it should emit, independently of the EoS. However, the radii of NSs are a notoriously difficult quantity to measure, and for this reason we chose to consider the two EoS which give the most different radii among the ones we studied [the APR4 (Akmal et al. 1998; Typel et al. 2013) and the NL3$\omega\rho$ (Horowitz & Piekarewicz 2001; Fortin et al. 2016)], and use them to calculate the radii of the NSs from their mass. With this approach, we expect that the results obtained by considering other EoS should be contained within the limits we find in these two cases.

In the following we present the results obtained from two different approaches: case study A and case study B. In case A we generate a population of NSs with the following characteristics. The mass is sampled from a bimodal Gaussian distribution by (Antoniadis et al. 2016), whose peaks are located at $1.396M_\odot$ and $1.84M_\odot$. The magnetic field is sampled from a log-normal distribution (Faucher-Giguère & Kaspi 2006) with a mean of $10^{12.65}$G. While this distribution is consistent with the observations of canonical pulsars contained in the ATNF catalogue, magnetic fields in MSPs are observed to have much lower values. A possible explanation for this is that the actual magnetic field of MSPs, which distorts their shape, is somehow hidden from observations, either through an accretion process (Bisnovatyi-Kogan & Komberg 1974; Romani 1990) or due to ambipolar diffusion (Cruces et al. 2019). In order to avoid possible selection biases, we chose to generate also the magnetic field of canonical pulsars, even if their magnetic field have been measured. In fact, NSs in the ATNF catalogue tend to have a slightly lower magnetic field than predicted by the aforementioned distribution, possibly due to the fact that pulsars with a stronger magnetic field shut off radio emission more rapidly and have a lower chance of being detected. The rotation frequency and the distance are taken from the ATNF catalogue (Manchester et al. 2005). This sample consists of 2796 NSs, that is the present number of NSs contained in the ATNF catalogue minus few records whose period or distance are missing. Their position in the Galaxy can be seen in Fig. 8.1. Case study B consists of a generated population of 10^4 NSs, which allows us to sample the strain distribution of pulsars with enough statistical accuracy. The mass is computed through three possible Gaussian bimodal mass distributions: the same as in case A (Antoniadis et al. 2016); another one peaked at $1.34M_\odot$ and $1.78M_\odot$, with a maximum mass cutoff at $2.9M_\odot$ (Alsing et al. 2018); a third one peaked at $1.34M_\odot$ and $1.47M_\odot$(Farrow et al. 2019). The magnetic field, as before, is sampled from a log-normal distribution (Faucher-Giguère & Kaspi 2006). The rotation frequency is computed by fitting the frequency distribution of the ATNF pulsars and then sampling from it; the position is computed by sampling nine different possible distributions (Narayan 1987; Lorimer et al. 1993, 2006; Kiel & Hurley 2009; Faucher-

Giguère & Loeb 2010; Lorimer 2012; Grégoire & Knödlseder 2013; Hooper et al. 2013; Ronchi et al. 2021). Thus, we considered a total of 28 different populations. We note that both the surface magnetic field strength contained in the ATNF catalogue and the one sampled from the expected distribution are computed from the spin-down formula in the case of orthogonal spin and magnetic axii, while B_s in Eq. 7.3 is that at the pole. For this reason, both the magnetic field taken from the catalogue and that sampled from the distribution need to be multiplied by a factor of 2. Moreover, we note that the strain of the plus and cross polarisations $h_{+,\times}$ of CGWs emitted at twice the rotation frequency of the NS contain a factor $\sin^2\alpha$, where α is the angle between the spin and magnetic axii (Bonazzola & Gourgoulhon 1996). By using the magnetic field induced deformation Eq. 7.3 and generating a magnetic field corresponding to that of the spin-down formula, one can obtain $h_{+,\times}$ without needing to specify the inclination angle α, because the factor $\sin^2\alpha$ gets simplified.

8.2 Detectability of continuous gravitational waves

In Fig. 8.2 we can see the predicted strain of CGWs emitted by the NSs contained in the ATNF catalogue (case study A). Each point denotes a specific NS in the catalogue, its position on the $x-$axis being the frequency at which it emits CGWs, that is twice its rotation frequency. The colour of the points indicates which EoS has been assumed to calculate the NS radius from its mass, either the APR (red points) or the NL3$\omega\rho$ (blue points). The lines are the minimum detectable strain of the advanced LIGO (aLIGO) detector at design sensitivity[1] (green lines), expected to be achieved during the O4 observing run (Buikema et al. 2020), and of the Einstein Telescope (ET) detector in the D configuration[2] (black lines) (Hild et al. 2011). The solid lines are the nominal sensitivity curves, while the dot-dashed and dashed lines are the minimum detectable strain in the case of continuous 1 month and 2 years observation time, respectively. For a search over time T, the minimum detectable strain by a ground-based interferometer is (Watts et al. 2008)

$$h_0 \approx 11.4\sqrt{\frac{S_n}{T}}\,, \tag{8.5}$$

where S_n is the power spectral density of the detector noise (thus $\sqrt{S_n}$ is the nominal sensitivity curve for the detectors plotted in Fig 8.2.). As can be seen from Fig. 8.2, there are two main NSs populations contained in the ATNF catalogue, that is MSPs, emitting CGWs at a frequency $f \gtrsim 50$Hz, and canonical pulsars. We see that CGWs emitted by MSPs have a much larger strain, making them potentially observable by both aLIGO

[1]The aLIGO design densitivity curves can be found at `https://dcc.ligo.org/LIGO-T1800044/public`.

[2]The ET sensitivity curves can be found at `http://www.et-gw.eu/index.php/etsensitivities`.

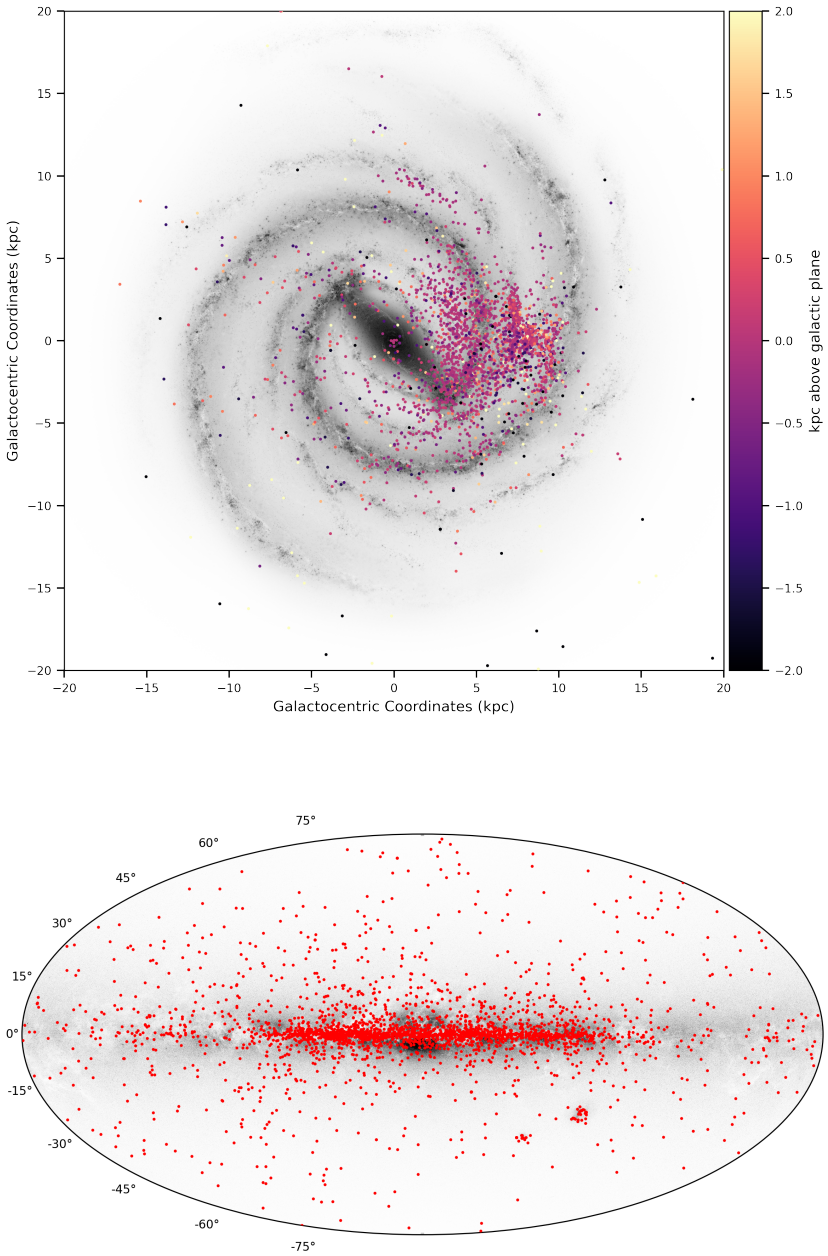

Figure 8.1: Face-on (top plot, in galactocentric coordinates) and edge-on (bottom plot, in ICRS coordinates) rendition of the Galaxy along with the position of the NSs contained in the ATNF catalogue (case study A). The color scale in the top plot was capped at ± 2 kpc for ease of visualisation. These plots were made using the `mw-plot` Python package: `https://pypi.org/project/mw-plot/`.

and ET with 1 month to 2 years observing time. Moreover, the only assumption regarding the EoS, that is used to compute the radii of the considered NSs, has the effect of increasing the strain by a factor of 2 to 9 when using the NL3$\omega\rho$ EoS instead of the APR EoS. On the other hand, canonical pulsars seem to be mostly invisible to even 3rd generation detectors.

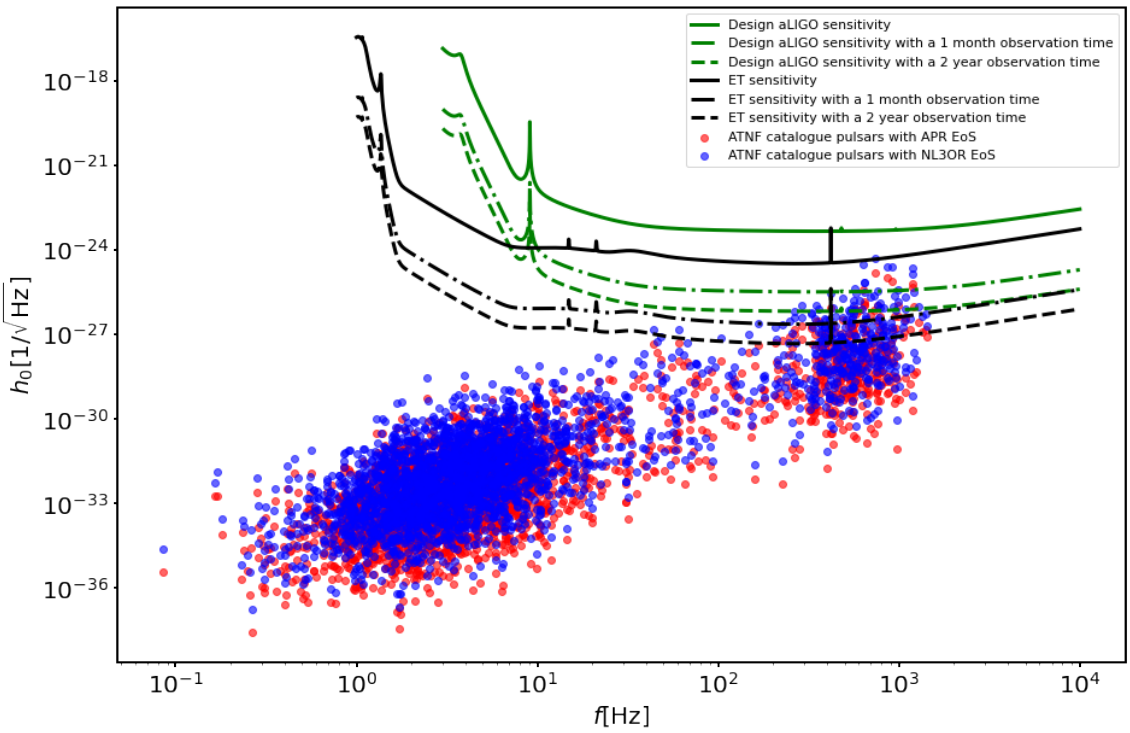

Figure 8.2: Strain of CGWs emitted by the pulsars contained in the ATNF catalogue. Each point is a specific NS in the catalogue, and its position on the $x-$axis denotes the frequency of the emission of CGWs. The colour of the points indicates which EoS has been assumed to calculate the NS radius from its mass, either the APR (red points) or the NL3$\omega\rho$ (blue points) EoS. The solid lines are the sensitivity curves of the aLIGO (green line) and ET detectors (black line). The dot-dashed and dashed lines are the minimum detectable strain by aLIGO (green lines) and ET (black lines) in the case of a continuous 1 month (dot-dashed lines) and 2 years (dashed lines) observation time.

Since sampling from the expected distributions of mass and magnetic field has the effect of randomly changing the strain when generating different populations, we generated another population consisting of case A randomly repeated 10 times: for each NS in the catalogue, with its fixed rotation frequency and distance, we extracted 10 random samples from the mass and magnetic field distributions, effectively generating a population of 55920 NSs (27960 NSs for each of the two EoS). Then, we used a

Gaussian kernel density estimation (KDE) procedure to estimate the probability density function of this population. The results are plotted in Fig. 8.3. The red contour plot is the probability density function associated to the generated NS population, while the two distribution on the top and right axii are the marginal distributions. The green and black lines are the sensitivity curves of the aLIGO and ET detectors, as in Fig. 8.2. The green and black points denote the minima of these curves, and the green and black lines on the axis on the right refer to the values of these minima. The fraction of the NS population that is above those lines is potentially observable with the given instrument and observing time. In particular, using the aLIGO detector with a 1 month (2 years) observation time, $\sim$ 3% ($\sim$ 9%) of the MSP population could be detected; instead, by using the ET telescope with a 1 month (2 years) observation time, $\sim$ 16% ($\sim$ 32%) of the MSP population could be detected. In any case, canonical pulsars seem to be out of both detectors' range. We note that these results are to be considered as the most optimistic case, as they are derived under the assumption of a purely poloidal field: if a toroidal component is present, the NSs magnetic deformation is smaller with respect to the case of a pure geometry, resulting in a lower detection rate. Since the pulsars we studied in case A have a corresponding name and entry in the ATNF catalogue, we estimated the probability of detection of the 5 most promising ones. In order to do so, we chose the 5 NSs, described by the NL3$\omega\rho$ EoS, with the largest median strain computed by considering 100 realisations of each. Then, we computed a KDE and estimated the probability of detection by aLIGO with a 1 month and 2 years observation time. The results are reported in Tab. 8.1.

In order to compute the strain of a more numerous samples of NSs, we consider the case study B, where we generate a population of 10^4 NSs. This sample size allows us to sample the strain distribution of pulsars with a sufficient statistical accuracy. We found that all the combinations of mass and position distributions give similar results regarding the strain distribution. For this reason, in the following we show only the combinations of one mass distribution [the same as in case A (Antoniadis et al. 2016)] and two position distributions (Lorimer et al. 2006; Kiel & Hurley 2009), denoted in the following as case B1 and case B2, respectively. In the first case the radial distribution of NSs on the Galactic plane is given by a gamma distribution peaked at $\sim$ 5.0 kpc from the Galactic centre [model C in the paper (Lorimer et al. 2006)], while the distribution of their height with respect to the Galactic plane is given by an exponential distribution with a scale height of 330 pc (model S in the paper). In the second case, the radial distribution is that of NSs at birth (Yusifov & Küçük 2004), shaped as a gamma distribution peaked at $\sim$ 6.2 kpc from the Galactic centre, while the height at birth is given by a uniform distribution between 150 pc and -150 pc [model C' in the paper (Kiel & Hurley 2009)]. We note that we considered two very different NSs populations - an evolved population (case B1) and a population at birth (case B2) - because our results

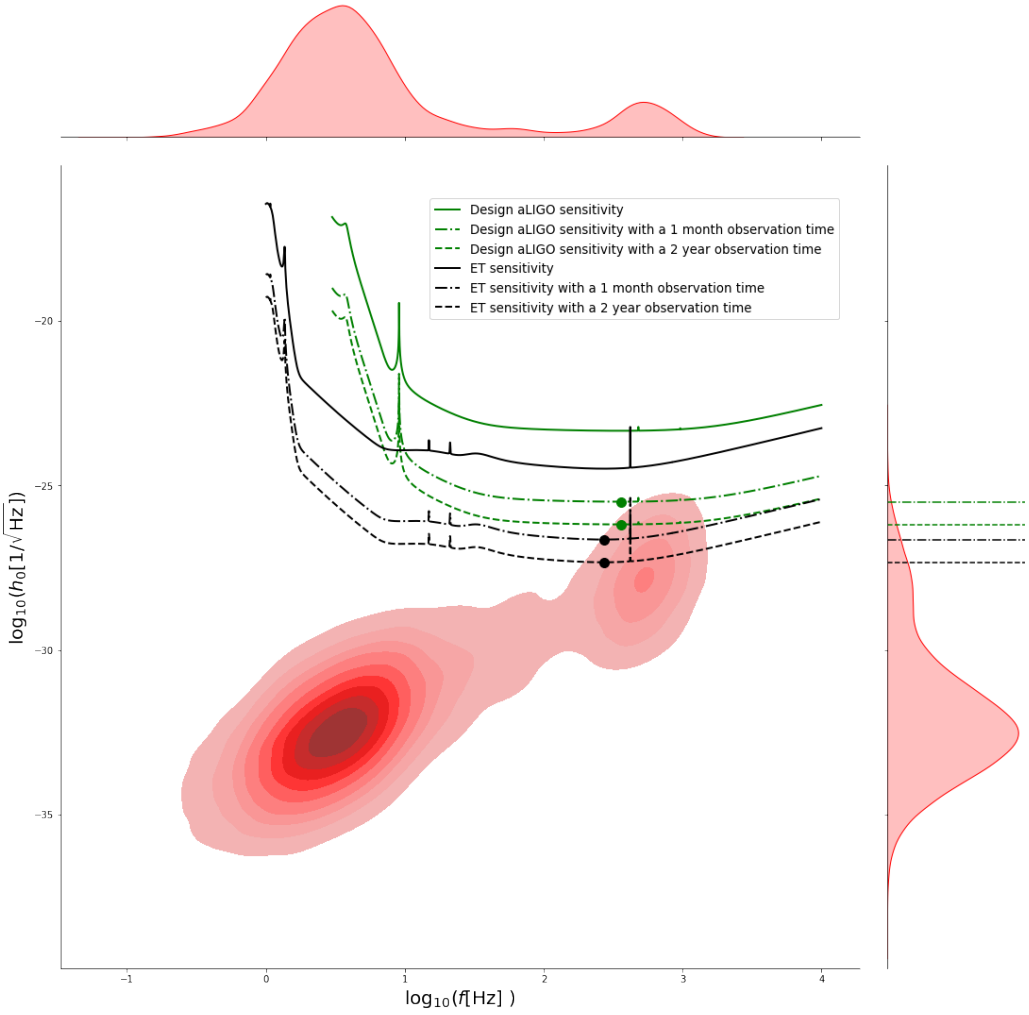

Figure 8.3: Plot of the probability density function (red contour plot) associated with model A randomly repeated 10 times (see text for more details). The two distribution on the top and right axii are the marginal distributions. The solid lines are the sensitivity curves of the aLIGO (green line) and ET detectors (black line). The dot-dashed and dashed lines are the minimum detectable strain by aLIGO (green lines) and ET (black lines) in the case of a continuous 1 month (dot-dashed lines) and 2 years (dashed lines) observation time. The green and black points denote the minima of these curves, and the green and black lines on the axis on the right refer to the values of these minima. The fraction of the NS population that is above those lines is potentially observable with the given instrument and observing time.

show that their position in the Galaxy does not seem to significantly influence their visibility by CGWs. Moreover, we note that the biggest difference between cases B1 and B2 lies in the distribution of heights above the Galactic plane, which has a scale length that is much lower than that of the radial distribution. For this reason, it is ex-

pected that these two cases give similar results. The position of the pulsar population

Table 8.1: Top 5 pulsars in the ATNF catalogue with the highest probability of detection according to our study. The pulsar's name, distance and period are reported, as recorded in the ATNF catalogue. The median strain column reports the median value of the strain h_0 for each pulsar, estimated by generating 100 samples of each. The last column contains the probability of detection of each NS by aLIGO with a 1 month (2 years) observation time.

Name	Distance [kpc]	Period [s]	Median strain $[1/\sqrt{\text{Hz}}]$	Detection probability
J0605+3757	0.215	0.002728	3.21×10^{-29}	18% (36%)
J0636+5129	0.210	0.002869	3.57×10^{-29}	15% (33%)
J0034-0534	1.348	0.001877	1.57×10^{-29}	14% (30%)
J1400-1431	0.278	0.003084	1.91×10^{-29}	13% (30%)
J1653-0158	0.840	0.001968	3.58×10^{-29}	12% (28%)

generated according to case B1 and case B2 are shown in Fig. 8.4 on the left and right, respectively. In fig. 8.5 we plot the resulting strain distributions for case study B1 and B2 (top and bottom plots, respectively). We clearly see that the differences in the resulting strain distribution are minimal, even though the positions of the two populations have a susbstantially different shape (see Fig. 8.4). In order to estimate the probability density distribution through KDE we increased the number of samples to generate to 10^5 for each EoS, resulting in a total population of 2×10^5 NSs. Given that cases B1 and B2 give practically equivalent results regarding h_0, we only plot the density obtained from case B1 in Fig. 8.6. We see that, using the aLIGO detector with a 1 month (2 years) observation time, $\sim$ 1% ($\sim$ 5%) of the MSP population could be detected; instead, by using the ET telescope with a 1 month (2 years) observation time, $\sim$ 10% ($\sim$ 23%) of the MSP population could be detected. As we found for case A, canonical pulsars seem to be out of both detectors' range.

In the case of a NS endowed with a superconducting core, the extent to which the magnetic field can deform the NS is much more enhanced (Cutler 2002; Frieben & Rezzolla 2012). In this case, we expect NS models to develop a distortion coefficient that is roughly $B_{\rm c1}/\langle B\rangle$ times higher than without a superconducting core, where $B_{\rm c1} \approx 10^{15}$G is the first critical magnetic field strength and $\langle B\rangle$ is the volume average of the magnitude of the magnetic field B (SBD21EOS). As we show in Fig. 8.7, the fraction of observable CGWs emitted by MSPs is greatly increased in this case: $\sim$ 18% ($\sim$ 48%) using the aLIGO detector with a 1 month (2 years) observation time and $\sim$ 69% ($\sim$ 90%) using the ET telescope with a 1 month (2 years) observation time. While the strain of CGWs emitted by canonical pulsars is certainly enhanced by the presence of a superconducting core, next generation telescopes like ET still fall short of the required sensitivity of at least one order of magnitude.

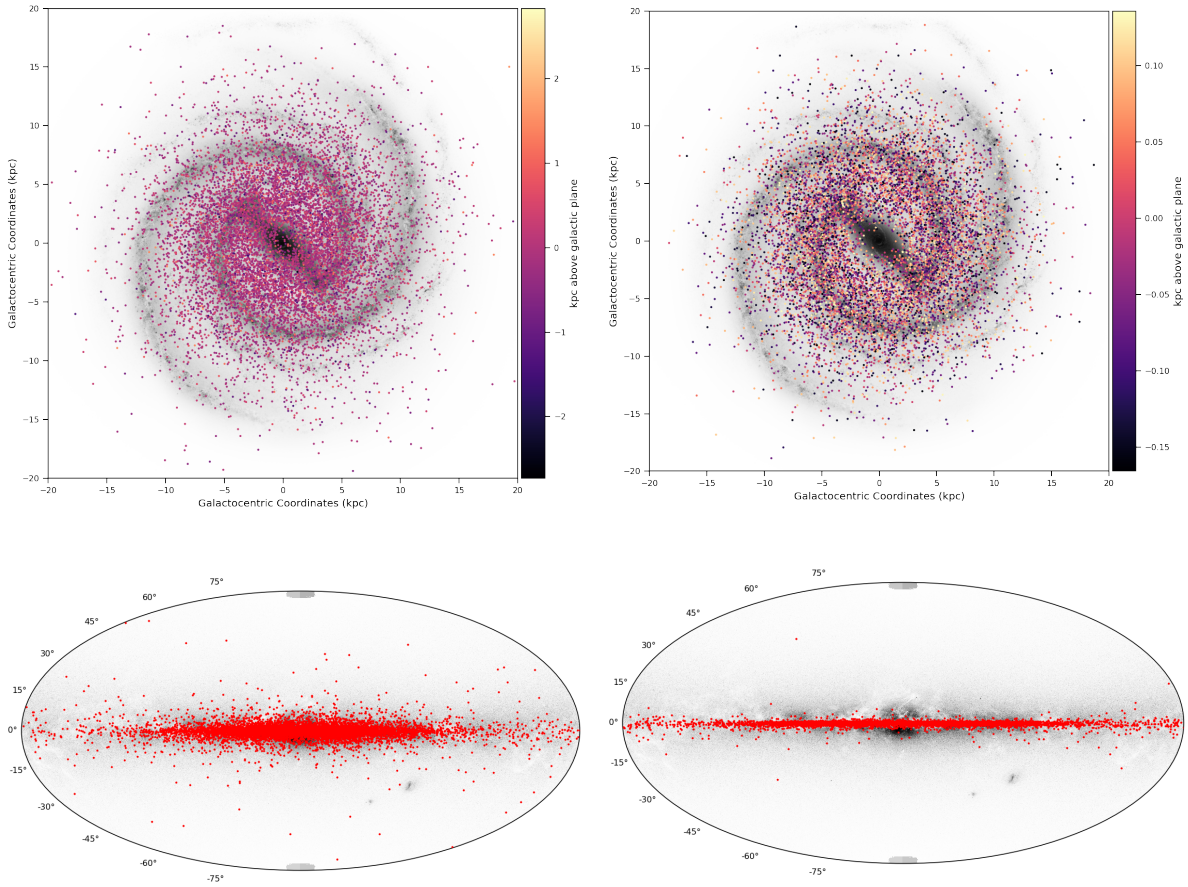

Figure 8.4: Face-on (top plot, in galactocentric coordinates) and edge-on (bottom plot, in ICRS coordinates) rendition of the Galaxy along with the position of the NSs population generated according to the position distributions of case study B1 (left plots) and case study B2 (right plots). These plots were made using the `mw-plot` Python package: `https://pypi.org/project/mw-plot/`.

8.3 Discussion

We have shown that the quasi-universal relation Eq. 7.4 linking the magnetic deformation of a NS to its mass, radius and surface magnetic field can be used to compute the strain of the CGWs they emit in a way that is independent of their EoS. This can be done once the NS mass, radius, surface magnetic field, rotation period and distance are known. Measuring directly the radius is notoriously difficult; however, once an EoS is assumed, there is a one to one relation with the mass, a much easier quantity to estimate, even from a statistical point of view. For this reason, we have chosen the

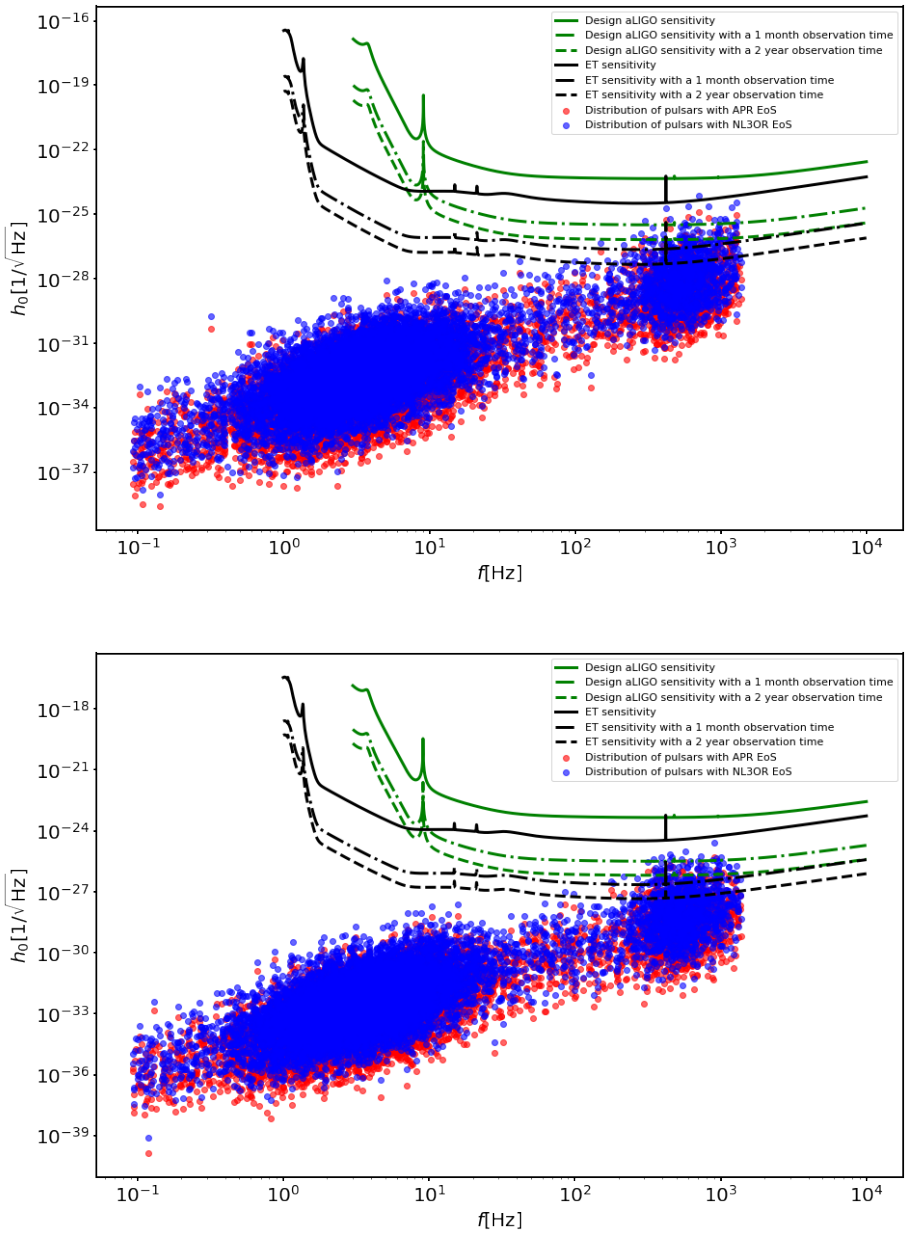

Figure 8.5: Strain of CGWs emitted by the pulsars generated according to the models of case study B1 (top plot) and case study B2 (bottom plot). Each point is a specific NS, and its position on the $x-$axis denotes the frequency of the emission of CGWs. The colour of the points indicates which EoS has been assumed to calculate the NS radius from its mass, either the APR (red points) or the NL3$\omega\rho$ (blue points) EoS. The solid lines are the sensitivity curves of the aLIGO (green line) and ET detectors (black line). The dot-dashed and dashed lines are the minimum detectable strain by aLIGO (green lines) and ET (black lines) in the case of a continuous 1 month (dot-dashed lines) and 2 years (dashed lines) observation time.

two EoS that give the most different radii, for the same NS mass, among the ones we used to infer the quasi-universal relation for c_s: this way, we expect that our results regarding the detectability of the Galactic NS population should encompass a much larger selection of possible NS EoS. As we discussed, the strain computed by adopting these two EoS can differ by up to an order of magnitude, and this can be taken as an estimate of the uncertainty due to our ignorance of the NS internal composition. Regarding the other quantities, we adopted two different approaches. In case A we used the values for the rotation period and distance of the known pulsars in the Galaxy contained in the ATNF catalogue, and we extracted their mass and surface magnetic field from the expected distributions. In the other case B, we synthesised the whole Galactic NS population by extracting all the necessary quantities from the expected distributions, allowing us to compute the strain of potentially undetected sources. In the last case, we chose a variety of distributions for the mass and distance of the expected NS population in the Galaxy, finding very similar results in all cases. Then, for each EoS we randomly generated a large population, and estimated the probability density distribution of h_0 using a KDE approach. This allows us to estimate the fraction of NSs in the Galaxy whose CGWs are within the range of ground-based future GW detectors. In particular, we considered the cases of the aLIGO and the ET detectors, both in the case of a continuous 1 month and 2 years observation time. In case A (see Fig. 8.3) we found that up to $\sim 9\%$ and $\sim 32\%$ of the total MSPs population lies within the reach of aLIGO and ET, respectively, considering a 2 years observing time. This amounts to a number of ~ 270 and ~ 960 detectable pulsars if one considers the expected number $\sim 3 \times 10^3$ of MSPs within 5 kpc of the Sun (Lorimer 2008). We note that those are the NSs such that the radio beaming intercepts our line of sight, and as such there exist a fraction of the total pulsar population which the ATNF catalogue does not account for but which may be observable through their CGWs emission. Lower fractions are obtained in case B1 (see Fig. 8.6): up to $\sim 5\%$ and $\sim 23\%$ of the total MSP population with aLIGO and ET, respectively, corresponding to ~ 2000 and ~ 9200 NSs considering the $\sim 4 \times 10^4$ MSPs expected to be present in the Galaxy (Lorimer 2008). We believe that this is due to a selection bias: as we see in Fig. 8.1 - top plot - the NS population that is observed is, as expected, roughly centred on the position of the Solar System, which lies at Galactocentric coordinates $(x, y, z) = (8.122, 0, 0.021)$ kpc, and many more pulsars close to the Sun have been observed than those further away. On the other hand, as we see in Fig. 8.4, the expected distributions of the NSs positions are computed for all NSs in the Galaxy, thus lowering the fraction of detectable NSs. Finally, we explored the case of NSs endowed with a superconducting core. In this case, the effective magnetic field that deforms the star is much stronger than without the effect of superconductivity, resulting in a greater emission of CGWs by the same NSs. In fact, in this case the fraction of detectable MSPs can reach values up to $\sim 48\%$ and even $\sim 90\%$ in the case of aLIGO and ET, respectively, for an observation of 2 years, corresponding to

$\sim$ 19200 and $\sim$ 36000 NSs. Even with just one month of observing time, $\sim$ 18% and $\sim$ 69% of the MSPs in the Galaxy lie within the reach of aLIGO and ET, amounting

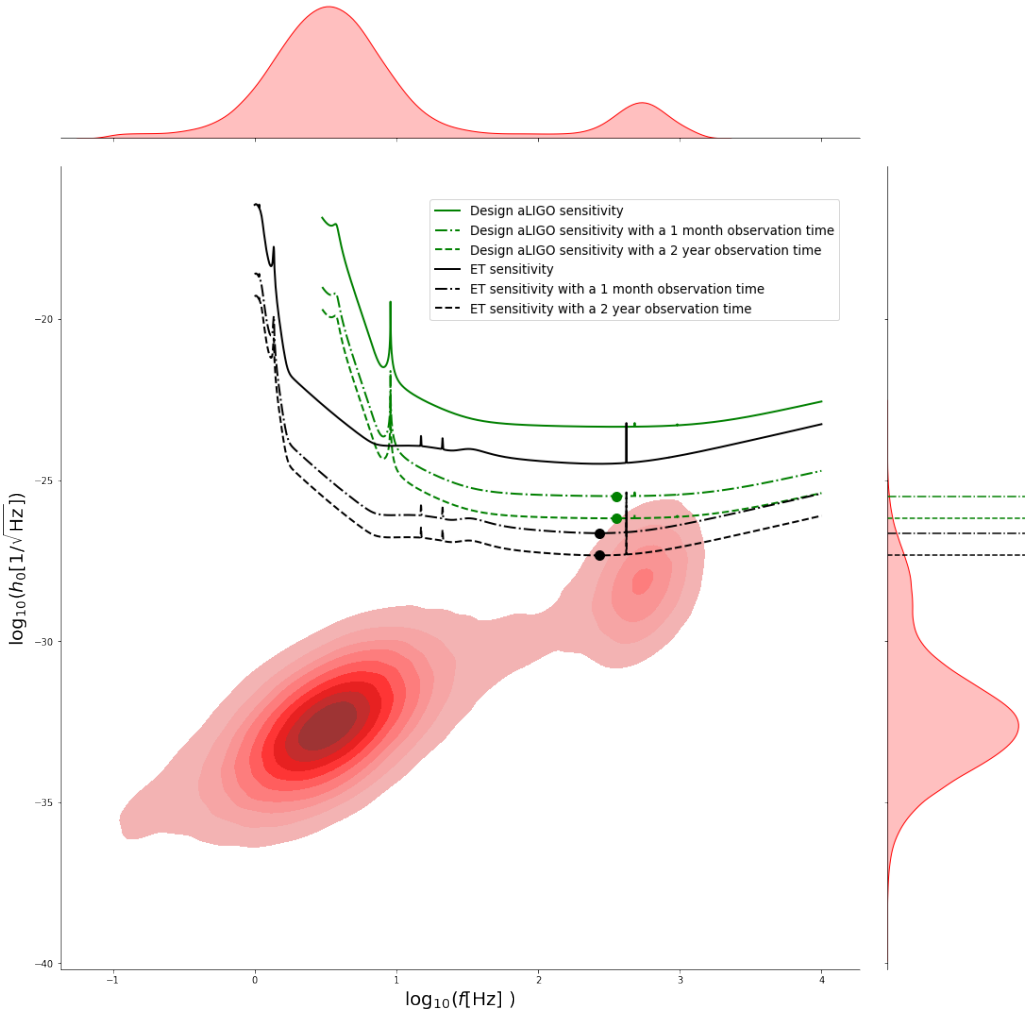

Figure 8.6: Plot of the probability density function (red contour plot) associated with a NS population of 10^5 samples made according to case B1 (see text for more details). The two distribution on the top and right axii are the marginal distributions. The solid lines are the sensitivity curves of the aLIGO (green line) and ET detectors (black line). The dot-dashed and dashed lines are the minimum detectable strain by aLIGO (green lines) and ET (black lines) in the case of a continuous 1 month (dot-dashed lines) and 2 years (dashed lines) observation time. The green and black points denote the minima of these curves, and the green and black lines on the axis on the right refer to the values of these minima. The fraction of the NS population that is above those lines is potentially observable with the given instrument and observing time.

to $\sim$ 7200 and $\sim$ 27600 NSs respectively. In all cases we considered, CGWs emitted by canonical pulsars seem to be far too weak even for 3rd generation ground-based

GW detectors, due to their slow rotation period. On the one hand, given that such a

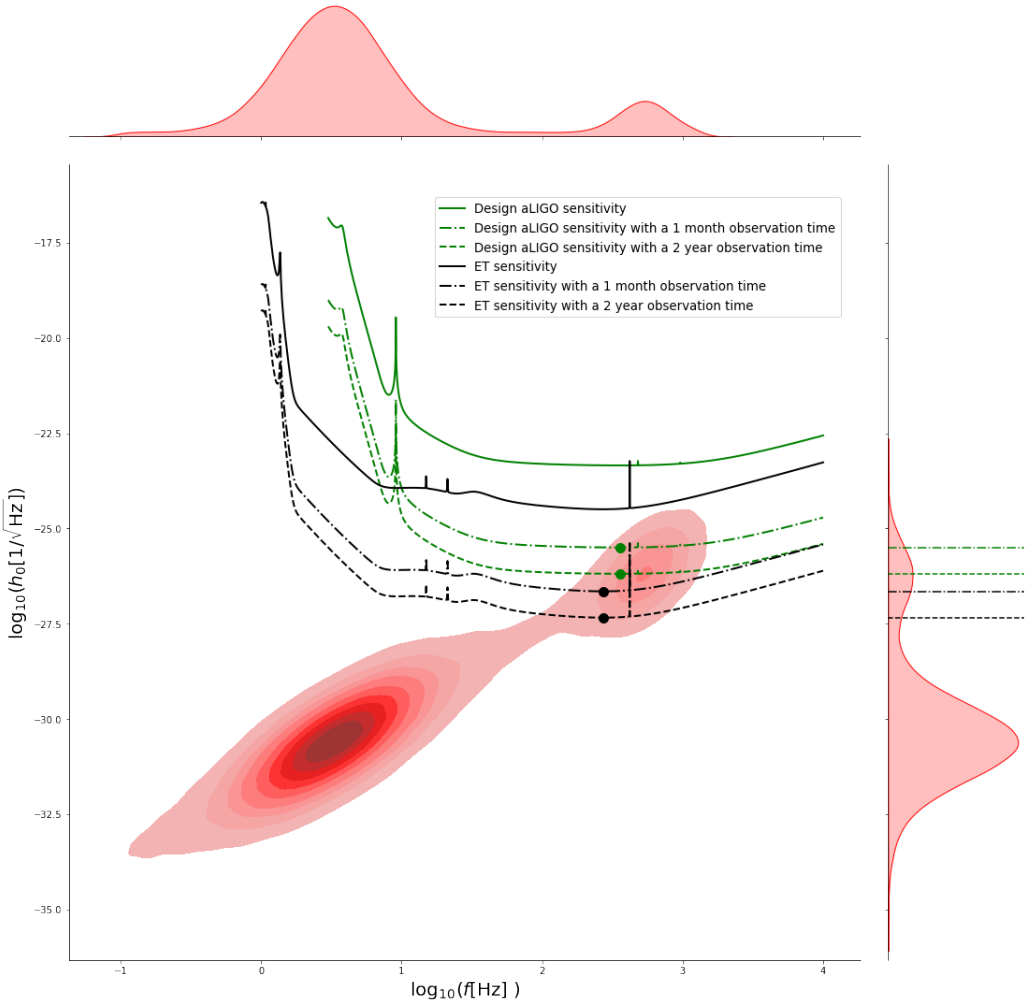

Figure 8.7: Plot of the probability density function (red contour plot) associated with a NS population of 10^5 samples made according to case B1 endowed with a superconducting core (see text for more details). The two distribution on the top and right axii are the marginal distributions. The solid lines are the sensitivity curves of the aLIGO (green line) and ET detectors (black line). The dot-dashed and dashed lines are the minimum detectable strain by aLIGO (green lines) and ET (black lines) in the case of a continuous 1 month (dot-dashed lines) and 2 years (dashed lines) observation time. The green and black points denote the minima of these curves, and the green and black lines on the axis on the right refer to the values of these minima. The fraction of the NS population that is above those lines is potentially observable with the given instrument and observing time.

large fraction of MSPs could be detectable by aLIGO and ET in the case of superconductivity, the absence of any CGWs detection could itself be an indication of the lack

of a superconducting core, effectively constraining the possibility of its existence. On the other hand, we note that all our results assume that the magnetic field inside NSs has a purely poloidal geometry. While this is clearly a simplifying assumption, it allows one to possibily infer information on the geometry of the internal magnetic field of MSPs: the presence of a toroidal component counteracts the effect of the poloidal component, effectively reducing the deformation with respect to NSs endowed with a purely poloidal field and potentially rendering invisible MSPs which, given their characteristics, should be detectable by GW detectors according to our study. Finally, we note that we focused on the strain h_0 as a way to measure the detectability of NSs independently from their orientation with respect to the detectors and the inclination between the magnetic and the rotation axii. Of course, the magnetic deformation of a NS does not lead to the emission of CGWs if the magnetic axis is aligned with the rotation axis. Moerover, GW detectors have a particular antenna pattern which renders them more or less sensitive to waves coming from certain angular positions in the sky. While we believe our findings can give a comprehensive overview of what to expect in terms of CGWs emission by pulsars in the Galaxy, a more in depth extension would be to consider also the expected distribution of the relative inclination between the two axii and to consider the time-varying angular position of the NSs systems with respect to the ground-based detectors on Earth.

Chapter 9

Iron line from neutron stars accretion disks in scalar-tensor theories

The results shown in this chapter were published in the paper Bucciantini & Soldateschi (2020).

In this chapter we investigate how the shape of the Fe K_α fluorescent line at 6.4 keV, which is a powerful probe of the spacetime metric in the vicinity of accreting compact objects, is modified in STTs with respect to GR. By taking into account both deviations from the GR orbital dynamics of the accreting disk, where the Fe line originates, and the changes in the light propagation around the NS, we compute line shapes for various inclinations of the disk with respect to the observer. We find that both the intensity of the low energy tails and the position of the high energy edge of the line change. Moreover we verify that even if those changes are in general of the order of a few percents, they are potentially observable with the next generation of X-ray satellites.

This chapter is structured as follows. In Sect. 9.1 we introduce the importance of the Fe K_α fluorescent line. In Sect. 9.2 we describe the problem of ray-tracing in vacuum in STTs. In Sect. 9.3 we present our results regarding the modification in the Fe line shape caused by the presence of a scalar field. Finally, we discuss our results in Sect. 9.4.

9.1 The iron line in low-mass X-ray binary systems

As we describe in Chaps. 1,2, the presence of a scalar field leads to new wave modes in binary NSs systems, beyond the standard quadrupole gravitational wave emission. However, the present limits on STTs based on the study of the orbital decay of binary pulsars (Shao et al. 2017; Anderson et al. 2019) can be easily accommodated introduc-

ing screening potentials or assuming massive scalar fields (Yazadjiev et al. 2016). On the other hand it is not clear how, and how much a scalar field modifies the final phases of binary NS inspiral before merger to a degree observable with current instruments, and with specific signatures that cannot be attributed to other causes (e.g. the EoS). Even the measure of the mass radius relation might not prove to be enough, if limited to few objects, given its degeneracy with the EoS. What we lack at present is a way to probe deviations from GR in the close vicinity of NSs. One of the most powerful probes of the space time geometry close to compact objects is light propagation. Light bending has been widely used in binary pulsar systems (Demorest et al. 2010; Antoniadis et al. 2013), and more recently in the case of the BH at the center of M87 (Event Horizon Telescope Collaboration et al. 2019). In accreting systems, one can also use emission from the accretion disk, and in particular the shape of the Fe K_α fluorescent line at 6.4 keV (Miller 2007; Dauser et al. 2016). This line has been extensively used in acceting BHs to measure their spin (Risaliti et al. 2013; Parker et al. 2018; Kammoun et al. 2018). Recently its has also been investigated in alternative gravitational theories that predict deviation also for the BH metric (Yang et al. 2018; Nampalliwar et al. 2018). Despite the fact that this technique has been used just for BHs, we know of many accreting NSs systems where we observe the presence of this line (Laor 1991; Matt et al. 1992; Degenaar et al. 2015; Coughenour et al. 2018; Homan et al. 2018). In principle Fe K_α could be used to constrain the metric properties outside the NS itself. It has been suggested that the Fe line in accreting NSs could be used to set limit on the NS radius, by modeling the effect on the shape of the line due to the disk occultation by the surface of the NS itself (Cackett et al. 2008; La Placa et al. 2020). However in general these effects are found to be small, of the order of few percents, and thus not measurable with current instruments. They might in principle be within reach of next generation X-ray satellites (Barret et al. 2016). In the line of Sotani (2017), who investigates light propagation from hot spots on the surface of a scalarized NS, here we investigate how the Fe line emission from an accreting disk around a NS is modified by the presence of a scalar field with respect to GR, including the effect of the possible occultation/truncation of the disk by the NS itself. In order to simplify the discussion, this study is mostly structured as a proof-of principle, and not as a full fledged investigation of the possible parameter space. For these reasons, neither we compute realistic NS models based on physical EoS, nor we include rotation, and for the same reason we opted for the simplest STT, trying to parametrise the vacuum solution outside, in order to provide a flexible estimate of the expected changes.

9.2 Metric and ray-tracing in the vacuum of scalar-tensor theories

If one assumes steady state, $\partial_t = 0$, and spherical symmetry (a reasonable approximation for NSs not rotating close to the break-up frequency), then it is possible to show that the line element in the E-frame can be written in spherical coordinates $[r, \theta, \phi]$ as (Just 1959; Doneva et al. 2014):

$$ds^2 = -f(r)^a dt^2 + f(r)^{-a} dr^2 + r^2 f(r)^{1-a} [d\theta^2 + \sin^2\theta d\phi^2] \tag{9.1}$$

where the function $f(r)$ and the exponent a depend on the E-frame Komar mass $M = M_{\rm k}$ and scalar charge $Q_{\rm s}$ of the NS according to:

$$f(r) = \left(1 - 2\sqrt{M^2 + Q_{\rm s}^2}/r\right) \ , \ a = M/\sqrt{M^2 + Q_{\rm s}^2}, \tag{9.2}$$

while the scalar field is:

$$\chi = \frac{Q_{\rm s}}{2\sqrt{M^2 + Q_{\rm s}^2}} \ln\left(1 - 2\sqrt{M^2 + Q_{\rm s}^2}/r\right). \tag{9.3}$$

However, in the E-frame, contrary to the J-frame, the WEP does not hold. In order to compute ray-tracing using the standard geodesic equations, one needs to move back to the J-frame and, to do so, to know the relation between the E-frame scalar field, χ, and the J-frame one, φ. One of the simplest possible choices is to take $\varphi = \mathcal{A}^{-2}(\chi) = {\rm Exp}[-2\alpha_0\chi - \beta_0\chi^2]$. The parameter α_0 sets how strong deviations from GR are in the weak field regime, and Solar system experiments constrain it to be less than $\approx 10^{-4}$. On the other hand, β_0 sets how strong scalarization effects can be in compact objects, and if smaller than $\simeq -4$, it gives rise to strongly scalarized systems (Will 2014). The J-frame metric is then fully parametrised by the quantities M, $Q_{\rm s}$, α_0, and β_0.

If one makes the further assumption $\alpha_0 = 0$, it is then possible to derive an analytical expression for the Keplerian frequency of matter orbiting the NS, using the effective potential approach (Abramowicz & Kluźniak 2005; Doneva et al. 2014):

$$\Omega_{\rm k} = \frac{-\left(1 - \frac{2M}{ar}\right)^{2a} \left[\frac{2M^2}{a} + \beta_0 Q_{\rm s}^2 \ln\left(1 - \frac{2M}{ar}\right)\right]}{r^2\left(1 - \frac{2M}{ar}\right)\left[\frac{2M^2}{a} + \frac{2M^2}{a^2} - \frac{2Mr}{a} - \beta_0 Q_{\rm s}^2 \ln\left(1 - \frac{2M}{ar}\right)\right]}, \tag{9.4}$$

which allows one to compute the radius of the innermost stable circular orbit (ISCO). Once the metric and the four-velocity of matter orbiting in the disk are known it is possible to reconstruct the shape of the Fe line, as in Psaltis & Johannsen (2012). Given an observer that sees the NS-disk system at an inclination ψ (the angle between the observer direction and the perpendicular to the disk plane) light rays are traced from

an image plane at the location of the observer, until they reach the disk (or until the intercept the surface of the NS in those cases, and for those inclinations, for which the NS can occult/truncate the disk). Then one can reconstruct the shape of the line, by integrating over the image plane (with coordinates $[\eta, \zeta]$), the intensity due to the emission of the disk. Ray-tracing maps each point $[\eta, \zeta]$ of the image plane to a point on the equatorial plane where the disk is located. For each point we can compute a transfer function that maps the frequency of the emitted photon ν_0 to that of the observed photon ν according to $\nu/\nu_0 = (k_\nu u^\nu_{\rm obs})/(k_\nu u^\nu_{\rm disk}) = F$, where k_ν is the photon wave four-vector (either at the position of the observer or of the emitter in the disk) whose value is provided by the geodesic equations of the ray-tracing, while $u^\nu_{\rm obs}$ and $u^\nu_{\rm disk}$ are respectively the four velocity of the observer (taken at rest) and of the matter in the disk. The intensity $I_{\rm obs}$ at the observer position can be computed, once the intensity of the radiation emitted in the disk $I_{\rm disk}$ is known, recalling that $I_{\rm obs}/(k_\nu u^\nu_{\rm obs})^3 = I_{\rm disk}/(k_\nu u^\nu_{\rm disk})^3$. Then, the spectrum can be derived integrating the intensity over the plane $[\eta, \zeta]$ at the observer location:

$$I(\nu) = \int I_{\rm obs}(\eta, \zeta)\delta(\nu - \nu_0)F(\eta, \zeta)d\eta d\zeta \tag{9.5}$$

In general one assumes that there is no emission coming from regions inside the ISCO, while in the disk the emissivity scales as a power-law of the circumferential radius, $r_c^\gamma = r^\gamma \tilde{g}^{\gamma/2}_{\phi\phi}$, where the equality comes from the definition of the circumferential radius itself. A typical value is $\gamma = -3$, and we use it in the following. The dependence on the radius is then steep enough that one can truncate the disk emission around a few ISCO radii without affecting the shape of the line.

9.3 Modifications to the iron-line profile

Given that we do not want to select a specific EoS, or scalar field coupling, to keep the discussion as general as possible we treat the NS E-frame Komar mass M (which is the same as in the J-frame, since $\alpha_0 = 0$), its J-frame circumferential radius $R_{\rm c}$ and the total scalar charge $Q_{\rm s}$ as independent quantities. This is not true, given that those three quantities are strongly related. This relation, however, is non trivial. Moreover, leaving these three quantities free, the result can be easily applied to any scalarised NS model. We chose $\alpha_0 = 0$ and $\beta_0 = -6$. Lowering β_0 to values around the limit for spontaneous scalarization does not substantially modify the results.

Before investigating how STTs, and scalarized NSs, change the shape of the Fe line, we begin by discussing under what conditions one can have a NS that causes occultation of the ISCO. In Fig. 9.1 we show the minimal coordinate radius, and the minimal circumferential radius (the only invariant quantity that can be physically measured), such that the NS occults the ISCO, for various inclination angles, together with the ra-

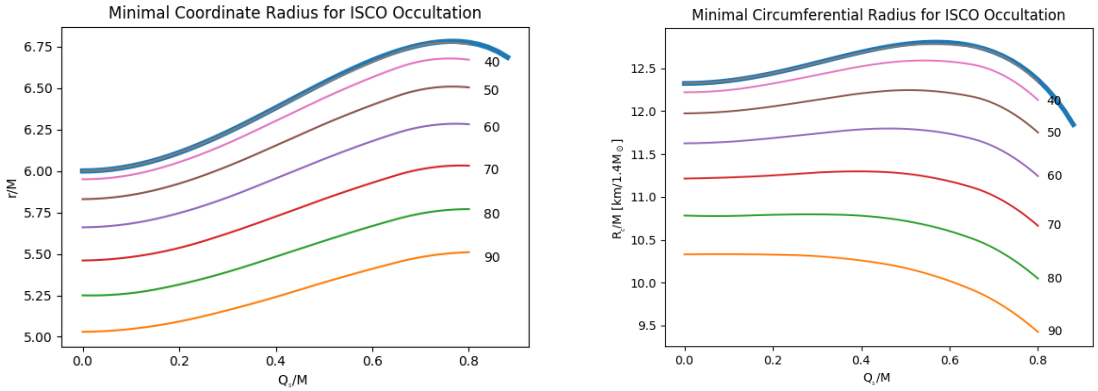

Figure 9.1: Minimal coordinate radius (left panel) and circumferential radius (right panel) for ISCO occultation by a NS as a function of the ratio of total scalar charge over the mass ($Q_s/M = 0$ is GR), for various inclination of the observer with respect to the normal of the disk plane. The thick blue line is the ISCO radius as a function of the scalar charge.

dius of the ISCO itself. It is evident that occultation/truncation can take place only if the inclination angle of the observer is $\psi > 30^\circ$. Interestingly this threshold does not depend on the presence of a scalar field. In GR, for systems seen edge on, when the inclination angle of the observer is $\psi = 90^\circ$, occultation/truncation of the ISCO requires the NS coordinate radius to be $> 5M$. In STTs this threshold increases by about 10% for a scalar charge $Q_s = 0.8M$. This difference between GR and STTs holds also for different viewing angles. Instead, in terms of the circumferential radius, we see that the threshold radius for occultation of scalarized NSs is smaller for large inclinations, and marginally larger approaching a viewing angle of $\psi \sim 30^\circ$. Given that one of the most relevant effect of a scalar field on the structure of NSs, is that scalarized NSs have larger circumferential radii than their GR counterparts of the same gravitations mass, occultation might be a more common phenomenon in scalarized systems than in GR. In particular, given that there is a mass threshold for spontaneous scalarization, one would expect occultation to be substantially more frequent above this mass.

In Fig. 9.2 we show the shape of the iron line for a viewing angle of $\psi = 30^\circ$ in the absence of occultation, for various values of Q_s/M. It is intersting to note that the location of the edge at $\simeq 6.74$ keV does not depend on the presence of a scalar charge. On the other hand the effects of the scalar charge are more evident in the shape of the line. In particular, the intensity in the range $[5.9 - 6.6]$keV is smaller than in GR, from $\sim 2\%$ for $Q_s = 0.3M$, to $\sim 7\%$ at $Q_s = 0.8M$. For $Q_s > 0.5M$ differences with respect to GR emerge also in the low energy tail. In particular we observe the formation of a 'second horn' at $\simeq 5.6$keV, and a tail which is about 2% brighter, and extends down to 3.2keV, with respect to the low energy limit of 3.7keV in GR.

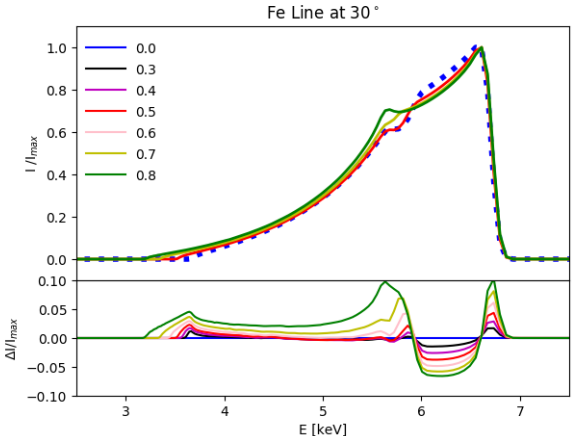

Figure 9.2: Upper panel: shape of the Fe K_α line, normalised to the maximum, for a viewing angle of 30°, and different values of the ratio of total scalar charge over the mass. The thick dotted blue line is the GR case. Lower panel: percentage deviation of the line shape as a function of the scalar charge with respect to GR.

In Fig. 9.3 we show the shape of the iron line for various viewing angles, and for selected values of the scalar charge. It is evident that the way a scalar field modifies the line shape depends strongly on the viewing geometry. At $\psi = 20°$, the largest deviations are found in the intensity and shape of the low energy tail, and only partially in the shape of the $[6.0 - 6.5]$ keV part. At $\psi = 45°$ instead the deviations are much smaller, while at $\psi = 70°$ they emerge again but now in the position of the high energy edge, which moves from $\simeq$ 8.2 keV to $\simeq$ 8.7 keV, while the rest of the line shape is unaffected. The reason for this change with viewing angle is due to the fact that, for small viewing angles the shape of the line is mostly affected by gravitational redshift, and light bending, whose effects are more prominent in the low energy tails. This is where deviations from GR have the largest impact. On the other hand, when the inclination rises, and the disk is progressively seen more edge on, special relativistic effects due to orbital motion, and the related Doppler boosting, become dominant. The shape of the line now is more a tracer of the location and dynamics of the ISCO, which impacts mostly the high energy part of the line and the location of the edge. In general deviations in the intensity in the body of the line are small, at most few percents.

In terms of occultation, for an observer inclination of $\psi = 70°$, the effect are small (less than few percents) and mostly concentrated in the low energy part of the line. However, when the NSs radius become larger than the ISCO (or in case the disk is truncated at radii larger than the ISCO radius), the high energy edge of the line begins to move to lower energy. For $Q_s = 0.8M$ and $R_c = 7M$ (greater than the ISCO radius for any Q_s/M) the leading edge is located at $\simeq$ 8.4keV. For an observer inclination of $\psi = 30°$, when occultation does not take place, the effect of a NS that truncates the

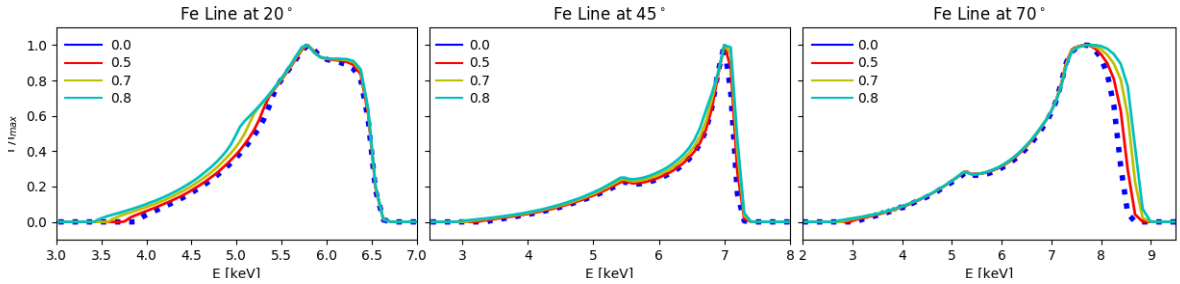

Figure 9.3: Shape of the Fe K_α line, normalised to the maximum, for various viewing angles (20° left, 45° center, 70° right), and different values of the ratio of total scalar charge over the mass. The thick dotted blue line is the GR case.

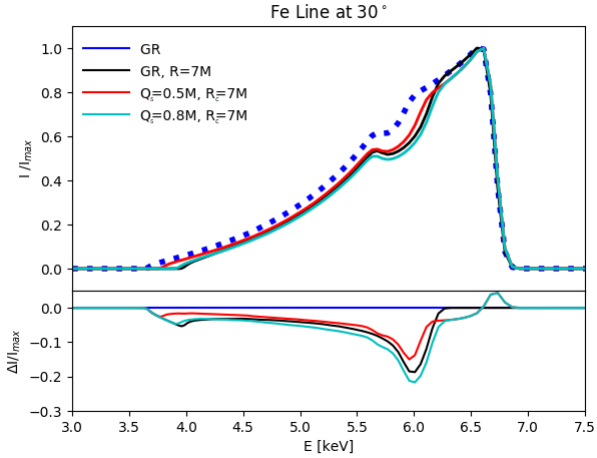

Figure 9.4: Shape of the Fe K_α line for 30° viewing angle, and various values of the scalar charge and NS radius normalised to the maximum (thick dotted blue line is unocculted GR). Lower panel percentage deviation of the line shape as a function of the ratio of total scalar charge over the mass, with respect to unocculted GR.

disk at radii larger than the ISCO, is mostly concentrated in the intermediate part of the line. Again the differences between the GR case, and STT are only few percents, as shown in Fig. 9.4.

9.4 Discussion

In the work presented in this chapter we have investigated how the spacetime deviations produced by a non-minimally coupled scalar field, as hypothesised in some alternative theory of gravity, could be probed using the shape of the Fe K_α line in accreting NS systems. Given that STTs satisfy the WEP, standard ray tracing techniques of GR can easily be applied. The presence of a scalar field affects the shape of the

line in two ways: on one hand, it changes the spacetime, affecting the gravitational redshift and light bending; on the other, it modifies the Keplerian dynamics of matter orbiting in the disk, and the location of the ISCO, which leads to further deviations in the line shape associated to special relativistic Doppler boosting. We found that such deviations however are at most a few percents, and only for large total scalar charges $Q_s > 0.5M$. However, given that the typical luminosity of low mass X-ray binaries (LMXBs), where the Fe line has been detected, is usually a sizeable fraction $0.05 - 0.11$ of the Eddington luminosity, and that the intensity of the Fe line is typically 5-10% of the continuum, with the next generation of large collecting area X-ray satellites like ATHENA (whose expected effective area at 6 keV is $\simeq$ 2500 cm^2, Barcons et al. 2017) we predict that deviations in the intensity of the line of the order of few percents could be detected with typical exposure times ranging from 10^5s in the brightest sources like Sco X-1 e Ser X-1 to a few 10^5s for weaker ones like 4U1608-52. More interesting is the fact that for large viewing angles, the high-energy edge can move enough to be revealed even with a low spectral resolution. This, in our opinion, could be the easiest deviation to measure.

There are of course several other issues, that can play a role in the correct modelling of the line shape (Miller 2007; Dauser et al. 2016). It is well known that the choice of the illuminator for example can affect it. The correct modelling of the background plays also a crucial role, as well as the presence of other lines that can blend (Iaria et al. 2009). Not to talk about the assumption of a disk truncated at the ISCO. It is also possible that scalarized NSs, having in general larger radii than in GR (Damour & Esposito-Farèse 1993), could lead to stronger occultation effects. However, even if this could provide an alternative way to measure the radius of the NS, it is not clear how degenerate the information it provides is with respect to the EoS.

We stress again that the work presented in this chapter was organised as a proof of principle, and we opted for the simplest possible approach to test the viability of this effect. Given however the potential of this kind of measure as a possible independent test of GR and its alternatives, we deem that a more accurate evaluations of the expected results, considering specific STTs, or more realistic EoS, to account for the mutual relation between mass, scalar charge and NS radius, and specifically targeted to known systems, is worth a further analisys.

Chapter 10

Conclusions

The extreme conditions that set the environment of NSs make them incredibly interesting objects to study. In order to be able to extract meaningful inferences from observations, NSs models must be as accurate as possible. Due to the strong gravitational field generated by their extreme density conditions, this means that they should be studied according the laws of GR. Moreover, the strength of their magnetic fields is so large that it induces potentially observable modifications to their structure, for example by causing the appearance of different particles or by deforming their shape, leading to the emission of CGWs, and for this reason also magnetic fields should be included in their modelling. Finally, the complex structure of NSs cannot be accurately probed without the use of physically motivated EoS, which attempt to capture all the nuances of their composition. While the study of NSs magnetic fields and EoS is an interesting subject per se, an even more challenging scenario arises when one begins to doubt the validity of the laws of GR themselves. In fact, both theoretical and observational arguments suggest that GR may not be the definitive theory that explains the laws of gravitation, and for this reason many ATG have been proposed to make up for these shortcomings, STTs being arguably the most studied. In particular, theories predicting the existence of non-linear strong field effects, like spontaneous scalarisation, are especially interesting because they can cause the appearance of observable modifications to the phenomenology of NSs, while satisfying severe observational constraints. Harbouring such a unique and complex environment, NSs possess a rich phenomenology which is determined by several factors, among which are their magnetic field, their EoS and the laws of gravitation. For this reason, these aspects are entangled and degenerate in complex ways, and in order to infer even more meaningful information on their structure - and on the validity of GR - an effort to separate their effects is needed.

The purpose of this Ph.D. project goes in this direction. In particular, we studied for the first time magnetised models of NSs in STTs, both with simple and realistic EoS, in the

full non-linear regime. In order to do so, we updated the well tested `XNS` code in order to study axisymmetric, magnetised NSs in a particular class of massless STTs, allowing also the use of realistic, tabulated EoS. We considered the case of purely toroidal and purely poloidal magnetic fields, which set the extreme boundaries of a real NS, which is expected to possess a mixed field magnetic structure. We have shown how to develop a strategy, within the framework of the 3+1 formalism, to extend standard techniques developed for GRMHD to the case of STTs, by making simultaneous use of the E-frame (where the metric equation have the same mathematical structure as in GR, and the same numerical schemes can be applied) and the J-frame (where the MHD equations retain their conservative, quasi-hyperbolic form, and thus are amenable to be treated with standard finite volume or finite difference conservative schemes for fluid dynamics).

Our formalism is based on the XCFC approximation, which has proved to be very accurate in GR - even for strongly deformed NSs - and in the fully dynamical regime, also for systems undergoing collapse to black hole, as long as one is not interested in the GW emission. The XCFC approach has several advantages in GR: the source terms of the metric equations are the same conserved variables evolved by the conservative algorithm for the fluid dynamics; the equations are decoupled and can be solved sequentially; local uniqueness is satisfied. We have verified that in STTs, the XCFC approach retains these properties. Even if, in principle, because of the sign of the scalar field term in the equation for $\alpha\psi$, local uniqueness could be violated, we have checked that, practically, this is never the case, even for the most scalarised of our configurations. We have shown that spontaneous scalarisation leads to multiple solutions for NSs, either weakly or strongly scalarised, and we have shown and characterised how the symmetry of the strongly scalarised branch is broken if one chooses a value $\alpha_0 \neq 0$. In particular, we verified that our numerical algorithm always selects the $\mathcal{S}_s^-$ branch (see Chap. 5). We also showed that the $\mathcal{S}_s^-$ solutions are not always the ones with the largest deviation from GR in the mass-density diagram, but are always the ones with the largest scalar charge and smallest compactness.

For simplicity and ease of discussion, we have focused on the case of static configurations, illustrating how the equations that describe the density and magnetic field distribution change in the presence of a scalar field, and how the effects of a scalar field can be fully encapsulated in the conformal scaling factor $\mathcal{A}$. While we focused on a particular, well-known form of $\mathcal{A}$, which allows the existence of spontaneous scalarisation, our approach is more general, and `XNS` is able to solve for the coupled Einstein-Maxwell-scalar system of equations in massless STTs defined by different forms of the coupling function. In Chap. 5 we first carried out a study of how the combined presence of a magnetic and a scalar field alters the properties of NSs, focusing both on the radial distribution of quantities like the density or the scalar field strength and on

global quantities like the mass and the magnetic deformation. In order to untangle the effects of the magnetic and of the scalar fields, we compared our solutions to both un-magnetised and un-scalarised solutions, finding for example that the radial structure of NSs is not heavilty affected by the presence of a scalar field; instead, global quantities like the mass and deformation of the NS can significantly differ from the GR counterparts. In any case, we highlighted the fact that in order to make a meaningful comparison with respect to GR models it is necessary to specify which quantity is held constant. Moreover, we found that scalarised NSs endowed with a toroidal field can undergo a novel type of scalarisation, induced by a diminishing magnetic field, which can happen, for example, in the presence of non ideal processes or magnetic instabilities.

After having tackeld the general problem of axisymmetric, magnetised NSs in STTs, we focused on the magnetic deformation of such models in Chap. 6. The magnetic deformation is a quantity which contains information about the distortion of a NS from the spherical shape, induced by its magnetic field. It is of particular importance in the context of CGWs: real NSs present a misalignment between the magnetic and the rotation axii, and this time-varying quadrupole moment leads to the emission of CGWs. Many efforts are being devoted to detect CGWs generated by NSs, emitted either because of their magnetic deformation or due to other kinds of distortions, unluckily without a confirmed detection at the present day. However, next generation GWs detectors should possess a much higher chance of detection of these faint signals, and even non-detections with current detectors are useful to constrain the degree of deformation that NSs are expected to display. The additional presence of a scalar field may in principle hinder the emission of CGWs in two ways. On the one hand, scalar fields tend to reduce the deformation of a NS in GR with the same mass. On the other hand, in STTs a new channel for the emission of GWs is open: while in GR only GWs of tensor nature exist, in STTs also those of scalar nature are possible. In order to tackle this problem, we adopted a particular parametrisation of the magnetic deformation, that of distortion coefficients, and we applied it to the case of scalarised NSs. Distortion coefficients allow one to expand the magnetic deformation of weakly magnetised models (where the strength of these magnetic fields is still entirely realistic with respect to what is their expected strength inside a real NS) as a simple function of either the maximum magnetic field or the magnetic to binding energy ratio. While in GR these coefficients depend only on the NS mass, in STTs we found that they are heavily dependent on the scalarisation parameter β_0, where a high scalarisation causes a important reduction of their value with respect to the GR model at the same mass. More interestingly, we found that in the full range of masses and scalarisation degrees of our study, distortion coefficients can be written as a simple power law of three quantities characterising the NS, namely its mass, its radius and its scalar charge. As distortion coefficients are

lower in STTs with respect to GR models with the same mass, a lower magnetic deformation is expected in STTs models with respect to their counterparts in GR. As we mentioned, the combination of this effect and the opening of a new channel for the emission of GWs imply an expected hindrance in the amount of CGWs that can be detected by GWs detectors. In order to study this problem from a quantitative point of view, we introduced two quantities which describe what fraction of the energy emitted in quadrupolar GWs is due to the quadrupolar moment of the mass distribution and to that of the scalar field distribution. We found that, depending on the mass, scalarised NSs can emit in the scalar channel almost double the energy they emit in tensor GWs. This leads to a reduction of the amount of tensor GWs that are emitted with respect to GR models with the same mass. As GWs detectors are mostly sensitive to tensor GWs, this may lead to uncorrect estimations of the energetics of the emitting system and of any quantity that is derived from it, as the distance or the strength of its magnetic field. Instead, the detection of scalar CGWs is heavily suppressed by the coupling of the scalar field to the detector, rendering their discovery even more unlikely.

While these previous studies were carried out in the case of NSs described by a polytropic EoS commonly used in previous works in the literature, it is important to model NSs with a realistic EoS. For this reason, we carried out an extension of our previous work using a selection of different EoS allowed by current observational and nuclear physics constraints, as showed in Chap. 7. We chose thirteen EoS that differ both in the methods used to compute them and in their particle content. Moreover, two of them describe strange quark stars, a different kind of NS that has been proposed to exist and whose observation may solve some puzzles regarding the physics of NSs, in particular regarding the large masses they are observed to reach. We computed the distortion coefficients for a large number of models, both in GR and in STTs, and introduced a new coefficient which allows the expansion of the magnetic deformation as a function of the magnetic field at the surface of the NS. In fact, while the former two coefficients are based on the internal magnetic field of the NS, which is not easily inferred, the latter is based on a quantity which is much more likely to be observed. Then, we looked for dependencies of these coefficients in terms of the NSs mass, radius and scalar charge. While, in general, each EoS predicts a different deformation at the same mass (or radius, or scalar charge), we found that there exist particular combinations of these quantities which render the distortion coefficients independent of the EoS. In other words, there exist some relations that allow one to compute the coefficients by knowing only the NSs mass, radius and scalar charge, but not the EoS. While this can be useful also for the purpose of computing the magnetic deformation of NSs models by knowing just these quantities, without going through a full numerical simulation, the fact that the distortion coefficient we introduced depends on an observable quantity, the surface magnetic field, renders that relation important from an observa-

tional point of view. In fact, the confrontation between the computed coefficient and that inferred from CGWs observations in GR can be used to extrapolate information on the internal magnetic field geometry of the observed NS without knowing its EoS. Moreover, we found that a quasi-universal relation also exists for the ratio between the scalar and the tensor quadrupole moments introduced in our previous work (see Chap. 6). Given that this ratio seems to be independent of the magnetic field configuration altogether (although this should be verified with further studies using models with a mixed field geometry), using the corresponding quasi-universal relation in concurrency with the detection of CGWs from a known source can be used to infer bounds on the scalar charge of that object.

As we described, the quasi-universal relations we found can be used to compute the magnetic deformation of a NS without knowing its EoS. In our following work, described in Chap. 8, we applied the relation involving the surface magnetic field to the problem of estimating the probability of detection of CGWs by NSs in the Galaxy. In order to do so, we computed the strain of CGWs emitted both by known sources, using the ATNF catalogue of radio pulsars, and by a synthetic population generated by using expected distributions of the Galactic NSs population. Then, we compared these results with the sensitivity of two GWs detectors: aLIGO at design sensitivity, expected to be reached in the next years, and the future 3rd generation detector ET. Interestingly, we found that while canonical pulsars are beyond the reach of even ET, a certain fraction of MSPs could be detected even by aLIGO when at design sensitivity. Given that our results are computed in the case of a purely poloidal magnetic field, these are to be considered as upper limits, since a real NS is expected to possess a mixed field and, as a consequence, a lower deformation, leading to lower CGWs strain. Since the pulsars in the ATNF catalogue do indeed exist, we also identified some of the NSs which have, according to our study, the highest chance of being detected. Finally, we considered also the case of NSs endowed by a superconducting core, in which case the effective magnetic field distorting the star is greatly boosted. In this situation, we found that a considerable fraction of all MSPs in the Galaxy is expected to be detected by means of CGWs in the next years; of course, also a non-detection can be used to put bounds on the possible existence of a superconducting core in MSPs.

Finally, as described in Chap. 9 we introduced a novel way to test GR in the vicinity of LMXBs, by means of the light bending property of the spacetime around compact objects. These are systems where accretion of matter onto a NS generates an accretion disk. A particular feature of these systems is the possibility of the emission of the fluorescent Fe K_α line at 6.4 KeV. As already known, observations of this line can be used to infer limits on the radius of the NS by modelling the effect of the disk occultation on the line by the NS itself. We applied this idea to the case of NSs in STTs. Given that scalarised NSs possess different radii than their GR counterparts at the same mass, we

found that the degree of scalarisation indeed affects the occultation of the accretion disk. As a consequence, the characterising shape of the Fe K_α line is modified with respect to GR in a way that depends on the scalar charge of the NS. While, in general, this effect is very small, we found that next generation X-ray satellites may be able to detect such small deviations with a reasonable observation time.

While our work already constitues an in depth exploration of the modelling of magnetised NSs in GR and in massless STTs, some extensions would allow one to infer even more meaningful information both on the structure of the NSs and on the properties of their CGWs emission. While the use of a purely poloidal and purely toroidal magnetic field allows us to describe the extreme boundaries of the possible magnetic field geometries, the modelling of mixed field configurations would allow to draw more precise conclusions when comparing models to observations. Moreover, the inclusion of rotation, possibly with realistic profiles, which is already implemented in `XNS` (see also App. A), would allow to model more realistic NSs, at the cost of enlarging the paramater space to explore. Finally, while the results we found concern the internal structure of NSs, and as such these are valid also in the case of STTs where the scalar field has a mass, as argued in Chap. 2, the remaining parameter space that is deemed valid for massless STTs is small. For this reason, it is important to generalise what we found to the case of scalar fields endowed with a mass. In this sense, our work can be regarded as the foundations onto which one can build more complex studies of magnetised NSs in more general STTs. As an example, we recall that STTs are just a subset of a more extended class of alternative theories of gravity, TeVeS (Bekenstein 2004), which predict also the possible existence of non-minimally coupled vector fields. As in STTs, even theories with vector fields can present phenomena of 'spontaneous vectorisation' (Hellings & Nordtvedt 1973; Heisenberg 2014; Kase et al. 2018, 2020). Interestingly the mathematics behind spontaneous vectorisation is not dissimilar to the one used to model non-linear current terms in magnetised NSs (Pili et al. 2014), and spontaneous magnetic-vectorisation has already been treated and discussed within the framework of the standard techniques that we have illustrated here (Bucciantini et al. 2015). This shows that the algorithms and approaches we have introduced, even if developed in the context of the specific case of magnetic fields, have a far larger applicability to vector fields in general.

Appendix A

XCFC for a rotating scalarised neutron star

We show here how the standard techniques of XNS, based on the XCFC approach to the solution of the metric functions, can be adapted to take into account the presence of a scalar field. For simplicity we are going to consider here only un-magnetised rotators. The generalisation to magnetised ones is trivial and strictly follows what was done in Pili et al. (2017). In the E-frame the standard set of XCFC equations is:

$$\Delta_L W^i = 8\pi f^{ij}\hat{S}_j \,, \tag{A.1}$$

$$\Delta\psi = -2\pi\hat{E}\psi^{-1} - \tfrac{1}{8}f_{ik}f^{jl}\hat{A}^{ij}\hat{A}^{kl}\psi^{-7} \,, \tag{A.2}$$

$$\Delta(\alpha\psi) = [2\pi(\hat{E}+2\hat{S})\psi^{-2} + \tfrac{7}{8}f_{ik}f^{jl}\hat{A}^{ij}\hat{A}^{kl}\psi^{-8}]\alpha\psi, \tag{A.3}$$

$$\Delta_L\beta^i = 16\pi\alpha\psi^{-6}f^{ij}\hat{S}_j + 2\hat{A}^{ij}\hat{\nabla}_j(\alpha\psi^{-6}) \,, \tag{A.4}$$

where $f_{ij}$is the flat 3-metric, $\hat{\nabla}_i$ is the flat covariant derivative ($\hat{\nabla}_k f_{ij} = 0$), and $\Delta = \hat{\nabla}_i\hat{\nabla}^i$ is the usual Laplacian operator in flat 3-space. Δ_L is defined as:

$$\Delta_L X^i = \Delta X^i + \tfrac{1}{3}\hat{\nabla}^i(\hat{\nabla}_j X^j) \tag{A.5}$$

and

$$\hat{A}^{ij} = \hat{\nabla}^i W^j + \hat{\nabla}^j W^i - \tfrac{2}{3}f^{ij}(\hat{\nabla}_k W^k) \,. \tag{A.6}$$

The source terms come from the 3+1 decomposition of the energy-momentum tensor in the E-frame:

$$\hat{E} = \psi^6\bar{n}_\mu\bar{n}_\nu(\bar{T}^{\mu\nu}_{\rm p} + \bar{T}^{\mu\nu}_{\rm s}) \,, \tag{A.7}$$

$$\hat{S}_j = \psi^6\bar{n}_\mu\bar{\gamma}_{j\nu}(\bar{T}^{\mu\nu}_{\rm p} + \bar{T}^{\mu\nu}_{\rm s}) \,, \tag{A.8}$$

$$\hat{S} = \psi^6\bar{\gamma}^j_\mu\bar{\gamma}_{j\nu}(\bar{T}^{\mu\nu}_{\rm p} + \bar{T}^{\mu\nu}_{\rm s}) \,. \tag{A.9}$$

For stationary ($\partial_t = 0$) and axisymmetric ($\partial_\phi = 0$) configurations, for the metric given by Eq. 3.27 (where the only non vanishing component of the shift vector is β^ϕ), assuming that the only non vanishing component of the velocity is v^ϕ, it can be shown that

$$\hat{E} = \psi^6 \left\{ \mathcal{A}^4 \left[\Gamma^2 (e + p) - p \right] + \tfrac{1}{8\pi} Q^2 \right\} , \tag{A.10}$$

$$\hat{S}_r = \hat{S}_\theta = 0 , \tag{A.11}$$

$$\hat{S}_\phi = \psi^6 \mathcal{A}^3 (e + p) \Gamma v_\phi , \tag{A.12}$$

$$\hat{S} = \psi^6 \left\{ \mathcal{A}^4 \left[\Gamma^2 (e + p) v^2 + 3p \right] - \tfrac{1}{8\pi} Q^2 \right\} , \tag{A.13}$$

where e, p, and $v^2 = \tilde{\gamma}_{ij} v^i v^j$ are all in the J-frame and $Q^2 = \bar{\gamma}_{ij} Q^i Q^j$ is instead in the E-frame.

If on a time slice the values of the physical quantities are provided as well as the scalar field, then the XCFC set of equations can be solved for the metric component in the E-frame. It is evident that the XCFC scheme retains its main interesting property of decoupling the various equations, allowing to solve them separately, one after the other. This holds also in the more general time dependent case. In fact 3+1 schemes for GRHD and MHD evolve the conserved quantities in the J-frame $\psi^6 \mathcal{A}^3 \tilde{E}_{\rm p}$ and $\psi^6 \mathcal{A}^3 \tilde{S}_i^{\rm p}$. Combined with a scheme that evolves also the 3+1 components of the scalar field P and Q^i, the XCFC equations can then be used to solve for the metric.

Appendix B

Global quantities

In this appendix we list the main global quantities used in this work. We give their general form, valid also in the case of a non-static, but stationary, spacetime.

The Komar mass in the E-frame is

$$\begin{aligned}\bar{M}_{\rm k} &= 2\int_{\Sigma_t}\left(\bar{T}_{\mu\nu}-\frac{1}{2}\bar{T}g_{\mu\nu}\right)n^\mu\xi^\nu\sqrt{\gamma}d^3x = \\ &= 2\pi\int\mathcal{A}^4\Big[2p+(\varepsilon+\rho+p)\Gamma^2\left(1+v^iv_i-2\alpha^{-1}\mathcal{A}v_i\beta^i\right)+ \\ &+E^iE_i+B^iB_i+\epsilon_{ijk}\alpha^{-1}\beta^i\mathcal{A}^2E^jB^k\Big]\sqrt{-g}drd\theta\ ,\end{aligned} \tag{B.1}$$

where Σ_t is a spacelike hypersurface of constant coordinate time t and ξ^ν is the time-like Killing vector associated to the stationarity of the spacetime. In our static case it reduces to

$$\bar{M}_{\rm k} = 2\pi\int\mathcal{A}^4\left[\varepsilon+\rho+3p+B^iB_i\right]\alpha\psi^6r^2\sin\theta drd\theta. \tag{B.2}$$

The baryonic mass, which is the same in the E-frame and in the J-frame, is

$$M_0 = \int_{\Sigma_t}\mathcal{A}^3\rho\Gamma\sqrt{\gamma}d^3x\ , \tag{B.3}$$

which in our case is

$$M_0 = 2\pi\int\mathcal{A}^3\rho\psi^6r^2\sin\theta drd\theta\ . \tag{B.4}$$

The proper mass, which is the same in the E-frame and in the J-frame, is

$$M_{\rm p} = 2\pi\int\mathcal{A}^3\left(\varepsilon+\rho\right)\psi^6r^2\sin\theta drd\theta\ . \tag{B.5}$$

The scalar charge of the star in the E-frame, $\bar{Q}_{\rm s}$, is defined as the monopole component of the scalar field at asymptotically large radii:

$$\lim_{r\to\infty}\chi(r) = \frac{\bar{Q}_{\rm s}}{r}\ . \tag{B.6}$$

By integrating Eq. 2.13 over a spherical volume of asymptotically large radius, using Stokes' theorem and using the fact that $\bar{T}_{\rm p} = 0$ outside the star's surface, we obtain

$$\bar{Q}_{\rm s} = 2\pi\int \alpha\alpha_{\rm s}(\chi)\mathcal{A}^4 T_{\rm p}\psi^6 r^2\sin\theta dr d\theta\ , \tag{B.7}$$

where $T_{\rm p} = 3p - \varepsilon - \rho$. The circumferential radius in the J-frame is

$$\tilde{R}_{\rm c} = \Big[\mathcal{A}\psi^2 r\Big]_{\theta=\pi/2} \tag{B.8}$$

The magnetic energy in the J-frame is

$$\tilde{\mathcal{H}} = -\int_{\Sigma_t}\frac{1}{2}\left(B_i B^i + E_i E^i\right)\mathcal{A}^2 u_\nu n^\nu\sqrt{\gamma}d^3x\ , \tag{B.9}$$

which reduces to

$$\tilde{\mathcal{H}} = \pi\int B_i B^i\mathcal{A}^3\psi^6 r^2\sin\theta dr d\theta\ . \tag{B.10}$$

The binding energy of the star in the E-frame is defined as

$$\bar{W} = M_{\rm p} - M_{\rm k} + \bar{\mathcal{H}}\ . \tag{B.11}$$

The flux of the toroidal magnetic field, which is the same in the E-frame and in the J-frame, is

$$\Phi = \int r\mathcal{A}^2\sqrt{B^i B_i}\psi^4 dr d\theta\ . \tag{B.12}$$

The magnetic dipole moment in the J-frame is

$$\tilde{\mu} = \check{A}_\phi\frac{4r^3}{4r + M_{\rm k}}\bigg|_{r\gg R_{\rm c}}\ . \tag{B.13}$$

The value converges already for $r \simeq 5 - 10R_{\rm c}$.

The quadrupole deformation of the star in the E-frame is defined as

$$\bar{e} = \frac{\bar{I}^{\rm p}_{zz} + \bar{I}^{\rm s}_{zz} - \bar{I}^{\rm p}_{xx} - \bar{I}^{\rm s}_{xx}}{\bar{I}^{\rm p}_{zz}}\ , \tag{B.14}$$

where the physical and scalar field moments of inertia around the polar axis z and the x axis are, respectively,

$$\bar{I}^{\mathrm{p}}_{zz} = 2\pi \int \mathcal{A}^4 \left(\varepsilon + \rho\right) r^4 \sin^3\theta dr d\theta \ , \tag{B.15}$$

$$\bar{I}^{\mathrm{s}}_{zz} = -\frac{1}{4} \int \psi^4 Q^2 r^4 \sin^3\theta dr d\theta \ , \tag{B.16}$$

$$\bar{I}^{\mathrm{p}}_{xx} = \pi \int \mathcal{A}^4 \left(\varepsilon + \rho\right) r^4 \sin\theta \left(1 + \cos^2\theta\right) dr d\theta \ , \tag{B.17}$$

$$\bar{I}^{\mathrm{s}}_{xx} = -\frac{1}{8} \int \psi^4 Q^2 r^4 \sin\theta \left(1 + \cos^2\theta\right) dr d\theta \ . \tag{B.18}$$

We note that we defined the moments of inertia of the scalar field in the same way as the usual physical ones: as integrals of the energy density $\bar{T}^{00}_{\mathrm{s}}$.

The quadrupolar deformation of the trace $\bar{e}_{\mathrm{s}}$ is related to the quadrupolar and monopolar distributions of the scalar field at asimptotically large radii, and is defined as

$$\bar{e}_{\mathrm{s}} = \frac{\int \alpha_{\mathrm{s}}(\chi) \mathcal{A}^4 T_{\mathrm{p}} \left(2 - 3\sin^2\theta\right) r^4 \sin\theta dr d\theta}{r_{\mathrm{e}}^2 \int \alpha_{\mathrm{s}}(\chi) \mathcal{A}^4 T_{\mathrm{p}} r^2 \sin\theta dr d\theta} \ . \tag{B.19}$$

We note that the denominator is the Newtonian equivalent of $\bar{Q}_{\mathrm{s}} \bar{R}_{\mathrm{c}}^2$.

Appendix C

The XNS package

The XNS code is written in the Fortran 90 language and consists of several files. In this appendix we briefly describe the modifications which have been done in the new version of XNS, how the code can be compiled and the contents of each file. A more in-depth explanation can be found in the official documentation: https://www.arcetri.inaf.it/science/ahead/XNS/html/intro.html.

The new version (4.0) of XNS allows to compute axisymmetric, magnetised, rotating models of NSs both in GR and in massless STTs. The magnetic configuration can be chosen to be purely poloidal, purely toroidal and the twisted torus one. Various rotation laws have been introduced, both uniform and differential, and the possibility to use a tabulated EoS has been added. We note that scalarised models were not tested neither using the twisted torus magnetic configuration nor rotation.

XNS can be compiled in three different ways:

- `make serial`: the standard way to compile XNS. In this case a single solution is found with the specified central density.
- `make nwtrps`: compiles XNS using a Newton-Raphson method to converge on the quantity specified by the user, either the gravitational or the baryonic mass.
- `make parspace`: compiles XNS various times with different initial conditions, in order to sample the parameter space spanned by the magnetic, rotation and density parameters. The computation of the various models is made in parallel using the MPI framework.

The files contained in the XNS package are:

- `XNS.f90`: the main program, which makes consistency checks and invokes `XNSMAIN.f90`. Depending on the compiling options, it can simply call `XNSMAIN.f90` (if XNS was

compiled using the `make serial` option), perform a Newton-Raphson search to converge on a specified quantity (if the `make nwtrps` option was used) or compute many models in parallel with different initial conditions (if `make parspace` was used).

- `XNSMAIN.f90`: the main kernel of the code, which defines the numerical grid, builds a 2D initial guess based on the 1D S-TOV output of `TOVINIMOD.f90`, performs the convergence loop calling all the various metric solvers and procedures in the appropriate order. When the loop is over, it writes all the outputs.
- `TOVINIMOD.f90`: solves the 1D S-TOV (either in GR or in STTs) equations in isotropic coordinates to provide the initial guess. It uses a relaxation method to achieve convergence.
- `HYDROEQ.f90`: given the CFC metric and a value of the central density, it computes the equilibrium configuration for the corresponding Bernoulli integral. Then, it computes local equilibrium quantities.
- `PHYSICS.f90`: contains functions used to define the numerical grid and to perform EoS-related computations.
- `ROTATION.f90`: contains functions related to the rotation profile of the NS.
- `FUNCTIONS.f90`: contains functions of generic use, like those used to solve linear systems or for interpolation.
- `SYSTEMXNS.f90`: contains the definition of common arrays used throughout the code and all parameters used by `XNS`, including those that must be specified by the user.

Included are some visualisation routines:

- `starplot_polo.py`, `starplot_toro.py`, `starplot_unmag.py`: plots a section of the star in the x-z plane along with the contours of the magnetic field (if the model is magnetised), the scalar field or the density.
- `profiles_polo.py`, `profiles_toro.py`, `profiles_unmag.py`: plots the radial profiles, both at the pole and at the equator, of the density, pressure, conformal factor, lapse function, scalar field and magnetic field (if the model is magnetised).

Bibliography

Abbott, B. P., Abbott, R., Abbott, T. D., et al. 2018, Living Rev. Relativ., 21, 3
Abbott, B. P., Abbott, R., Abbott, T. D., et al. 2016, Phys. Rev. Lett., 116, 061102
Abbott, B. P., Abbott, R., Abbott, T. D., et al. 2017a, ApJ, 848, L13
Abbott, B. P., Abbott, R., Abbott, T. D., et al. 2017b, Phys. Rev. Lett., 119, 161101
Abbott, B. P., Abbott, R., Abbott, T. D., et al. 2017c, ApJ, 848, L12
Abbott, B. P., Abbott, R., Abbott, T. D., et al. 2017, ApJ, 851, L16
Abbott, B. P., Abbott, R., Abbott, T. D., et al. 2018, Phys. Rev. Lett., 121, 161101
Abbott, R., Abbott, T. D., Abraham, S., et al. 2021a, arXiv e-prints, arXiv:2104.14417
Abbott, R., Abbott, T. D., Abraham, S., et al. 2021b, ApJ, 913, L27
Abbott, R., Abbott, T. D., Abraham, S., et al. 2020, ApJ, 902, L21
Abbott, R., Abbott, T. D., Abraham, S., et al. 2020, ApJ, 896, L44
Abramowicz, M. A. & Kluźniak, W. 2005, Ap&SS, 300, 127
Aguilera, D. N., Pons, J. A., & Miralles, J. A. 2008, ApJ, 673, L167
Akgün, T., Reisenegger, A., Mastrano, A., & Marchant, P. 2013, MNRAS, 433, 2445
Akgün, T. & Wasserman, I. 2008, MNRAS, 383, 1551
Akmal, A., Pandharipande, V. R., & Ravenhall, D. G. 1998, Phys. Rev. C, 58, 1804–1828
Alcock, C., Farhi, E., & Olinto, A. 1986, ApJ, 310, 261–272
Alcubierre, M. 2008, Introduction to 3+1 Numerical Relativity, International Series of Monographs on Physics (OUP Oxford)
Alsing, J., Silva, H. O., & Berti, E. 2018, MNRAS, 478, 1377
Anderson, D., Freire, P., & Yunes, N. 2019, Class. Quantum Gravity, 36, 225009
Anderson, D. & Yunes, N. 2019, Class. Quantum Gravity, 36, 165003
Andersson, N. 1998, ApJ, 502, 708
Andreou, N., Franchini, N., Ventagli, G., & Sotiriou, T. P. 2019, Phys. Rev. D, 99, 124022
Antoniadis, J., Freire, P. C. C., Wex, N., et al. 2013, Science, 340, 448
Antoniadis, J., Tauris, T. M., Ozel, F., et al. 2016, arXiv e-prints, arXiv:1605.01665
Archibald, A. M., Gusinskaia, N. V., Hessels, J. W. T., et al. 2018, Nature, 559, 73
Asseo, E. & Khechinashvili, D. 2002, MNRAS, 334, 743
Avancini, S. S., Menezes, D. P., Pinto, M. B., & Providência, C. 2012, Phys. Rev. D, 85, 091901
Baade, W. & Zwicky, F. 1934, Proc. Natl. Acad. Sci. USA, 20, 254
Barausse, E. 2017, in Proceedings of The 3rd International Symposium on "Quest for the Origin of Particles and the Universe", Vol. 294 (SISSA Medialab), 029

Barausse, E., Palenzuela, C., Ponce, M., & Lehner, L. 2013, Phys. Rev. D, 87, 081506
Barcons, X., Barret, D., Decourchelle, A., et al. 2017, Astron. Nachr., 338, 153
Barret, D., Lam Trong, T., den Herder, J.-W., et al. 2016, Society of Photo-Optical Instrumentation Engineers (SPIE) Conference Series, Vol. 9905, The Athena X-ray Integral Field Unit (X-IFU), 99052F
Bassett, B. A., Kunz, M., Parkinson, D., & Ungarelli, C. 2003, Phys. Rev. D, 68, 043504
Bauswein, A. 2019, Ann. Physics, 411, 167958
Bauswein, A., Just, O., Janka, H.-T., & Stergioulas, N. 2017, ApJ, 850, L34
Baym, G., Furusawa, S., Hatsuda, T., Kojo, T., & Togashi, H. 2019, ApJ, 885, 42
Baym, G., Hatsuda, T., Kojo, T., et al. 2018, Rep. Prog. Phys., 81, 056902
Baym, G., Pethick, C., & Sutherland, P. 1971, ApJ, 170, 299
Bekenstein, J. D. 2004, Phys. Rev. D, 70, 083509
Bekenstein, J. D. & Oron, A. 2001, Found. Phys., 31, 895
Beloborodov, A. M. 2017, ApJ, 843, L26
Bergmann, P. G. 1968, Int. J. Theor. Phys., 1, 25
Berti, E., Barausse, E., Cardoso, V., et al. 2015, Class. Quantum Gravity, 32, 243001
Bertolami, O. & Páramos, J. 2016, Gen. Relativ. Gravit., 48, 34
Bertotti, B., Iess, L., & Tortora, P. 2003, Nature, 425, 374
Bhat, N. D. R., Bailes, M., & Verbiest, J. P. W. 2008, Phys. Rev. D, 77, 124017
Bignami, G. F., Caraveo, P. A., De Luca, A., & Mereghetti, S. 2003, Nature, 423, 725
Bilous, A. V., Watts, A. L., Harding, A. K., et al. 2019, ApJ, 887, L23
Biryukov, A. & Abolmasov, P. 2021, MNRAS
Bisnovatyi-Kogan, G. S. & Komberg, B. V. 1974, SvA, 18, 217
Bocquet, M., Bonazzola, S., Gourgoulhon, E., & Novak, J. 1995, A&A, 301, 757
Bodmer, A. R. 1971, Phys. Rev. D, 4, 1601–1606
Bombaci, I., Drago, A., Logoteta, D., Pagliara, G., & Vidaña, I. 2021, Phys. Rev. Lett., 126, 162702
Bombaci, I. & Logoteta, D. 2018, A&A, 609, A128
Bonazzola, S. & Gourgoulhon, E. 1996, A&A, 312, 675
Boyles, J., Lynch, R. S., Ransom, S. M., et al. 2013, ApJ, 763, 80
Braithwaite, J. 2009, MNRAS, 397, 763
Braithwaite, J. & Nordlund, A. 2006, A&A, 450, 1077
Braithwaite, J. & Spruit, H. C. 2006, A&A, 450, 1097
Brans, C. & Dicke, R. H. 1961, Phys. Rev., 124, 925
Brax, P., Davis, A.-C., & Jha, R. 2017, Phys. Rev. D, 95, 083514
Breu, C. & Rezzolla, L. 2016, MNRAS, 459, 646
Brown, J. D. 1993, Class. Quant. Grav., 10, 1579
Bucciantini, N. & Del Zanna, L. 2011, A&A, 528, A101
Bucciantini, N. & Del Zanna, L. 2013, MNRAS, 428, 71
Bucciantini, N., Pili, A. G., & Zanna, L. D. 2015, MNRAS, 447, 1
Bucciantini, N. & Soldateschi, J. 2020, MNRAS, 495, L56
Buchdahl, H. A. 1970, MNRAS, 150, 1
Buikema, A., Cahillane, C., Mansell, G. L., et al. 2020, Phys. Rev. D, 102, 062003

Burgess, C. P. 2015, The cosmological constant problem: why it's hard to get dark energy from microphysics (Oxford University Press)
Cackett, E. M., Miller, J. M., Bhattacharyya, S., et al. 2008, ApJ, 674, 415
Cai, B.-J., Fattoyev, F. J., Li, B.-A., & Newton, W. G. 2015, Phys. Rev. C, 92, 015802
Camelio, G., Dietrich, T., Marques, M., & Rosswog, S. 2019, Phys. Rev. D, 100, 123001
Capozziello, S. & De Laurentis, M. 2010, Invariance Principles and Extended Gravity: Theory and Probes, Physics Research and Technology (Nova Science Publishers)
Capozziello, S. & de Laurentis, M. 2011, Phys. Rep., 509, 167
Capozziello, S. & Fang, L. Z. 2002, Int. J. Mod. Phys. D, 11, 483
Capozziello, S., Nojiri, S., Odintsov, S. D., & Troisi, A. 2006, Phys. Lett. B, 639, 135
Cartan, É. 1986, On Manifolds with an Affine Connection and the Theory of General Relativity, Monographs and Textbooks in Physical Science (Bibliopolis)
Carter, B. 1969, J. Mat. Phys., 10, 70
Carter, B. 1970, Commun. Mat. Phys., 17, 233
Carter, B. 2009, Gen. Relativ. Gravit., 41, 2873
Carter, B. 2010, Gen. Relativ. Gravit., 42, 653
Chabanat, E. 1995, PhD thesis, Lyon 1
Chandrasekhar, S. & Fermi, E. 1953, ApJ, 118, 116
Chandrasekhar, S. & Kendall, P. C. 1957, ApJ, 126, 457
Chandrasekhar, S. & Prendergast, K. H. 1956, Proc. Natl. Acad. Sci. USA, 42, 5
Chatterjee, D., Elghozi, T., Novak, J., & Oertel, M. 2015, MNRAS, 447, 3785
Chatterjee, D. & Vidaña, I. 2016, Eur. Phys. J. A, 52, 29
Cieślar, M., Bulik, T., Curyło, M., et al. 2021, A&A, 649, A92
Ciolfi, R., Kastaun, W., Kalinani, J. V., & Giacomazzo, B. 2019, Phys. Rev. D, 100, 023005
Ciolfi, R. & Rezzolla, L. 2013, MNRAS, 435, L43
Copeland, E. J., Sami, M., & Tsujikawa, S. 2006, Int. J. Mod. Phys. D, 15, 1753
Cordero-Carrión, I., Cerdá-Durán, P., Dimmelmeier, H., et al. 2009, Phys. Rev. D, 79, 024017
Costa, P., Ferreira, M., Hansen, H., Menezes, D. P., & Providência, C. 2014, Phys. Rev. D, 89, 056013
Coughenour, B. M., Cackett, E. M., Miller, J. M., & Ludlam, R. M. 2018, ApJ, 867, 64
Cruces, M., Reisenegger, A., & Tauris, T. M. 2019, MNRAS, 490, 2013
Cutler, C. 2002, Phys. Rev. D, 66, 084025
Dall'Osso, S., Shore, S. N., & Stella, L. 2009, MNRAS, 398, 1869
Dall'Osso, S. & Stella, L. 2021, arXiv e-prints, arXiv:2103.10878
Damour, T. & Esposito-Farese, G. 1992, Class. Quantum Gravity, 9, 2093
Damour, T. & Esposito-Farèse, G. 1993, Phys. Rev. Lett., 70, 2220
Damour, T. & Esposito-Farèse, G. 1996, Phys. Rev. D, 54, 1474
Damour, T., Piazza, F., & Veneziano, G. 2002, Phys. Rev. Lett., 89, 081601
Danielewicz, P. & Lee, J. 2009, Nuclear Phys. A, 818, 36–96
Das, U. & Mukhopadhyay, B. 2015, J. Cosmology Astropart. Phys., 2015, 016
Dauser, T., García, J., & Wilms, J. 2016, Astron. Nachr., 337, 362
De Felice, A. & Tanaka, T. 2010, Prog. Theor. Phys., 124, 503

De Grandis, D., Turolla, R., Wood, T. S., et al. 2020, ApJ, 903, 40
DeFelice, A., Hindmarsh, M., & Trodden, M. 2006, J. Cosmology Astropart. Phys., 2006, 005
Degenaar, N., Miller, J. M., Chakrabarty, D., et al. 2015, MNRAS, 451, L85
Del Zanna, L. & Bucciantini, N. 2018, MNRAS, 479, 657
Del Zanna, L. & Chiuderi, C. 1996, A&A, 310, 341
Del Zanna, L., Papini, E., Landi, S., Bugli, M., & Bucciantini, N. 2016, MNRAS, 460, 3753
Del Zanna, L., Zanotti, O., Bucciantini, N., & Londrillo, P. 2007, A&A, 473, 11
Delphenich, D. 2005, in 6th International Conference on Symmetry in Nonlinear Mathematical Physics (SNMP 05) Kiev, Ukraine, June 20-26, 2005
Demorest, P. B., Pennucci, T., Ransom, S. M., Roberts, M. S. E., & Hessels, J. W. T. 2010, Nature, 467, 1081
Dergachev, V. & Papa, M. A. 2020, Phys. Rev. Lett., 125, 171101
Deruelle, N. 2011, Gen. Relativ. Gravit., 43, 3337
Deser, S. 2000, Ann. Phys. (Berl.), 9, 299
Di Casola, E., Liberati, S., & Sonego, S. 2015, Am. J. Phys., 83, 39
Dicke, R. H. 1962, Phys. Rev., 125, 2163
Dimmelmeier, H., Novak, J., Font, J. A., Ibáñez, J. M., & Müller, E. 2005, Phys. Rev. D, 71, 064023
Dimmelmeier, H., Stergioulas, N., & Font, J. A. 2006, MNRAS, 368, 1609
Dohi, A., Kase, R., Kimura, R., Yamamoto, K., & Hashimoto, M.-a. 2021, Progress of Theoretical and Experimental Physics, 2021, 093E01
Doneva, D. D. & Yazadjiev, S. S. 2016, J. Cosmology Astropart. Phys., 2016, 019
Doneva, D. D. & Yazadjiev, S. S. 2020, Phys. Rev. D, 101, 064072
Doneva, D. D., Yazadjiev, S. S., Staykov, K. V., & Kokkotas, K. D. 2014, Phys. Rev. D, 90, 104021
Doneva, D. D., Yazadjiev, S. S., Stergioulas, N., & Kokkotas, K. D. 2013, Phys. Rev. D, 88, 084060
Doneva, D. D., Yazadjiev, S. S., Stergioulas, N., & Kokkotas, K. D. 2018, Phys. Rev. D, 98, 104039
Doneva, D. D., Yazadjiev, S. S., Stergioulas, N., Kokkotas, K. D., & Athanasiadis, T. M. 2014, Phys. Rev. D, 90, 044004
Douchin, F. & Haensel, P. 2001, A&A, 380, 151–167
Drago, A., Lavagno, A., Pagliara, G., & Pigato, D. 2016, Eur. Phys. J. A, 52, 40
Duncan, R. C. & Thompson, C. 1992, ApJ, 392, L9
Dyer, E. & Hinterbichler, K. 2009, Phys. Rev. D, 79, 024028
Event Horizon Telescope Collaboration, Akiyama, K., Alberdi, A., et al. 2019, ApJ, 875, L1
Faraoni, V. & Capozziello, S. 2011, Beyond Einstein Gravity, Vol. 170
Farhi, E. & Jaffe, R. L. 1984, Phys. Rev. D, 30, 2379–2390
Farrow, N., Zhu, X.-J., & Thrane, E. 2019, ApJ, 876, 18
Faucher-Giguère, C.-A. & Kaspi, V. M. 2006, ApJ, 643, 332
Faucher-Giguère, C.-A. & Loeb, A. 2010, J. Cosmology Astropart. Phys., 2010, 005
Ferrario, L., Melatos, A., & Zrake, J. 2015, Space Sci. Rev., 191, 77
Ferraro, V. C. A. 1954, ApJ, 119, 407
Ferreira, M., Costa, P., Menezes, D. P., Providência, C., & Scoccola, N. N. 2014, Phys. Rev. D, 89, 016002
Fonseca, E., Cromartie, H. T., Pennucci, T. T., et al. 2021, ApJ, 915, L12

Fortin, M., Providencia, C., Raduta, A. R., et al. 2016, Phys. Rev. C, 94
Fraga, E. S., Kurkela, A., & Vuorinen, A. 2014, ApJ, 781, L25
Franceschetti, K. & Del Zanna, L. 2020, Universe, 6, 83
Franzon, B., Dexheimer, V., & Schramm, S. 2016, Phys. Rev. D, 94, 044018
Frederick, S. G., Thompson, K. L., & Kuchera, M. P. 2021, MNRAS, 503, 2764
Freire, P. C. C., Wex, N., Esposito-Farèse, G., et al. 2012, MNRAS, 423, 3328
Fricke, K. 1969, A&A, 1, 388
Frieben, J. & Rezzolla, L. 2012, MNRAS, 427, 3406
Friedman, J. L. & Stergioulas, N. 2013, Rotating Relativistic Stars, Cambridge Monographs on Mathematical Physics (Cambridge University Press)
Fujii, Y. & Maeda, K.-i. 2003, The Scalar-Tensor Theory of Gravitation, Cambridge Monographs on Mathematical Physics (Cambridge University Press)
Fujisawa, K. & Eriguchi, Y. 2015, PASJ, 67, 53
Gao, H., Zhang, B., & Lü, H.-J. 2016, Phys. Rev. D, 93, 044065
Gavriil, F. P., Kaspi, V. M., & Woods, P. M. 2002, Nature, 419, 142
Gerosa, D., Sperhake, U., & Ott, C. D. 2016, Class. Quantum Gravity, 33, 135002
Glendenning, N. K. 2000, Compact Stars: Nuclear Physics, Particle Physics, and General Relativity, 2nd edn., Astronomy and Astrophysics Library (Springer-Verlag)
Godzieba, D. A., Radice, D., & Bernuzzi, S. 2021, ApJ, 908, 122
Gold, T. 1968, Nature, 218, 731
Gomes, R. O., Pais, H., Dexheimer, V., Providência, C., & Schramm, S. 2019, A&A, 627, A61
Gonzalez, M. E., Stairs, I. H., Ferdman, R. D., et al. 2011, ApJ, 743, 102
Gourgoulhon, E. 2010, arXiv e-prints, arXiv:1003.5015
Gourgoulhon, É. 2012, 3+1 Formalism in General Relativity: Bases of Numerical Relativity, Lecture Notes in Physics (Springer Berlin Heidelberg)
Grandclément, P., Bonazzola, S., Gourgoulhon, E., & Marck, J. A. 2001, J. Comput. Phys., 170, 231
Grandclément, P. & Novak, J. 2009, Living Rev. Relativ., 12, 1
Green, M. B., Schwartz, J. H., & Witten, E. 1988, Astron. Nachr., 309, 297
Grégoire, T. & Knödlseder, J. 2013, A&A, 554, A62
Guerra Chaves, A. & Hinderer, T. 2019, J. Phys. G: Nucl. Part. Phys., 46, 123002
Gulminelli, F. & Raduta, A. R. 2015, Phys. Rev. C, 92, 055803
Güver, T., Göğüş, E., & Özel, F. 2011, MNRAS, 418, 2773
Haensel, P., Potekhin, A. Y., & Yakovlev, D. G. 2007, Neutron stars 1: Equation of state and structure, Vol. 326 (New York, USA: Springer)
Haensel, P., Urpin, V. A., & Yakovlev, D. G. 1990, A&A, 229, 133
Hagihara, Y., Era, N., Iikawa, D., Takeda, N., & Asada, H. 2020, Phys. Rev. D, 101, 041501
Harada, T. 1998, Phys. Rev. D, 57, 4802
Harry, G., Fritschel, P., Shaddock, D., Folkner, W., & Phinney, E. 2006, Class. Quant. Grav., 23, 4887, [Erratum: Class.Quant.Grav. 23, 7361 (2006)]
Haskell, B., Jones, D. I., & Andersson, N. 2006, MNRAS, 373, 1423
Haskell, B., Samuelsson, L., Glampedakis, K., & Andersson, N. 2008, MNRAS, 385, 531

Haskell, B. & Sedrakian, A. 2018, in The Physics and Astrophysics of Neutron Stars, ed. L. Rezzolla, P. Pizzochero, D. I. Jones, N. Rea, & I. Vidaña (Cham: Springer International Publishing), 401–454
Hawking, S. W. 1972, Commun. Mat. Phys., 25, 167
Hawking, S. W. & Ellis, G. F. R. 1973, The Large Scale Structure of Space-Time, Cambridge Monographs on Mathematical Physics (Cambridge University Press)
Heisenberg, L. 2014, J. Cosmology Astropart. Phys., 2014, 015
Hellings, R. W. & Nordtvedt, K. 1973, Phys. Rev. D, 7, 3593
Hempel, M. & Schaffner-Bielich, J. 2010, Nuclear Phys. A, 837, 210–254
Hessels, J. W. T. 2018, arXiv e-prints, arXiv:1804.06149
Hewish, A., Bell, S. J., Pilkington, J. D. H., Scott, P. F., & Collins, R. A. 1968, Nature, 217, 709
Hild, S., Abernathy, M., Acernese, F., et al. 2011, Class. Quantum Gravity, 28, 094013
Hofmann, F. & Müller, J. 2018, Class. Quantum Gravity, 35, 035015
Homan, J., Steiner, J. F., Lin, D., et al. 2018, ApJ, 853, 157
Hooper, D., Cholis, I., Linden, T., Siegal-Gaskins, J. M., & Slatyer, T. R. 2013, Phys. Rev. D, 88, 083009
Horowitz, C. J. & Piekarewicz, J. 2001, Phys. Rev. Lett., 86, 5647–5650
Iaria, R., D'Aí, A., di Salvo, T., et al. 2009, A&A, 505, 1143
Iosif, P. & Stergioulas, N. 2014, Gen. Relativ. Gravit., 46, 1800
Isenberg, J. A. 2008, Int. J. Mod. Phys. D, 17, 265
Jankowski, F., van Straten, W., Keane, E. F., et al. 2017, MNRAS, 473, 4436
Just, K. 1959, Z. Naturforsch. A, 14, 751
Kamenshchik, A., Moschella, U., & Pasquier, V. 2001, Phys. Lett. B, 511, 265
Kammoun, E. S., Nardini, E., & Risaliti, G. 2018, A&A, 614, A44
Kanakis-Pegios, A., Koliogiannis, P. S., & Moustakidis, C. C. 2021, Symmetry, 13, 183
Kandel, D. & Romani, R. W. 2020, ApJ, 892, 101
Kase, R., Minamitsuji, M., & Tsujikawa, S. 2018, Phys. Rev. D, 97, 084009
Kase, R., Minamitsuji, M., & Tsujikawa, S. 2020, Phys. Rev. D, 102, 024067
Kaspi, V. M. & Beloborodov, A. M. 2017, ARA&A, 55, 261–301
Kawamura, S., Ando, M., Nakamura, T., et al. 2008, J. Phys. Conf. Ser., 122, 012006
Kiel, P. D. & Hurley, J. R. 2009, MNRAS, 395, 2326
Kim, M., Kim, Y.-M., Sung, K. H., Lee, C.-H., & Kwak, K. 2021, A&A, 650, A139
Kiuchi, K., Kotake, K., & Yoshida, S. 2009, ApJ, 698, 541
Kiuchi, K. & Yoshida, S. 2008, Phys. Rev. D, 78, 044045
Konno, K. 2001, A&A, 372, 594
Kontorovich, V. M. 2015, Astron. Rep., 59, 277
Kouveliotou, C., Dieters, S., Strohmayer, T., et al. 1998, Nature, 393, 235
Kramer, M., Stairs, I. H., Manchester, R. N., et al. 2006, Science, 314, 97
Kramer, M., Stairs, I. H., Manchester, R. N., et al. 2021, Phys. Rev. X, 11, 041050
Kundt, W. & Trümper, M. 1966, Z. Phys. A, 192, 419
Kuzur, D., Mallick, R., R, P., & Singh, S. 2021, arXiv e-prints, arXiv: 2104.00422
La Placa, R., Stella, L., Papitto, A., et al. 2020, ApJ, 893, 129

Lalazissis, G. A., Nikšić, T., Vretenar, D., & Ring, P. 2005, Phys. Rev. C, 71, 024312
Landau, L. D. 1932, Phys. Zs. Sowjet, 2, 46
Lander, S. K. 2013, Phys. Rev. Lett., 110, 071101
Lander, S. K. 2014, MNRAS, 437, 424
Lander, S. K., Andersson, N., & Glampedakis, K. 2012, MNRAS, 419, 732
Lander, S. K. & Jones, D. I. 2018, MNRAS, 481, 4169
Laor, A. 1991, ApJ, 376, 90
Lasky, P. D. 2015, Publ. Astron. Soc. Aust., 32, e034
Lasky, P. D., Zink, B., Kokkotas, K. D., & Glampedakis, K. 2011, ApJ, 735, L20
Lattimer, J. & Prakash, M. 2007, Phys. Rep., 442, 109–165
Lattimer, J. M. & Prakash, M. 2001, ApJ, 550, 426
Lim, Y., Bhattacharya, A., Holt, J. W., & Pati, D. 2021, Phys. Rev. C, 104, L032802
Lorimer, D. R. 2008, Living Rev. Relativ., 11, 8
Lorimer, D. R. 2012, Proc. Int. Astron. Union, 8, 237–242
Lorimer, D. R., Bailes, M., Dewey, R. J., & Harrison, P. A. 1993, MNRAS, 263, 403
Lorimer, D. R., Faulkner, A. J., Lyne, A. G., et al. 2006, MNRAS, 372, 777
Lovelock, D. 1971, J. Mat. Phys., 12, 498
Lugones, G. & Grunfeld, A. G. 2019, Phys. Rev. C, 99, 035804
Lynch, R. S., Boyles, J., Ransom, S. M., et al. 2013, ApJ, 763, 81
Lyubarsky, Y. 2014, MNRAS, 442, L9
Madsen, J. 1991, in Primordial Nucleosynthesis and Evolution of Early Universe, ed. K. Sato & J. Audouze, Astrophysics and Space Science Library (Springer Netherlands), 69–78
Manchester, R. N., Hobbs, G. B., Teoh, A., & Hobbs, M. 2005, AJ, 129, 1993
Margalit, B. & Metzger, B. D. 2017, ApJ, 850, L19
Markey, P. & Tayler, R. J. 1973, MNRAS, 163, 77
Markey, P. & Tayler, R. J. 1974, MNRAS, 168, 505
Mastrano, A., Lasky, P. D., & Melatos, A. 2013, MNRAS, 434, 1658
Mastrano, A., Suvorov, A. G., & Melatos, A. 2015, MNRAS, 447, 3475
Matt, G., Perola, G. C., Piro, L., & Stella, L. 1992, A&A, 257, 63
Melatos, A. & Payne, D. J. B. 2005, ApJ, 623, 1044
Mendes, R. F. & Ortiz, N. 2016, Phys. Rev. D, 93, 124035
Mereghetti, S., Pons, J., & Melatos, A. 2015, Space Sci. Rev., 191, 315
Metzger, B. D., Giannios, D., Thompson, T. A., Bucciantini, N., & Quataert, E. 2011, MNRAS, 413, 2031
Metzger, B. D., Margalit, B., & Sironi, L. 2019, MNRAS, 485, 4091
Miketinac, M. J. 1975, Ap&SS, 35, 349
Miller, J. M. 2007, ARA&A, 45, 441
Miller, M. C., Lamb, F. K., Dittmann, A. J., et al. 2019, ApJ, 887, L24
Miller, M. C., Lamb, F. K., Dittmann, A. J., et al. 2021, ApJ, 918, L28
Moffat, J. W. 2006, J. Cosmology Astropart. Phys., 2006, 004
Monaghan, J. J. 1965, MNRAS, 131, 105
Monaghan, J. J. 1966, MNRAS, 134, 275

Müller, J., Murphy, T. W., Schreiber, U., et al. 2019, J. Geod., 93, 2195
Nampalliwar, S., Bambi, C., Kokkotas, K. D., & Konoplya, R. A. 2018, Phys. Lett. B, 781, 626
Narayan, R. 1987, ApJ, 319, 162
Nojiri, S. & Odintsov, S. D. 2006, eConf, C0602061, 06
Nojiri, S. & Odintsov, S. D. 2006a, Phys. Rev. D, 74, 086005
Nojiri, S. & Odintsov, S. D. 2006b, Gen. Relativ. Gravit., 38, 1285
Nordtvedt, K. 1968, Phys. Rev., 170, 1186
Novak, J. 1998a, Phys. Rev. D, 58, 064019
Novak, J. 1998b, Phys. Rev. D, 57, 4789
Olausen, S. A. & Kaspi, V. M. 2014, ApJS, 212, 6
Oppenheimer, J. R. & Volkoff, G. M. 1939, Phys. Rev., 55, 374
Oron, A. 2002, Phys. Rev. D, 66, 023006
Ostriker, J. P. & Gunn, J. E. 1969, ApJ, 157, 1395
Ostriker, J. P. & Hartwick, F. D. A. 1968, ApJ, 153, 797
Ostrogradsky, M. 1850, Mem. Acad. St. Petersbourg, 6, 385
Ott, C. D., Dimmelmeier, H., Marek, A., et al. 2007, Class. Quantum Gravity, 24, S139
Özel, F. & Freire, P. 2016, ARA&A, 54, 401
Pacini, F. 1967, Nature, 216, 567
Padmanabhan, T. 2002, Phys. Rev. D, 66, 021301
Padmanabhan, T. 2003, Phys. Rep., 380, 235
Page, D., Lattimer, J. M., Prakash, M., & Steiner, A. W. 2004, ApJS, 155, 623
Pani, P. & Berti, E. 2014, Phys. Rev. D, 90, 024025
Papantonopoulos, E. 2015, Modifications of Einstein's Theory of Gravity at Large Distances, Lecture Notes in Physics (Springer International Publishing)
Papitto, A., Torres, D. F., Rea, N., & Tauris, T. M. 2014, A&A, 566, A64
Pappas, G., Doneva, D. D., Sotiriou, T. P., Yazadjiev, S. S., & Kokkotas, K. D. 2019, Phys. Rev. D, 99, 104014
Parker, M. L., Miller, J. M., & Fabian, A. C. 2018, MNRAS, 474, 1538
Parthasarathy, A., Johnston, S., Shannon, R. M., et al. 2020, MNRAS, 494, 2012
Peebles, P. J. E. & Ratra, B. 2003, Rev. Mod. Phys., 75, 559
Pili, A. G., Bucciantini, N., & Del Zanna, L. 2014, MNRAS, 439, 3541
Pili, A. G., Bucciantini, N., & Del Zanna, L. 2015, MNRAS, 447, 2821
Pili, A. G., Bucciantini, N., & Del Zanna, L. 2017, MNRAS, 470, 2469
Pili, A. G., Bucciantini, N., Drago, A., Pagliara, G., & Del Zanna, L. 2016, MNRAS, 462, L26
Platts, E., Weltman, A., Walters, A., et al. 2019, Phys. Rep., 821, 1
Pons, J. A. & Viganò, D. 2019, Living Rev. Comput. Astrophys., 5, 3
Popov, S. B. 2016, A&AT, 29, 183
Prendergast, K. H. 1956, ApJ, 123, 498
Psaltis, D. & Johannsen, T. 2012, ApJ, 745, 1
Punturo, M., Abernathy, M., Acernese, F., et al. 2010, Class. Quantum Gravity, 27, 194002
Raaijmakers, G., Greif, S. K., Hebeler, K., et al. 2021, ApJ, 918, L29
Raithel, C. A., Özel, F., & Psaltis, D. 2018, ApJ, 857, L23

Ramazanoğlu, F. M. & Pretorius, F. 2016, Phys. Rev. D, 93, 064005
Ramazanoğlu, F. M. 2017, Phys. Rev. D, 96, 064009
Ransom, S. M., Stairs, I. H., Archibald, A. M., et al. 2014, Nature, 505, 520
Rather, I. A., Rahaman, U., Dexheimer, V., Usmani, A. A., & Patra, S. K. 2021, ApJ, 917, 46
Raynaud, R., Guilet, J., Janka, H.-T., & Gastine, T. 2020, Sci. Adv., 6, eaay2732
Rea, N., Esposito, P., Turolla, R., et al. 2010, Science, 330, 944
Rea, N., Israel, G. L., Esposito, P., et al. 2012, ApJ, 754, 27
Reitze, D., Adhikari, R. X., Ballmer, S., et al. 2019, in BAAS, Vol. 51, 35
Riley, T. E., Watts, A. L., Ray, P. S., et al. 2021, ApJ, 918, L27
Risaliti, G., Harrison, F. A., Madsen, K. K., et al. 2013, Nature, 494, 449
Roark, J. & Dexheimer, V. 2018, Phys. Rev. C, 98, 055805
Roberts, P. H. 1955, ApJ, 122, 508
Rodríguez Castillo, G. A., Israel, G. L., Tiengo, A., et al. 2016, MNRAS, 456, 4145
Romani, R. W. 1990, Nature, 347, 741
Ronchi, M., Graber, V., Garcia-Garcia, A., Rea, N., & Pons, J. A. 2021, ApJ, 916, 100
Rosen, N. 1940, Phys. Rev., 57, 147
Rowlinson, A., O'Brien, P. T., Metzger, B. D., Tanvir, N. R., & Levan, A. J. 2013, MNRAS, 430, 1061
Roxburgh, I. W. 1966, MNRAS, 132, 347
Ruderman, M. 1995, J. Astrophys. Astron., 16, 207
Sahni, V. & Starobinsky, A. 2000, Int. J. Mod. Phys. D, 09, 373
Salgado, M. 2006, Class. Quantum Gravity, 23, 4719
Salgado, M., Martínez del Río, D., Alcubierre, M., & Núñez, D. 2008, Phys. Rev. D, 77, 104010
Salgado, M., Sudarsky, D., & Nucamendi, U. 1998, Phys. Rev. D, 58, 124003
Samuelsson, L. & Andersson, N. 2007, MNRAS, 374, 256
Santiago, D. I. & Silbergleit, A. S. 2000, Gen. Relativ. Gravit., 32, 565
Schubert, G. 1968, ApJ, 151, 1099
Shao, L., Sennett, N., Buonanno, A., Kramer, M., & Wex, N. 2017, Phys. Rev. X, 7, 041025
Shapiro, I. I. 1964, Phys. Rev. Lett., 13, 789
Shibata, M. & Sekiguchi, Y.-i. 2005, Phys. Rev. D, 72, 044014
Sieniawska, M. & Bejger, M. 2019, Universe, 5, 217
Silva, H. O., Macedo, C. F. B., Berti, E., & Crispino, L. C. B. 2015, Class. Quant. Grav., 32, 145008
Silva, H. O., Sakstein, J., Gualtieri, L., Sotiriou, T. P., & Berti, E. 2018, Phys. Rev. Lett., 120, 131104
Soldateschi, J. & Bucciantini, N. 2021, Galaxies, 9, 101
Soldateschi, J., Bucciantini, N., & Del Zanna, L. 2020, A&A, 640, A44
Soldateschi, J., Bucciantini, N., & Del Zanna, L. 2021, A&A, 645, A39
Soldateschi, J., Bucciantini, N., & Del Zanna, L. 2021, A&A, 654, A162
Sotani, H. 2012, Phys. Rev. D, 86, 124036
Sotani, H. 2015, Phys. Rev. D, 92, 104024
Sotani, H. 2017, Phys. Rev. D, 96, 104010
Sotani, H. & Kokkotas, K. D. 2005, Phys. Rev. D, 71, 124038

Sotiriou, T. P. 2006, Class. Quantum Gravity, 23, 5117
Spruit, H. C. 2009, in IAU Symposium, Vol. 259, Cosmic Magnetic Fields: From Planets, to Stars and Galaxies, ed. K. G. Strassmeier, A. G. Kosovichev, & J. E. Beckman, 61–74
Stairs, I. H., Thorsett, S. E., Taylor, J. H., & Wolszczan, A. 2002, ApJ, 581, 501
Staubert, R., Trümper, J., Kendziorra, E., et al. 2019, A&A, 622, A61
Staykov, K. V., Doneva, D. D., Popchev, D., & Yazadjiev, S. S. 2019, in American Institute of Physics Conference Series, Vol. 2075, American Institute of Physics Conference Series, 040006
Staykov, K. V., Popchev, D., Doneva, D. D., & Yazadjiev, S. S. 2018, Eur. Phys. J. C, 78, 586
Steiner, A. W., Hempel, M., & Fischer, T. 2013, ApJ, 774, 17
Stückelberg, E. 1938, Helv. Phys. Acta, 11, 225
Suvorov, A. G. 2018, Phys. Rev. D, 98, 084026
Taniguchi, K., Shibata, M., & Buonanno, A. 2015, Phys. Rev. D, 91, 024033
Tayler, R. J. 1973, MNRAS, 161, 365
Tayler, R. J. 1980, MNRAS, 191, 151
Thompson, C. & Duncan, R. C. 1993, ApJ, 408, 194
Thompson, C. & Duncan, R. C. 1995, MNRAS, 275, 255
Thompson, C. & Duncan, R. C. 1996, ApJ, 473, 322
Togashi, H., Nakazato, K., Takehara, Y., et al. 2017, Nuclear Phys. A, 961, 78–105
Tolman, R. C. 1939, Phys. Rev., 55, 364
Tomei, N., Del Zanna, L., Bugli, M., & Bucciantini, N. 2020, MNRAS, 491, 2346
Tomimura, Y. & Eriguchi, Y. 2005, MNRAS, 359, 1117
Touboul, P., Métris, G., Rodrigues, M., et al. 2017, Phys. Rev. Lett., 119, 231101
Trimble, V. 1987, ARA&A, 25, 425
Typel, S., Oertel, M., & Klaehn, T. 2013, arXiv e-prints, arXiv:1307.5715
Uryū, K., Gourgoulhon, E., Markakis, C. M., et al. 2014, Phys. Rev. D, 90, 101501
Uryū, K. b. o., Yoshida, S., Gourgoulhon, E., et al. 2019, Phys. Rev. D, 100, 123019
Ushomirsky, G., Cutler, C., & Bildsten, L. 2000, MNRAS, 319, 902
Usov, V. V. 1992, Nature, 357, 472
van Dantzig, D. & Dirac, P. A. M. 1934, Math. Proc. Camb. Philos. Soc., 30, 421
Van Nieuwenhuizen, P. 1981, Phys. Rept., 68, 189
Voisin, G., Cognard, I., Freire, P. C. C., et al. 2020, A&A, 638, A24
Wagoner, R. V. 1970, Phys. Rev. D, 1, 3209
Wallace, D. 2000, arXiv e-prints, arXiv:gr-qc/0004005
Watts, A. L., Krishnan, B., Bildsten, L., & Schutz, B. F. 2008, MNRAS, 389, 839
Weisberg, J. M., Nice, D. J., & Taylor, J. H. 2010, ApJ, 722, 1030
Wentzel, D. G. 1960, ApJS, 5, 187
Will, C. M. 2014, Living Rev. Relativ., 17
Will, C. M. 2018, Theory and Experiment in Gravitational Physics, 2nd edn. (Cambridge University Press)
Wilson, J. R. & Mathews, G. J. 2003, Relativistic Numerical Hydrodynamics, Cambridge Monographs on Mathematical Physics (Cambridge University Press)
Wilson, J. R., Mathews, G. J., & Marronetti, P. 1996, Phys. Rev. D, 54, 1317

Witten, E. 1984, Phys. Rev. D, 30, 272–285
Witten, L. 1962, New York: Wiley
Woltjer, L. 1960, ApJ, 131, 227
Woodard, R. P. 2015, arXiv e-prints, arXiv:1506.02210
Wright, G. a. E. 1973, MNRAS, 162, 339
Yakovlev, D. G., Gnedin, O. Y., Gusakov, M. E., et al. 2005, Nuclear Phys. A, 752, 590
Yang, J., Ayzenberg, D., & Bambi, C. 2018, Phys. Rev. D, 98, 044024
Yazadjiev, S. S. 2012, Phys. Rev. D, 85, 044030
Yazadjiev, S. S., Doneva, D. D., & Popchev, D. 2016, Phys. Rev. D, 93, 084038
Yoshida, S., Yoshida, S., & Eriguchi, Y. 2006, ApJ, 651, 462
Yusifov, I. & Küçük, I. 2004, A&A, 422, 545
Zdunik, J. L. & Haensel, P. 2013, A&A, 551, A61
Zhang, X., Liu, T., & Zhao, W. 2017, Phys. Rev. D, 95, 104027, arXiv: 1702.08752
Zhang, X., Niu, R., & Zhao, W. 2019, Phys. Rev. D, 100, 024038

Acknowledgments

I would like to thank my supervisors for having led and aided me through this complex but rewarding path and for having helped me grow immensely both from a professional and a human perspective. I will always remember your dedication, your support as well as the endless coffee breaks and the dreaded journal clubs.

Nothing of this would have been possible without the continuous support of my family and my friends. I know that there have been times of trouble, of cheerful joy, of shared passion and disagreement. The communal sentiment of belonging to the Arcetraz family. The relaxed lunches under the burning sun. The articulated curses against the vending machines. The artistic posters we used to personalise our offices. The mysteries we investigated. These are just a handful of the endless experiences that remain engraved in my memory. This winding path stops here and a new one lies ahead. I will never forget what you meant to me. I will never forget that Arcetri is home.